Doctoral Dissertation
Doctoral Program in Aerospace Engineering (38^{th}cycle)

Aerodynamics of a small-scale drone propeller in challenging operative conditions

By

Alessandro Grava

******

Supervisor(s):
Prof. Gioacchino Cafiero, Supervisor
Ing. Luis Bernardos, Co-Supervisor
Prof. Gaetano Iuso, Co-Supervisor

Doctoral Examination Committee:
Prof. Daniele Ragni, Referee, Delft University of Technology
Prof. Alex Zanotti, Referee, Politecnico di Milano
Prof. Francesco Avallone, Politecnico di Torino

Politecnico di Torino
2026

Declaration

I hereby declare that, the contents and organization of this dissertation constitute my own original work and does not compromise in any way the rights of third parties, including those relating to the security of personal data.

Alessandro Grava
2026

* This dissertation is presented in partial fulfillment of the requirements for **Ph.D. degree** in the Graduate School of Politecnico di Torino (ScuDo).

Vorrei dedicare la tesi a mio nonno, che ormai manca da tanti anni. Vivere nella tua vecchia casa durante l'ultimo anno di dottorato mi ha fatto tanto pensare a te

Acknowledgements

Sono stati 3 anni spaventosi ma fantastici e ricchi di emozioni. Chi mi conosce sa quando io sia ansioso e mi spaventino certe novità. Mi spaventava trasferirmi all'estero, mi spaventava avere un lavoro monotono e poco gratificante, mi spaventava fare CFD. Questi 3 anni mi hanno insegnato a darmi una calmata, respirare e buttarmi anche laddove sapevo che non sarei stato il migliore. Alla fine ne è valsa davvero la pena, perché ho imparato tanto e ne sono uscito più solido e sempre più curioso, con la voglia di continuare a studiare e sbagliare altre mille volte.

Per questo non posso che iniziare col ringraziare Gioacchino, il mio supervisor, che ha saputo rompermi le paehm spronarmi quando necessario, facendomi innamorare ancor più della materia e indirizzandomi con successo verso il mio futuro accademico. In secondo luogo, I would like to thank my co-supervisor, Luis. I arrived in ONERA knowing 3 French words, 2 Python commands, and 1 RANS simulation run in my entire career. You have been an amazing teacher and co-worker, making me overcome every expectation I had for my visiting period in Meudon. Now I can proudly state that I can deal with challenging simulations, I've become a good friend with Python, and I know at least 4 French words. Proseguo col ringraziare Jacopo, il mio secondo co-supervisore acquisito. Grazie a te ho imparato l'importanza per il dettaglio e per l'ordine sia negli esperimenti che nei paper. Non esiste titolo di un mio articolo che non sia stato rifinito in almeno 4 step da te parola per parola e non posso che ringraziarti per il meraviglioso risultato finale, di cui spero siate fieri anche voi come me. Un enorme grazie va al Professor Iuso, specialmente per l'ispirazione che mi ha dato nei vari corsi di Gasdinamica e Aerodinamica Sperimentale. So che è ancora deluso per il mio no a Dallara, ma parte di questo no è dovuta alla passione per l'insegnamento e per l'aerodinamica che mi ha trasmesso proprio lei durante i corsi e che ora voglio continuare a coltivare.

Non sarebbe stato lo stesso dottorato senza quei simpaticoni dei miei colleghi. Primi fra tutti gli sperimentali del lab, con cui ho trascorso inverni gelidi e estati bollenti in mezzo all'amianto. Fare esperimenti è roba da ricercatori tosti e il vostro supporto l'ha reso più facile, anche a chi come me tosto lo diventerà forse un giorno lontano. Grazie ai miei compagni di ufficio, in particolare al mio compagno di banco Pablo Escobar e all'esperto massimo spagnolo di aerodinamica di droni. Manuel, non hai idea di quanto tu mi abbia aiutato, con le infinite chiamate su Teams e i consigli su come usare il preconditioner. È stato davvero un piacere lavorare assieme e spero sinceramente di continuare a farlo quando sarai Professore Ordinario in qualche università spagnola. Last but not least, I would

like to thank my ONERA colleagues. Everyone in H2T unity warmly welcomed me and helped me when in need, showing a strong sense of unity. A special thought goes to my office coloc Johan, the man who would break every Spotify Wrapped record if he didn't download all of his music. You are truly an astonishing researcher and a very good friend. Uno speciale, specialissimo grazie va inoltre ai miei butei, con la speranza che ci ritroveremo tutti a lavorare assieme a Bruxelles un giorno (tranne il Dottore che si trasferirà in Egitto per evitare la pioggia). Anche le giornate più monotone sono diventate un bellissimo ricordo con voi, ma GIURO che verrò a trovarvi più spesso ora che siamo più vicini.

Siamo giunti ora agli amici di zona che mi accompagnano ormai da anni e sono stati parte di tutti i miei ringraziamenti di tesi. Tornare a Torino dopo l'esperienza a Parigi è stato meno triste sapendo che c'eravate voi ad accogliermi e scoprire che, nonostante tutto, le cose importanti non erano cambiate. Federico non ha ancora imparato a giocare a scacchi, Elia mi tratta sempre male, Radi non si è ancora tagliata le unghie da baddie e Thomas non ha ancora imparato a camminare a piedi. Una delle mie persone preferite al mondo ha sentito il richiamo e si è trasferita anche lei in zona, almeno temporaneamente. Ringrazio anche lei, Claudia, chissà se si ricorderà di me quando diventerà il Cristiano Ronaldo dell'intelligenza artificiale. È stato faticoso, ma sono anche riuscito a diventare amico di persone provenienti da altre parti di Torino. Persone nuove, come Giorgia e Mati, ma anche persone riscoperte come Marra e Matti. Grazie per tutte le serate (e che serate) nei posti più disparati, dall'Everness Chill Garden a un ponte sotto l'autostrada di Parigi. L'ultimo ringraziamento agli amici del cuore è invece destinato ai miei due angeli custodi di Parigi. Silvia, grazie per avermi accolto come un fratello e avermi lanciato in tutte le situazioni sociali. Insomma, diciamocelo, ormai siamo amici anche senza Clara. The second thought goes to Louis, the best coloc I have ever had. He will probably never understand this since he still has to practice a bit with his English, but I am sure he knows how much I love him. I miss annoying you and organising parties in our house. I still owe you a dinner!

Da buon torinese sono stato cresciuto con il credo che la miglior attrazione di Milano sia il treno per Torino. Com'è finita? Che all'inizio del dottorato ho portato a casa una milanese e me ne sono pure innamorato. Questa non si è ancora scollata e ha deciso di supportarmi e amarmi per tutti questi fantastici anni assieme (spero di aver ricambiato adeguatamente). Si è chiusa la porta del dottorato e ora se ne apre un'altra che finalmente ci permette di vivere appiccicati l'uno all'altro. Potrebbe essere Bruxelles, Rio de Janeiro o Bangkok, non ho paura di trasferirmi da nessuna parte se tu vieni con me. Grazie di tutto, ti amo.

Concludo ringraziando a famigghia, partendo dai nonni e dallo zio. Quando eravate lontani facevo di tutto per organizzare in compagnia i pranzi della domenica, piuttosto che i sabati sera. Il cibo non era altrettanto buono e le imitazioni dei sardi erano più scadenti, ma fortunatamente c'erano le vostre spezie a tirarmi su il morale. Grazie a quella buffona di mia sorella, la mia coinquilina della vita. Senza di te casa mia sarà molto più pulita, ma sicuramente più silenziosa. Pompare Pitbull e Tiziano Ferro non ha lo stesso sapore se non ci sei tu a fare smart working. So che ti mancherò, ma vedi di comportarti bene a Verona e prenderti sta patente. L'ultimo ringraziamento va a quei vecchietti dei

miei genitori. Potrei scrivere un'intera tesi per prendervi in giro, ma oggi vi voglio solo ringraziare per avermi amato, supportato e reso la persona che sono oggi. Torino mi mancherà, i miei amici e colleghi mi mancheranno, ma niente e nessuno mi mancherà come voi. Ovunque mi porterà la vita, spero che sarete in grado di fare da nonni ai miei figli, perché so che sareste fantastici, come siete stati dei fantastici genitori.

Grazie di cuore a tutti quelli a cui sto ancora simpatico e a quelli che invece sono forzati a starmi intorno e a sopportarmi. Amo la mia vita e amo tutti voi, grazie.

Abstract

The proliferation of small unmanned aerial vehicles (SUAVs) over the last decades has greatly increased the demand for compact, efficient, and reliable propulsion systems. Despite significant technological progress, small-scale propellers still suffer from low aerodynamic efficiency due to the low chord-based Reynolds numbers and the challenging operative conditions encountered in a typical mission profile. These challenges lead to unsteady loading and performance degradation, ultimately limiting flight endurance, payload capability, and platform stability. This thesis addresses these critical aerodynamic issues by conducting a comprehensive experimental and numerical investigation of an open-geometry, small-scale propeller operating in challenging scenarios, such as non-axial inflow and dynamic maneuvers.

An extensive experimental campaign was performed in the wind tunnel at Politecnico di Torino, using load measurements and planar Particle Image Velocimetry to characterize thrust, torque, and wake topology in both axial and cross-flow conditions. Large Eddy Simulations (LES) were then used to provide high-fidelity insights into the unsteady flow physics, including vortex dynamics, wake deflection mechanisms, and azimuthally varying blade aerodynamics. This numerical dataset enabled the formulation of a simplified wake-skew modelling approach suitable for propellers in cross-flow.

To explore transient operational conditions, a mid-fidelity Vortex Particle Method solver (VULCAINS), developed at ONERA, was validated against experiments and URANS simulations in steady-state conditions. The validated tool was subsequently employed to analyse maneuvering scenarios relevant to typical SUAV missions, including rapid rotational speed variations and propeller tilting. These analyses revealed the presence of load hysteresis, transient performance overshoots, and significant changes in the wake structure that are not captured under steady-state assumptions.

The findings deepen the current understanding of small-scale propeller aerodynamics and expand the available performance and wake database beyond classical axial-flow/hovering configurations. This work supports the development of more robust design and control strategies for next-generation SUAV propulsion systems.

Contents

List of Figures

List of Tables

Nomenclature

Other Symbols

α	angle of attack [°]
β	blade twist angle [°]
χ_{MB}	mean vortices skew angles computed with the momentum-based simplified approach
$\chi_{V_{ID}}$	mean vortices skew angles computed with the Γ_2 criterion from LES velocity fields
$\Delta\psi$	azimuthal angle swept by the blades per time-step [%]
$\dot{\theta}$	tilting rate $[°/s]$
Γ	blade dihedral angle [°]
Γ_2	scalar function for vortex edge detection according to the Γ_2 criterion
Γ_v	circulation of identified vortices [m^2/s]
Λ	blade sweep angle [°]
λ_i	non dimensional propeller's axial induced velocity, $\lambda_i = v'/\Omega R$
C_{CPU}	computational cost per core
μ	non dimensional cross-flow/forward flight advance ratio, $\mu = V_\infty/\Omega R$
ν	air kinematic viscosity [m^2/s]
Ω	propeller's rotational speed [rad/s]
ω_i	vorticity field along the i direction
$\overline{C_{Mx}}$	mean roll moment coefficient
$\overline{C_{Mz}}$	mean pitch moment coefficient

$\overline{V_i}$ time-averaged velocity along the i direction [m/s]

Φ velocity vectors orientation with respect to V_∞ [°]

ϕ_i POD spatial eigenfunctions along the i direction

ψ azimuthal angle swept by the blades

ρ air density [kg/m^3]

σ_k relative energy content of each POD mode

τ_w local wall shear stress value on the blades surface projected along the chordwise direction [N]

θ tilting angle [°]

c blade chord [m]

c_D non-dimensional blade element drag coefficient

c_f non dimensional friction coefficient on the blades' surface, $c_f = \frac{\tau_w}{\frac{1}{2}\rho(\Omega R)^2}$

c_L non-dimensional blade element lift coefficient

C_P non-dimensional integral power coefficient, $C_P = C_Q$

c_p non dimensional pressure coefficient on the blades' surface, $c_p = \frac{p-p_\infty}{\frac{1}{2}\rho(\Omega R)^2}$

C_Q non-dimensional integral torque coefficient, $C_Q = \frac{Q}{\rho\pi R^3(\Omega R)^2}$

C_T non-dimensional integral thrust coefficient, $C_T = \frac{T}{\rho\pi R^2(\Omega R)^2}$

f_0 enstrophy filter cutoff frequency [Hz]

J advance ratio, $J = \frac{V_\infty}{\Omega R}$

k turbulent kinetic energy [m^2/s^2]

k_χ wake topology modelling correction factor

$k_{1,2,3}$ corrective coefficients for C_P interpolation

L distance between the propeller's hub and the center of rotation in tilting maneuvers [m]

M Mach number

m_r acceleration rate [rpm/s]

n revolutions per minute [rpm]

N_S number of particle sources shed from the lifting lines per time-step

N_{crit} critical boundary layer disturbances integral amplification

p local pressure value on the blades' surface [N]

Q scalar used in the Q-criterion to identify vortex-dominated regions in a flow field [s^-2]

R propeller radius [m]

r reference coordinate along the propeller radius [m]

Re_c chord-based Reynolds number, $Re_c = \frac{c\Omega r}{\nu}$

s_{C_T} non-dimensional thrust per unit length along the spanwise direction

Ti turbulence intensity [%]

u' tangential induced velocity in the propeller's rotating frame [m/s]

v' propeller's axial induced velocity [m/s]

V_∞ inflow velocity [m/s]

V_{kT} relative kinematic velocity due to the tilting maneuvers [m/s]

W relative velocity seen by the blade element [m/s]

x reference axis parallel to the wind tunnel jet streamwise direction

x_c reference coordinate in the chordwise direction [N]

x_c/c_{Sep} non-dimensional chordwise coordinate where the flow separation occurs on the blade suction side

y reference axis perpendicular to x and parallel to the test section floor

z reference axis perpendicular to x and perpendicular to the test section floor

Acronyms / Abbreviations

BEMT Blade Element Momentum Theory

BPF Blade Passing Frequency

CFD Computational Fluid Dynamics

CSM Core Spreading Method

CVP Counter-rotating Vortex Pair

DNS Direct Numerical Simulation

DVM Diffusion Velocity Method

FMM Fast Multipole Method

HV Hub Vortex

LES Large Eddy Simulations

LSB Laminar Separation Bubble

NS Navier-Stokes

PIV Particle Image Velocimetry

POD Proper Orthogonal Decomposition

PSD Power Spectral Density

PSE Particle Strength Exchange

RO Rated Output

ROI Region of interest

SSTLM Shear Stress Transport turbulence model coupled with Langtry Menter transitional model

SUAV Small Unmanned Air Vehicle

TV Tip Vortices

UAM Urban Air Mobility

URANS Unsteady Reynolds-Averaged Navier Stokes

VPM Vortex Particle Method

VTOL Vertical Take-Off and Landing

Chapter 1

Introduction

1.1 Motivation

Over the last decade, the global interest in small unmanned aerial vehicles (SUAVs) has experienced a dramatic surge, driven by advancements in miniaturized electronics, battery technologies, and low-cost manufacturing processes [3]. The appeal of SUAVs lies in their peculiar technical features: lightweight structures, low energy consumption, high maneuverability, vertical take-off and landing (VTOL) capabilities, and compact footprints that enable deployment in constrained environments. These aircraft, typically characterized by a maximum take-off weight under 25 kilograms, have evolved from hobbyist gadgets into critical tools across both military (e.g. [4]) and civilian sectors (e.g. [5]). With operational capabilities ranging from territorial monitoring (e.g. [6]) and disaster assessment to package delivery (e.g. [7]) and precision agriculture (e.g. [8]), these small drones are now integral to the technological landscape of the 21st century.

While their applications have become increasingly diverse, SUAVs continue to face fundamental technical limitations. Chief among these is the inefficiency of their propulsion systems, particularly in terms of aerodynamic performance. Unlike full-scale rotorcraft, which mostly operate at high Reynolds numbers, SUAVs' propellers operate in the low Reynolds number regime [9]. Laminar to turbulent flow transition phenomena dominate, leading to a complex boundary layer behaviour, large laminar separations, and significantly reduced aerodynamic efficiency [10]. The propeller is the primary source of thrust and lift for most SUAVs, and thus any inefficiency in its aerodynamic design directly reduces the vehicle's endurance, payload capacity, and stability. Most off-the-shelf designs are suboptimal, either because they are scaled-down versions of larger propellers or because they are designed without sufficient attention to transitional phenomena. A focus is rather made on their durability and cost-effectiveness, leading to thick geometries often featuring excessive surface roughness. In practice, it translates into reduced efficiency, increased power consumption, and unpredictable aerodynamic loads. Given that SUAVs are usually powered by batteries with limited energy storage, even modest

improvements in the aerodynamic efficiency can result in substantial gains in flight time and payload capacity.

Another crucial point of SUAV performance involves non-ideal operative conditions. Most propellers are indeed designed to operate in on-design conditions, such as steady-state axial inflow or hovering. SUAVs, however, frequently operate under challenging off-design conditions, such as:

- non-axial inflow during forward flight or gust encounters,
- propeller-propeller interference in multicopter configurations,
- rapid transient maneuvers such as pitching, rolling, or yawing,
- sudden changes in rotational speed due to control inputs or obstacle avoidance.

These conditions introduce complex unsteady flow phenomena that significantly affect the efficiency, stability, noise, and structural integrity. In these scenarios, the flow across a given blade changes not only in magnitude but also in direction over time, causing dynamic stall, cyclic loading, and hysteresis effects that are difficult to predict using steady-state models. Non-axial inflow conditions, for instance, result in flow non-uniformity across the propeller disk, which leads to asymmetric loading [11–13]. In such scenarios, the interaction between unsteady aerodynamics, control systems, and vehicle dynamics becomes critical. Yet, the bulk of aerodynamic data and models available in the literature focus on steady-state hovering (e.g. [14–17]), axial flow conditions (e.g. [18, 19]), creating a knowledge gap that limits optimization and design efforts for real-world scenarios.

The motivation of this thesis stems from the need to improve the aerodynamic understanding and prediction capabilities for small-scale drone propellers, particularly operating under non-axial inflows or dynamic operative conditions, which are furthermore characterized by low Reynolds numbers. For this purpose, an open-geometry small-scale propeller is considered to obtain results that are repeatable and extendible. The analysis is carried out through the use of a multitude of techniques, ranging from an experimental approach to numerical methodologies of high and mid-fidelity. The focus is initially made on the cross-flow condition, initially approached with an experimental campaign conducted in Politecnico di Torino. This campaign involved the use of planar Particle Image Velocimetry (PIV) and load sensors, respectively, for the velocity field and performance evaluation. The experimental campaign was then used to validate a numerical high-fidelity dataset of Large Eddy Simulations (LES) in similar conditions. With the multitude of data available from the LES campaign, the analysis of the cross-flow condition was expanded, additionally leading to a simplified model for the wake deflection prediction. A mid-fidelity code from the vortex particle method (VPM) category is then introduced for the simulation of the more computationally demanding maneuvers, such as dynamic rotational speed variations or tilting. The code was in-house built by ONERA and named VULCAINS [20–22]. It is initially validated through the comparison with higher fidelity methodologies, such as Unsteady Reynolds-Averaged Navier-Stokes (URANS) simulations and an experimental campaign, assessing the

code's capability of correctly predicting the small-scale propeller aerodynamics in on-design conditions. The maneuvers are subsequently simulated, assessing their impact on the propeller's performance and induced flow field. The results shown in this thesis aim to contribute new knowledge toward a more robust and efficient design of SUAV propellers, closing existing gaps in the understanding of their aerodynamic behaviour under some non-ideal operative conditions and laying the groundwork for future studies, mainly on dynamic maneuvers, which are still scarce in the present literature.

1.2 Literature review

1.2.1 Low Reynolds numbers propellers and airfoil aerodynamics

Recent studies have specifically focused on the transitional aerodynamics of isolated airfoils to improve the understanding of the fluid dynamics phenomena that occur on small-scale propellers. This is done on one side to improve the airfoil design to be implemented in 3D blades, but additionally to extract the airfoil polars (lift, drag, and moment coefficients as a function of the angle-of-attack, Reynolds, and Mach number) for lifting lines/surfaces approaches. The aerodynamic behaviour of airfoils at low chord-based Reynolds numbers ($Re_c = \frac{cW}{\nu}$, being c hereby the airfoil chord, W the relative velocity, and ν the kinematic viscosity) represents one of the most nuanced and challenging areas within the field of rotary-wing fluid dynamics. This is especially true for small unmanned aerial vehicles (SUAVs), where propeller blades typically operate in flow regimes that differ dramatically from those of larger aircraft. In these regimes, defined approximately by Re_c below 1,000,000, and often between 10,000 and 100,000, the flow undergoes complex transitional phenomena that are markedly sensitive to geometry [23], angle of attack [10], freestream turbulence, and surface conditions [24]. Such effects challenge both experimental reproducibility and numerical simulation representativeness.

In large-scale aeronautical applications, where Re_c often exceeds 1,000,000, the boundary layer transitions to turbulence early in its development. The flow typically remains attached along the surface, separating only near the trailing edge under high adverse pressure gradients, as represented in Figure 1.1(a). However, when the Reynolds number drops below this threshold, the aerodynamic characteristics of airfoils differ considerably. At intermediate Re_c, roughly between 500,000 and 1,000,000, laminar flow separation emerges on the suction side near the leading edge, followed by reattachment further downstream, as illustrated in Figure 1.1(b). This leads to the formation of a laminar separation bubble (LSB) [9], a flow structure that fundamentally alters pressure recovery and increases drag, even as it maintains attached flow along the rest of the chord.

As Re_c is further decreased until around 50,000, the LSB becomes larger and more unstable. The extent of laminar flow along the chord diminishes, and the point of reattachment shifts downstream, sometimes with the LSB extending as much as 40 percent of the chord length, as represented in Figure 1.1(c). Under such conditions, the airfoil is subject to enhanced parasitic drag and unpredictable lift

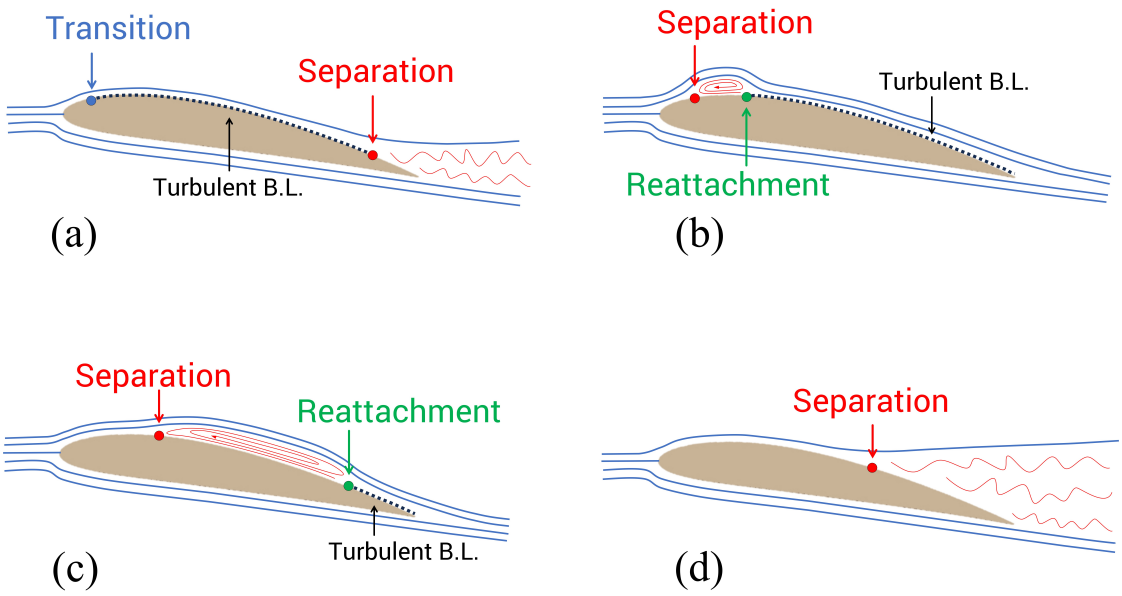

Fig. 1.1 Schematic illustration of flow evolution around a 2D airfoil at (a) $Re_c > 1,000,000$, (b) $1,000,000 > Re_c > 500,000$, (c) $500,000 > Re_c > 50,000$, (c) $Re_c < 50,000$.

behaviour. Near the stall, the flow may exhibit alternating phases of reattachment and full separation, introducing aerodynamic hysteresis and unsteady loads [25]. This regime is of particular concern for SUAV propellers, whose efficiency and control characteristics are critically dependent on precise lift and drag predictions under a range of operational angles of attack.

When Re_c drops below 50,000, laminar separation may persist over most of the airfoil's suction side, with the shear layer failing to reattach altogether, as shown in Figure 1.1(d). This scenario results in a dramatic degradation of aerodynamic performance, with diminished lift and significantly increased pressure drag. The flow becomes increasingly dominated by viscous effects, and the airfoil effectively operates in a near-stalled condition across its entire operative range. Such flow behaviour not only limits propulsive efficiency but also introduces vibration, instability, and control challenges for the vehicle [10].

A critical factor that exacerbates these effects at low Re_c is the heightened sensitivity of the boundary layer to the level of turbulence in the freestream. As shown in the study by Wang et al. [24], increasing the freestream turbulence intensity can significantly alter the transition dynamics. Turbulence tends to destabilize the laminar boundary layer, delaying separation and promoting earlier transition. This, in turn, supports the formation of an LSB in regions where otherwise a full separation might occur. While beneficial in some contexts, this turbulence-induced transition is not uniformly desirable, as it introduces variability in performance and complicates modelling strategies. Moreover, its influence becomes negligible at Re_c higher than around 50,000, emphasizing its specificity to the very low-Re_c regime.

The airfoil's geometry plays an equally pivotal role in determining its aerodynamic response in these conditions. Thickness, camber, and the position of maximum thickness all exert significant influence on boundary layer stability and separation characteristics. Ma et al. [23] demonstrated that increasing the relative thickness of the airfoil tends to enlarge the LSB and decrease the lift-to-drag ratio, particularly at low angles of attack. This is primarily because the separation point moves upstream, reducing the effective laminar evolution and increasing the adverse pressure gradient over the airfoil surface. Conversely, shifting the position of maximum thickness toward the trailing edge can improve the overall c_L/c_D performance by stabilizing the laminar boundary layer and delaying separation. However, such geometrical alterations are not without trade-offs. Trailing-edge thickening, for example, may compromise maximum lift and deteriorate stall behaviour, necessitating a balance between cruise efficiency and maneuvering performance. Designing airfoils optimized for such environments demands a sophisticated understanding of the interplay between geometry, turbulence, and transitional mechanisms. The behaviour of the LSB, for instance, is influenced not only by the boundary layer profile but also by pressure gradient distributions, which are directly linked to the curvature and thickness distribution of the airfoil. While thin, highly cambered airfoils may offer enhanced lift at moderate angles of attack, they are often prone to early stall due to leading-edge separation. On the other hand, thicker sections may stabilize the flow at higher angles but incur performance penalties in cruise.

Adding another layer of complexity is the phenomenon of flow hysteresis that arises near stall [25]. At low Reynolds numbers, the transition from attached to separated flow and back is not symmetric. That is, the aerodynamic forces and moments experienced by the airfoil during increasing angle of attack differ from those during the decreasing phase. This hysteresis is particularly evident in the pitching moment and contributes to control difficulties in rapidly maneuvering SUAVs.

1.2.2 Non-axial inflow and forward flight conditions

In typical mission profiles, propellers are frequently exposed to non-axial inflows, especially during translational motion or when subjected to environmental disturbances such as gusts and wind shears. A non-axial inflow can be referred to as cross-flow or edgewise flow if it is perpendicularly oriented to the propeller's rotation axis. This scenario introduces a fundamental complexity in the understanding and predicting the propellers' performance, efficiency, and wake behaviour. Unlike the case of hovering or axial inflow, non-axial inflow conditions impose spatial and temporal variations in the angle of attack across the propeller disk. Each blade element, during its rotation, encounters a continuously changing relative inflow direction and magnitude [26, 27]. As a result, the effective angle of attack, the local Reynolds number, and the aerodynamic loading of each section become functions of both the azimuthal position and the flight condition. This introduces unsteady and non-uniform loads that influence thrust, torque, and moment coefficients, as well as flow separation and dynamic stall behaviour. While classical helicopter aerodynamics has long addressed similar problems, especially in forward

flight [28–30], the conditions faced by small drones introduce unique challenges. The low-Re_c regime (where, in propellers, Re_c is usually calculated considering the blade's chord located at around 75% of the radial extension), typical of SUAVs' propellers, causes the boundary layer to remain laminar over a significant portion of the blade. This makes the flow more sensitive to variations in angle of attack and more susceptible to early separation. Additionally, SUAV rotors typically lack blade pitch control, which limits their capacity to adjust for asymmetrical inflow and further complicates the aerodynamic response. Recent literature has sought to explore these effects in the context of small-scale fixed-pitch propellers. Notably, the studies by Cerny and Breitsamter [11], Theys et al. [12], and Moreira et al. [31] examined how non-axial inflows impact thrust and torque variation at different inflow angles and advance ratios. These works highlighted that even modest deviations from axial flow can lead to a significant decline in performance. The interaction of the rotating blade with an oblique inflow causes uneven aerodynamic loading, which not only introduces significant periodic oscillations in forces and moments over each revolution but also affects the time-averaged loads.

The wake behaviour under non-axial inflow is of particular concern for applications involving multicopters, distributed propulsion systems, and urban air mobility vehicles (UAM), where propellers often operate in proximity. In such configurations, the wake of one propeller can interfere with another [32], generating inflow distortions that are both spatially and temporally unsteady. Instead of being shed axisymmetrically downstream, the wake is deflected and distorted [11, 33], depending on the flight direction and the propeller's orientation. This leads to regions of increased turbulence intensity and potential recirculation zones, both of which are problematic for precision flight and control. Furthermore, at a significant inflow velocity, the formation of a counter-rotating vortex pair (as in jets in cross-flow [34]) can be observed [35], further complicating this picture. The phenomenon of dynamic stall, well documented in helicopter literature [2, 27], becomes increasingly relevant in this context. As the blade rotates through regions of high relative inflow and then enters shielded or reversed-flow zones, the angle of attack can vary rapidly. If this variation exceeds the static stall angle, flow separation occurs, followed by vortex shedding and delayed reattachment. The resulting unsteady lift and moment behaviour leads to dynamic overshoots and hysteresis effects that are difficult to predict with quasi-steady models. While such effects are often mitigated in helicopters through active blade pitch control and complex blade articulation, SUAV propellers generally lack these mechanisms, making them more susceptible to performance degradation and control anomalies.

Beyond vehicle performance, the implications of non-axial inflow extend into application-specific challenges. In precision agriculture [35, 36], for instance, the ability of the propeller-induced flow to effectively disperse chemical agents such as pesticides or fertilizers depends on the wake behaviour. When the flow is deflected or distorted, the spatial distribution of droplets becomes uneven, reducing application efficiency and increasing the risk of environmental contamination. The strong vortex structures indeed can transport particles over long distances away from the intended target zone [37]. The relevance of non-axial inflow investigations also extends to safety in swarm flight and obstacle-rich environments [5, 38, 39]. As drones maneuver around buildings, trees, or other aerial vehicles, they

frequently encounter non-uniform and rapidly changing flow fields. In these cases, local gusts, wake interference, and flow separation become dominant factors in determining flight trajectory and stability. The absence of real-time flow sensing or adaptive control surfaces in many SUAV platforms exacerbates these vulnerabilities.

Thus, a robust understanding of how non-axial inflow alters aerodynamic forces and wake evolution is crucial for developing resilient control laws and stability augmentation systems. In applications ranging from package delivery and agricultural monitoring to emergency response and surveillance, drones navigate complex and unpredictable environments; their ability to maintain stable flight and deliver consistent performance hinges on accurately predicting and compensating for the aerodynamic disturbances induced by non-axial inflows. In summary, the study of non-axial inflow conditions is not a marginal consideration but a central aspect of SUAV aerodynamics. The deviation from the ideal axial inflow condition, whether due to vehicle motion, environmental effects, or rotor interactions, introduces a host of unsteady aerodynamic phenomena that affect performance, stability, and control. Addressing these issues requires a combination of advanced modelling techniques, high-resolution experimentation, and robust aerodynamic understanding. In this thesis, the cross-flow condition is explored through experimental techniques and a follow-up LES campaign to obtain a comprehensive and global understanding of the phenomenon.

1.2.3 Dynamic operative conditions

SUAVs are often tasked with performing rapid maneuvers during a typical mission profile. Unlike fixed-wing aircraft that primarily operate in quasi-steady flight conditions or large rotorcraft with mechanical and computational support for gradual control transitions, SUAVs frequently perform abrupt tilting, acceleration, deceleration, or thrust variations in response to control commands or environmental disturbances. These maneuvers might significantly affect the aerodynamics of the propellers, introducing transient flow phenomena that challenge both aerodynamic predictability and structural integrity. Such maneuvers raise regulatory and certification challenges, especially in the context of autonomous operation [40]. Vehicles that cannot maintain stable flight under transient maneuvers may not be allowed to operate in public airspace, particularly near people or infrastructure. Standards for UAV reliability increasingly include requirements for handling gusts, performing emergency avoidance maneuvers, and recovering from degraded flight states, all of which are directly influenced by the aerodynamics of dynamic response. Therefore, the need for a predictive framework that links maneuver profiles to aerodynamic behaviour and structural loading is foundational to the future deployment of autonomous aerial systems.

Dynamic maneuvers in SUAVs can be broadly categorized into smooth transitions, such as pitching into a new flight angle or ascending with increased thrust, and impulsive or high-rate movements, such as evasive turns or gust rejection. In either case, the underlying issue is that the propellers are subjected to unsteady conditions, and the standard assumptions of steady or even quasi-steady aerodynamics

might no longer be valid. Each change in propeller orientation, angular velocity, or surrounding flow direction gives rise to unsteady aerodynamic forces and induced wake, which in turn influence vehicle attitude, control responses, and flight stability.

One of the primary effects of such maneuvers is indeed the induction of transient loading on the propeller blades. These loads arise from the combined influence of the blade's angular acceleration or deceleration and the variation in inflow distribution resulting from vehicle motion. Möhren et al. [41] showed that during significantly rapid dynamic rotational speed variations, propellers experience structural deformations that differ significantly from those observed under steady-state conditions. The dynamic inertial loads, especially in high acceleration phases, contribute to blades' bending and torsion, which in turn modify the effective pitch distributions. This coupling between structure and aerodynamics introduces non-linearities in the thrust response, leading to discrepancies between commanded and achieved performance. Rapid rotational speed changes induce torque transients through the drive shaft and motor, potentially causing fatigue loading that accumulates over repeated missions. Zosimovych [42] analysed such transient dynamics during VTOL transition phases and proposed methodologies for predicting blade deformation and fatigue life. The work revealed that traditional safety margins based on static loading scenarios may underestimate the cyclic stresses encountered during real-world operations. For electric SUAVs, which often rely on lightweight composite materials with directional stiffness properties, the accumulation of such fatigue loads can lead to premature failure if not considered in the design process.

The effect of the rotational speed variation is not only structural but also deeply fluid dynamic. Changes in rotation rate lead to rapid shifts in blade tip velocity and local Reynolds number, thereby altering the boundary layer characteristics along the blade. As the flow transitions from laminar to turbulent, separation bubbles may form, detach, or collapse in unpredictable ways. These dynamics affect lift and drag production in a time-dependent manner, often leading to oscillatory behaviour in thrust and torque output. In cases of deceleration, reverse flow phenomena may even occur near the root, further complicating the flow field.

The acoustic implications of dynamic maneuvers are also fundamental to evaluate. As noted by Bergmann et al. [43], changes in rotor speed and orientation result in fluctuating loading on the blades, which generates broadband noise that differs from tonal emissions observed in steady flight. Their analysis of VTOL vehicles revealed that noise peaks are strongly correlated with periods of rapid acceleration and horizontal transition, suggesting that control strategies should consider not only aerodynamic but also acoustic optimization. This is particularly important in urban environments, where noise constraints may limit drone operation, especially in proximity to sensitive areas such as hospitals, schools, or residential buildings.

In addition to the acoustic impact, flight control stability is closely tied to how dynamic maneuvers influence the thrust vector and force distribution. Pavel [44] investigated control systems for VTOLs undergoing pitch and RPM variations, highlighting the importance of coupling control inputs to achieve

smoother transitions and reduced oscillatory behaviour. By jointly tuning the pitch angle and rotational speed, the study showed that more stable and efficient transitions could be achieved, especially in the presence of external disturbances. This suggests that the design of SUAVs' control systems must account not only for steady-state gains and delays, but also for the transient aerodynamic response of the propellers.

The thrust vectoring that emerges during tilting maneuvers is another critical aspect. As the rotor axis is tilted from the vertical direction to accommodate translational motion, the thrust vector shifts, and the rotor begins to act both as a lift and propulsion source. This alters the inflow angle across the rotor disk and induces asymmetrical loading on the blades. The combination of angular velocity and tilting motion results in time-varying effective angles of attack, leading to localized flow separation, delayed reattachment, and, in some cases, dynamic stall. The extent to which these phenomena affect performance depends on blade geometry, rotation speed, and maneuver aggressiveness.

Experimental exploration of these phenomena is not straightforward. Wind tunnel setups typically focus on steady-state conditions or slow transitions due to the limitations of actuation systems and measurement response time. To explore dynamic maneuvers, specialized rigs with rapidly controllable pitch mechanisms or variable-speed drives are required. Load sensors must have high temporal resolution to capture transient spikes, while flow visualization tools like high-speed PIV must be synchronized to track rapid changes in vorticity and separation. From a numerical perspective, such effects are challenging to capture using traditional high-fidelity approaches, mostly due to the prohibitive computational cost. Different from steady-state conditions, dynamic maneuvers must be entirely simulated, and even fractions of a second can be excessively expensive. Furthermore, computing averaged quantities requires the repetition of the same test multiple times. Mid-fidelity tools such as VPM stand out in this context and are used in the present work. Maneuvers are straightforward to implement, and no mesh is required. The reduced computational cost makes these simulations also affordable for various repetitions of the tests. However, they still depend heavily on accurate airfoil polars, notoriously difficult to measure or compute for low-Re_c conditions.

In conclusion, the study of dynamic maneuvers in SUAVs is essential for developing robust, efficient, and safe flight capabilities. These maneuvers introduce time-dependent aerodynamic forces that are challenging to predict but crucial for understanding control stability, structural integrity, acoustic footprint, and vehicle performance. The complexity of modelling these effects, the difficulty of replicating them experimentally, and their relevance across mission scenarios make them a central theme in modern drone research. The present thesis particularly focuses on the rotational speed variations and tilting maneuvers, aiming to provide a deeper understanding of transient behaviour in small-scale propellers and showing the suitability of mid-fidelity tools such as the VPM, further confirming the necessity of enhanced efforts in the development of these methodologies for a bright future of SUAVs in the unmanned air mobility.

1.3 Chapters summary

This thesis compiles the research work conducted throughout the Ph.D. path and presents it across dedicated chapters.

Chapter 2 provides a detailed description of the open-geometry propeller selected as the case study for this thesis. The chapter also outlines the experimental and numerical methodologies employed for its aerodynamic characterization. It begins with a thorough presentation of the experimental setup, including the wind tunnel setup and instrumentation, and proceeds to report the outcomes of the wind tunnel campaign that was carried out for the flow characterization before the propeller testing. The numerical tools implemented throughout the thesis are furthermore presented, with a particular emphasis on the ONERA-developed VPM solver, VULCAINS. This tool is validated through the comparison with higher-fidelity methods and experimental data, establishing its accuracy in simulating the propeller's aerodynamics in steady-state operative conditions. This chapter concludes with a summary of the most relevant data reduction techniques used in the analyses.

Chapter 3 is devoted to the investigation of the propeller's aerodynamic performance under cross-flow conditions. A detailed analysis of this operative condition is conducted with the use of experimental techniques and a subsequent LES campaign.

Chapter 4 focuses on the unsteady aerodynamic behaviour of the propeller during transient maneuvers. These include dynamic variations in rotational speed and tilting motions, which are simulated using the validated VPM code. The results provide insight into the propeller's performance and flow structures under maneuvering conditions, which are critical for SUAV applications.

Finally, **Chapter 5** concludes the thesis by summarising the key findings and outlining potential directions for future research.

1.4 Publications

Journal articles:

- Grava A., Serpieri J., Iuso G., Bernardos L., and Cafiero G. (2024) "*Experimental investigation of a small drone propeller aerodynamics in forward flight*", AIAA Journal.
- Grava A., Serpieri J., Bernardos L., and Cafiero G. (under review), "*Aerodynamics of small-scale propellers undergoing dynamic variations of rotational speed*", AIAA Journal.
- Grava A., Serpieri J., Bernardos L., and Cafiero G. (under review) "*Aerodynamics of small-scale propellers undergoing dynamic tilting maneuvers*", AIAA Journal.

- Carreño Ruiz M., Grava A., Serpieri J., Cafiero G., and D'Ambrosio D. (under review), "*Low-Reynolds number propellers in cross-flow: wake dynamics and aerodynamic performance*". Journal of Fluid Mechanics.

Conference proceedings:

- Grava A., Picillo M., Serpieri J., Iuso G., Bernardos L., and Cafiero G. (2024) "*Aerodynamic investigation of a drone propeller in cross-flow*", AIAA SCITECH 2024 Forum, 8-12 January 2024, Orlando, FL.
- Grava A., Serpieri J., Bernardos L., and Cafiero G. (2025) "*Multi-fidelity analysis of a small-scale propeller using VPM against URANS and experimental data*", AIAA AVIATION FORUM 2025, 21-25 July 2025, Las Vegas, NV.

Chapter 2

Methodologies

Understanding the aerodynamic performance of SUAVs' propellers requires a combination of experimental and numerical tools, each with its strengths, limitations, and applicable scales. This chapter explores the methodologies employed to assess the aerodynamics of a small-scale propeller under different conditions, ranging from wind tunnel testing to numerical simulations of high- and mid-fidelity.

Experimental investigations represent the cornerstone of aerodynamic research in the propellers' field, as they provide the most tangible and trustworthy means of assessing the flow physics, directly capturing the intricate interplay of laminar to turbulent transition, separation, and unsteady vortex dynamics while simultaneously reflecting the real structural and manufacturing characteristics of the blades. Advanced methodologies such as PIV allow for an accurate assessment of the flow characteristics. PIV is a widely used non-intrusive technique for measuring velocity fields in fluid flows [45]. The method consists of seeding the flow with tracer particles, which are illuminated by a laser sheet and recorded by cameras. The particle displacement between two successive images is then evaluated through cross-correlation, providing a detailed reconstruction of the instantaneous velocity field over the measurement plane. By averaging these measurements in time, PIV enables an accurate description of mean flow structures and serves as a reliable experimental benchmark for validating numerical simulations. This methodology has been widely used in propellers' aerodynamics, assessing the flow physics in the blades' proximity ([19]) and in the induced wake ([16]). Experimental campaigns specific to small-scale propellers, however, face two major difficulties. First, the forces involved are often very small, which makes their measurement prone to noise and uncertainty. Highly sensitive small-scale load cells are required to capture lift, drag, and thrust with acceptable accuracy. Second, the propeller geometry itself presents manufacturing challenges: the small size of blades increases the impact of imperfections, such as surface roughness and trailing edge inaccuracies, which can fundamentally alter flow characteristics in laminar or transitional regimes. The small thickness additionally makes the blades prone to bending and torsion in on and off-design conditions. While this last feature is not

itself a downside, it might be complicated to account for these deformations in numerical simulations, leading to non-negligible deviations with respect to the experimental measurements.

Numerical simulations have indeed become indispensable tools in the analysis and design of SUAV propellers. To pursue a high-fidelity solution, scale-resolving simulations such as LES can be employed. LES is a turbulence modelling approach in which the largest, energy-containing turbulent structures are directly resolved, while only the smaller scales are modelled using a subgrid-scale model. By applying a spatial filter to the NS equations, LES captures the unsteady, three-dimensional nature of the large eddies that dominate momentum and energy transport, providing an accurate description of turbulent flows [46]. However, this high fidelity comes at a significantly higher computational cost, especially near solid boundaries where fine spatial and temporal resolutions are required. In particular, the LES approach usually necessitates finer meshes and higher-order discretisation schemes to minimise numerical diffusion and accurately resolve vortex structures.

The most widespread methods are, however, RANS and URANS approaches, which have found wide applicability in the simulation of SUAVs [47–49]. Reynolds-averaged approaches reach a lower level of fidelity than LES, but are characterised by a significantly reduced computational burden, which makes them pivotal for industrial applications. In particular, RANS are obtained by decomposing each flow variable into mean and fluctuating components and applying a time- or ensemble-averaging procedure to the NS equations [50]. This process introduces additional terms, the Reynolds stresses, which account for the effect of turbulence on the mean flow and require closure through turbulence models. These simulations are relatively affordable in terms of computational resources and are widely used for predicting global performance metrics, such as thrust and torque, under steady-state conditions. URANS extends this framework by solving the unsteady form of the NS equations in an inertial reference frame, typically using rotating grids or body-fitted meshes to capture the motion of the blades. This method is more computationally demanding but allows for the resolution of periodic blade passing effects, unsteady wake development, and some forms of vortex shedding.

Finally, mid-fidelity methods stand out especially when it is required to reduce the computational cost and the simulation complexity. A popular modelling approach is the VPM [51–53, 20], which discretises the vorticity field into Lagrangian particles that are convected with the flow. Acceleration techniques such as the Fast Multipole Method (FMM) help mitigate the computational cost by grouping particle interactions. Unlike traditional panel or blade element methods, VPM does not assume steady-state or axisymmetric flow, making it well-suited for modelling unsteady dynamic conditions. It can furthermore handle multiple propellers, complex wake mixing, and non-axial inflow without requiring direct mesh connectivity between vortical structures [54]. The lifting surfaces are typically simulated with the lifting line/panels approach to keep the computational cost low. Novel codes such as VULCAINS additionally implement a hybrid approach [55], which combines a high-fidelity Eulerian solver near solid boundaries to resolve boundary layers and generate vortices, with a Lagrangian vortex particle method to efficiently simulate and transport vortices in the far field, reducing the computational cost compared to full URANS or LES simulations while maintaining high accuracy near the walls.

Codes such as DUST [56] and FLOWUnsteady [53] also implement variations of the vortex particle approach, enabling variable-fidelity simulations by adjusting the particle resolution. These tools have gained popularity in the study of distributed propulsion systems and urban air mobility vehicles, where multiple rotors interact within constrained environments. Their ability to resolve complex wake phenomena makes them attractive for scenarios where control robustness, acoustic emissions, and rotor-rotor interference are of concern.

2.1 Definition of a reference propeller geometry

The aerodynamic analyses of this thesis are carried out on an open-geometry propeller, defined by taking the propeller employed in [57] as a reference and then scaling it for the current purpose to a radius R = 7.5 cm. It originally derives from a two-bladed APC-9x6 model, by reshaping each profile from r/R = 0.2 to the tip with NACA 4412 profiles, where r is the reference coordinate along the propeller radius. An elliptical root section is merged with such profiles starting from the hub to r/R = 0.2. The blade geometry is defined by variable distributions of chord (c), twist angle (β), sweep angle (Λ), and dihedral angle (Γ) along the bladespan direction. β is the NACA 4412 profiles' absolute pitch angle around the first quarter-chord. Λ is the in-plane azimuthal offset of the blade. Finally, Γ is the out-of-plane deflection of the blade relative to the propeller's plane. The propeller's CAD is shown in Figure 2.1(a). The chord and the three angles distributions along the bladespan direction are displayed in 2.1(b).

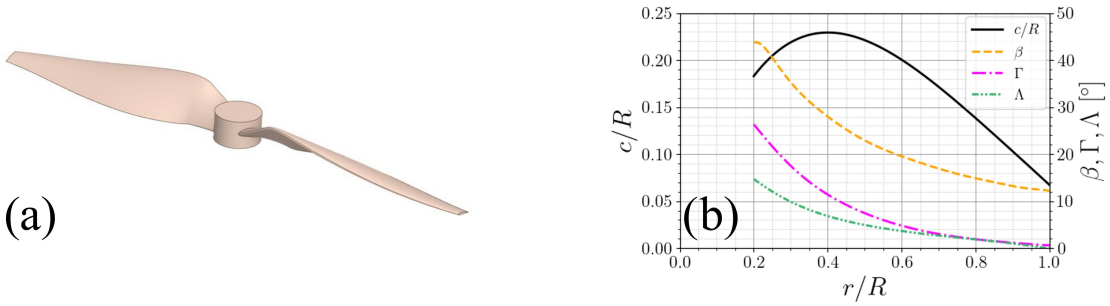

Fig. 2.1 (a) CAD view of the reference propeller, (b) blades' geometrical features along the blade span direction

2.2 Experimental methodologies

2.2.1 Particle Image Velocimetry (PIV)

The flow field surrounding the propeller was investigated via PIV, which is a non-intrusive optical measurement technique that has become one of the standard tools for the experimental investigation of

fluid flows [45]. The content of this section is intended to provide an overview of the principles and capabilities of the PIV, while a more comprehensive coverage can be found, for instance, in the work of Raffael et al. [58].

PIV's main advantage lies in the ability to provide instantaneous, two- or three-dimensional velocity fields over an extended region, in contrast to point-wise measurement techniques such as hot-wire anemometry or Laser Doppler Velocimetry. This makes PIV particularly well-suited for the study of complex and unsteady flows, such as wakes, vortices, or turbulent boundary layers. The basic principle of PIV relies on seeding the flow with tracer particles that follow the motion of the surrounding fluid. These particles are illuminated by a thin laser sheet, which defines the measurement plane, and their scattered light is recorded by one or more cameras. By acquiring two successive images separated by a short time interval Δt, the particle displacement within small interrogation windows can be measured. Assuming that the particles act as flow tracers, their displacement provides a direct estimate of the local fluid velocity as: $\vec{u}(\vec{x}) \approx \frac{\Delta \vec{x}_p}{\Delta t}$, where $\Delta \vec{x}_p$ denotes the average particle displacement vector within the interrogation region. To evaluate these displacements, a cross-correlation algorithm is typically employed. For two interrogation windows $I_1(\vec{x})$ and $I_2(\vec{x})$, corresponding to consecutive images, the normalised cross-correlation function is defined as in Eq. 2.1. The displacement vector $\Delta \vec{x}_p$ is estimated from the location of the maximum correlation peak. Repeating this procedure over all the interrogation regions yields a vector field representing the instantaneous velocity distribution across the illuminated plane.

$$R_c(\Delta \vec{x}) = \frac{\int I_1(\vec{x})\, I_2(\vec{x} + \Delta \vec{x})\, d\vec{x}}{\sqrt{\int I_1^2(\vec{x})\, d\vec{x} \int I_2^2(\vec{x})\, d\vec{x}}}, \tag{2.1}$$

By acquiring a large dataset of PIV images, not only instantaneous but also statistical properties of the flow can be obtained. In particular, the time-averaged velocity field is computed as in Eq. 2.2, where N is the number of samples and $\vec{u}_i$ denotes the velocity field obtained from the i-th PIV image pair. This averaging procedure provides reliable information on the mean flow topology, while fluctuations around the mean can be used to characterise the turbulence intensity and the Reynolds stresses.

$$\overline{\vec{u}}(\vec{x}) = \frac{1}{N} \sum_{i=1}^{N} \vec{u}_i(\vec{x}) \tag{2.2}$$

Over the years, several variants of PIV have been developed to enhance its capabilities, starting from the simplest planar PIV. This approach allows for the computation of two-dimensional velocity fields using a single camera perpendicularly oriented to the laser sheet. Stereoscopic PIV [59] enables the measurement of all three velocity components within a plane, while tomographic PIV [60] reconstructs the full three-dimensional flow field within a volume. Time-resolved PIV, using high-speed cameras

and pulsed lasers, extends the technique to the study of highly unsteady phenomena by resolving the temporal evolution of coherent structures.

In summary, PIV offers a powerful experimental approach for investigating fluid flows, combining non-intrusiveness with the ability to deliver instantaneous velocity fields over extended regions. These characteristics also make it a valuable benchmark for the validation of numerical simulations, particularly in applications where wake dynamics, vortical structures, or turbulent mixing play a crucial role.

2.2.2 Wind tunnel flow characterization

The experiments were performed in the "Ferrari" open-circuit suction-type wind tunnel at Politecnico di Torino. The wind tunnel features a honeycomb and two mesh screens at its inlet section, followed by a contraction with an area ratio of 3.25:1, which leads into a cubic enclosed open test section with a side equal to 88 cm. The jet presents a circular section with an inlet diameter of D_{jet} = 40 cm. The diffuser has a diffusing ratio of 1:2.4. A 7-blade fan is mounted downstream of the diffuser, run by a three-phase asynchronous motor with a maximum power of 7.5 kW. The wind speed range is approximately between 1 and 24 m/s. A schematic illustration of the wind tunnel along with the adopted reference system is reported in Figure 2.2. In particular, the x-axis is oriented according to the jet streamwise direction. The y-axis and z-axis are oriented toward the jet crosswise direction, respectively, in the parallel and perpendicular direction to the test section floor.

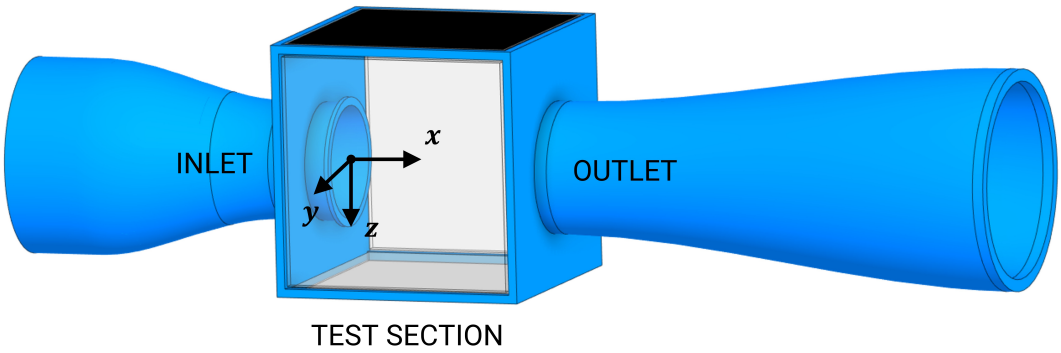

Fig. 2.2 Schematic representation of the Ferrari wind tunnel.

The flow characteristics inside the test section are evaluated using a Dantec P11 hot-wire probe [1]. The hot wire probe is positioned at two different distances from the jet inlet in the streamwise direction, HW_A = 2 cm and HW_B = 44 cm, as shown in Figure 2.3. In this way, the flow characteristics are evaluated approximately in correspondence with the jet inlet and at mid-section, where the propeller is subsequently positioned.

[1] https://www.dantecdynamics.com/product/miniature-wire-probe-straight/

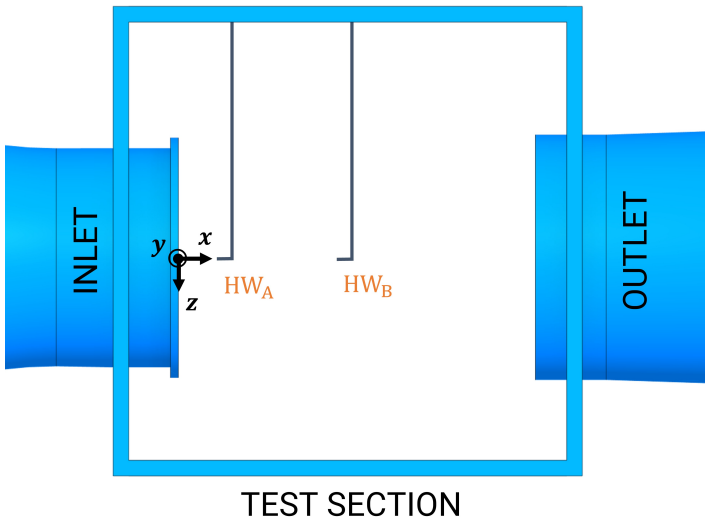

Fig. 2.3 Hot wire probe streamwise positioning inside the test section for the jet flow features characterisation.

The probe is then translated along the y and z axes to evaluate the streamwise flow characteristics along the two cross-jet directions. In particular, the flow homogeneity is evaluated as the relative deviation of the local time-averaged streamwise velocity ($\overline{V_x}$) with respect to the time-averaged inflow velocity evaluated at the centreline position (V_∞): $\delta\overline{V_x} = \frac{\overline{V_x} - V_\infty}{V_\infty}$. The turbulence intensity is additionally evaluated as: $Ti = \frac{v_{x\ RMS}}{\overline{V_x}}$, being $v_{x\ RMS}$ the root mean square of the velocity fluctuations along the x-axis. The analyses are conducted for four different inflow velocities (V_∞ = 5.9, 10.9, 16.5, and 22.2 m/s), revealing small differences among them in terms of non-dimensional velocity and turbulence intensity distributions along both the y and z axes. The results in terms of potential core diameter, maximum $\delta\overline{V_x}$ and maximum Ti within the potential core region are summarised in Table 2.1 and are consistent for all four V_∞ investigated. At HW$_A$, the jet's potential core exhibits a uniform velocity distribution with $\delta\overline{V_x}$ below 2% along the y-axis and below 1.2% along the z-axis within a potential core diameter of approximately $0.93D_{\text{jet}}$. The turbulence intensity in this region remains below 1%. Further downstream at HW$_B$, the potential core region extends for approximately $0.67D_{\text{jet}}$, where the $\delta\overline{V_x}$ values remain below 3% on both axes and the turbulence intensity below 2%.

Table 2.1 Jet flow features at the streamwise positions HW$_A$ and HW$_B$, expressed in terms of potential core diameter and maximum $\delta\overline{V_x}$ and Ti values within the potential core. The results are consistent among the four V_∞ values investigated

	Potential core diameter	max($\delta\overline{V_x}$)	max(Ti)
HW$_A$ (near inlet)	$0.93D_{\text{jet}}$	$< 2\%$ (y), $< 1.2\%$ (z)	$< 1\%$
HW$_B$ (mid-section)	$0.67D_{\text{jet}}$	$< 3\%$	$< 2\%$

Based on these measurements, the propeller was subsequently positioned at the streamwise position HW$_B$ such that its entire swept area and the near-wake region remained within the uniform and

low-turbulence region of the jet potential core, which locally extends for a diameter of around $3.6R$. Only in cross-flow conditions, the propeller's setup is moved by $1R$ from the centre of the test section along the negative y-axis. In this way, the wake is contained inside the potential core region for an axial distance up to $3R$ from the propeller's hub, and thus the near wake is not significantly affected due to the high turbulence level and velocity gradients of the jet mixing region.

2.2.3 Experimental setup

Focusing on the propeller and its support, the main components are presented in Figure 2.4 and herein briefly described. The reference propeller presented in section 2.1 is 3D printed in VisiJet Armor M2G-CL resin. The drivetrain is composed of a TRX370 1000KV brushless motor with a diameter of 2.8 cm and a maximum power output of 150 W. The motor is controlled by an external electronic speed controller (ESC), which receives the input commands through an Arduino Uno board. The rotational speed of the shaft is measured using a Hobbywing RPM sensor that is connected to two of the three phases of the brushless motor. The sensor counts the voltage changes at the two phases within a time interval of 0.1 s and converts the information to a value of rpm (n). The sensor has a rated output which ranges from n = 1000 rpm to n = 300000 rpm for the case of a 2-pole motor, as the one hereby considered. The drivetrain was mounted on a 3D printed support realised in polylactic acid (PLA). The support shape was designed to host two load sensors to evaluate the propeller thrust and torque. To this end, a bi-directional axial load cell, LSB201 Futek, excited with 5 V, was chosen for the thrust measurements. The sensor is characterised by a rated output (RO) of 2.5 N, non-linearity and hysteresis of ± 0.1% of RO, and an operating temperature range of 223–365 K. A TFF400 Futek torque sensor excited with 10 V was instead selected for the torque measurements. Thanks to the acquisition of the motor's rotational speed (Ω), it is straightforward to obtain the power consumption from the torque measurements as $P = Q\Omega$. The torque sensor is characterised by a RO of 0.07 Nm, non-linearity and hysteresis of ± 0.2% of RO, and an operating temperature range of 223–365 K. The sensor is mounted at a distance of about three times the radius R downstream of the propeller, to limit its blockage effects [61–63]. To characterise the accuracy and robustness of the load-cell measurements, data were acquired at a sampling frequency of 10,000 Hz, with each operating point recorded over a time window of 60 s. A dedicated repeatability analysis was first conducted in hovering conditions at a rotational speed of 3000 rpm. Thrust, torque, and rotational speed were measured over ten consecutive repetitions, with a waiting time of approximately two minutes between successive tests. The results of this repeatability analysis are reported in Figure 2.5. The measurements exhibited good repeatability characteristics: the dispersion of the thrust measurements corresponded to approximately 3.5% of the mean thrust value, while the dispersion of the torque measurements corresponded to approximately 2.9% of the mean torque value. The rotational speed measurements showed an even smaller dispersion, corresponding to approximately 0.17% of the mean rotational speed. For both axial inflow and cross-flow conditions, the thrust and power coefficients were obtained by averaging the results of four independent repetitions for

each operating point. The uncertainty bars associated with these measurements represent the standard deviation among the four repetitions at each operating point. The largest relative deviations were observed in hovering conditions at 3000 rpm, with maximum deviations of approximately 3.7% for the thrust coefficient and 2.6% for the torque coefficient. These values are consistent with the results obtained during the dedicated hovering repeatability analysis. Since the resulting uncertainty bars are extremely small and would require substantial magnification to be clearly visible, they are not displayed in the plots presented in the manuscript.

The PLA support is connected to an Optosigma OSMS-120YAW servo-motor, which allows a 360° rotation around the vertical axis passing through the propeller's hub. The support is, in turn, mounted on the ceiling of the test section at a streamwise distance of 44 cm from the jet inlet, so that the propeller's hub is located approximately at the centre of the test section. Thanks to the servomotor, the propeller can be oriented at the desired incidence to the jet inlet, while remaining inside the potential core region of the wind tunnel jet. At first, the characterisation of the propeller was carried out in axial inflow, orienting the propeller with its rotation axis parallel to the jet axis. In a second instance, the cross-flow condition was investigated in detail, orienting the propeller with its rotation axis perpendicular to the jet axis.

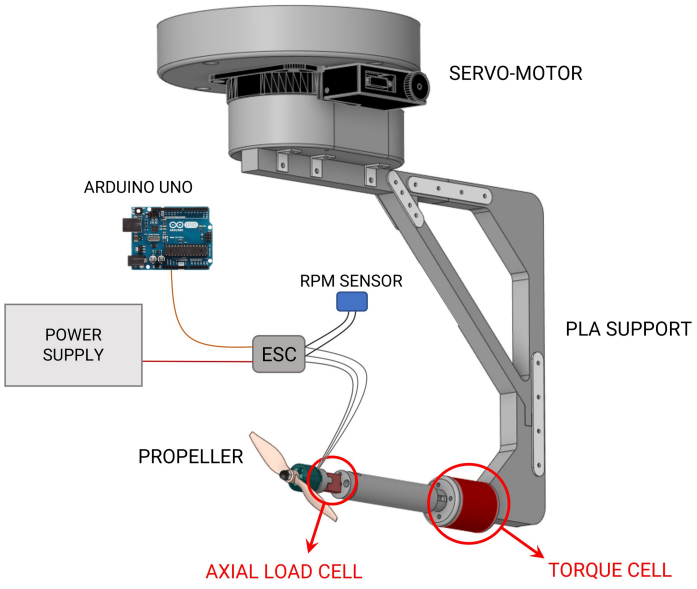

Fig. 2.4 Schematic representation of the propeller's support.

In the experimental campaigns carried out in this thesis, the planar version of PIV was considered. In particular, a focus is made on assessing the wake flow generated by the propeller in axial inflow conditions and cross-flow conditions. In the first case, being the wake on average axisymmetric, a single region of interest (ROI) was considered, which extends for approximately $2.6R$ in the stream-wise direction and $1.4R$ in the cross-wise direction (19.5 x 10.5 cm^2), as illustrated in Figure 2.6(a). In the case of cross-flow investigations, the wake region is no longer axisymmetric. Two ROI are therefore

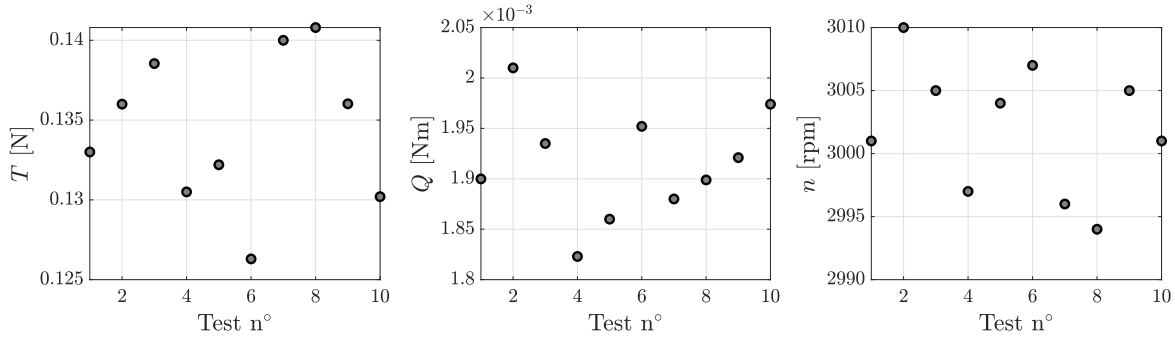

Fig. 2.5 Repeatability tests conducted in hovering at 3000 rpm for thrust (T), torque (Q) and rpm (n) measurements.

investigated in the upwind and downwind regions with respect to the propeller's support, as illustrated in Figure 2.6(b). The upwind ROI extended for about $1.8R$ x $2.1R$ (13.5 x 15.7 cm^2), whereas the downwind ROI extended for approximately $1.9R$ x $2.1R$ (14.2 x 15.7 cm^2). The adopted reference system in the PIV measurements features the same axes orientation considered in the wind tunnel characterisation. The axis x is hence oriented toward the wind tunnel jet direction, while y and z are parallel and perpendicular to the ground, respectively. Different from what was discussed in section 2.2.2, the origin of the reference system is translated from the jet inlet to the propeller's hub for all the propeller's measurements. For coherence, the same reference system will also be adopted in the numerical setup. The flow was seeded upstream of the contraction using a Laskin nozzle, which produces particles of about 1 μm fuelled with the high-performance seeding fluid 'PIVLIGHT'. A Dantec Dynamics Nd:YAG Dual Power 200 laser (200 mJ/pulse, 15 Hz maximum repetition rate) operated in dual pulse mode was used to illuminate the tracing particles. The laser was shaped into a thin sheet using an optical setup consisting of a set of appropriate lenses and illuminated the ROI. One Andor Zyla 5.5 Mpx sCMOS camera (sensor size of 2560x2160 pixel^2, pixel size of 6.5 μm, 16 bits) was used to capture images of the illuminated tracing particles. The camera was synchronised with the laser system using an NI - PCIe 6612. The camera was equipped with a Nikon 60 mm Macro lens, with a value of the aperture $f_\# = 8$. The optical resolution resulted in approximately 12.1 px/mm in axial inflow and 13.2 px/mm in cross-flow. In this latter case, the upwind region was first analysed, and then the camera was moved to the downwind region. The tests' acquisition frequency was set to 14.1175 Hz, in order to avoid phase-locked measurements and ensure well-converged statistics.

Each measurement consisted of 2500 image pairs. The raw images were first pre-processed with a historical minimum subtraction to reduce the light reflection from the propeller blades and the support. The vector fields were obtained by processing the collected images using a correlation-based algorithm. A spline interpolation of the images and the velocity fields was performed, as recommended by [64, 65]. A Blackmann weighting window was used to tune the spatial resolution [66]. The algorithm is based on a multi-pass approach, and the final interrogation window size was 32 x 32 pixels^2 (2.4 x 2.4

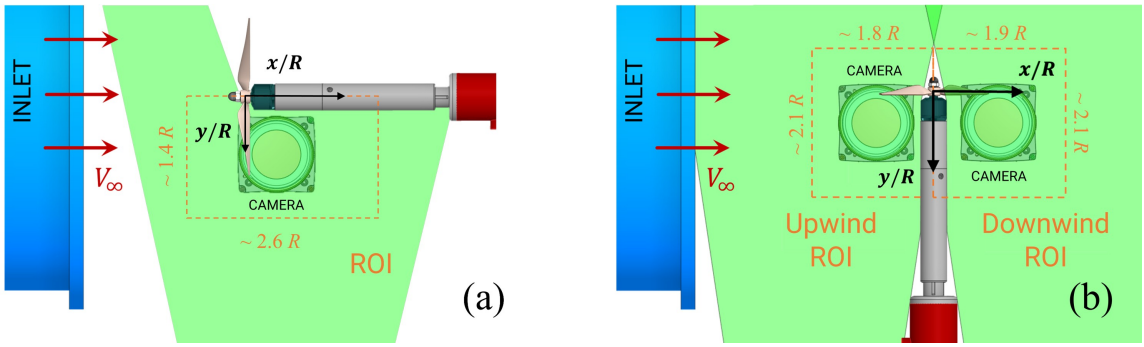

Fig. 2.6 Schematic representation of planar PIV setup. (a) Axial inflow conditions, (b) cross-flow conditions.

mm^2), with 75% overlap, corresponding to a final vector spacing of about 8e-3R (0.6 mm). The PIV measurements were carried out imposing a time delay between the two frames, which led to a mean displacement of the tracer particles of about 12 pixels. Considering the common figure of an absolute error of 0.1 pixels on the mean field, the error can then be estimated as lower than 0.1% on the averaged quantities. Conversely, the error on the second-order statistics and the computation of the vorticity component is less than 5% [67]. The turbulent kinetic energy k and Reynolds stresses were furthermore post-processed with the use of a six-sigma to reduce the effect of any spurious vectors on such higher order statistics. The image processing was carried out using the open source software PaIRS [2], developed at the University of Naples Federico II [68]. PaIRS implements a state-of-the-art iterative multi-grid image deformation method, which is central to achieving both high accuracy and spatial resolution in PIV measurements.

2.3 Large Eddy Simulations (LES)

LES were considered to expand the experimental dataset obtained in cross-flow, allowing for the computation of 3D vortex trajectories and providing more details on the unsteady propeller's loading.

The LES approach is a turbulence modelling strategy that resolves the large, energy-containing turbulent structures directly, while modelling only the smallest scales [46]. This approach is motivated by the fact that the largest eddies, which are highly dependent on geometry and boundary conditions, contain most of the turbulent kinetic energy and are primarily responsible for momentum and energy transport. In contrast, the smallest eddies, which tend to be more isotropic and universal in character, can be represented by subgrid-scale models without a significant loss of accuracy. By combining the numerical resolution of the large eddies with subgrid-scale modelling of the small structures, LES provides a high-fidelity resolution with lower computational cost than direct numerical simulations (DNS).

[2] https://www.pairs.unina.it/

The starting point of LES is the filtered NS equations, obtained by applying a spatial filtering operation to the instantaneous flow variables. For example, the filtered velocity field is defined as in Eq. 2.3, where G is the filter kernel and Ω_{SD} the spatial domain.

$$\overline{\vec{u}_i}(\vec{x},t) = \int_{\Omega_{SD}} G(\vec{x}-\vec{r})\,\vec{u}_i(\vec{r},t)\,d\vec{r} \tag{2.3}$$

The filter width Δf is typically related to the local grid spacing in the numerical discretisation. Applying this operation to the incompressible NS equations yields the LES formulation, which features the term τ_{ij}^{SGS}. This is the subgrid-scale stress tensor, defined as: $\tau_{ij}^{SGS} = \overline{u_i u_j} - \overline{u_i}\,\overline{u_j}$ and representing the influence of unresolved scales on the resolved ones. This term, however, requires closure modelling. One of the most widely used SGS models is the Smagorinsky model, which introduces an eddy viscosity ν_t proportional to the strain rate of the resolved flow: $\nu_t = (C_s \Delta f)^2 \sqrt{2\,\overline{S_{ij}}\,\overline{S_{ij}}}$, where C_s is the Smagorinsky constant, and $\overline{S_{ij}}$ the rate-of-strain tensor of the resolved field. More advanced dynamic models, such as the dynamic Smagorinsky model by Germano [69], adjust C_s locally based on the resolved flow conditions, improving accuracy in transitional or near-wall flows.

The strength of the LES approach lies in its ability to capture the inherently unsteady and three-dimensional nature of turbulence, including coherent vortical structures and their interactions. Compared to RANS or URANS, LES provides a more faithful representation of turbulence physics, which makes it a valuable tool for fundamental studies and for applications where accurate unsteady flow details are essential. However, the computational cost of LES is substantially higher, particularly near solid boundaries, where the resolution requirements to capture small eddy scales increase with the Reynolds number. Despite this limitation, LES has seen increasing use in aeroacoustics, bluff-body aerodynamics, and turbomachinery research, where unsteady flow phenomena dominate performance and noise generation.

The LES approach is particularly effective in the simulation of small-scale propellers operating at low Reynolds numbers, since they are characterised by laminar-to-turbulent transitions, laminar separation bubbles, and intermittent flow separation. These transitional phenomena are difficult to accurately capture with RANS or URANS models, which rely on turbulence closures designed for fully developed turbulence and usually higher Reynolds numbers. LES, by directly resolving the large structures and transition processes, offers the potential to provide more accurate predictions of the unsteady aerodynamic behaviour of low-Reynolds-number propellers. The low Reynolds numbers additionally favour a coarser mesh close to the solid boundaries, decreasing the computational burden compared to simulations of larger propellers.

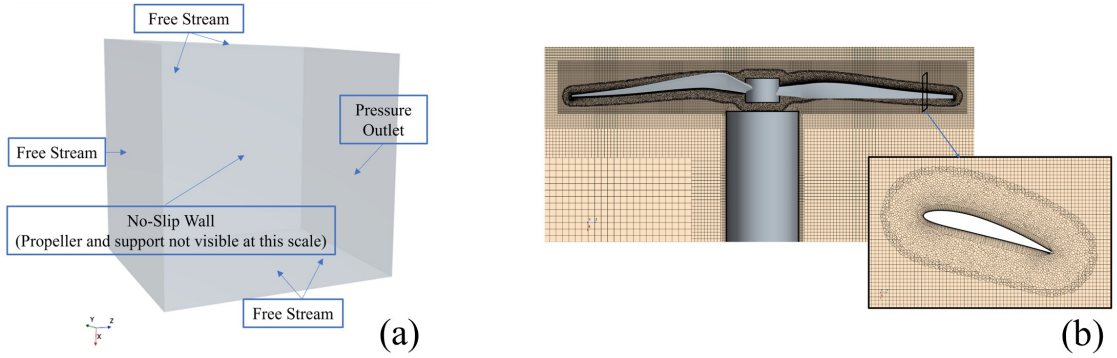

Fig. 2.7 LES setup. (a) Computational domain and Boundary conditions, (b) baseline grid.

2.3.1 Simulations setup

LES simulations are run with the STAR CCM+ solver on the high-performance computing facility from Politecnico di Torino (HPC@POLITO). The compressible NS equations were used as the mathematical model in the simulations, filtering the smaller turbulent scales with the dynamic Smagorinsky model by Germano [69], using the modification proposed by Lilly [70]. The dynamic filtering permits the prediction of both laminar and turbulent regions, allowing the capturing of separation-induced laminar-turbulent transition [71, 72]. The evaluation of the viscous fluxes uses a second-order approximation. In contrast, the calculation of inviscid fluxes uses a third-order central difference reconstruction with a 4% upwind blending using the preconditioned Roe's Scheme proposed by Weiss et al. [73]. Additionally, the model uses a second-order implicit dual-time integration method. The inner gear is run for 10 iterations, allowing for the reduction of residuals over 2 orders of magnitude.

The computational domain is modelled as a cube with a size of $166R$, as shown in Figure 2.7(a). The numerical setup initially includes the presence of the propeller's support, simulated as a cylinder with a radial extension equal to 19% of R. The support was initially simulated using LES to replicate the same setup used in the experimental campaign. In a following numerical campaign, the support is instead removed to evaluate the isolated propeller's wake evolution without the support influence. The rotation of the grid is modelled with an overset near-body grid that overlaps with a background grid, as shown in Figure 2.7(b). The near-body grid is made from polyhedra that allow a good resolution of complex geometries with a contained number of cells and a prism layer with a y+ below one to capture strong wall-normal gradients. Conversely, the background grid is a Cartesian grid to reduce the numerical dissipation in the wake [74]. Overset grids for rotation modelling help the sampling of statistics in the near rotor region in a computationally efficient way.

Table 2.2 Grid and Time-Step refinement study.

Base Size	Number of Cells	Time-Step	$\overline{C_T}$	$\overline{C_Q}$	CPU hours
2	5.9 Millions	1.38e-5	0.0174	0.00259	1,300
1.5	10.6 Millions	1.04e-5	0.0168	0.00271	4,000
1.25	15.7 Millions	8.68e-6	0.0168	0.00276	8,200
1	26.8 Millions	6.94e-6	0.0168	0.00286	20,000
0.8	47.0 Millions	5.55e-6	0.0167	0.00288	45,800

2.3.2 Spatial and Temporal Discretisation Refinement Study

A sufficiently refined grid is considered to resolve the vortices containing most of the energy in the flow, modelling only the smallest scales. In this work, a baseline grid was defined with a target cell size of the order of the Taylor micro-scale in the relevant regions of the flow where transition to turbulence is expected. This grid was generated with a base size equal to 1. The base size is a parameter used to refine the grid systematically by scaling all the mesh control target sizes. Table 2.2 shows that 3 grids coarser than the baseline grid were created along with a finer version of it. Initially, ten revolutions were carried out at a time step of 2.5° per iteration, and then six revolutions at a time step of 0.125° per iteration for the baseline grid, ensuring a CFL≈1 in the whole domain. The first revolutions with a larger time step allow the flow to develop by advecting the starting vortex downstream. Then, the following iterations with a smaller time step ensure a time-accurate solution. The time step is chosen to maintain a CFL≈1 for all the grids, a requirement to adequately capture small flow structures. It can be appreciated how the baseline grid (base size = 1) presents errors below 1% in the time-averaged thrust ($\overline{C_T}$) and torque ($\overline{C_Q}$) coefficients compared to the finest grid and therefore will be used in the rest of the analyses presented in this paper.

2.4 Unsteady Reynolds-Averaged Navier Stokes (URANS)

URANS simulations were exclusively performed in hovering and axial inflow conditions, serving as a higher-fidelity tool for the VPM code validation in canonical operative conditions, along with the experimental data. In the present section, an overview of the URANS formulation and the considered turbulence and transition models is first given. Subsequently, the simulation setup is described along with a spatial and temporal discretisation study.

The DNS/LES of turbulent flows by directly solving the NS equations is generally prohibitive for practical applications due to the enormous range of spatial and temporal scales that must be resolved. The RANS approach is one of the most established strategies to resolve the NS equations by modelling the turbulence [50] with a lower computational cost. The RANS equations are derived

by decomposing each instantaneous flow variable into a mean and a fluctuating part according to the Reynolds decomposition. For instance, the velocity field is expressed as: $u_i(\vec{x},t) = \overline{u_i}(\vec{x}) + u_i'(\vec{x},t)$, where $\overline{u_i}$ denotes the time-averaged (or ensemble-averaged) velocity and u_i' the turbulent fluctuation along the i direction. Compared to the laminar NS equations, the RANS equations contain an additional term, $-\partial\overline{u_i'u_j'}/\partial x_j$, which represents the divergence of the Reynolds stress tensor: $\tau_{ij}^R = -\rho\,\overline{u_i'u_j'}$. This term accounts for the effects of turbulence on the mean flow and introduces a closure problem: additional equations or models are required to express τ_{ij}^R in terms of mean quantities. This necessity has led to the development of a wide range of turbulence models, such as algebraic eddy-viscosity formulations, one- or two-equation models (e.g. $k-\varepsilon$, $k-\omega$).

While the classical RANS approach is inherently steady, many engineering applications involve unsteady phenomena. To account for these, the URANS framework is employed. The URANS equations retain the same form as RANS but allow the mean quantities $\overline{u_i}$ to vary in time. URANS simulations are hence capable of capturing large-scale unsteady effects, such as vortex shedding or blade passing interactions, while the small-scale turbulence is still modelled through the chosen turbulence closure.

The appeal of RANS and URANS lies in their computational affordability: by solving only for the mean flow (and possibly its time evolution), the need to resolve the entire turbulent spectrum is avoided. This makes them suitable for engineering applications involving complex geometries and high Reynolds numbers, where DNS or LES would be computationally prohibitive. Nevertheless, the accuracy of RANS/URANS strongly depends on the turbulence model adopted and its calibration. While they can reliably predict integral performance quantities such as lift, drag, thrust, and torque, discrepancies may arise in wake dynamics or flows dominated by laminar-to-turbulent transition, flow separation, and strong anisotropy. Their application in low Reynolds numbers is indeed still trivial, as even the most popular transitional models are mostly calibrated for higher Reynolds numbers.

In summary, the RANS framework provides the time-averaged equations of motion and relies on turbulence models to account for unresolved scales, while URANS extends this formulation to capture large-scale unsteadiness. Together, they represent the key tool of industrial computational fluid dynamics, providing a pragmatic compromise between fidelity and computational cost.

2.4.1 SSTLM turbulence and transition model

The SST $k-\omega$ turbulence model, developed by Menter [75], is one of the most reliable and widely used eddy-viscosity models in engineering simulations involving wall-bounded flows, adverse pressure gradients, and flow separation. It represents a hybrid model that blends the near-wall accuracy of the $k-\omega$ model with the numerical stability of the $k-\epsilon$ model in the freestream. This is achieved using blending functions that switch smoothly between the two formulations as a function of wall distance. The governing equations for the SST $k-\omega$ model consist of transport equations for the turbulent kinetic

energy k and the specific dissipation rate ω, respectively expressed as in Eq. 2.4 and Eq. 2.5.

$$\frac{\partial \rho k}{\partial t} + \frac{\partial \rho u_j k}{\partial x_j} = P_k - \beta^* \rho k \omega + \frac{\partial}{\partial x_j}\left[(\mu_m + \sigma_k \mu_t)\frac{\partial k}{\partial x_j}\right] \tag{2.4}$$

$$\frac{\partial \rho \omega}{\partial t} + \frac{\partial \rho u_j \omega}{\partial x_j} = \alpha \frac{\omega}{k} P_k - \beta \rho \omega^2 + \frac{\partial}{\partial x_j}\left[(\mu_m + \sigma_\omega \mu_t)\frac{\partial \omega}{\partial x_j}\right] + 2(1 - F_1)\rho \sigma_{\omega 2} \frac{1}{\omega}\frac{\partial k}{\partial x_j}\frac{\partial \omega}{\partial x_j} \tag{2.5}$$

In these equations, ρ is the fluid density and μ_m is the molecular dynamic viscosity. The turbulent eddy viscosity μ_t is modelled as in Eq. 2.6.

$$\mu_t = \frac{\rho k}{\omega} \cdot \max\left(\frac{1}{\alpha^*}, \frac{S_r}{\omega F_2}\right) \tag{2.6}$$

where S_r is the strain-rate magnitude and F_1, F_2 are blending functions that regulate the transition between the $k-\omega$ and $k-\epsilon$ behaviour. Despite its robustness in fully turbulent regimes, the SST model assumes a flow that is turbulent from the onset, which makes it unsuitable for problems where transition from laminar to turbulent flow occurs. To address this, Langtry and Menter [76] introduced a four-equation transition model, known as the Langtry-Menter model. This extension adds two additional transport equations: one for the intermittency (γ), and one for a local transition momentum-thickness Reynolds number (Re_{θ_t}), enabling the model to capture natural and bypass transition processes dynamically. γ acts as a switch that modulates the production of turbulence, and is governed by Eq. 2.7, where the production and destruction terms P_γ and E_γ are defined through empirically calibrated correlations that depend on local flow quantities and Re_{θ_t}.

$$\frac{\partial \rho \gamma}{\partial t} + \frac{\partial \rho u_j \gamma}{\partial x_j} = P_\gamma - E_\gamma + \frac{\partial}{\partial x_j}\left[\left(\mu_m + \sigma_\gamma \mu_t\right)\frac{\partial \gamma}{\partial x_j}\right] \tag{2.7}$$

Eq. 2.8 instead governs the evolution of Re_{θ_t}, where P_{θ_t} is a source term calibrated to drive the transition location prediction based on freestream turbulence intensity and pressure gradient.

$$\frac{\partial \rho Re_{\theta_t}}{\partial t} + \frac{\partial \rho u_j Re_{\theta_t}}{\partial x_j} = P_{\theta_t} + \frac{\partial}{\partial x_j}\left[\sigma_{\theta_t}(\mu_m + \mu_t)\frac{\partial Re_{\theta_t}}{\partial x_j}\right] \tag{2.8}$$

These two new variables are coupled to the original SST equations by modifying the production term P_k in the turbulent kinetic energy equation. Specifically, the turbulence production is multiplied by the intermittency factor γ, effectively delaying the growth of turbulence until a physically realistic transition onset is reached. This coupling ensures that turbulence is not generated prematurely in laminar regions.

The $\gamma - Re_{\theta_t}$ or Langtry-Menter model relies on two main empirical correlations: one for the transition onset and another for the transition length. These correlations are formulated as functions of local Reynolds numbers, turbulence intensity, and pressure gradient. Their calibration has been performed against a comprehensive experimental database, ensuring model applicability across a wide range of flow regimes, including natural transition, separation-induced transition, and low freestream turbulence conditions. The primary advantage of this transition model lies in its capability to predict transition in a fully local and computationally efficient manner, without requiring non-local integral quantities or boundary layer thickness estimates. Moreover, its compatibility with unstructured grids and complex geometries makes it a practical choice for industrial CFD applications in aerospace, turbo-machinery, and external aerodynamics. On the other hand, the model was mainly calibrated to accurately predict the flow evolution for higher Reynolds numbers than the ones treated in the present work. Few attempts in the literature showed, however, a good accuracy of the model for small-scale propellers featured by low Reynolds numbers [77, 78].

2.4.2 Simulations setup

The URANS simulations of the rotating propeller were performed using the elsA solver developed by ONERA [79]. The computational workflow, including grid generation, simulation, and postprocessing, was executed using toolchain MOLA v1.18[3]. As anticipated, URANS simulations were exclusively performed in hovering and axial inflow conditions. An overset meshing or "Chimaera" technique was used to simulate the blades' motion as done in LES for the cross-flow condition. The two blades were initially simulated from $r/R = 0.2$ to their tip to reproduce the same setup of the VPM simulations. The two rotating meshes were generated with a structured grid starting from a wall cell height that guarantees a Δy^+ of around 0.2 in the considered operative conditions. The grid was extruded for a normal-to-wall distance of 0.12 R. The rotating meshes were subsequently overlapped on a static Cartesian background mesh. A further refined cylindrical region was then generated to adequately capture the flow evolution in the wake. The cells in this region have characteristic dimensions that are very similar to the outermost cells of the rotating domain, in order to ensure an exchange of information between the two meshes, which minimises numerical dissipation. The entire computational domain is modelled as a cube with a size of $40R$. A slice of the final mesh close to the propeller is reported in Figure 2.8(a). The cylindrical support was subsequently added to the mesh generation to additionally replicate a similar setup used in the experiments, as shown in Figure 2.8(b). As it will be shown in section 2.6.1, the support showed a negligible influence both in hovering and axial inflow. Among the available turbulence models, the SST $k - \omega$ [75] was chosen as one of the most widely used for external aerodynamics. It was coupled with the $\gamma - Re_\theta$ transition model developed by Langtry and Menter [76] to attempt to capture the laminar-to-turbulent transition that characterises the flow around propeller blades at these low Reynolds numbers. The coupled model is henceforth referred to as

[3]https://github.com/onera/mola

SSTLM for simplicity. In elsA, the implemented model follows the standard NASA Langley version of the Langtry-Menter four-equation model, as described in the NASA documentation[4]. Only the standard transition model is considered, without the inclusion of additional modifications such as the "Stationary Crossflow Extension" or high-lift-specific correlations.

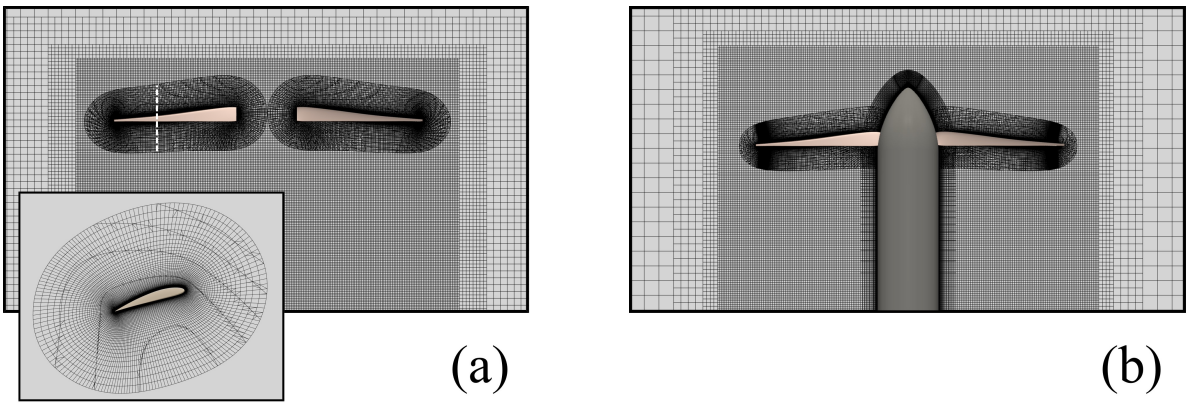

Fig. 2.8 Computational grid in URANS simulations. The wall cell dimension is locally chosen to obtain a $\Delta y^+ < 0.2$, the rotating region extends until $0.12R$, and the last cell has a size of approximately $0.02R$, which is the same size as the cells in the refined region of the Cartesian mesh. (a) Grid with the blades simulated between $0.2 < r/R < 1$ as in the VPM simulations, (b) propeller entirely simulated with its cylindrical support. The support features the same cell size growth as the propeller blades.

2.4.3 Spatial and temporal discretisation

A spatial and temporal discretisation study was conducted for both hovering and axial inflow, using three different meshes and corresponding time steps. The propeller was rotated at a rotational speed $\Omega = n\pi/30 = 523$ rad/s, with $n = 5014$ rpm. For the axial inflow condition, the propeller was subjected to an axial inflow of $V_\infty = 3.4$ m/s, hence operating at an advance ratio of $J = \frac{V_\infty}{\Omega R} = 0.1$. The tests were conducted for 30 revolutions, and the loads were averaged over the last 10 revolutions. The meshes differ mainly in the number of points on the blades' surfaces and in the extrusion direction. Consequently, the refined background is adapted according to the mesh features in the rotating domain. The time-step value in seconds is calculated as $\Delta t = \Delta\psi/(6n)$, being $\Delta\psi$ the azimuthal angle swept by the blades per time-step. The discretisation parameters and the resulting time-averaged thrust and torque coefficients are reported in Table 2.3.

The time-averaged non dimensional loads $\overline{C_T}$ and $\overline{C_Q}$ present almost negligible differences between M2 and M3 both in hovering ($J = 0$) and axial inflow ($J = 0.1$). The loads evaluated for the M1 case instead result in slightly deviating from the other two cases, with relative errors up to 5-6% for $\overline{C_T}$ and 7-8% for $\overline{C_Q}$ in hovering conditions. The M2 mesh was consequently chosen for the comparison with the experimental results and the baseline VPM case, presenting almost equivalent integral load values

[4]https://turbmodels.larc.nasa.gov/langtrymenter_4eqn.html

Table 2.3 Grid and Time-Step Convergence Parameters.

			J=0.0		J=0.1	
Mesh Name	Number of Cells	$\Delta\psi$ [°]	$\overline{C_T}$	$\overline{C_Q}$	$\overline{C_T}$	$\overline{C_Q}$
M1	8.3e6	1.5	1.45e-02	2.21e-03	1.03e-03	2.20e-03
M2	17.1e6	0.75	1.36e-02	2.39e-03	9.97e-03	2.11e-03
M3	31.8e6	0.25	1.35e-02	2.38e-03	9.97e-02	2.11e-03

of the most refined mesh M3, but with a considerable decrease in computational cost. A further mesh was realised from M2 by adding the spinner geometry. The number of points increased to 21.1e6 due to the presence of the spinner.

2.5 Vortex Particle Method (VPM)

The VPM code VULCAINS [20–22] is a central tool in this thesis, as it is used for the simulation of challenging dynamic operative conditions due to its ease of use and low computational cost. This section aims to present an overview of the methodology, focusing on peculiar features that characterise VULCAINS with respect to the other available codes in the literature.

A viscous, unbounded, and incompressible flow can be resolved by formulating the NS equations into their vorticity form. This is done by taking the curl over the original momentum equation from a Lagrangian point of view, leading to the expression in Eq. 2.9, given $\vec{\omega} = \vec{\nabla} \times \vec{U}$ as the flow vorticity.

$$\frac{D\vec{\omega}}{Dt} = \frac{\partial \vec{\omega}}{\partial t} + \left(\vec{U} \cdot \vec{\nabla}\right)\vec{\omega} = \left(\vec{\omega} \cdot \vec{\nabla}\right)\vec{U} + \nu\Delta\vec{\omega} \tag{2.9}$$

The material derivatives expressed in Eq. 2.9 are well suited for a Lagrangian description. The two terms on the right-hand side respectively account for the vortex stretching and the viscous effects in the flow. The flow is spatially discretised by introducing a finite set of particles, which act as a radial-basis Gaussian function of core radius σ. Each particle induces velocity at any point of the flow field according to the Biot-Savart law. This discretisation process is equivalent to a spatial filter of size σ. Hence, all flow structures smaller than σ cannot be resolved, and they represent the unresolved scales. For the VPM to converge, the particles must overlap [80], i.e., the inter-particle distance h must satisfy $h < \sigma$.

Eq. 2.9 can be filtered in space to account for such unresolved scales, and therefore a term $\vec{E}_{trunc}$ appears on the right-hand side. The term in Eq. 2.10 represents the error between the resolved and the unresolved quantities, due to the filtering of the small scale [53]. A turbulent viscosity model can be used for its approximation since it represents the enstrophy loss transferred to the small scales.

$$\vec{E}_{trunc} = -\vec{\nabla} \cdot \left(\nu_t \left[\left(\vec{\nabla} \times \tilde{\vec{\omega}} \right) + \left(\vec{\nabla} \times \tilde{\vec{\omega}} \right)^t \right] \right) \tag{2.10}$$

In Eq. 2.10, the $\tilde{\vec{\omega}}$ is the filtered vorticity, while ν_t is the turbulent kinematic viscosity. The second term on the right-hand side is here neglected [81].

Each particle is characterised by a strength $\vec{\alpha}_s$, obtained by integrating the vorticity of the flow in the volume of the particles. The vorticity of the flow can be, in turn, retrieved from the particles' strength, taking into account a Gaussian distribution for the spatial filter. The evolution equation of the particles' strength is written in Eq. 2.11.

$$\frac{d\vec{\alpha}_{s_i}}{dt} = \left(\vec{\alpha}_{s_i} \cdot \vec{\nabla}^t \right) \vec{U}_i + V_i \vec{\nabla} \cdot \left(\left(\nu + \nu_{t_i} \right) \left(\vec{\nabla} \times \vec{\omega}_i \right) \right) \tag{2.11}$$

The flow velocity is obtained with the Helmholtz Decomposition Theorem as $\vec{U} = \vec{U}_\infty + \vec{u}_\phi + \vec{u}_\psi$, where the last two terms correspond respectively to the curl-free and solenoidal parts of the total velocity. No irrotational sources are considered in this approximation, the only contributions to the total velocity are hence the divergence-free velocity which is induced by the particles and is obtained from the Biot-Savart law $\vec{u}_\psi = \int_V \frac{1}{4\pi r^3} \vec{\omega} \times \vec{r}\, dV$ and the freestream velocity. The solenoidal velocity is regularised by a smoothing function, obtained directly from the spatial filter.

The particles are advected in the flow according to the total velocity. In this work, the curl-free velocity sources $\vec{u}_\phi$ are neglected, thus leading to Eq. 2.12, used to compute the position of each particle $\vec{x}_i$.

$$\frac{d\vec{x}_i}{dt} = \tilde{\vec{U}}(\vec{x}_i, t) \approx \vec{U}_i = \vec{U}_\infty + \vec{u}_{\psi_i} \tag{2.12}$$

The direct solution of the terms involved in the vorticity equation is costly, being the inter-particles interaction of $O(N^2)$. The Fast Multipole Method (FMM) can be used to efficiently reduce these interactions and reduce the cost to approximately $O(N)$. The open source module ExaFMM [82] was considered for the purpose, parallelised with OpenMP.

2.5.1 Viscous treatment of the flow

One of the principal advantages of the VPM, in comparison to other potential flow methods, lies in its intrinsic ability to account for viscous effects. The diffusion term of the VPM equations can be solved to simulate viscous interactions among vortex structures. The VULCAINS code implements 3 different schemes for the diffusion modelling: the Core Spreading Method (CSM), the Particle Strength Exchange (PSE), and the Diffusion Velocity Method (DVM). The DVM particularly aims to accurately compute the diffusion effects in the flow, without requiring a frequent redistribution or excessive growth

of the particle size. For such reasons, the DVM was considered in the current study, and its main features are hereby summarised. For a more detailed description, see the work [20].

The DVM rewrites the vorticity equation as an advection equation by incorporating part of the diffusion term inside the material derivatives. The unfiltered vorticity equation (Eq. 2.9) can be rewritten considering a diffusion velocity $\vec{u}_d$ as done in Eq. 2.13.

$$\frac{\partial \vec{\omega}}{\partial t} + \vec{\nabla} \cdot \left(\left(\vec{U} + \vec{u}_d \right) \times \vec{\omega} \right) = \left(\vec{\omega} \cdot \vec{\nabla} \right) \vec{U} + \vec{\nabla} \cdot \left(\left(\nu \vec{\nabla} + \vec{u}_d \right) \times \vec{\omega} \right) \tag{2.13}$$

The diffusion velocity aims to represent the diffusion occurring in the rotation plane of the particles and can be written as $\vec{u}_d = -\nu \frac{\vec{\nabla}||\vec{\omega}||}{||\vec{\omega}||}$. In this fashion, $\vec{u}_d$ becomes singular when the vorticity becomes null, which usually happens at the edge of the domain [83, 84]. This is avoided using: $\frac{1}{||\vec{\omega}||} \approx \frac{||\vec{\omega}||}{\omega_0{}^2 + ||\vec{\omega}||^2}$, being ω_0 a cutoff vorticity set to a small fraction of the highest vorticity value in the flow [85]. Different from what is done in previous works [83, 84], in VULCAINS the diffusion velocity is directly computed, instead of updating the particles' volume, solving the strength α_s for each particle. In this fashion, the volume of the particles V has to evolve according to $\frac{dV}{dt} = \int_V \vec{\nabla} \cdot \vec{u}_d \, dV$.

The diffusion velocity calculated in a discrete formulation for the particles is added to the total velocity. The complete system of equations that governs the particles' evolution with the DVM is written in Eq. 2.14.

$$\begin{cases} \frac{d\vec{\alpha}_{s_i}}{dt} = \left(\vec{\alpha}_{s_i} \cdot \vec{\nabla}^t \right) \vec{U}_i + V_i \vec{\nabla} \cdot \left(\left(\nu \vec{\nabla} + \vec{u}_d \right) \times \vec{\omega} \right) \\ \frac{d\vec{x}_i}{dt} = \vec{U}_\infty + \vec{u}_{\psi_i} + \vec{u}_{d_i} \\ \frac{dV_i}{dt} = V_i \vec{\nabla} \cdot \vec{u}_{d_i} \end{cases} \tag{2.14}$$

2.5.2 Turbulent viscosity modelling

The turbulent viscosity used to account for the truncation error and to close the VPM equations is computed through a model, to avoid solving the smallest scales [86]. For this purpose, the mixing length theory is taken into account, as it allows to approximate the turbulent viscosity as: $\nu_t \propto \Delta^2 ||\bar{\bar{S}}||$, with $\Delta \approx \sigma$ as the flow filter width and $||\bar{\bar{S}}||$ the strain tensor [87]. Depending on the resolved scales, ν_t can be approximated with the use of the Smagorinsky constant C_s: $\nu_t = C_s \sigma^2 ||\bar{\bar{S}}||$. Many LES turbulent viscosity models are available in the literature, but the limited number of physical quantities directly accessible in VPM restricts the number of possibilities. Three models were implemented in VULCAINS: the Smagorinsky model, the Mansour model [88], and the Vreman model [89]. These three models come from the hypothesis of homogeneous and isotropic turbulence; each model depends on the value of the constant C_s, which can emphasise or defuse the role of turbulence in the flow.

2.5.3 Control of the particles

To preserve the divergence-free nature of the modelled flows and to prevent numerical instabilities, it is necessary to intervene by redistributing, resizing, or reorienting the particles according to the vorticity field. In this section, an enstrophy-based control filter developed in VULCAINS is introduced. The intensity of this filter can be increased or decreased by the user through the scalar f_0. This filter results in impacting the flow solution, mostly in highly turbulent flows, such as the wake of a propeller in hover or at high Reynolds numbers. In the past, Pedrizzetti [90] proposed an approach for the filter only based on the re-orientation of particles, with a minor side effect on their magnitude. In VULCAINS, a new approach based on the active control of the enstrophy ($\mathcal{E}$) is proposed. After each sub-iteration of the Runge-Kutta integration scheme, the particle's strength is adjusted both in magnitude ($||\vec{\alpha}_s||$) and direction ($\hat{\alpha}_s$), according to: $\vec{\alpha}_{s_{new}} = \vec{\mathcal{F}}_{\mathcal{E}}(\vec{\alpha}_s, \Delta t_0) = \mathcal{F}_{mag}(\vec{\alpha}_s, \Delta t_0)\vec{\mathcal{F}}_{dir}(\vec{\alpha}_s, \Delta t_0)$. The two filters of magnitude $\mathcal{F}_{mag}$ and direction $\vec{\mathcal{F}}_{dir}$ are defined as functions of the particle strength and depend also upon the time interval Δt_0 over which they are applied. The filters can be initially defined as in Eq. 2.15, being f_{mag} f_{dir} the cutoff frequencies of the two filters and $\mathcal{E}$ the enstrophy of the flow ($\mathcal{E} = \int_{R^3} ||\vec{\nabla} \times \vec{U}||^2 dV$) in its filtered and self-induced forms ($\tilde{\mathcal{E}}_0$, $\tilde{\mathcal{E}}_{f_0}$).

$$\begin{cases} \mathcal{F}_{mag}(\vec{\alpha}_s, \Delta t_0) = 1 + \Delta t_0 f_{mag}\left(\sqrt{\frac{\tilde{\mathcal{E}}_0}{\tilde{\mathcal{E}}_{f_0}}} - 1\right) \\ \vec{\mathcal{F}}_{dir}(\vec{\alpha}_s, \Delta t_0) = (1 - \Delta t_0 f_{dir})\vec{\alpha}_s + \Delta t_0 f_{dir} \frac{||\vec{\alpha}_s||}{||\vec{\nabla} \times \tilde{\vec{U}}||} \vec{\nabla} \times \tilde{\vec{U}} \end{cases} \tag{2.15}$$

Using constant values of f_{mag} and f_{dir} might lead to inadequate adjustments of the particles' properties, trying to match the local divergence-free fields. If the particles' vorticity is not already close to the vorticity field in terms of magnitude and orientation, sudden and often insufficient changes might occur to their magnitude and direction features. The cutoff frequencies are hence written as a function of the particles' enstrophy, calibrating their properties changes with respect to this quantity. The magnitude of the cutoff frequency is tailored according to the particles strength, to avoid the spatial filtering of weak particles and to overlook the strong ones: $f_{mag_i} \propto \mathcal{E}_{f_i} - \overline{\mathcal{E}}$ for each i particle, being $\overline{\mathcal{E}}$ the mean enstrophy of the flow. The directional cutoff frequency is instead updated based on the angle between each particle's vorticity and the vorticity field. The non-constant cutoff frequencies can be hence written as in equation 2.16, given f_{mag_0} and f_{dir_0} user-defined constants, $\mathcal{E}_0$ the maximum enstrophy among the particles immediately shed by the propeller blades.

$$\begin{cases} \Delta t_0 f_{mag_i} = f_{mag_0} \frac{\tilde{\mathcal{E}}_i - \overline{\mathcal{E}}}{\mathcal{E}_0 - \overline{\mathcal{E}}} \\ \Delta t_0 f_{dir_i} = \frac{f_{dir_0}}{\pi} arccos\left(\frac{\tilde{\mathcal{E}}_i}{||\vec{\alpha}_{s_i}|| \cdot ||\vec{\nabla} \times \tilde{\vec{u}}_i||}\right) \end{cases} \tag{2.16}$$

As a best practice, the authors suggest the use of $f_{mag_0} = \Delta\psi\, f_0$ and $f_{dir_0} = 2\Delta\psi\, f_0$ for the rotating lifting lines, being $\Delta\psi$ the azimuthal angle swept per each time-step. The enstrophy filter is consequently

controlled by the user, varying the cutoff frequency f_0, which must be increased for highly turbulent flows, such as the wake of a propeller in hovering.

2.5.4 Coupling with lifting lines

The propeller blades are simulated with a lifting line module, added to VULCAINS for its low computational cost and simplicity, following the approaches proposed in the literature[91, 92]. The two lifting lines, positioned at the first quarter of the blades' chord distribution, are discretised in 100 segments with a hyperbolic tangent distribution along the radial direction. The blades are only simulated between $r/R = 0.2$ and $r/R = 1$, where the smallest segments are located. The lifting lines are moved according to the propeller's rotation axis to simulate the propeller motion. As the blades rotate, discrete particle sources are shed from the lifting lines with a vorticity value that preserves the local circulation calculated on the corresponding lifting line element. The local angle of attack is computed by considering the kinematic velocity of the lifting lines, the freestream velocity, and the induced velocity from the particle sources. The aerodynamic loads are calculated on each segment leveraging an airfoil polar database, which links the local angle of attack, the Reynolds number, and the Mach number to the corresponding values of the aerodynamic loads, namely lift and drag. Once the loads are computed, it is possible to calculate the relative circulation with the Kutta-Joukowski theorem. According to Kelvin's theorem, the introduction of a solid in the flow needs to be balanced with vorticity generation due to the variations of circulation in the lifting lines. To satisfy this, particle sources are shed from the lifting lines and set free in the wake. The particles are generated with a distribution that can also be independent of the lifting lines' discretisation. In the current application, it is appropriate to shed more particles close to the blades' tips to properly capture the tip vortex dynamics. The particles generated in the wake induce in turn a velocity on the blades' elements, affecting the angle of attack and consequently the loads and the circulation.

2.5.5 Airfoil polars computation

The NACA 4412 airfoil polars are calculated for Re_c = 10,000, 20,000, and 30,000 and α from 0° to 15°, keeping the Mach number (M) fixed to the value of 0.2. The loads' solution is the result of the interpolation among these curves. The solution is extrapolated between the chosen polars and a dataset of polars obtained for the NACA 0012 airfoil in post-stall condition [93] if α or Re_c falls out of the computed polars' range.

Due to the low Re_c regime, it is not straightforward to compute an adequate set of airfoil polars for the VPM simulations. The first approach features the use of XFoil, which integrates a panel method based on potential flow theory and an integral boundary layer formulation described by Drela [94]. The purpose of XFoil was indeed to assess the effectiveness of airfoils under low Reynolds number conditions. XFoil can determine the pressure distribution and incorporate the effects of laminar separation bubbles

and mild trailing edge separation. This work is based on the XFoil 6.99 version, executed through MOLA. XFoil employs the $e^{N_{crit}}$ envelope method to predict the transition to turbulence. This method examines the highest amplified frequency at a specific location on the airfoil, downstream from the instability point, to estimate the magnitude of the disturbance. Transition is assumed to occur when the integrated amplitude tops a value defined empirically. N_{crit} can be related to the freestream turbulence intensity Ti as for the Mack's relationship [95]: $N_{crit} = 8.43 - 2.4ln(Ti)$. Uranga [96] demonstrated that XFoil can predict transition caused by separation, provided that turbulence intensity is appropriately adjusted through the choice of an adequate value of N_{crit}. For high Reynolds numbers ($Re_c > 100,000$), the aerodynamic polars are found to be almost unaffected by the value of N_{crit}, while, for lower Re_c values, significant differences are instead observed [97]. In particular, the c_L is observed to increase with N_{crit}, while the c_D decreases, leading to an improved airfoil efficiency with the increase of the turbulence level. The NACA 4412 polars obtained with XFoil at $Re_c = 20,000$, $M = 0.2$ at different N_{crit} are displayed in Figure 2.9. As anticipated, the N_{crit} plays a fundamental role in evaluating the lift and the drag coefficients of the airfoil at such a low Reynolds number. At $\alpha = 6°$ for instance, the c_L increases by 35%, 75%, and 100% if the N_{crit} is respectively decreased from the default value of 9 to 7, 5, and 3. On the contrary, the c_D is less affected, showing almost negligible difference between $N_{crit} = 7$ and $N_{crit} = 9$. By further lowering the N_{crit} value to 5, significant differences are mostly noticeable for $\alpha > 8 - 9°$. The $c_D - \alpha$ curve with $N_{crit} = 3$ finally shows significantly lower values compared to the curve obtained at $N_{crit} = 9$, with differences up to 40% at high angles of attack. In the absence of reliable high-fidelity data, it is difficult to determine which polar is most suitable for the lifting line simulations. In section 2.6, a VPM validation campaign is conducted, also exploring the influence of N_{crit} on the propeller's performance in hovering and axial inflow. The analysis led to the choice of $N_{crit} = 5$ as an optimal value for the present propeller. This value is then used to investigate more complex maneuvers such as rotational speed variation and tilting in Chapter 4.

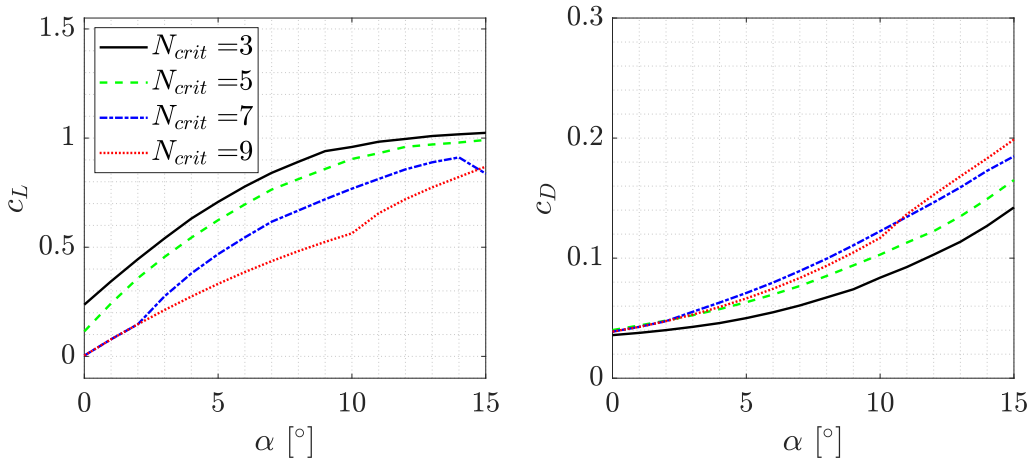

Fig. 2.9 Lift ($c_L(\alpha)$) and drag ($c_D(\alpha)$) coefficients of the NACA 4412 airfoil at $Re_c = 20,000$ and $M = 0.2$ computed using XFoil at different N_{crit} values.

The second approach considered for the polar computation features elsA for 2D URANS simulations of the NACA 4412. For this purpose, the SSTLM model was taken into account. To capture the periodic vortex shedding that occurs on the suction side from the point of separation, it is necessary to use an unsteady solver with an adequate time step. Capturing these vortices is therefore crucial as they significantly affect the performance of the airfoil [98]. As observed by the authors, the lift considerably increases due to the low-pressure zone periodically generated by these vortices on the suction side. As the angle of attack increases, the turbulence model activates, and turbulent flow regions begin to appear on the suction side in the separated area. The averaging introduced by activating the model dampens instabilities and vortex shedding, causing the flow to tend toward a stable solution, practically equivalent to that obtainable with a RANS solver. At equivalent angles of attack, the laminar solution is usually found at higher lift coefficients, still characterised by vortex shedding phenomena with lower frequency but larger structures. The use of an unsteady solver is essential, especially at very low Reynolds numbers and low angles of attack, while at higher angles, a RANS solver may be sufficient, which is certainly less computationally expensive. For such reason, an unsteady solver with a second-order integration in time is used, considering the gear method with 20 sub-iterations. For the spatial integration, a second-order Roe scheme was considered, with the minmod limiter as a slope limiter.

The influence of the low Mach preconditioning is furthermore taken into account, noticing that it plays a major role in the present case, most likely due to the low Re_c range. Low Mach number preconditioning is a numerical technique employed to enhance the accuracy and convergence of compressible flow solvers in regimes where the Mach number is low (typically $M < 0.3$) [99]. In such conditions, conventional compressible solvers suffer from stiffness due to the disparity between acoustic and convective time scales, leading to slow convergence and poor numerical conditioning. Preconditioning modifies the compressible NS equations by rescaling the eigenvalues of the system to reduce this disparity, effectively restoring numerical efficiency and maintaining solution fidelity. This approach enables the use of compressible solvers in low-speed aerodynamic applications while preserving consistency with the incompressible limit. The low Mach preconditioning can be implemented in its steady or unsteady form, as formulated by Venkateswaran and Merkle in their work [100]. Steady preconditioning methods, originally developed for steady-state problems, enhance convergence by modifying the wave speeds of the governing equations to address the imbalance between acoustic and convective time scales. While effective for steady problems and certain unsteady cases with large physical time steps, these preconditioners prove inadequate when applied directly to unsteady simulations with small time steps. In contrast, unsteady preconditioning, as developed within the dual time-stepping framework, introduces a pseudo-time derivative with a tailored preconditioning matrix that dynamically adapts to the unsteady character of the flow. This approach preserves the favourable damping properties of the time-derivative term at small time steps while ensuring numerical stability and convergence across a wide range of flow regimes. As shown in [100], unsteady preconditioning yields superior performance for low-speed, time-accurate flows, such as vortex propagation and mixing

layers, where steady preconditioning would otherwise lead to slow or even divergent convergence behaviour.

The unsteady features of the flow in this analysis might, however, be suitable for the use of a steady preconditioner. As the flow separates close to the leading edge, large vortex structures are shed in the wake from the airfoil suction side, characterised by a low frequency and a large scale. As a consequence, these structures can be adequately captured with quite large timesteps. As elsA only features the low Mach steady preconditioning, a first convergence study is carried out at $Re_c = 20{,}000$ and $\alpha = 6°$ with the use of a steady preconditioner and without the preconditioning. The time-step is normalised with respect to the characteristic convective time of the airfoil simulation ($t_c = \frac{c}{V_\infty}$). The results in terms of time-averaged c_L and c_D are reported in Table 2.4.

Table 2.4 Grid and Time-Step Convergence Parameters.

			Pre-conditioning		No pre-conditioning	
Mesh Name	Number of Cells	$\Delta t/t_c$ [%]	c_L	c_D	c_L	c_D
M1	2e5	1	0.66	0.09	0.49	0.079
M2	4e5	0.5	0.62	0.085	0.47	0.075
M3	6e5	0.25	0.61	0.085	0.47	0.074

The time-averaged non-dimensional lift and drag coefficients c_L and c_D present almost negligible differences between M2 and M3, both with and without the use of the steady preconditioner. The coefficients evaluated for the M1 case instead result in slightly deviating from the other two cases, with relative errors up to 6% for the c_L and for the c_D. The M2 mesh was consequently chosen for the computation of the full set of polars, presenting almost equivalent aerodynamic coefficient values of the most refined mesh M3, but with a reduced computational cost. The $c_L - \alpha$ and drag $c_D - \alpha$ obtained with the mesh M2 and a $\Delta t/t_c$ of 1% at $Re_c = 20{,}000$ and $M = 0.2$ are displayed in Figure 2.10. The curves obtained with XFoil and $N_{crit} = 5$ are superimposed for comparison. The use of the steady pre-conditioner has the effect of increasing the lift coefficients and the drag coefficients. This is most likely due to the enhanced vortex shedding generated from the airfoil suction side, as also observable from the increased standard deviation at a given angle of attack. In the present thesis, the purpose is to find the most suitable set for the VPM computations of the analysed propeller. Without the presence of reliable high-fidelity datasets in the literature, it is not straightforward to choose a priori the best of polars, so in subsection 2.6.3, a comparison of the VPM results is carried out with the three sets of polars shown in Figure 2.10.

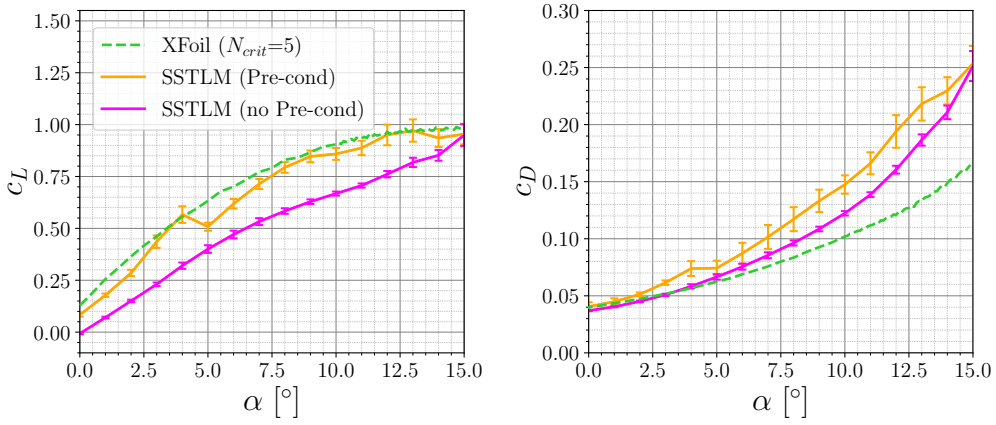

Fig. 2.10 Lift ($c_L(\alpha)$) and drag ($c_D(\alpha)$) coefficients of the NACA 4412 airfoil at $Re_c = 20{,}000$ and $M = 0.2$.

2.6 Validation of the VPM code in hovering and axial inflow

The analysis of complex dynamic maneuvers with VULCAINS required an initial validation campaign. The validation is carried out in steady-state hovering ($J = 0$) and axial inflow conditions ($J = 0.1$), comparing the VPM time-averaged results with higher fidelity URANS simulations and experimental data. URANS simulations are carried out with the presence of the support (URANS$_{Sp}$), to simulate a similar setup used in the experimental campaign, and without the presence of the support (URANS), to simulate a similar setup used in the VPM. This validation is divided into three main parts: the definition of a VPM baseline case (VPM$_{BL}$) and the comparison with URANS and experiments in section 2.6.1; the influence of the main VPM input parameters in section 2.6.2; the influence of the airfoil polars in section 2.6.3.

The VPM$_{BL}$ case is defined starting from parameters suggested by the Literature ([20]), for small drone propellers in similar operative conditions. XFoil polars are chosen due to their significantly lower computation cost compared to the URANS polars shown in Figure 2.10. A value of $N_{crit} = 5$ was chosen, leading to the smallest relative deviation from the experimental thrust and torque coefficient. The analysis on the input parameters focuses on the influence of the number of particle sources shed by each blade at each timestep (N_S), the azimuthal angle swept per timestep ($\Delta\psi$), the order of the Runge-Kutta scheme for the integration in time, the diffusion modelling scheme, the turbulent viscosity model and finally the cutoff frequency (f_0) to regulate the intensity of the enstrophy control filter. One of the advantages of VPM is that these parameters do not need a specific calibration for each different test case, and the same values might be used in various applications. However, their choice might affect the computations in terms of final results or computational cost. The influence of airfoil polars is then evaluated, comparing VPM results obtained through the different sets of polars shown in Figure 2.10. These VPM simulations are conducted with an improved set of VPM input parameters, in light of the main findings of section 2.6.2.

2.6.1 Comparison of the VPM baseline case with URANS and experiments

A VPM baseline case (VPM_{BL}) is defined with the input parameters displayed in Table 2.5.

Table 2.5 Input parameters for VPM baseline case

2D polars	N_S	$\Delta\psi$ [°]	Int. Order	Diff. Scheme	Turb. Visc. Model	f_0
XFoil (N_{crit}= 5)	40	5	3	DVM	Vreman	0.75

The time-averaged axial velocity fields $\overline{V_x}/\Omega R$ in hovering ($J = 0$) and axial inflow ($J = 0.1$) are displayed in Figure 2.11. In the same Figure, the time-averaged non-dimensional thrust $\overline{C_T}$ and torque values $\overline{C_Q}$ are reported for the different methodologies. The velocity profiles extracted at x/R = -0.5, 0.7, and 1.5 are instead displayed in Figure 2.12 for a quantitative comparison among the different cases.

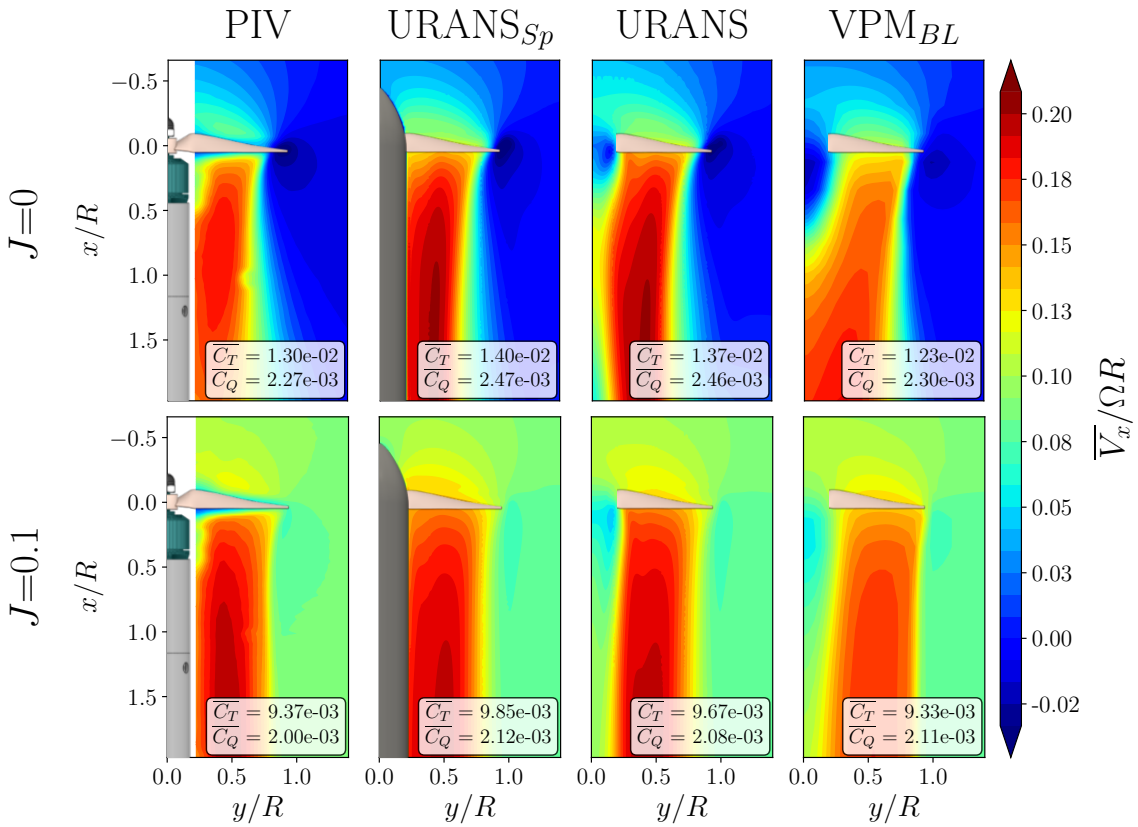

Fig. 2.11 Colourmaps of the normalized time-averaged velocity along the x-axis ($\overline{V_x}/\Omega R$). The propeller-shaped mask is added to improve the clarity.

Initially focusing on the comparison between the URANS$_{Sp}$ and the URANS case, it is noticeable how the presence of the support does not significantly affect the time-averaged loads and flow field. The relative differences in loads are below 2%, while the velocity profiles appear almost superimposed.

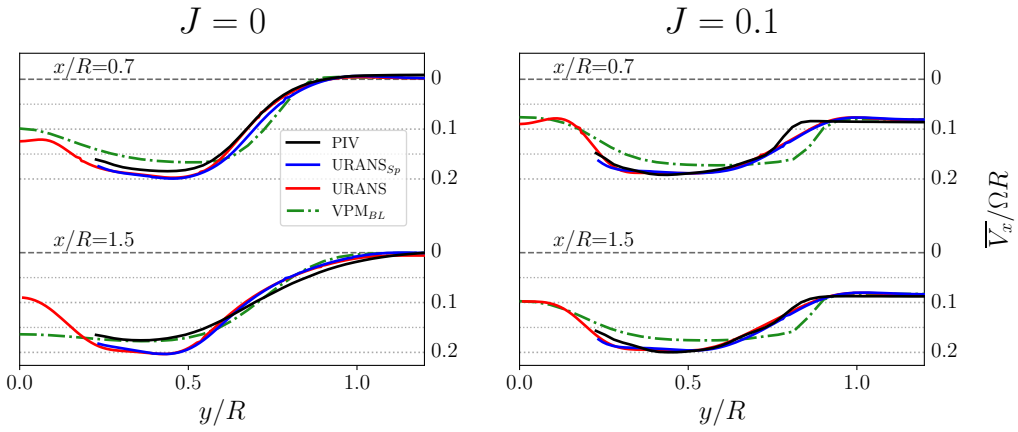

Fig. 2.12 Axial velocity ($\overline{V_x}$) profiles extracted from the flow fields in Figure 2.11 at x/R = -0.5, 0.7 and 1.5.

On the other hand, the URANS$_{Sp}$ and URANS simulations tend to overestimate the loads evaluated in experiments, both in hovering and axial inflow. In hovering, the deviation is more pronounced, being around 5.5% for $\overline{C_T}$ and 8.3% for $\overline{C_Q}$ between experiments and the URANS case. Such relative error decreases in the case of axial inflow, dropping to 3.2% for $\overline{C_T}$ and 3.9% for $\overline{C_Q}$ between the same cases. Similar considerations can be made by analysing the axial velocity field or the velocity profiles for a quantitative comparison. The greatest differences are again found in the case of $J = 0$, especially in the core of the wake, between $y/R > 0.3$ and $y/R < 0.6$. As can be observed in the velocity profiles extracted at $x/R = 0.7$, the relative error between the experiments and the URANS simulations is of the order of 8%. For $y/R > 0.75$, the two velocity profiles instead tend to overlap, thus indicating a good match of the wake width prediction in the radial direction between the two methodologies. At $x/R = 1.5$, the URANS overestimates the experimental axial velocity in the wake with errors around 14%. At this distance, the velocity profiles at $y/R > 0.6$ do not smoothly overlap as previously observed, but instead show a slight difference, indicating that the experimentally measured wake is, on average, wider in the radial direction compared to the URANS wake. These differences are obtained both in the presence and in the absence of the propeller's support in the URANS simulations. In axial inflow with $J = 0.1$, an overlap of the velocity profiles and a strong similarity between the flow fields are observed almost everywhere. Relative deviations between loads are below 5%, while velocity profiles appear almost superimposed, both close to the propeller ($x/R = 0.7$) and farther at $x/R = 1.5$. Small differences are exclusively observed around $(x/R, y/R) = (1.5, 0.8)$, where the experimental wake appears to be narrower than the URANS and URANS$_{Sp}$ wake, with local relative errors around 12%.

Focusing on the results of the VPM$_{BL}$ case, a good prediction of the time-averaged loads can be observed, both in hovering and axial inflow. Particularly at $J = 0$, the relative errors are around 5.0% for $\overline{C_T}$ and 1.4% for $\overline{C_Q}$. The slight underestimation of thrust and overestimation of torque are found again at $J = 0.1$, where the errors respectively become 0.4% and 5.1%. The value of N_{crit} has a significant influence on the time-averaged loads. Increasing N_{crit} leads to a decrease in thrust and

torque, resulting in errors up to 8-9% already at $N_{crit} = 6$. Conversely, decreasing N_{crit} leads to an overprediction of the loads, with errors up to 7%. $N_{crit} = 5$ is finally the most suitable choice for the propeller in the analysis, leading to loads' prediction errors below 5.1%. Although the errors on the loads are small, non-negligible differences are present in the induced velocity field. In the hovering case, the VPM$_{BL}$ case tends to underestimate the wake velocity near the propeller, as observable in the velocity profiles extracted at $x/R = 0.7$. The wake velocity is thereby on average lower than the experimental velocity, with about 8% error, and it is consequently also lower than the URANS velocity. The wake, however, appears to be wider in the radial direction, presenting higher axial velocity values for $y/R > 0.6$ compared to the experimental and the URANS fields. At $z/R = 1.5$, the wake velocity increases, yet still underestimates the velocity evaluated through the URANS, while being almost superimposed on the experimental velocity profile. Unlike the URANS case without support, the wake evaluated through the VPM significantly expands towards $y/R = 0$ from $x/R > 1$. A further difference is observable near the tip and root of the blade. The negative velocity induced by the presence of the tip vortex is lower in absolute value, indicating that the VPM might underestimate the intensity of this vortex. On the contrary, at the blade root, a more extended zone with greater velocity in absolute value can be observed compared to the URANS case, indicating that the root vortex might have been overestimated instead.

In the case of axial inflow at $J = 0.1$, despite the integral values of $\overline{C_T}$ and $\overline{C_Q}$ being close to the experimental and the URANS values, the axial velocity field still displays non-negligible differences. The axial velocity is generally lower compared to the other two methodologies, with errors around 5-6% in the core of the wake, both at $x/R = 0.7$ and $x/R = 1.5$. However, the wake obtained with the VPM appears wider in the radial direction, displaying higher velocity values compared to the experiments and the URANS between $y/R > 0.6$ and $y/R < 0.9$. Unlike the hovering case, in the region close to the propeller's rotation axis, the velocity profiles of the VPM case overlap with those extracted from the URANS simulations. This is an indication that, at significantly high advance ratios, the wake evaluated with the VPM no longer expands towards the propeller's rotation axis, being closer to the URANS simulations.

The VPM$_{BL}$ case is characterised by a significantly reduced computational cost compared to URANS simulations. A single revolution in hovering is, on average, simulated by VULCAINS in a CPU time of about 7.6% of the time needed in the URANS computations. Negligible differences (2%) are obtained between the URANS and URANS$_{Sp}$ simulations. In the case of axial inflow, the computational cost per CPU is further reduced, reaching approximately 4.8% relative to the URANS.

2.6.2 Influence of the VPM input parameters

The input parameters (N_S, $\Delta\psi$, time integration order, diffusion scheme, turbulent viscosity model) are varied one at a time to investigate their isolated influence compared to the baseline case. The number of sources per time-step N_S was initially varied between 20 and 60, while $\Delta\psi$ was varied between 2.5°

and 10°. The time integration order of the Runge-Kutta scheme was instead compared from the 1^{st} to the 4^{th}. The influence of the diffusion scheme and the turbulent viscosity model was analysed by comparing the implemented models in VULCAINS. Particularly for the choice of the diffusion scheme, the DVM model was compared with CSM and PSE. Regarding the turbulent viscosity model, the Vreman model was compared with the Mansour and the Smagorinsky models. Finally, the enstrophy filter cutoff frequency f_0 was varied from 0.25 to 1.25. The impact on the final solution was evaluated in terms of propeller loads, induced velocity in the wake, and computational cost. The loads are compared to the baseline case in terms of time-averaged non-dimensional thrust and torque coefficients ($\overline{C_T}$, $\overline{C_Q}$), non-dimensional thrust standard deviation (σ_{C_T}), and time-averaged non-dimensional thrust per unit-length distribution along the blade span direction ($\overline{s_{C_T}}$). The induced velocity in the wake is evaluated as a time-averaged non-dimensional axial velocity profile ($\overline{V_z}/\Omega R$) extracted at $z/R = 1$. Finally, the computational cost is evaluated in terms of total time required per core (C_{CPU}) to complete the simulation. The averaging operation of the listed quantities was carried out over the last 30 revolutions at both advance ratios. The comparison is finally carried out by computing the relative deviation ($\delta(\cdot)$) of the listed quantities $\delta(\cdot)$ compared to the baseline values. In the case of scalar quantities such as $\overline{C_T}$, $\overline{C_Q}$, $\overline{s_{C_T}}$, and C_{CPU}, the relative deviation is computed as a relative error compared to the baseline case. On the other hand, in the case of the sectional thrust distribution $\overline{s_{C_T}}$ and the axial velocity profile $\overline{V_z}/\Omega R$, the relative deviation is computed as a mean relative deviation, thus evaluating point-by-point the relative error in absolute value compared to the baseline case.

In Tables 2.6 and 2.7, the values of $\delta(\cdot)$ obtained for each of the analysed cases are displayed. The input parameters corresponding to the baseline case are highlighted in bold.

Table 2.6 Relative deviation ($\delta(\cdot)$) compared to the baseline case quantities. Influence of the number of sources (N_S), the azimuthal angle swept per time-step ($\Delta\psi$), and the integration order.

		N_S					$\Delta\psi$ [°]			Integration Order			
J	$\delta(\cdot)$ [%]	20	30	**40**	50	60	2.5	**5**	10	1	2	**3**	4
0.0	$\overline{C_T}$	-1.2	+0.0	-	-0.1	-3.4	+0.0	-	+0.6	-1.4	+0.1	-	-0.2
	$\overline{C_Q}$	-3.7	-0.9	-	+0.1	-2.4	+0.0	-	+0.3	-1.4	+0.2	-	-0.5
	σ_{C_T}	-37.0	-62.0	-	+67.8	+173.0	+4.1	-	+17.3	+9.5	+12.6	-	+5.3
	$\overline{s_{C_T}}$	3.4	1.4	-	1.3	4.0	0.3	-	1.2	1.1	0.1	-	0.4
	$\overline{V_z}/\Omega R$	12.5	9.4	-	6.9	21.7	0.8	-	2.3	5.7	0.7	-	3.2
	C_{CPU}	-62.2	-29.1	-	+47.6	+117.0	+113.0	-	-51.7	-48.3	-25.7	-	+34.9
0.1	$\overline{C_T}$	+0.2	+0.0	-	+0.1	+0.1	-0.1	-	+0.5	-0.3	+0.0	-	+0.1
	$\overline{C_Q}$	-0.4	-0.2	-	+0.2	+0.3	+0.0	-	+0.1	-0.1	+0.0	-	+0.0
	σ_{C_T}	-15.3	-3.5	-	+11.8	+21.7	+10.0	-	-13.0	-12.2	+4.7	-	-17.0
	$\overline{s_{C_T}}$	3.3	1.5	-	1.2	1.8	0.6	-	1.3	0.2	0.0	-	0.1
	$\overline{V_z}/\Omega R$	9.8	3.0	-	1.8	2.8	0.5	-	1.8	0.5	0.0	-	0.7
	C_{CPU}	-66.8	-39.1	-	+42.2	+102.0	+109.0	-	-44.9	-44.8	-22.7	-	+21.2

Table 2.7 Relative deviation ($\delta(\cdot)$) compared to the baseline case quantities. Influence of the diffusion scheme, the turbulent viscosity model, and the enstrophy filter cutoff frequency (f_0).

		Diffusion Scheme			Turbulent Viscosity Model			f_0		
J	$\delta(\cdot)$ [%]	PSE	**DVM**	CSM	Mansour	**Vreman**	Smagorinsky	0.25	**0.75**	1.25
0.0	$\overline{C_T}$	+0.0	-	0.2	+0.2	-	-0.5	+0.5	-	-0.3
	$\overline{C_Q}$	-0.2	-	-0.1	+0.2	-	-0.5	+0.9	-	-0.5
	σ_{C_T}	+23.7	-	-35.3	+13.3	-	+22.6	+95.4	-	-29.3
	$\overline{s_{C_T}}$	0.5	-	0.45	0.2	-	0.6	0.7	-	0.4
	$\overline{V_z}/\Omega R$	2.4	-	1.7	0.7	-	1.8	3.9	-	2.1
	C_{CPU}	+95.6	-	+13.9	-5.5	-	+6.4	-11.6	-	+11.4
0.1	$\overline{C_T}$	+0.2	-	-0.1	+0.0	-	+0.1	-0.1	-	+0.1
	$\overline{C_Q}$	+0.1	-	+0.0	+0.0	-	+0.0	+0.0	-	+0.0
	σ_{C_T}	-12.7	-	+18.0	+3.1	-	-12.4	+19.2	-	-13.5
	$\overline{s_{C_T}}$	0.2	-	0.1	0.0	-	0.1	0.2	-	0.1
	$\overline{V_z}/\Omega R$	1.5	-	0.7	0.2	-	0.8	1.3	-	0.7
	C_{CPU}	+8.6	-	-5.35	-0.4	-	-0.2	-1.8	-	+0.4

Number of sources (N_S)

The influence of N_S is more significant in hovering compared to the axial inflow case, where generally lower $\delta(\cdot)$ values are obtained. Regarding the impact on the time-averaged loads, the relative errors are not negligible but do not exceed in absolute value 3.4% for the thrust and 3.7% for the torque in hovering. Focusing on σ_{C_T}, an increasing trend can be observed with the increase of N_S. At N_S = 60 particles, σ_{C_T} increases by +173% with respect to the baseline case. It's necessary, however, to highlight that in the baseline case, σ_{C_T} is about 0.4% of $\overline{C_T}$; consequently, even such a significant increase leads to a small value of $\sigma_{C_T}/\overline{C_T}$.

The C_T time histories of the different cases are displayed in Figure 2.13, and it can be noted that the amplitude of the high-frequency C_T oscillations increases with the number of sources, likely due to the numerous interactions between the lifting lines and the growing number of surrounding particles at each iteration. At N_S = 50 and 60, lower frequency oscillations around the time-averaged value are also noticeable, while they were less visible or practically negligible at lower N_S values. Finally, although C_T converges to slightly different values, this convergence is reached approximately after 30 revolutions at the largest N_S value. In Figure 2.13, the C_T time histories in the case of axial inflow are also displayed. Under these operating conditions, the time-averaged value is almost identical across the various N_S values, with errors in absolute value below 0.4%. C_T converges in all cases after approximately 10 revolutions, presenting a $\sigma_{C_T}/\overline{C_T}$ around 3.16e-5, which, despite again appearing to increase with N_S, remains small and almost negligible even at N_S = 60.

Analysing the $\delta\overline{s_{C_T}}$ values, non-negligible values are obtained for N_S = 20 and 60. In Figure 2.14, the thrust per unit-length distributions are shown, and they almost overlap up to about r/R = 0.8, then

show some differences near the tip at r/R close to 1. At $J = 0$, the sectional thrust obtained for $N_S = 60$ appears to slightly underestimate the one obtained at lower N_S values, while more significant differences towards the tip are also observable among all the remaining cases. The higher the N_S value, the more the load towards the tip appears underestimated. This aspect also occurs in axial inflow. Such peculiarity in the tip region is typical of potential methods that see strong positive thrust gradients due to the tip vortex induction and due to the methods' intrinsic inability to capture the virtual camber effect. For this purpose, specific analytical correction functions have been implemented in other solvers, managing to improve the loads computation close to the blades' tip [101]. This effect is indeed not present in higher-fidelity simulations as URANS or LES, where the thrust and torque peak is recorded between 60 and 80% of the radius with a monotonically decreasing trend towards the tip. Another fundamental aspect to evaluate is the influence of N_S on the axial velocity in the wake. The variation of N_S results in the highest $\delta\overline{V_z}/\Omega R$, reaching values as high as 21.7% at $N_S = 60$ in hovering and 9.8% for $N_S = 20$ in axial inflow. In Figure 2.15, the velocity profiles extracted at $z/R = 1$ for the different N_S values are displayed. In hovering, the greatest differences are observed, especially in the wake core (approximately between $x/R > 0.3$ and $x/R < 0.6$). As N_S increases, a trend of increasing $\overline{V_z}/\Omega R$ is observed in this area. The $N_S = 60$ case stands out, showing a strong increase both in the core and in the inner zone towards $x/R = 0$. In this latter area, the greatest differences are concentrated for the axial inflow operative condition at $J = 0.1$. The differences between the profiles are indeed exclusively confined to $x/R < 0.3$, while in the wake core, the profiles almost overlap. In conclusion, an additional trend can be observed regarding the computational cost. The computational cost per core C_{CPU} appears to increase with the number of particles in both hovering and axial inflow. At $N_S = 60$, C_{CPU} is almost doubled for both the J values.

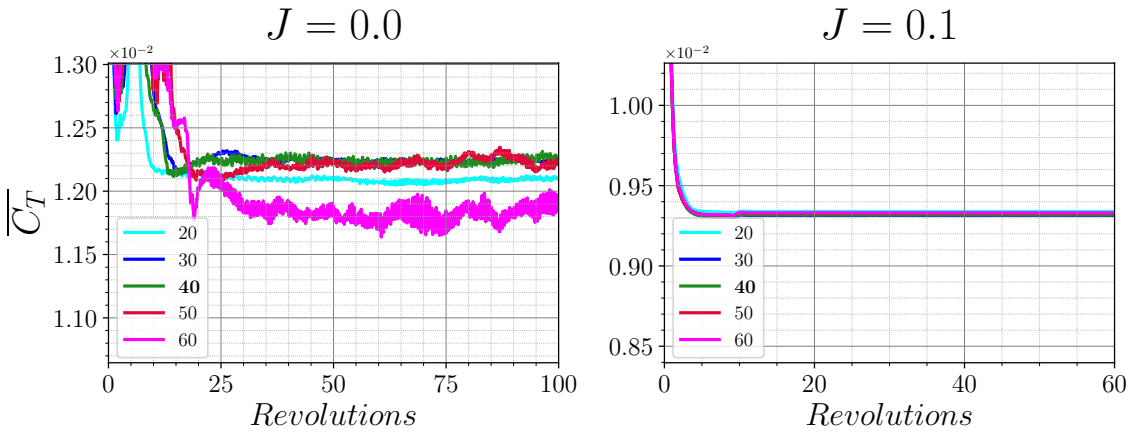

Fig. 2.13 Time-histories of C_T for the different values of N_S.

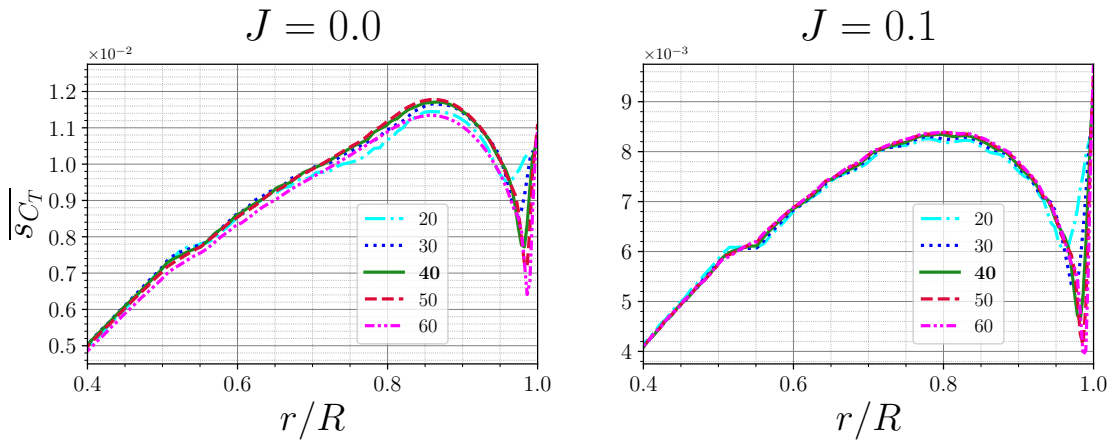

Fig. 2.14 Non-dimensional thrust per unit-length $\overline{s_{C_T}}$ along r/R for the different values of N_S.

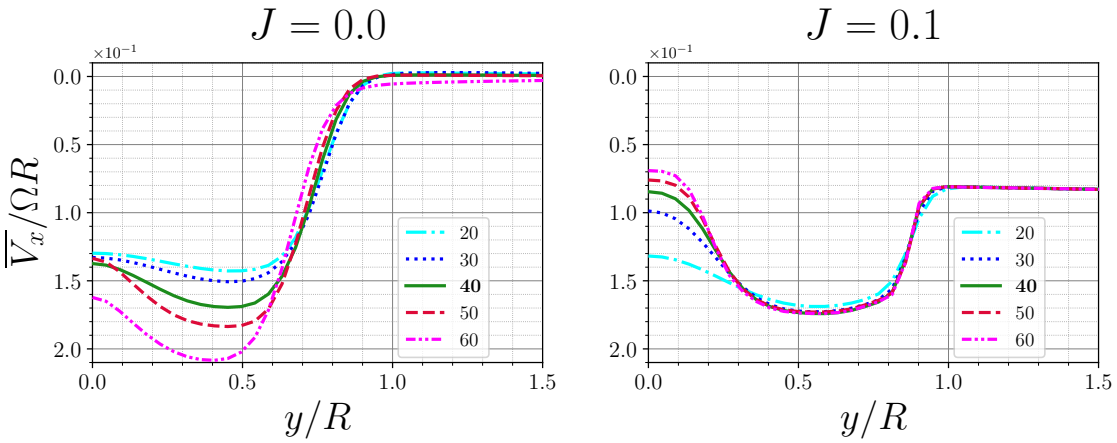

Fig. 2.15 Non-dimensional axial velocity $\overline{V_x}/\Omega R$ profile extracted at $z/R = 1$ for the different values of N_S

Discretization in the azimuthal direction ($\Delta\psi$)

The azimuthal angle swept per iteration ($\Delta\psi$) shows an almost negligible influence on the analysed quantities. Both in hovering and axial inflow, errors in average loads are lower than 0.6%, and no significant variations are observed in σ_{C_T}. The only remarkable effect of the $\Delta\psi$ increasing to 10° is a slight reduction in the wake velocity for $x/R < 0.3$, being, however, almost negligible if compared to what is observed for N_S. Nevertheless, it is expected that a much higher $\Delta\psi$ might significantly influence the final solution, even though $\Delta\psi > 10°$ is seldom taken into account in the numerical simulation of rotating lifting lines. Finally, the only significant effect of increasing $\Delta\psi$ is to decrease C_{CPU} by about 50% when moving from 5° to 10°, and to increase it by about 100% when reducing $\Delta\psi$ from 5 to 2.5°.

Order of Integration in Time

The choice of the order of integration in time does not impact the final solution as significantly as N_S. In particular, the average loads are not affected beyond 1.4% in hovering and 0.3% in axial inflow, and σ_{C_T} is not particularly impacted either. However, observing the C_T time histories at $J = 0$ in Figure 2.16, the choice of a 1^{st} order integration scheme leads to a C_T trend which is initially very similar to the 2^{nd} and 3^{rd} order trends, but C_T seems to slightly diverge from the average solution calculated for higher orders as the simulation advances. For what concerns the 4^{th} order, the solution reaches convergence only around the 40^{th} revolution, displaying strong oscillations in the previous iterations, not present in lower orders' time histories. Almost negligible differences are instead present in the wake velocity profile. The choice of a higher integration order ensures better accuracy of the solution over time, but it comes with some disadvantages, including an increased computational cost. However, this increase is limited to what is observed for small $\Delta\psi$ or high N_S.

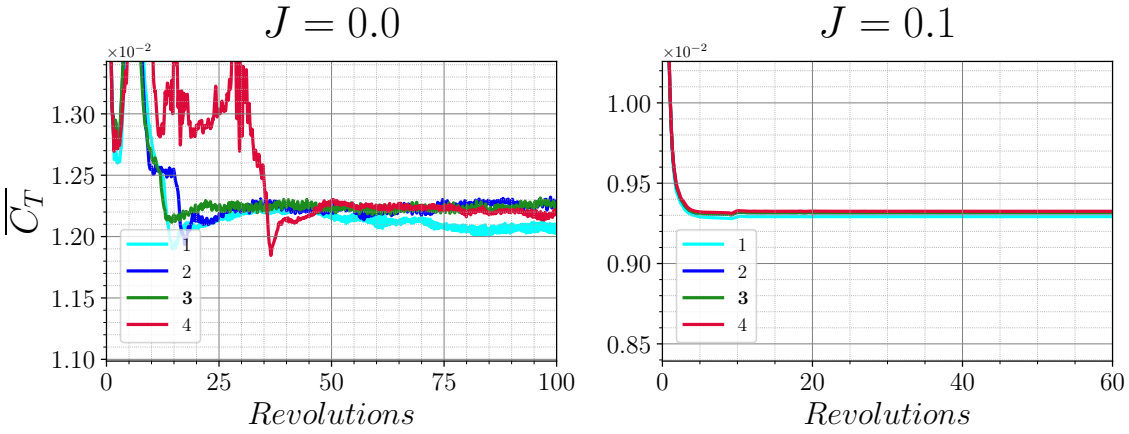

Fig. 2.16 Time-histories of C_T for the different orders of integration.

Diffusion Scheme

The choice of the diffusion scheme is almost negligible in terms of how it affects the time-averaged loads and wake velocity, particularly the velocity profiles being almost overlapped. However, by observing the C_T time histories in hovering as reported in Figure 2.17, an unexpected trend of the CSM solution is observed. The solution significantly oscillates above the mean value until almost the 60^{th} revolution, however, ultimately converging to a mean value which is very close to the other schemes. This behaviour makes the numerical scheme unreliable, especially because the simulations are typically run for fewer revolutions to save on computational cost. Regarding the computational cost, C_{CPU} increases by only +13.9% in hovering for the CSM scheme, while it increases by up to +95.6% for the PSE scheme, making the latter less advantageous due to the frequently required particle distribution in the domain.

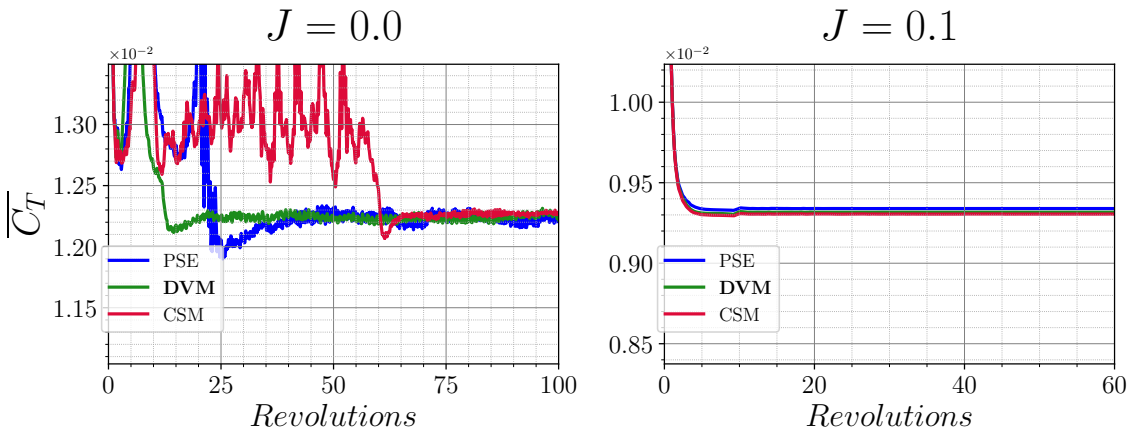

Fig. 2.17 Time-histories of C_T for the different considered diffusion schemes.

Turbulent Viscosity Model

The turbulence viscosity model does not appear to have a significant influence on the solution, neither in terms of loads nor wake velocity. Moreover, it does not seem to have a significant impact on the computational time either, which varies at most by +6.4% for the Smagorinsky model in the hovering conditions.

Enstrophy filter cutoff frequency (f_0)

The last investigated parameter is the enstrophy filter cutoff frequency f_0, which determines the intensity of the filter to control the particles' strength in magnitude and orientation. A higher value of this parameter indicates a greater filter intensity, often useful in highly turbulent flows to maintain a divergence-free velocity field. The effect of f_0 appears to be almost negligible in both hovering and axial inflow conditions regarding average loads and load distribution along the blade. The σ_{C_T} is reduced with the increase of f_0; however, as observable in Figure 2.18 at $J = 0$, the case with $f_0 = 1.25$ requires more revolutions to reach convergence. On the other hand, in axial inflow conditions, negligible differences are instead observable among the different C_T time histories. Choosing an f_0 different from the baseline also leads to slight differences in velocity profiles, as observable in 2.19. In hovering, an increase of f_0 results in a decrease of the axial velocity in the wake core, while it has a negligible effect in the case of axial inflow. To conclude, no significant effect is observed in the computational cost of the simulations.

2.6.3 Influence of the airfoil polars

The parametric investigation carried out in Section 2.6.2 revealed a non-negligible sensitivity of the VPM solver to the number of sources shed from the propeller blades. Among the analysed values,

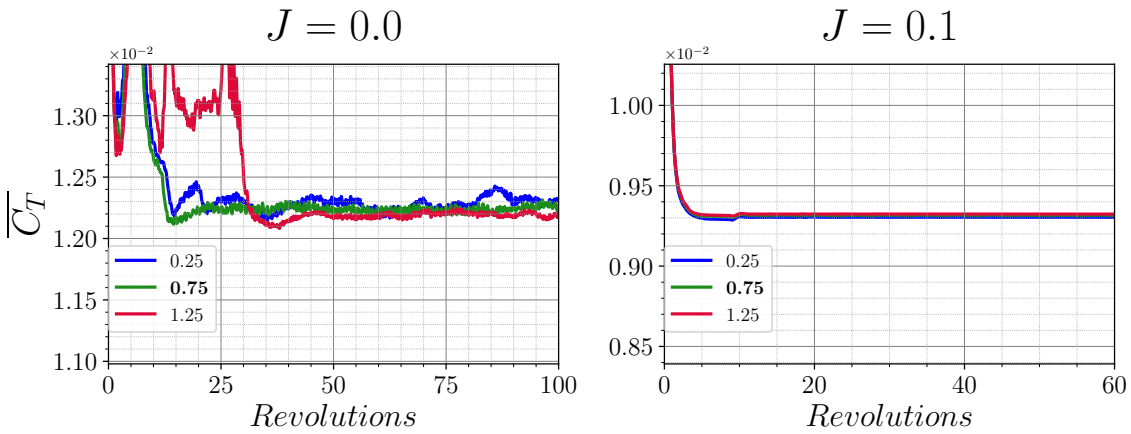

Fig. 2.18 Time-histories of C_T for the different values of the cutoff frequency f_0.

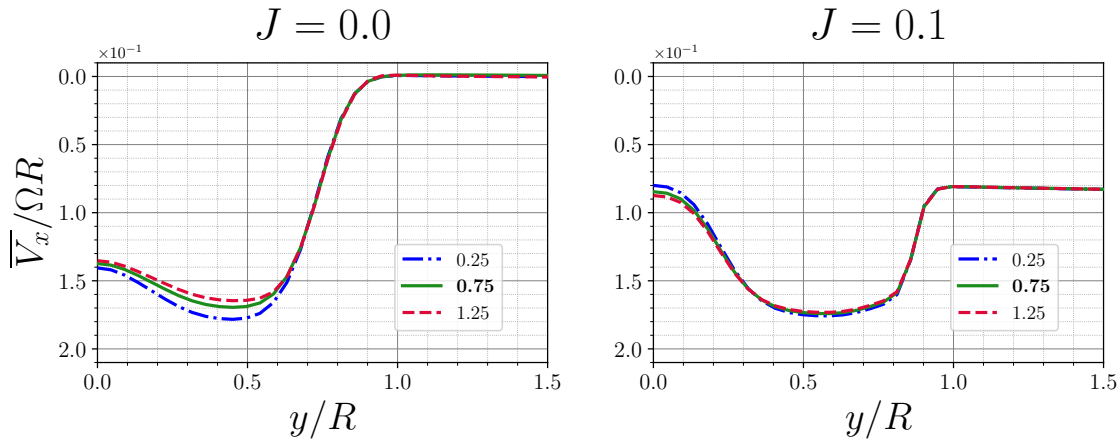

Fig. 2.19 Non-dimensional axial velocity $\overline{V_x}/\Omega R$ profile extracted at $z/R = 1$ for the different values of the cutoff frequency f_0.

$N_S = 50$ was identified as the most appropriate choice, providing the most accurate prediction of the induced flow field. The assessment of the airfoil polars influence is consequently conducted starting from the VPM_{BL} case, with the input parameters listed in Table 2.5, but now increasing N_S to 50 for improved agreement with the PIV axial velocity measurements. This refined configuration is hereafter referred to as VPM_{X5}, denoting the use of XFoil-based airfoil polars. To evaluate the airfoil polars' influence, two additional cases are considered, both employing 2D URANS polar sets obtained with the SSTLM turbulence model: one including the low-Mach Pre-conditioner (VPM_{S-Pc}), and one without it (VPM_{S-noPc}). The three sets of polars were previously displayed in Figure 2.10 in section 2.5.5, at $M = 0.2$ and $Re_c = 20,000$.

The time-averaged axial velocity fields ($\overline{V_x}/\Omega R$) obtained from experiments, URANS, and the different VPM cases, are reported in Figure 2.20 for both hovering ($J = 0$) and axial inflow ($J = 0.1$). The corresponding $\overline{C_T}$ and $\overline{C_Q}$ values are also included in the same figure. For a quantitative comparison, the axial velocity profiles extracted at $x/R = -0.5, 0.7$, and 1.5 are shown in Figure 2.21. Starting with

the VPM_{X5} case, the integral time-averaged loads remain close to those of the VPM_{BL} configuration. Table 2.6 confirms that the increase of N_S from 40 to 50 produces relative variations below 0.2%. However, more substantial differences are observed in the wake flow field. The higher number of sources indeed enhances the predicted axial velocity. In hovering conditions ($J = 0$), the velocity profiles of VPM_{X5} nearly overlap with URANS for $y/R > 0.25$, although discrepancies remain near the rotation axis, with relative differences reaching 50% at $x/R = 1.5$. At $x/R = 0.7$, VPM_{X5} additionally shows good agreement with the experiments, while at $x/R = 1.5$ it overestimates the velocity by approximately 14%, similarly to URANS. In axial inflow ($J = 0.1$), the match improves significantly: deviations in the wake core are reduced to about 4%, with VPM_{X5} displaying better overall predictions than VPM_{BL}. Nonetheless, the VPM wake remains broader in the radial direction, with higher velocity levels observed in the range $0.06 < y/R < 0.9$.

The VPM_{S-Pc} case produces thrust values close to VPM_{X5}, with relative deviations of only 0.3% in hovering and 3% in axial inflow. This consistency can be explained by the similarity of the $c_L - \alpha$ curves at high angles of attack (around 9-10°), which dominate the hovering condition (Figure 2.10). At lower angles of attack (5-7°), more relevant at $J = 0.1$, the differences between the $c_L - \alpha$ curves are more pronounced, explaining the observed thrust discrepancies. For the torque, however, significant deviations occur in both conditions: VPM_{S-Pc} overpredicts $\overline{C_Q}$ compared to both experiments and URANS, by 19% and 17% respectively in hovering and axial inflow, and by about 13% relative to URANS. VPM_{S-Pc}, however, significantly overpredicts experimental $\overline{C_Q}$ values by 19% in hovering and 17% in axial inflow. This case also overpredicts URANS torque values by about 13%, both in hovering and axial inflow. These errors reflect the higher drag coefficients of the $c_D - \alpha$ curve. Despite this, the axial velocity fields remain nearly indistinguishable from VPM_{X5}, since the thrust levels are similar, resulting in comparable wake features.

The VPM_{S-noPc} case exhibits the opposite trend. $\overline{C_T}$ is consistently underpredicted: by 18% and 15% relative to experiments, and by 29% and 21% relative to URANS in hovering and axial inflow, respectively. This reduced thrust leads to significantly lower axial velocity in the wake core. Interestingly, $\overline{C_Q}$ is instead accurately captured, with deviations below 4% from both experiments and URANS, thus yielding a better torque prediction than the other considered VPM cases.

The comparative analysis can be expanded by considering the radial distributions of the non-dimensional time-averaged thrust per unit length ($\overline{s_{C_T}}$) and torque per unit length ($\overline{s_{C_Q}}$). These distributions, obtained by integrating the loads along the blades' chord, are only available from numerical simulations. Figure 2.22 reports $\overline{s_{C_T}}$ as a function of r/R, while Figure 2.23 shows $\overline{s_{C_Q}}$. The URANS and URANS_{Sp} distributions are nearly superimposed, with the support producing only minor shifts of the maximum load toward larger R, particularly in hovering. In contrast, VPM consistently underpredicts thrust in the inboard blade region ($r/R < 0.65$). At $J = 0$, VPM_{S-Pc} and VPM_{X5} show an approximately constant offset around 2×10^{-3} with respect to the URANS, while at $J = 0.1$ this difference reduces to about 1×10^{-3}. VPM_{S-noPc} initially follows the other VPM cases but diverges toward lower thrust levels for $r/R > 0.4$, worsening the mismatch with URANS.

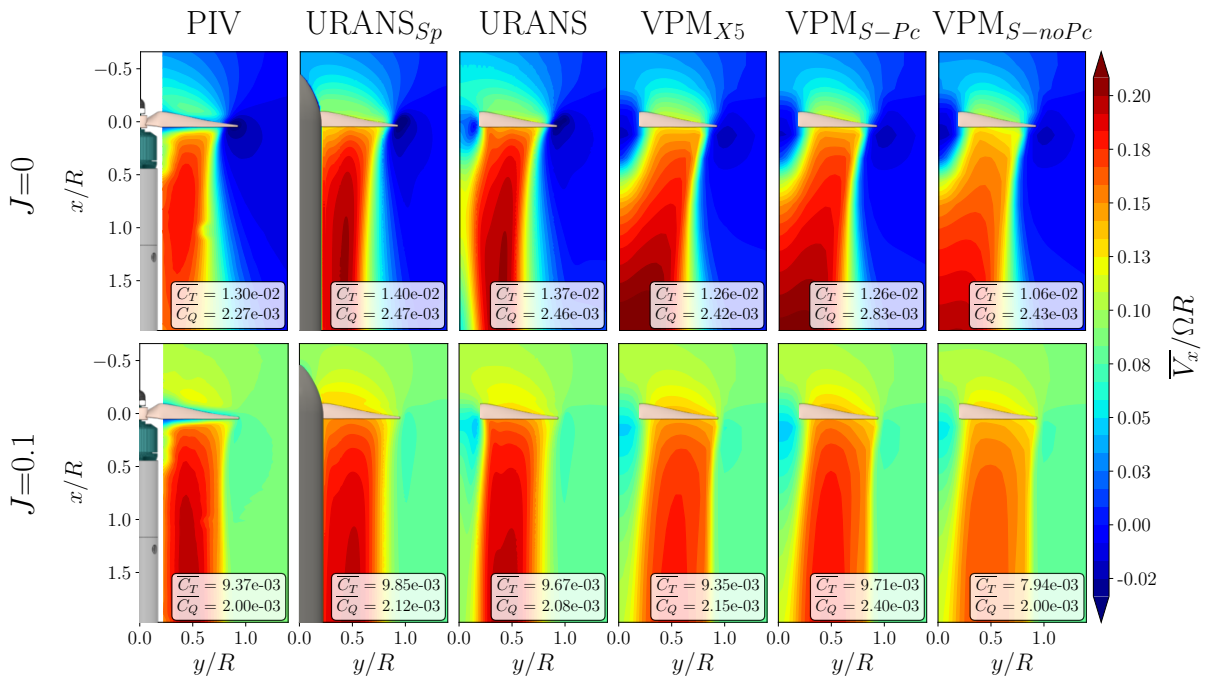

Fig. 2.20 Colourmaps of the normalized time-averaged velocity along the x-axis ($\overline{V_x}/\Omega R$). The propeller-shaped mask is added to improve the clarity.

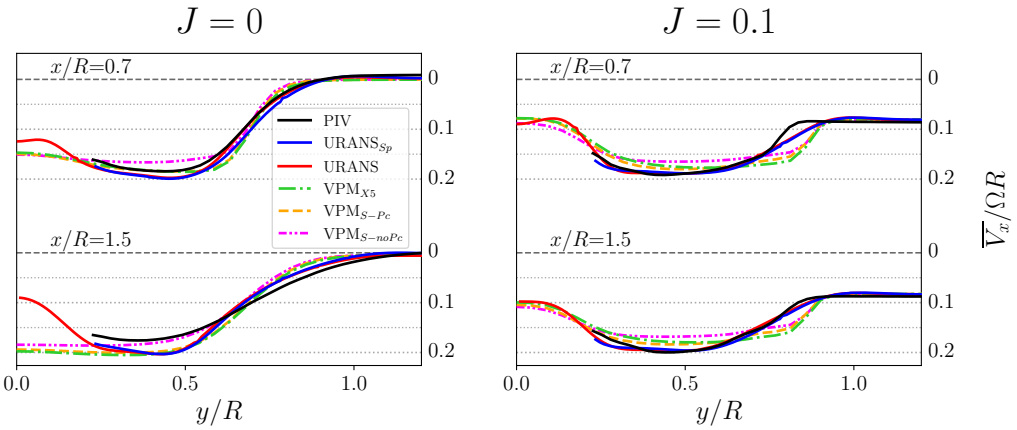

Fig. 2.21 Axial velocity ($\overline{V_x}$) profiles extracted from the flow fields in Figure 2.20 at $x/R = -0.5, 0.7$ and 1.5.

In the outboard region ($r/R > 0.65$), VPM$_{S-Pc}$ and VPM$_{X5}$ initially agree well with URANS, but progressively overestimate the loads approaching the tip, with significant errors of 40-50% in hovering. At $J = 0.1$, the URANS maximum is observed around $r/R = 0.65$, while the VPM places the maximum more outboard ($0.7 < r/R < 0.8$), depending on the used set of polars. With the XFoil polars, the maximum thrust closely matches the URANS, while VPM$_{S-Pc}$ underpredicts it by 8% and VPM$_{S-noPc}$ by 25%. Concerning the torque distributions, VPM$_{S-noPc}$ shows good agreement with URANS across the span, mostly in hovering, with slight overestimations at $J = 0.1$ close to the tip region. The VPM$_{X5}$ shows good accordance with the higher-fidelity URANS results also in hovering, with, however, greater

overestimations in axial inflow. VPM_{S-Pc} shows, in conclusion, the worst match with URANS data, featuring high torque values already in hovering conditions.

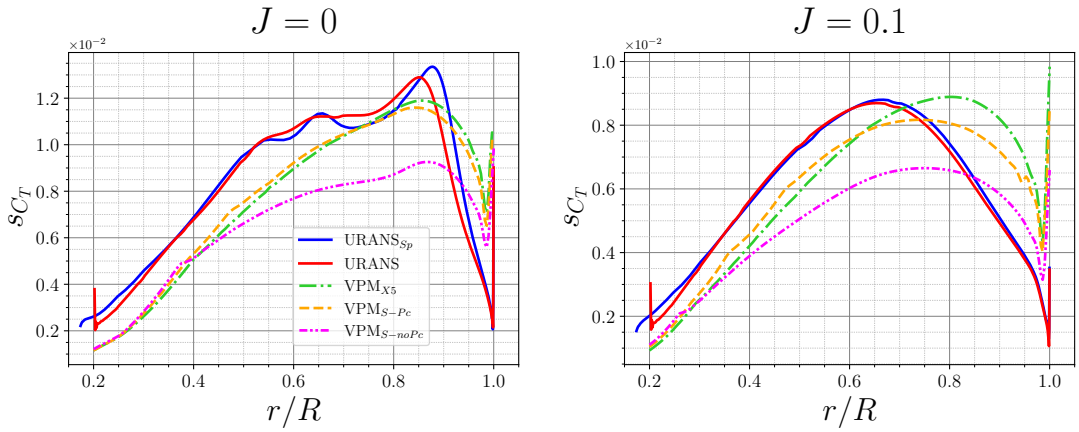

Fig. 2.22 $\overline{s_{C_T}}$ distribution as a function of r/R.

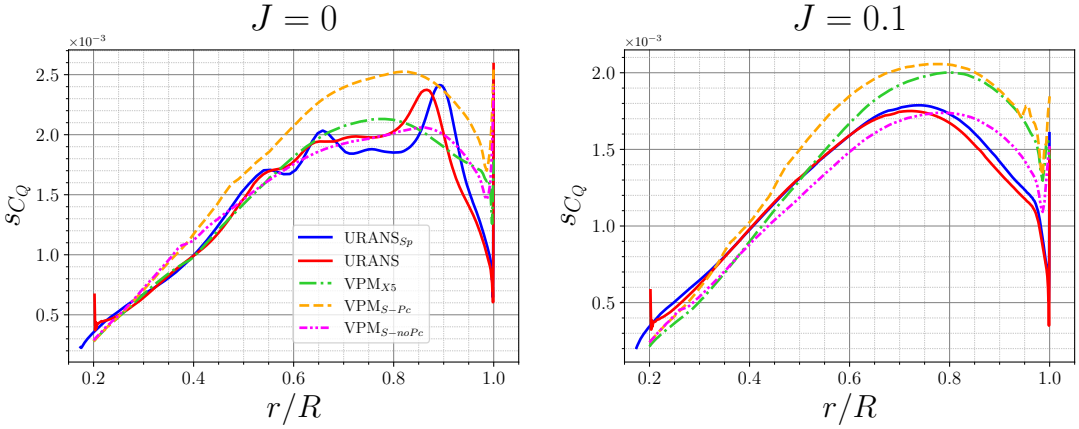

Fig. 2.23 $\overline{s_{C_Q}}$ distribution as a function of r/R.

To further explore the discrepancies between the loading distributions, the pressure coefficient (c_p) distributions on the blade surface are analysed. c_p is defined as: $c_p = \frac{p-p_\infty}{\frac{1}{2}\rho(\Omega R)^2}$, with p the local pressure value, and is plotted along the chordwise non-dimensional coordinate (x_c/c) at three radial coordinates, i.e. $r/R = 0.4, 0.6$, and 0.8, respectively in Figures 2.24, 2.25, and 2.26). URANS and URANS_{Sp} show again superimposed c_p distributions, mostly at lower chordwise coordinates ($x_c/c < 0.6$). In hovering conditions, c_p displays typical features of laminar separation bubbles on the suction side, being characterised by a first steep pressure recovery followed by a pressure plateau, where the flow is detached, and finally by a further pressure recovery towards the blade tip. This behaviour is mostly evident at $r/R = 0.4$, while at greater radial coordinates these features are less clear to identify. In axial inflow at $J = 0.1$, a smoother pressure recovery is instead observed, and a large pressure plateau with

no subsequent recovery is present at $r/R = 0.8$, indicating that no separation bubble is likely present in these conditions. Among the VPM cases, VPM_{X5} provides the best prediction of the URANS c_p distributions. At $r/R = 0.6$ and 0.8 in hovering, VPM_{X5} nearly overlaps URANS on both the pressure and suction side, predicting pressure plateaus and steep gradients. At $r/R = 0.4$, slight deviations can be observed, with suction-side separation and reattachment occurring earlier than in URANS. At $J = 0.1$, significant overprediction of thrust at $r/R = 0.8$ corresponds to slight discrepancies in c_p. Conversely, VPM_{S-Pc} and VPM_{S-noPc} systematically show a mismatch with URANS and VPM_{X5} distributions, not only in predicted values, but more generally in the prediction of the flow behaviour. In particular, no pressure recovery is found after the pressure plateaus, resulting in larger values in the chordwise direction. These polars are indeed not able to predict a separation bubble as observed with the XFoil polars, leading to significant discrepancies with higher-fidelity URANS results.

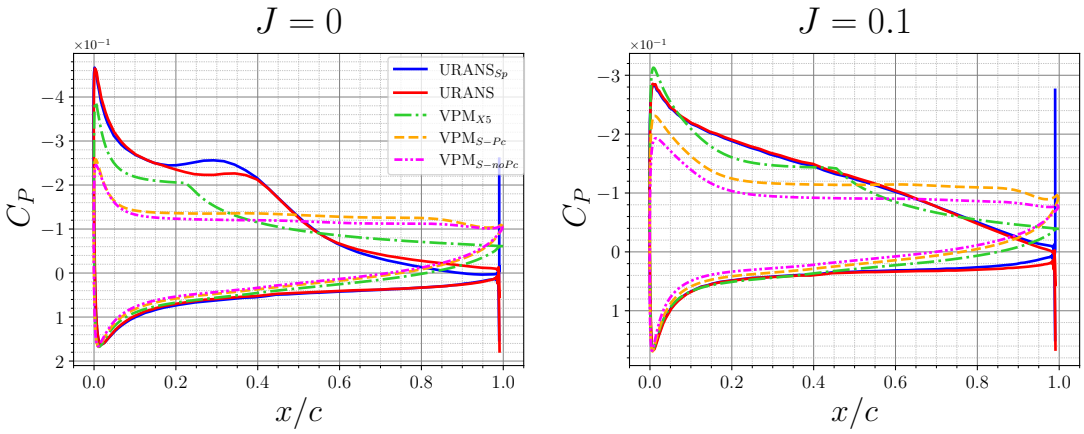

Fig. 2.24 c_p distribution at $r/R = 0.4$ as a function of x_c/c.

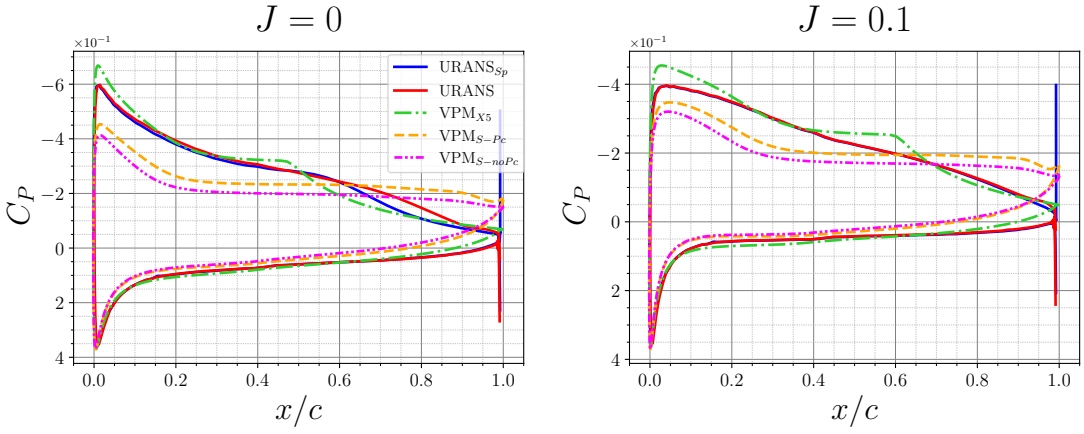

Fig. 2.25 c_p distribution at $r/R = 0.6$ as a function of x_c/c.

To complement the pressure analysis, the skin friction coefficient is examined: $c_f = \frac{\tau_w}{\frac{1}{2}\rho(\Omega R)^2}$, where τ_w is the wall shear stress projected along the chordwise direction. The chordwise location where $c_f = 0$

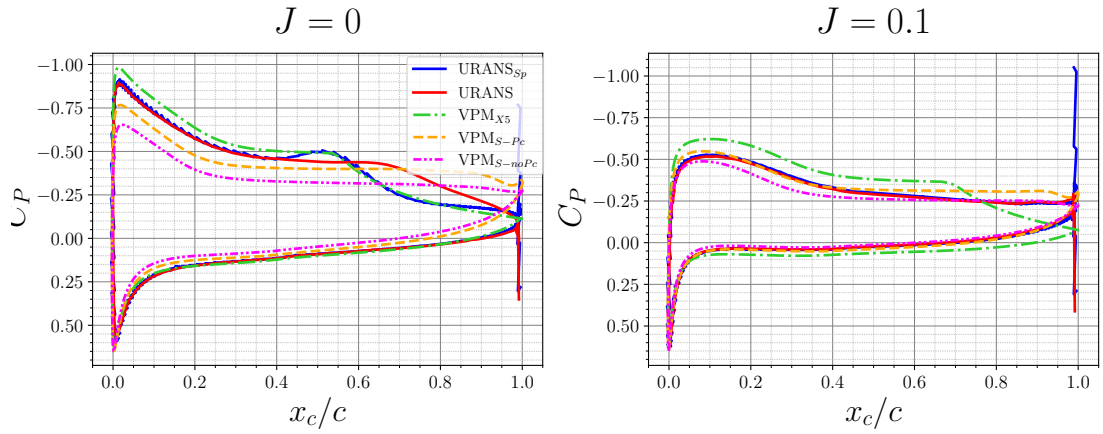

Fig. 2.26 c_p distribution at $r/R = 0.8$ as a function of x_c/c.

provides an approximate indicator of flow separation onset on the suction side. While this criterion is not exact for rotating blades due to radial velocity gradients, it remains useful to highlight systematic differences in the flow separation between the analysed cases. The c_f contours are displayed in Figure 2.27, with white dashed lines marking the separation coordinates (x_c/c_{Sep}) on the blades' suction side. The corresponding normalised values x_c/c_{Sep} are reported as a function of r/R in Figure 2.28 for a quantitative comparison. At $J = 0$, URANS and URANS$_{Sp}$ show nearly identical trends: separation occurs near the leading edge in the inboard blade region, moving towards $x_c/c_{Sep} = 0.27$ at mid-span and then again near the leading edge close to the blades' tip. Similar distributions are also found in axial inflow at $J = 0.1$. However, the support affects the blade region close to the root ($r/R < 0.35$), where separation occurs much earlier in URANS$_{Sp}$ than in URANS. The VPM cases systematically predict earlier separations in the inboard region and delayed separation in the outboard one, consistent with the thrust predictions in the two regions observed in Figure 2.22. Among the VPM cases, VPM$_{X5}$ yields the largest separation coordinates, followed by VPM$_{S-Pc}$ and then VPM$_{S-noPc}$. Discrepancies are most pronounced near the tip, where URANS predicts separation around $x_c/c_{Sep} = 0.1$, while VPM$_{X5}$ delays it to about 0.3.

2.6.4 Conclusions

In this section, a comprehensive multi-fidelity analysis was performed to assess the predictive capabilities of the VPM code VULCAINS against higher-fidelity methodologies, such as URANS and experiments. The analysis focused on the small-scale propeller operating in both hovering and axial inflow conditions.

A first comparison employed the input parameters and airfoil polars reported in Table 2.5 for the baseline VPM case. In this configuration, experiments, URANS, and VPM provided overall consistent predictions. In axial inflow, the relative differences in thrust and torque coefficients with respect to experiments remained below 4% for both URANS and VPM. Nevertheless, URANS delivered superior

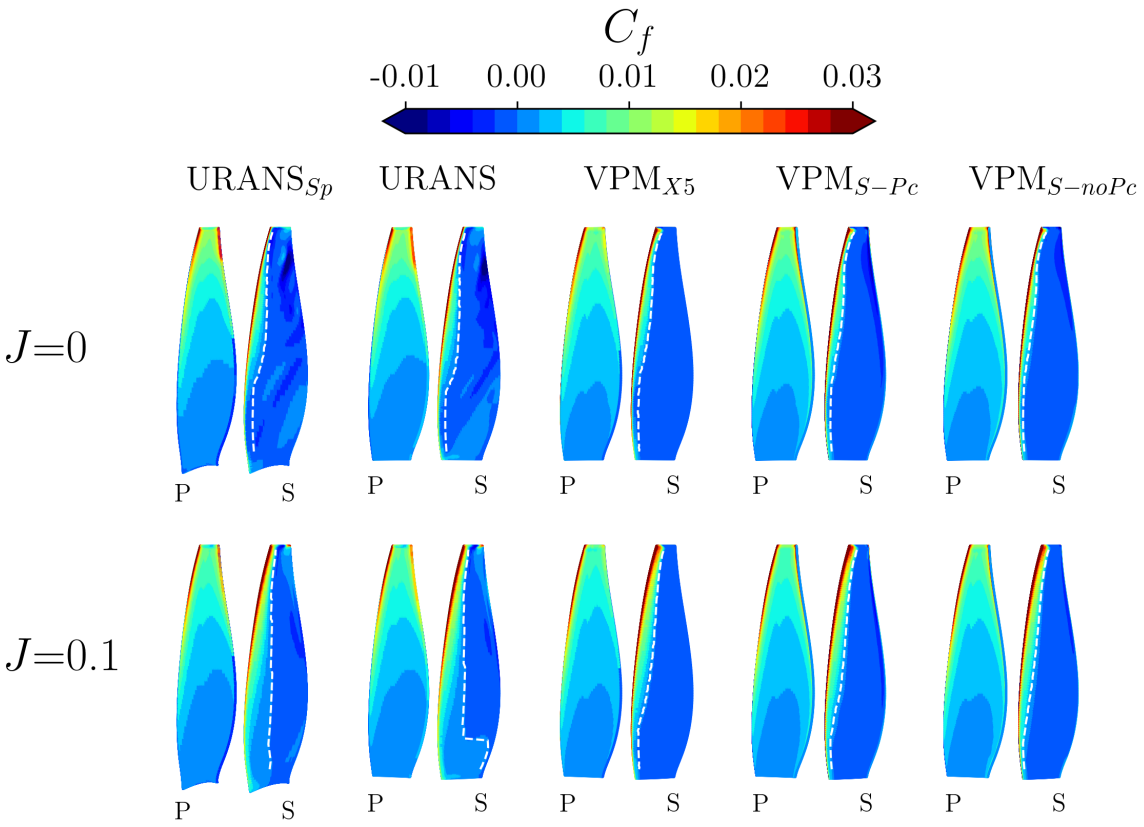

Fig. 2.27 c_f distribution on the blades surfaces. P is the pressure side, while S represents the suction side. The white dashed lines represent the first flow separation coordinates x_c/c_{Sep} occurring on the blades' suction side. The normalised separation coordinates x_c/c_{Sep} are shown in Figure 2.28.

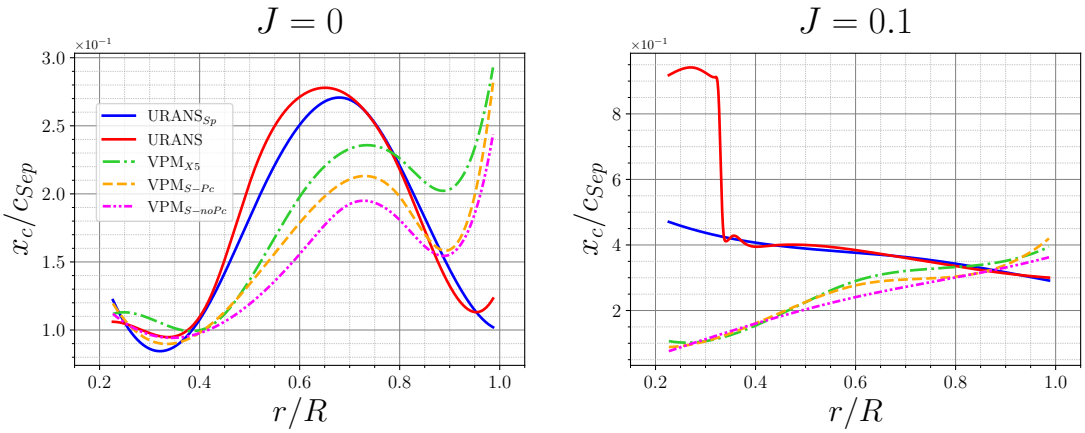

Fig. 2.28 Chordwise separation coordinate x_c/c_{Sep} as a function of r/R.

predictions of the induced axial velocity field, overlapping experimental data across most of the wake region, with slight discrepancies near the rotation axis due to the absence of the spinner in the numerical setup. The VPM, on the other hand, tended to underestimate the wake core velocity, with errors on the

order of 5%. In hovering, larger differences arose among the methods: thrust and torque errors reached up to 8%, while URANS overestimated the wake velocity by 8 to 15% and VPM underestimated it by about 5%, particularly near the propeller disk. The VPM additionally showed a wake spreading towards the rotation axis that is not observed in the other methodologies. Furthermore, experiments revealed a localised maximum velocity region around half a radius downstream of the disk, whereas in both URANS and VPM, the axial velocity continued to increase up to at least 1.5 R.

Following this baseline assessment, a parametric analysis was undertaken to evaluate the sensitivity of VPM to its main input parameters. Among these, the number of vorticity sources shed per time step (N_S) emerged as the most influential. Increasing N_S from the baseline value of 40 to 60 resulted in thrust and torque variations of up to 3% in hovering and 0.2% in axial inflow, but a much stronger effect was observed in the induced wake. Particularly in hovering, the axial velocity magnitude in the wake core increased by about 15%, while in axial inflow, the wake appeared negligibly affected. Increasing the number of particles leads to a greater computational cost, which nearly doubled when increasing N_S from 40 to 60. Other parameters investigated showed little influence on global results, although the convergence behaviour was noticeably affected in some cases. For instance, with the CSM diffusion scheme, more than 60 propeller revolutions were required in hovering to reach convergence of thrust loads, compared to about 20 revolutions with the DVM scheme in the baseline case. This emphasises that while most parameters are not critical to the accuracy, they may substantially influence numerical efficiency.

Based on these findings, a further investigation into the choice of the airfoil aerodynamic polars was carried out. A refined baseline case (VPM_{X5}), with input parameters as in Table 2.5 but with $N_S = 50$ for a better match with higher-fidelity results, was compared with two additional configurations employing SSTLM-derived polars: VPM_{S-Pc}, using the low-Mach preconditioner, and VPM_{S-noPc}, without the preconditioner. Among the three, VPM_{X5} delivered the closest agreement with experiments and URANS. Integral thrust and torque coefficients were predicted within 4% error, and the wake velocity profiles overlapped almost entirely with URANS results, thanks to the increased N_S. VPM_{S-Pc} also showed reasonable agreement in thrust and wake velocity, but overestimated torque by up to 19%. Conversely, VPM_{S-noPc} reproduced torque accurately, with errors below 4%, but significantly underestimated thrust (by up to 29%) and wake velocities. The comparison was extended by examining radial distributions of thrust and torque per unit length, along with surface pressure and skin-friction distributions. These analyses revealed systematic discrepancies between VPM and URANS. In all VPM cases, thrust was underestimated inboard ($r/R < 0.65$) and overestimated outboard ($r/R > 0.65$), leading to a spanwise redistribution of loading. The skin-friction distributions confirmed this behaviour: regions of delayed flow separation corresponded to higher local thrust predictions, while earlier separation was associated with thrust underestimation. Among the three VPM cases, VPM_{X5} again provided the closest match to URANS, particularly in reproducing laminar separation bubbles on the suction side, characterised by localised pressure plateaus bracketed by non-zero gradients. In contrast, both VPM_{S-Pc} and VPM_{S-noPc} displayed a more simplified pattern of initial suction recovery followed

by extended plateaus up to the trailing edge, failing to replicate the characteristic pressure trends captured in URANS.

Overall, this analysis has enabled a clear assessment of the capabilities and limitations of the VPM code VULCAINS for the simulation of small-scale propellers in hovering and axial inflow. The mid-fidelity method, characterised by low computational requirements and straightforward setup, proved to be an efficient tool for preliminary design. The VPM code demonstrated reliable predictions of integral time-averaged quantities, such as thrust and torque coefficients, and, particularly in axial inflow, captured the induced wake with good accuracy in both radial extent and core velocity. The limited sensitivity of the results to most input parameters suggests that extensive calibration is unnecessary, though careful parameter selection may still improve agreement with higher-fidelity references. In contrast, the choice of aerodynamic polars emerged as a critical factor, especially at the low Reynolds numbers considered. Among the tested options, XFoil polars with $N_{crit} = 5$ were found to provide the most accurate results at negligible computational cost. Nevertheless, the correct selection of N_{crit} remains Reynolds-dependent and requires guidance from higher-fidelity data, limiting its general applicability to other geometries or operative conditions. The SSTLM-based polars offer broader generalizability without the need for such calibration, but show poorer accuracy in both performance and induced flow field predictions. In the present work, the SSTLM model was employed with its standard calibration. Although alternative calibrations may potentially improve the prediction of aerodynamic polars, they require dedicated tuning and validation against higher-fidelity data, which adds complexity and reduces general applicability. An additional strategy could be to rely on even higher-fidelity approaches, such as Large Eddy Simulations (LES), which are capable of providing detailed aerodynamic information. However, the computational cost associated with LES makes them impractical in the context of mid-fidelity tools like VPM, whose main advantage lies in their reduced cost and suitability for preliminary design phases.

In conclusion, XFoil polars at $N_{crit} = 5$ are identified as the most suitable choice for VPM simulations at the tested Reynolds numbers, and are therefore adopted for the subsequent analysis of dynamic maneuvers. Chapter 4 extends this validation campaign to dynamic operative conditions, maintaining the same input parameters as defined for the VPM_{X5} configuration.

2.7 Data reduction

2.7.1 Vortex Identification

In order to quantify how the vortical structures evolve in the propeller's wake, two vortex identification and characterisation methods are exploited in this work. Multiple methods exist in the literature and have become rather popular in the past years [102]. In the classical fluid mechanics theories, vortices are thought of as regions of high vorticity. The simplest detection method is indeed based on the

relation between local vorticity maxima and vortex centres. However, this presents some intrinsic flaws, not being able to accurately predict the vortex centre when a shear flow is superimposed on pure rotation [102]. To cope with this problem, different gradient-based approaches have been proposed in the literature. These methods are Galilean invariant, due to the independence of the velocity gradient tensor from the considered inertial system. Furthermore, they are based on a threshold, which permits distinguishing between regions with a prevalence of rotation and those regions where the strain instead dominates. Such a threshold can either be physics-related or arbitrary. In the present work, the Q-criterion [103] and the Γ_2 criterion [104] were chosen for the analysis of numerical data and experimental data.

The Q-criterion is one of the most commonly employed due to its intuitive physical interpretation and ease of implementation in numerical environments. It derives from the analysis of the velocity gradient $\nabla\vec{u}$, where $\vec{u}$ is the velocity vector field. This tensor can be decomposed into a symmetric part S, representing the rate-of-strain, and an antisymmetric part Ω_Q, representing the local rotation as $\nabla\vec{u} = S_Q + \Omega_Q$. S_Q and Ω_Q can be written as $S_Q = \frac{1}{2}\left(\nabla\vec{u} + (\nabla\vec{u})^T\right)$ and $\Omega_Q = \frac{1}{2}\left(\nabla\vec{u} - (\nabla\vec{u})^T\right)$. Physically, S_Q accounts for deformation without rotation, while Ω_Q captures the rigid-body rotation component. The Q-criterion then defines a scalar field Q based on the second invariant of $\nabla\vec{u}$, that is written in Eq. 2.17

$$Q = \frac{1}{2}\left(\|\Omega_Q\|^2 - \|S_Q\|^2\right) \tag{2.17}$$

Here, $\|\cdot\|$ denotes the Frobenius norm. A region of the flow is considered vortical if $Q > 0$, meaning that the local rotation dominates over strain. This provides an objective and Galilean-invariant way to extract coherent structures, independent of the observer's frame of reference. The vortices' centres can be identified at this stage in correspondence with local Q maxima in connected regions featured by $Q > 0$. The vortex area, therefore, extends until $Q > 0$ in the surrounding connected region. Once the area is evaluated, making use of the Stokes-Kelvin theorem, it is possible to compute the vortex circulation as the integral of the vorticity. To isolate the stronger structures, it might be necessary to consider rotational regions with Q greater than an arbitrary threshold, in turn greater than 0. This is particularly effective in the case of the tip vortices, typically stronger than other vortical structures shed by propellers.

From a numerical standpoint, the Q-criterion is especially suitable for large-scale CFD simulations because it involves quantities readily available from the computed velocity field and does not require pressure or vorticity derivatives. It allows for the clear visualisation of vortical structures by plotting iso-surfaces of positive Q, which is particularly useful in studying vortex shedding, turbulence, and instabilities in wakes or boundary layers. Moreover, its relatively low computational cost makes it ideal for post-processing in high-resolution, unsteady simulations such as LES or DNS.

Despite being the state-of-the-art of vortex identification criteria in multiple applications, the Q-criterion might not work properly if applied to PIV data, where experimental noise is also present. In dedicated work [105], De Gregorio et al. tested the effectiveness of different methods for the identification of the tip-vortices shed by a small helicopter rotor. Inaccuracies in the velocity fields computation due to laser reflections on the blades, lack of seeding, and low signal-to-noise ratio put a strain on the velocity gradient-based methods, resulting in an often inaccurate vortex identification. To overcome such limitations, a further method introduced in [104] and widely used in the PIV analysis [106–108] was taken into account by De Gregorio et al. for a comparison. The method, based on a scalar function Γ_2, relies solely on the local flow topology, thereby avoiding the computation of the velocity gradient and resulting in greater robustness for PIV data. In particular, let P be a fixed point in the 2D rectangular grid where the velocity is evaluated through the PIV technique. It is possible to define a dimensionless scalar denominated Γ_2 in the point P as in eq. 2.18, being S_D a rectangular domain of fixed size which surrounds P, M a point in S_D, $\vec{PM}$ the vector which links the two points, and z a normal vector to the considered plane.

$$\Gamma_2(P) = \frac{1}{N} \sum_{S_D} \frac{[\vec{PM} \wedge (U_M - \vec{U_P})] \cdot z}{\|\vec{PM}\| \cdot \|U_M - \vec{U_P}\|} \tag{2.18}$$

In the limit of $S_D \to 0$, it can be shown that Γ_2 is only a function of the rotation rate corresponding to the anti-symmetrical part of the velocity gradient and the eigenvalue of the tensor's symmetrical part [104]. Despite of the still unknown exact relation between $|\Gamma_2|$ and the two quantities, it is shown that it is possible to discriminate among regions dominated by strain ($|\Gamma_2| < 2/\pi$), regions of pure shear ($|\Gamma_2| = 2/\pi$) and regions of the flow dominated by rotation ($|\Gamma_2| > 2/\pi$) [104]. The overall method represents a robust way to identify vortical structures. On the other hand, the evaluation of vortex dimensions is instead highly dependent on the chosen value for N. For this purpose, in [107] it is suggested to choose N to evaluate the two scalar functions in a domain S_D of the order of the tip-vortices present in the flow field. The vortices' centres can be identified at this stage in correspondence with local $|\Gamma_2|$ maxima which overcome an arbitrary threshold Γ_{2-thr}. The vortex area is then evaluated around the centre, and it is retained to extend until $|\Gamma_2| > 2/\pi$ in the surrounding connected region. Once the area is evaluated, making use of the Stokes-Kelvin theorem, it is possible to compute the vortex circulation as the integral of the vorticity. The choice of the parameter N instead significantly influences the calculation of both vortices' area and circulation. In particular, the vortex area is subjected to a magnification with the increase of N. This inevitably leads to non-negligible uncertainties in the exact area and circulation values. Fixing the value for N among the investigated cases, however, allows a comparative assessment of the area of the vortices.

2.7.2 Proper Orthogonal Decomposition

Proper Orthogonal Decomposition (POD) is a powerful and extensively used modal decomposition technique to analyse complex fluid flows. It enables the extraction of coherent structures from large-scale datasets, which can originate from either numerical simulations or experimental measurements. Originally introduced to the fluid mechanics community by Lumley [109], the method is based on the Karhunen–Loève theorem [110] and shares strong mathematical similarities with techniques such as the Principal Component Analysis (PCA) used in statistics. Its central goal is to find an optimal set of orthogonal basis functions, or modes, that best represent the energy content of a given dataset, thus providing a low-dimensional approximation of a high-dimensional system.

Let us denote a flow field variable (e.g., velocity or vorticity) as $\vec{q}(\vec{x},t)$, where $\vec{x}$ is the spatial coordinate vector and t denotes time. The field is first decomposed into a temporal mean $\bar{\vec{q}}(\vec{x})$ and a fluctuating part: $\vec{q}(\vec{x},t) = \bar{\vec{q}}(\vec{x}) + \vec{q}'(\vec{x},t)$. The fluctuating component is then expressed as a linear combination of spatial modes weighted by time-dependent coefficients: $\vec{q}'(\vec{x},t) = \sum_{k=1}^{K} \vec{a}_k(t)\vec{\phi}_k(\vec{x})$ Here, $\vec{\phi}_k(\vec{x})$ are the POD modes, which form an orthonormal basis in the spatial domain, and $\vec{a}_k(t)$ are the temporal coefficients.

The POD modes are determined by solving an eigenvalue problem associated with the covariance matrix of the data as reported in Eq. 2.19, where $\vec{x}(t_i)$ represents the data vector at time t_i (with the mean removed), and $X \in \mathbb{R}^{n\times m}$ is the data matrix constructed by stacking m snapshots of $n \times 1$ dimension. The original multi-dimensional snapshots are indeed vectorised on 1 dimension n to solve the eigenvalue problem.

$$R = \frac{1}{m}\sum_{i=1}^{m} \vec{x}(t_i)\vec{x}^T(t_i) = \frac{1}{m} XX^T \tag{2.19}$$

The eigenvalue problem reads $R\vec{\phi}_k = \lambda_k \vec{\phi}_k$, where the eigenvalues λ_k indicate the energy associated with each mode $\vec{\phi}_k$, ranked in descending order, and orthonormal under the L^2 inner product.

In high-dimensional problems, such as those arising from large-eddy simulation (LES) or PIV data, computing the full covariance matrix $R \in \mathbb{R}^{n\times n}$ is computationally prohibitive. To address this issue, Sirovich proposed the method of snapshots [111], which reformulates the problem using a smaller $m \times m$ matrix, since usually $m \ll n$. This approach dramatically reduces the computational burden and is widely adopted in different fluid dynamics applications. Alternatively, the Singular Value Decomposition (SVD) provides a numerically robust and mathematically equivalent framework for computing the POD: $X = \Phi\Sigma\Psi^T$, where Φ contains the spatial modes (POD modes), Ψ the temporal coefficients, and Σ the singular values such that $\sigma_k^2 = \lambda_k$. The equivalence between SVD and POD is discussed in foundational works such as [112, 113].

One of the key reasons for the popularity of POD in fluid mechanics is that it minimizes the mean-square error between the original signal and its low-rank approximation. This makes POD particularly effective for tasks such as data compression, coherent structure identification, and reduced-order modelling (ROM). In the ROM context, POD modes are often used in conjunction with Galerkin projection to derive low-dimensional dynamical systems that approximate the full NS equations [114]. However, POD presents some limitations. Since it ranks modes solely by energy content, the most energetic modes are not necessarily the most dynamically relevant. Additionally, for convective flows, coherent structures such as travelling vortices often appear as paired modes with a phase shift (e.g., sine and cosine components), which complicates physical interpretation. Moreover, the standard POD does not isolate frequencies, resulting in temporal coefficients that may contain mixed spectral content. To address these issues, extensions such as spectral POD [109] and balanced POD [115] have been developed. Spectral POD, for instance, decomposes flow structures by frequency and is particularly effective for analysing statistically stationary flows. Balanced POD, on the other hand, introduces adjoint simulations to assess both controllability and observability of modes, improving suitability for flow control applications.

In summary, the POD provides a mathematically rigorous and practically efficient framework for extracting dominant flow features from complex datasets. Its optimality and compatibility with reduced-order modelling make it an indispensable tool in modern computational and experimental fluid mechanics.

Chapter 3

Cross-flow conditions

In this chapter, a focus is made on the aerodynamic effects of the cross-flow conditions on the reference propeller. A first experimental analysis is conducted, and the results are described in section 3.1. A subsequent analysis is conducted via Large Eddy Simulations in section 3.2 to expand the experimental dataset and assess the causes behind the increase of time-averaged thrust and torque with the cross-flow velocity. The wake topology is also analysed in detail, presenting a simplified approach to predict the deflection of the vortical structures starting from the thrust distribution on the disk and the cross-flow velocity.

The primary and most intuitive effect of the cross-flow is to locally increase or decrease the relative tangential velocity perceived by the blade as a function of the azimuthal position. To illustrate such an effect, a schematic representation of the propeller's top view is shown in Figure 3.1(a). The reference frame used to describe the position of the blades during their rotation is chosen in analogy to vertical-axis wind turbines [116], as they exhibit a coherent evolution of the relative tangential velocity, also operating under cross-flow conditions. For this reason, the region corresponding to the azimuthal angles (ψ) around $\psi = 0°$ is defined as the *upwind* region, whereas the *downwind* region is located around $\psi = 180°$. The propeller rotates counter-clockwise in this view, so around $\psi = 90°$ it crosses the *leeward* region, whereby the relative velocity is at its minimum given the different signs of the cross-flow velocity (V_∞) and of the kinematic tangential velocity ($\Omega r - u'$). The dual region is named the *windward* region, located around $\psi = 270°$, where, for the opposite arguments, the relative velocity seen by the blade is maximum. An isolated blade element at a distance r from the propeller's hub is shown in Figure 3.1(b). The relevant velocities, forces, and angles are reported in the same figure, in accordance with the 2D BET theory. Compared to the canonical hovering case, the cross-flow contribution ($V_\infty sin(\psi)$) is added to the kinematic tangential velocity ($\Omega r - u'$). Depending on the sine of the angle ψ, the cross-flow contribution can either increase or decrease the relative velocity seen by the blade element ($W = \sqrt{(\Omega r - u' + V_\infty sin(\psi))^2 + v'^2}$). The cross-flow velocity particularly affects W both in terms of magnitude and orientation, and thus, the local α. This leads to a periodic influence on both the elementary lift ($dL = \frac{1}{2}\rho c_L(\alpha)W^2 c$) and drag ($dD = \frac{1}{2}\rho c_D(\alpha)W^2 c$, where ρ is

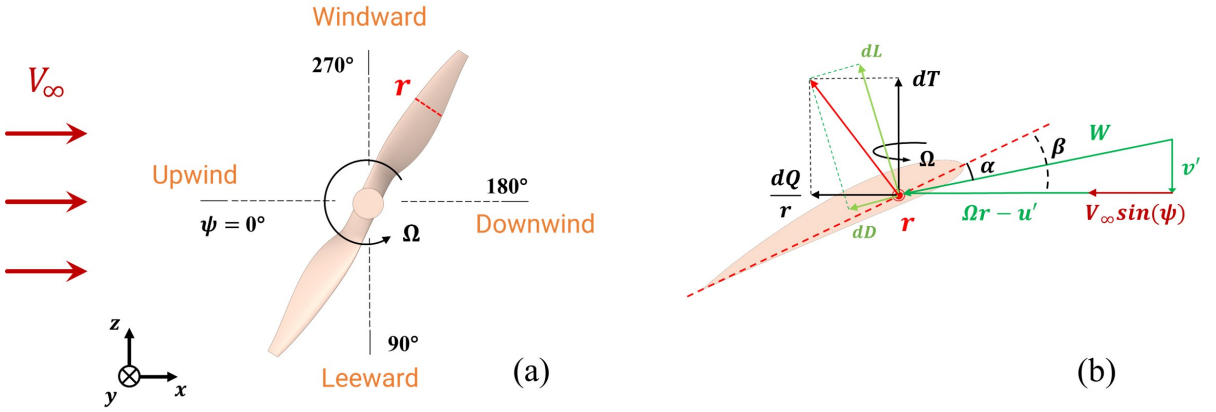

Fig. 3.1 Schematic representation of a propeller in cross-flow: a) frontal view; b) isolated blade section at a distance r from the propeller hub with forces, velocity components, and angles according to the BET theory.

the flow density. The trends of elementary thrust (dT) and torque (dQ) are closely related to those of lift and drag, allowing, at first order, to write: $dT \approx dL$ and $dQ/r \approx dD + dL(\beta - \alpha)$. Such small-angle approximations are often considered in studies of helicopter rotors in forward flight ([117]). Therefore, the presence of $V_\infty sin(\psi) > 0$ leads to an increase in dT. At the same time, dQ variation is due to two contributions: dD, which increases if $V_\infty sin(\psi) > 0$, and a second contribution that increases if the dL increment is greater than the decrease of the term $(\beta - \alpha)$.

The primary effect of the cross-flow is therefore to generate unsteady loads throughout the propeller's revolution, with maximum loads occurring around $\psi = 270°$, where the blades experience maximum relative velocity, and minimum loads around $\psi = 90°$; under these conditions, the blades may even encounter reverse flow conditions. The loading is therefore expected to be periodic over the propeller's revolution. The frequency associated with this phenomenon is called Blade Passing Frequency (BPF), which is equal to the revolution frequency times the number of blades. This primary effect can be interpreted through the Blade Element Theory (BET) ([118]). Nevertheless, this theory does not provide information on the propeller's induced velocity from its wake or the streamtube deflection, which in turn affects the blade loading. Typical inflow models used in BET-based tools to determine induced velocities consider azimuthally uniform induced flows and are, therefore, unable to accurately predict the propeller performance in cross-flow conditions.

The secondary effect of cross-flow is indeed associated with the interaction with the propeller's streamtube and wake. The streamtube tends to align with the cross-flow as the intensity of this latter becomes significant, showing noticeable differences between the upwind and downwind regions. Furthermore, an appreciable shift of the tip vortices generated at the leeward tip of the blade can be detected, with the shedding point significantly displaced towards the cross-flow direction close to the propeller's support. Both effects of the non-uniform streamtube and the wake deviation contribute to modifying the loading distribution along the blade span and azimuthal direction, displacing the position of the maximum and minimum loads at different azimuthal positions than $\psi = 270°$ and ψ

= 90°. The aforementioned azimuthal asymmetry also affects the wake topology, generating skewed tip vortices and strong blade-vortex interactions ([13]). In cross-flow, the wake advects downstream, developing into a complex three-dimensional structure characterised by multiple macro-scale vortical structures. The main non-dimensional parameter that drives the wake behaviour is the cross-flow ratio, defined as the ratio between the cross-flow velocity and the tip velocity ($\mu = \frac{V_\infty}{\Omega R}$). At low values of μ, the classical vortex structures already observed in hovering can be found: strong tip vortices and weaker root vortices that coil into a helical structure and a central vortex downstream of the hub. In hovering conditions, this vortex system typically undergoes an early breakdown close to the propeller disk due to the absence of an advecting external inflow ([119]). This behaviour is different from that of propellers subject to axial inflow. The latter has a stabilising effect on the vortical structures, since it leads to an increased pitch of the vortices. As μ increases, the vortical system is advected towards the cross-flow direction, promoting a stabilising effect similar to the axial inflow and leading to increased propulsive efficiency in a specific μ range ([120]).

The vortex system is initially deflected rigidly until a critical condition is reached, beyond which a coherent counter-rotating vortex pair (CVP) emerges. According to [121], this transition occurs at an advance ratio of approximately $\mu = 0.1$, while [26] identified a threshold of $\mu = 1.15\sqrt{C_T}$. Beyond this limit, CVP is generated through a mechanism similar to that of jets in cross-flow ([122, 123]) near the momentum source (i.e., the propeller or jet nozzle), as the wake shear layer rolls up due to the pressure differential between the upwind and downwind wake regions ([34]). Unlike jets, however, the momentum distribution on the propeller's disk is azimuthally non-uniform in cross-flow, due to the aforementioned primary effect on the blades, leading to the formation of an asymmetric CVP. The windward branch of CVP is typically stronger, reflecting the locally higher blade loading, and consequently follows a different trajectory compared with its leeward counterpart. The formation of this asymmetric CVP has been previously reported in the aerodynamics of drones ([124, 125, 35]), although referred to as a horseshoe vortex, wing-tip vortices, or super-tip vortices, and was also documented in early studies of helicopter rotors ([126]). At sufficiently high μ, the wake of helicopter rotors exhibits strong similarities to the tip-vortex system of low-aspect-ratio wings ([127]), indicating a transition towards a lifting-surface-like behaviour of the propeller.

Particularly in the context of helicopter-rotor aerodynamics, simplified analytical models are employed to predict the mean wake deflection in cross-flow conditions. One of the most classical approaches is the actuator disk model, in which the propeller is idealised as a uniformly loaded, infinitesimally thin disk imparting a steady momentum jump to the flow ([128]). Under the rigid wake assumption, the wake is treated as a cylindrical surface that remains aligned with the resultant velocity vector formed by the axial induced velocity and the cross-flow component. The wake deflection, in this case, can be derived from geometric considerations. A refinement of this model accounts for the axial acceleration along the wake due to pressure recovery, typically assuming a far-wake axial velocity that is twice the induced velocity at the disk, as in the classical actuator disk theory. An alternative approach is provided by the flat wake model, originally introduced by [26], which assumes that, at sufficiently

high advance ratios, the wake is strongly deflected and collapses into a planar sheet nearly aligned with the cross-flow direction. This model is particularly suited to regimes where the rotor begins to behave like a lifting surface and has been shown to accurately predict wake deflection when the advance ratio exceeds a threshold dependent on the thrust coefficient, typically $\mu > 1.15\sqrt{C_T}$. These models provide useful theoretical limits for estimating overall wake deflection and remain valuable tools for predicting wake-induced effects in both helicopter and multi-rotor configurations. Nevertheless, these models struggle to provide a detailed description of the different vortical structures contributing to the wake. As the cross-flow velocity is increased, the asymmetries in the wake grow significantly, and each macro-structure features its own peculiar trajectory. As a consequence, integral quantities are no longer representative of the wake topology. To this purpose, this work proposes a simplified model to predict the evolution of each macro-scale vortical structure based on quantities evaluated on specific portions of the disk loading distribution.

3.1 Experimental investigation of the cross-flow influence

The results of the experimental campaign carried out on the reference propeller in cross-flow conditions are reported in this section. The measurement of the forces and the flow field in the $x-y$ plane is carried out with the setup illustrated in Figures 2.4 and 2.6(b). The main scope is to investigate how the propeller's performance and the induced flow field are affected by the presence of a cross-flow, which can be representative of the forward flight condition for a drone's propeller. In addition, starting from the one-dimensional momentum theory (1D MT) for helicopters' rotors in forward flight [121], some modifications are proposed to fit the measured thrust and power of small-scale fixed pitch propellers. In particular, starting from the thrust data, the induced velocity is evaluated through the 1D MT to finally estimate the consumed power. Such a simplified approach might indeed result in a useful tool to quickly assess the consumed power of a drone propeller without the need for a direct measurement.

In the 1D MT for rotors in forward flight, the inflow velocity vector V_∞ presents a significantly high angle α_{disk} with respect to the actuator disk's rotation axis, as illustrated in Figure 3.2. According to this approach, the axial induced velocity (v') is assumed to be constant over the entire surface of the actuator disk.

From the momentum balance, it is possible to derive a formulation for C_T, which depends on the non-dimensional axial induced velocity on the actuator disk $\lambda_i = v'/\Omega R$, α_{disk}, and μ. This relation is further simplified by imposing $\alpha_{disk} = 90°$ in cross-flow conditions and is therefore written in Eq. 3.1.

$$C_T = 2\lambda_i\sqrt{\lambda_i^2 + \mu^2} \tag{3.1}$$

Eq. 3.1 is representative of the operative conditions analysed in the present work and more generally of a propeller in cross-flow. From Eq. 3.1 it is possible to isolate the induced velocity λ_i as a function

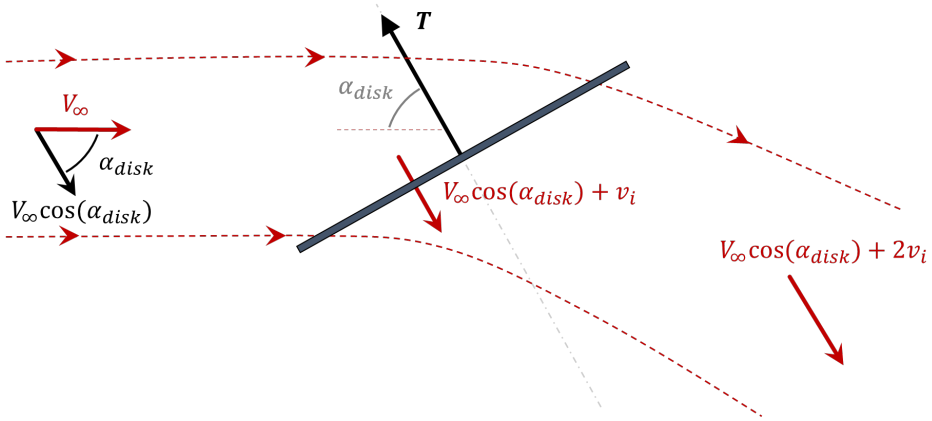

Fig. 3.2 Actuator disk model in non-axial inflow conditions.

of C_T and μ, as written in Eq. 3.2. Furthermore, at considerably high μ, λ_i results in being negligible compared to μ, leading to the Glauert high speed approximation (GHS) [121], reported in Eq. 3.3.

$$\lambda_i = \sqrt{-\frac{\mu^2}{2} \pm \frac{\sqrt{\mu^4 + C_T^2}}{2}} \tag{3.2}$$

$$\lambda_{i-GHS} = \frac{C_T}{2\mu} \tag{3.3}$$

This simplified formulation of λ_i is particularly useful for the evaluation of the propeller's consumed power. For a generic rotary wing aircraft, the non-dimensional consumed power (C_P) is hence evaluated as the sum of three contributions: the induced power (C_{P_i}), the profile power (C_{P_0}), and the parasitic power (C_{P_p}) [1]. The parasitic power C_{P_p} is, however, the power necessary to overcome the drag of the aircraft, and it is therefore neglected in this analysis. C_p can be consequently written as in Eq. 3.4, being k_1 an empirical corrective coefficient typically around 1.15 for the helicopters' rotors [1], σ_s the blades solidity, c_{D_M} the mean blade profile drag coefficient and k_2 a further corrective coefficient, which is usually taken between 4.5-4.7 in the helicopters' preliminary design [2].

$$C_P = C_{P_i} + C_{P_0} = k_1 C_T \lambda_i + \frac{\sigma_s k_3 c_{D_0}}{8}(1 + k_2 \mu^2) \tag{3.4}$$

The evaluation of c_{D_M} is trivial for a twisted blade with a significant chord length variation in the radial direction. Furthermore, unsteady loading conditions in cross-flow make its evaluation even more complicated. A proposed approach is: $c_{D_M} \approx k_3 c_{D_0}$, where c_{D_0} is the blade profile drag coefficient at zero angle of attack, evaluated from the airfoil polars in 2.10 at the average Reynolds and Mach Numbers encountered by the blades, and k_3 is a corrective coefficient, empirically evaluated with the performance data shown in this section. Averaged values of average $M = 0.1$ and $Re_c = 10{,}000$ approximately lead to a $c_{D_0} = 0.05$. In particular, Eq. 3.1 is used to obtain λ_i from the experimental

non-dimensional thrust data ($C_{T_{EXP}}$). $C_{T_{EXP}}$ and λ_i are given as inputs of the semi-empirical relation in Eq. 3.4, used to fit the experimental power data ($C_{P_{EXP}}$). The fitting is carried out with the least squares method, using k_1, k_2, and k_3 as free interpolation coefficients. The resulting values of k_1 and k_2 are finally compared with the literature values.

3.1.1 Tests Matrix

The load sensors measurements were conducted at a fixed value of n = 3000, while V_∞ ranged from 0 m/s to 15 m/s with a step of 1 m/s, thus corresponding to values of μ between 0 and 0.64. The PIV tests were exclusively conducted at inflow velocities between V_∞ = 0 m/s and V_∞ = 5 m/s. The blades' chord-based Reynolds number Re_c varies along the blade-span between 5000 and 15000, depending on the radial station r/R where it is calculated and the local velocity due to the influence of the external cross-flow.

3.1.2 Propeller's aerodynamic performance

The results in terms of $C_{T_{EXP}}$ as a function of μ are shown in Figure 3.3(a). $C_{T_{EXP}}$ displays a monotonically increasing trend as a function of μ. At small μ values, the $C_{T_{EXP}}$ growth appears to be contained. As μ is increased above 0.1, the thrust shows a steeper increase, establishing a quasi-linear trend.

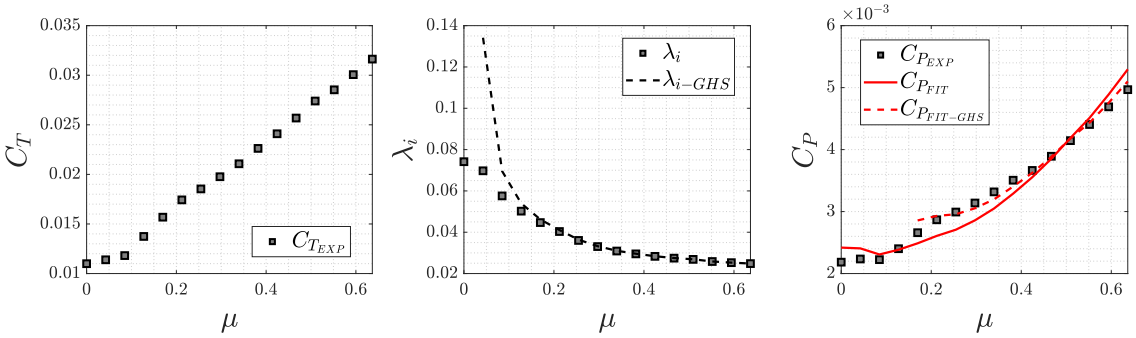

Fig. 3.3 (a) C_T, (b) λ_i, and (c) C_P as a function of μ. λ_i is calculated with the equations 3.2 and 3.3, imposing $C_T = C_{T_{EXP}}$. $C_{P_{EXP}}$ are displayed along with the best fitting curves obtained from the semi-empirical formula in Eq. 3.4. The interpolation is respectively carried out on the entire experimental data set ($C_{P_{FIT}}$, continuous red line) and for $\mu > 0.15$ ($C_{P_{FIT-GHS}}$, dashed red line).

Eqs. 3.2 and 3.3 are now taken into account to evaluate the trend of λ_i and λ_{i-GHS} as a function of μ. To this aim, the $C_{T_{EXP}}$ values shown in Figure 3.3(a) are used in the equations, and the results are displayed in Figure 3.3(b). The dimensionless induced velocity λ_i obtained from the equation 3.1 exhibits a monotonically decreasing trend, starting from the initial value obtained for the hovering condition at μ = 0. Such a decrease appears steeper for small μ values, but becomes considerably smaller as μ increases. The induced velocity evaluated with the GHS approximation λ_{i-GHS} shows a

similar trend, overlapping with the λ_i values from $\mu > 0.15$. For lower μ values, this approximation loses its validity, leading to λ_{i-GHS} values which tend to infinity as μ approaches the null value.

In Figure 3.3(c), the non-dimensional experimental consumed power $C_{P_{EXP}}$ is displayed as a function of μ. $C_{P_{EXP}}$ shows a similar trend to $C_{T_{EXP}}$, featured by a contained growth for $\mu < 0.1$ followed by a steep increase for greater cross-flow ratio values. As outlined in the introduction to this chapter, the behaviour of the time-averaged loads results from the interplay of two main effects. At low values of μ, the dominant contribution arises from the periodic variation of thrust and torque over one revolution. This mechanism produces only a limited increase in the time-averaged loads, since the larger loads generated when the blade is in the windward sector are partly compensated by the smaller loads produced in the leeward region. As $\mu > 0.1$, a secondary effect becomes increasingly important: the deflection of both the incoming streamtube and the propeller wake. This deflection leads to a reduction in the axial induced velocity across the propeller disk, thereby increasing the effective angle of attack of the blade. As a consequence, both thrust and torque exhibit a monotonic rise with increasing μ. A more detailed assessment of the instantaneous thrust and torque trend is carried out via LES in section 3.2.3.

The same plot also includes the interpolation of the experimental data obtained using Eq. 3.4 with k_1, k_2, and k_3 as the free interpolation coefficients. A first interpolation is carried out on the totality of the experimental points ($C_{P_{FIT}}$). Furthermore, a second interpolation is carried out by only taking into account the points for $\mu > 0.15$ ($C_{P_{FIT-GHS}}$), hence about the range of μ where the GHS approximation was shown to be valid. The curves shown in the figure represent the best fits obtained, and the values assumed by the free interpolation coefficients are summarized in Table 3.1. The fitting curve $C_{P_{FIT}}$, represented with a solid red-coloured line in figure 3.3(c), results in accurately approximating the $C_{P_{EXP}}$ data in the considered μ range. The $C_{P_{FIT}}$ curve deviates more significantly from the experimental data in the hovering condition ($\mu = 0$) and for μ values between 0.21 and 0.38. Even in these cases, the relative error among the data does not, however, exceed 10%. The corrective coefficients k_1 and k_2 of this first fit result in being very close to the values used in the helicopters' preliminary design, as displayed in table 3.1. The third corrective coefficient k_3 can be multiplied by the blades' airfoil c_{D_0} to obtain an approximation of the profile mean drag coefficient c_{D_M} for the given propeller in cross-flow conditions. In the same figure, the $C_{P_{FIT-GHS}}$ fitting curve is displayed with a dashed red-coloured line. The curve is obtained and plotted for $\mu > 0.15$, according to the observations made for the results in Figure 3.3(b) regarding the GHS approximation validity. The interpolation results are even more accurate, with relative errors averaging under 3% and a maximum relative error equal to 7% at $\mu = 0.15$. In this case, k_2 is closer to the literature value with respect to the $C_{P_{FIT}}$ fitting; however, k_1 is considerably increased, as shown in table 3.1. In conclusion, k_3 is closer to 1, indication that c_{D_M} is closer to c_{D_0} in the GHS approximation.

The quality of the two interpolations can be additionally inferred from the evaluation of the coefficient of determination R^2 [129]. The coefficient quantifies the proportion of variance in the dependent variable ($C_{P_{FIT}}$ or $C_{P_{FIT-GHS}}$) that is predictable from the independent variable ($C_{P_{EXP}}$).

The resulting R^2 values are respectively equal to 95 % for the $C_{P_{FIT}}$ fitting and 98 % for the $C_{P_{FIT-GHS}}$ fitting. Such results suggest an excellent data fitting and the choice of an adequate semi-empirical model for the scope. The fitting coefficients k_1 and k_2 result in being close to the literature values, mostly in the first interpolation on the larger μ range. Some differences were, however, expected due to the propeller's low Reynolds number and the blades' high pitch. Moreover, there was the necessity of introducing a third coefficient k_3 to approximate c_{D_M} directly from c_{D_0}. The value of k_3 is most likely non-generalizable to different geometries or operative conditions; however, it should not be excluded that further experimental campaigns might lead to a value of k_3 that can be ultimately generalized in the field of small-scale propellers.

	k_1	k_2	k_3
Literature	1.15	4.5-4.7	-
$C_{P_{FIT}}$	1.20	5.00	1.82
$C_{P_{FIT-GHS}}$	2.05	4.67	1.53

Table 3.1 Corrective coefficients obtained from the $C_{P_{EXP}}$ data interpolation. The coefficients k_1 and k_2 used in literature [1, 2] for helicopters in forward flight are also reported for the sake of comparison.

3.1.3 Time-averaged flow features

The time-averaged absolute velocity magnitude ($|\overline{V}|/\Omega R$) fields are shown as colourmaps with overlaid streamlines in Figure 3.4. In the hovering condition, as shown in figure 3.4(a), the wake mainly develops in the axial direction toward the y axis. The propeller operates in still air, inducing a velocity field in the wake region which reaches values up to around 0.19 ΩR. At $\mu > 0$, the flow field loses its axisymmetry. Already at small values of μ, the flow field topology appears to be significantly affected by the cross-flow, as noticeable in Figures 3.4(b) and 3.4(c). The wake generated by the blade passing in the upwind ROI indeed begins to be visible in the downwind ROI. In the cases characterized by greater μ values (Figures 3.4(d), 3.4(e) and 3.4(f)), the wake generated in the upwind ROI is mostly visible in the downwind region, while the upwind ROI is mainly characterized by the progressive deceleration of the flow impacting against the propeller support. In addition to this, a large recirculating flow region, identifiable by the local streamlines pattern, is generated in the downwind ROI. Such a low-speed structure grows in size at higher μ values, due to a stronger wake deflection. As concerns the propeller's inlet region, located above the propeller itself, it is clear that the streamlines are deflected towards the x direction due to the presence of the cross-flow. Such deflection becomes more evident as μ increases. In particular, at $\mu = 0.21$ (Figure 3.4(f)), the streamtube entering the propeller is almost aligned with the x axis in the upwind ROI, to then deviate towards the y axis in the downwind ROI, owing to the momentum transfer of the propeller blades.

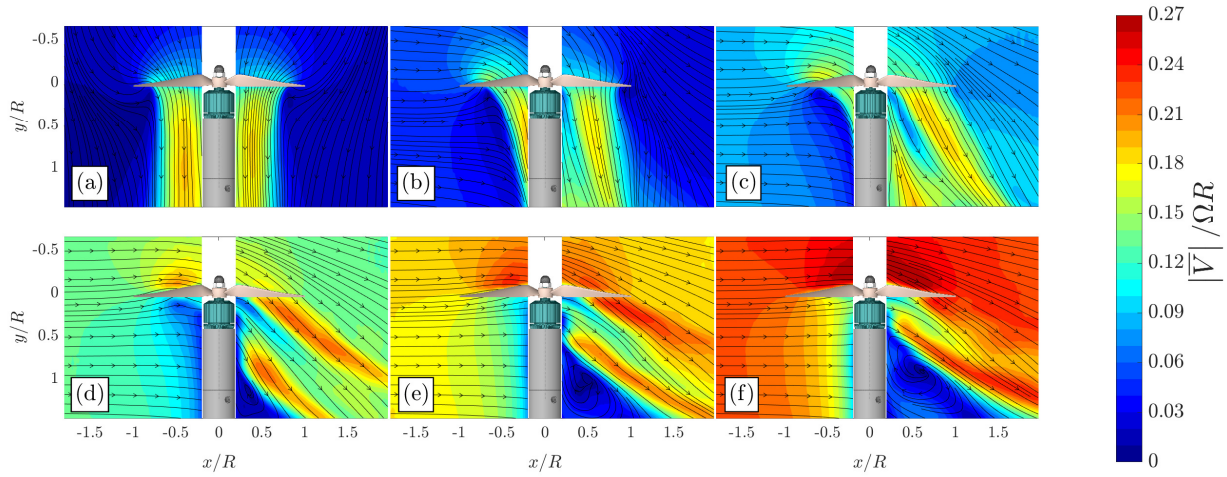

Fig. 3.4 Colourmaps of the normalized time-averaged velocity $|\overline{V}|/\Omega R$ with overlaid streamlines in the x/R-y/R plane. (a) $\mu = 0$, (b) $\mu = 0.04$, (c) $\mu = 0.08$, (d) $\mu = 0.13$, (e) $\mu = 0.17$, (f) $\mu = 0.21$.

Figure 3.5 shows the axial velocity ($\overline{V_y}/\Omega R$) fields as colourmaps with overlaid streamlines at the same μ values as Figure 3.4. The axial velocity $\overline{V_y}/\Omega R$ decreases in the wake region as μ is increased. The wake indeed gains momentum in the x direction at the expense of the y direction. The different streamline orientations close to the propeller are quantitatively compared by evaluating the orientation angle $\Phi = atan(\overline{V_y}/\overline{V_x})$ of the local velocity vectors at $y/R = 0$. The angle Φ as a function of x/R for the different cases is reported in Figure 3.6(a), where $\Phi = 0°$ indicates a velocity aligned with the x axis. The velocity vectors located in the propeller's inlet region tend to orient in the x direction as μ is increased. Especially in the upwind ROI, the Φ profiles obtained for $\mu = 0.17$ and 0.21 are representative of a velocity almost aligned with the x axis.

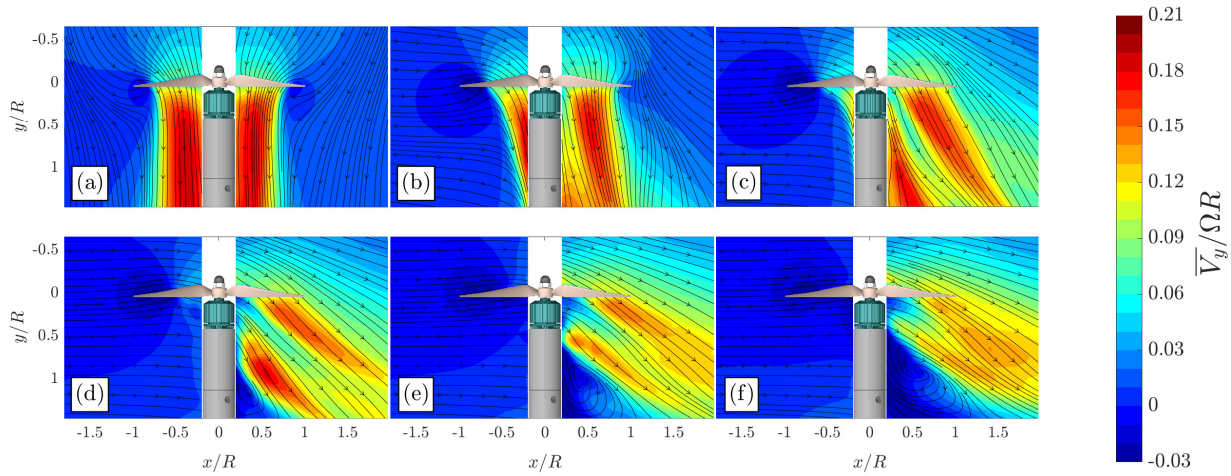

Fig. 3.5 Colourmaps of the normalized time-averaged velocity $\overline{V_y}/\Omega R$ with overlaid streamlines in the x/R-y/R plane. (a) $\mu = 0$, (b) $\mu = 0.04$, (c) $\mu = 0.08$, (d) $\mu = 0.13$, (e) $\mu = 0.17$, (f) $\mu = 0.21$.

The $\overline{V_y}/\Omega R$ values extracted at $y/R = 0$ from the velocity fields in 3.5 are instead representative of the non-dimensional induced velocity λ_i distribution at the propeller plane. Such velocity profiles are displayed in Figure 3.6(b) for a more detailed comparison. In the hovering condition ($\mu = 0$), the velocity profile is approximately axisymmetric. For $|x/R| > 1$, the velocity assumes a small constant value, while it reaches a local minimum at x/R = -1 and $x/R = 1$. These minima are caused by the presence of strong tip vortices, which locally induce a negative velocity on the flow. The flow is advected in the axial direction in the region between x/R > -1 and x/R < 1. As x/R approaches 0, a gradual decrease in $\overline{V_y}/\Omega R$ can be noted. This is mostly due to the lower tangential speed of the blades close to the hub, and to the presence of the propeller's support, which generates a blocking effect on the flow. The presence of the cross-flow alters the symmetry observed between the upwind and the downwind ROI in the hovering condition. In the upwind ROI, $\overline{V_y}/\Omega R$ tends to decrease as μ is increased. Furthermore, both the local minimum and the maximum are shifted towards the cross-flow direction. On the other hand, in the downwind ROI, an increase in the $\overline{V_y}/\Omega R$ velocity is observed with a stronger cross-flow.

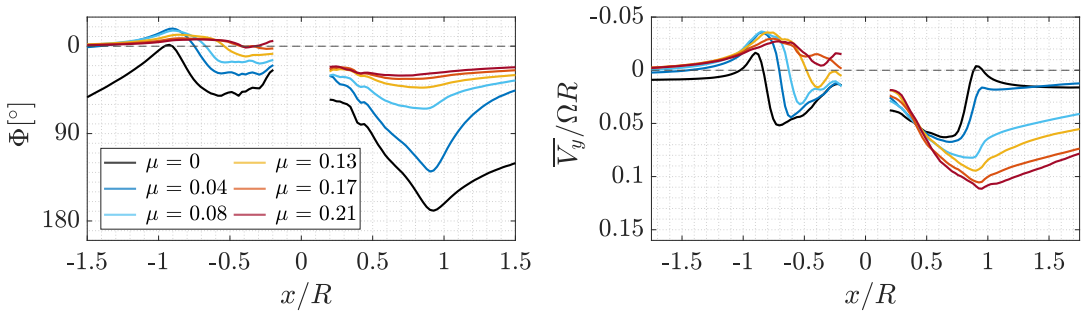

Fig. 3.6 (a) Velocity vectors orientation angle Φ as a function of x/R evaluated at $y/R = 0$. (b) $\overline{V_y}/\Omega R$ as a function of x/R extrapolated at $y/R = 0$.

The analysis of the propeller's wake can be further expanded to account for the distribution of the higher-order statistics. The non-dimensional turbulent kinetic energy $\left(k/(\Omega R)^2 = 1/2(\overline{V_x'^2} + \overline{V_y'^2})/(\Omega R)^2\right)$ fields are displayed in Figure 3.7 as colourmaps with overlaid streamlines. In Figures 3.7(a) and 3.7(b), the largest values of k are attained in the wake shear layer, where the vortices shed from the blades' tip are located. Furthermore, the wake's portion located in the upwind ROI shows larger k values as μ increases. For μ greater than 0.08, the wake generated in the upwind ROI interacts with the propeller support, resulting in a significant increase in turbulent kinetic energy, which cannot be exclusively associated with the increase in the cross-flow velocity. The wake generated by the cylindrical support plays, in fact, a significant role at high cross-flow velocities, considerably affecting the higher-order statistics of the flow field generated by the isolated propeller. In Figure 3.7(b), a small circular region of high k is located under the blade at x/R = -0.75. This can be associated with the average position of the early-age strong tip vortices. This local peak of k tends to shift towards greater x/R coordinates as μ increases, until it is no longer visible in Figures 3.7(e) and 3.7(f). In these cases, the wake generated in the upwind ROI results in being almost completely deflected in the downwind

region. Thus, the early age tip vortices end up interacting with the propeller's hub, resulting in an expanded region of high k, which eventually extends also for positive x/R coordinates. The wake's portion generated in the downwind ROI exhibits a less straightforward behaviour. While the turbulent kinetic energy in the shear layer initially seems to be slightly enhanced from $\mu = 0$ to $\mu = 0.13$, it then undergoes a noticeable drop in the shear layer for the cases in Figures 3.7(c) and 3.7(d). When μ is further increased, a growth in the shear layer's k values is again observable, most likely due to the interaction with the propeller's support wake.

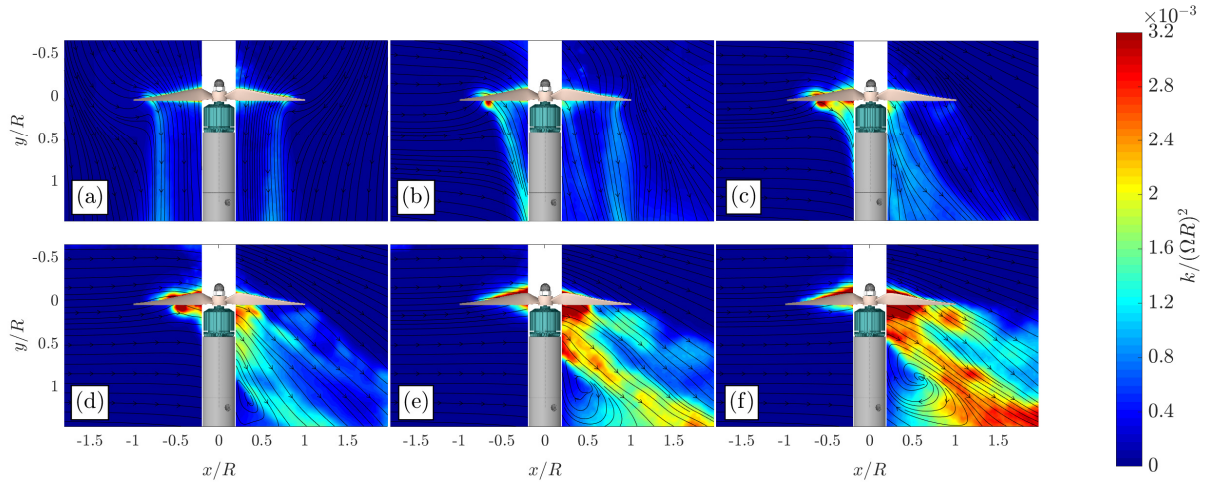

Fig. 3.7 Colourmaps of the normalized time-averaged $k/(\Omega R)^2$ with overlaid streamlines in the x/R-y/R plane. (a) $\mu = 0$, (b) $\mu = 0.04$, (c) $\mu = 0.08$, (d) $\mu = 0.13$, (e) $\mu = 0.17$, (f) $\mu = 0.21$.

Similar considerations can be inferred from the component of the Reynolds stress tensor $\overline{V_x'V_y'}/(\Omega R)^2$, as reported in Figure 3.8. This quantity indicates the evidence of high turbulence dynamics in the flow, which is predominantly registered in the wake shear layer and close to the propeller's blades. Large negative $\overline{V_x'V_y'}/(\Omega R)^2$ values are indeed obtained in the wake's shear layer generated in the upwind ROI. For μ between 0.13 and 0.40, a peak of negative Reynolds stress is registered close to the blade, as reported in figures 3.7(b), 3.8(c), and 3.8(d). As already discussed for the k fields, this local peak represents the average location of the early age tip vortices, and it is advected towards the cross-flow direction as μ attains greater values. As μ is equal to 0.17, this local peak is no longer present, most likely due to the interaction of the tip vortices with the propeller support. Such interaction additionally contributes to the generation of two distinct high $\overline{V_x'V_y'}/(\Omega R)^2$ zones of opposite signs in the wake shear layer. This is observable mostly in Figures 3.8(e) and 3.8(f), where the support's wake effect starts to become prominent. The wake generated in the downwind ROI undergoes a different modification due to the cross-flow presence. In the hovering condition in Figure 3.8(a), the Reynolds stress distribution appears to be symmetric to the stress distribution in the upwind ROI. As μ is increased over 0.13, the positive $\overline{V_x'V_y'}/(\Omega R)^2$ region generated in the wake shear layer is no longer visible, and a region of negative Reynolds stress takes place. The interaction with the propeller's support generates an

additional region of positive $\overline{V_x' V_y'}/(\Omega R)^2$ values, visible for $\mu > 0.17$, which becomes predominant as μ is further increased.

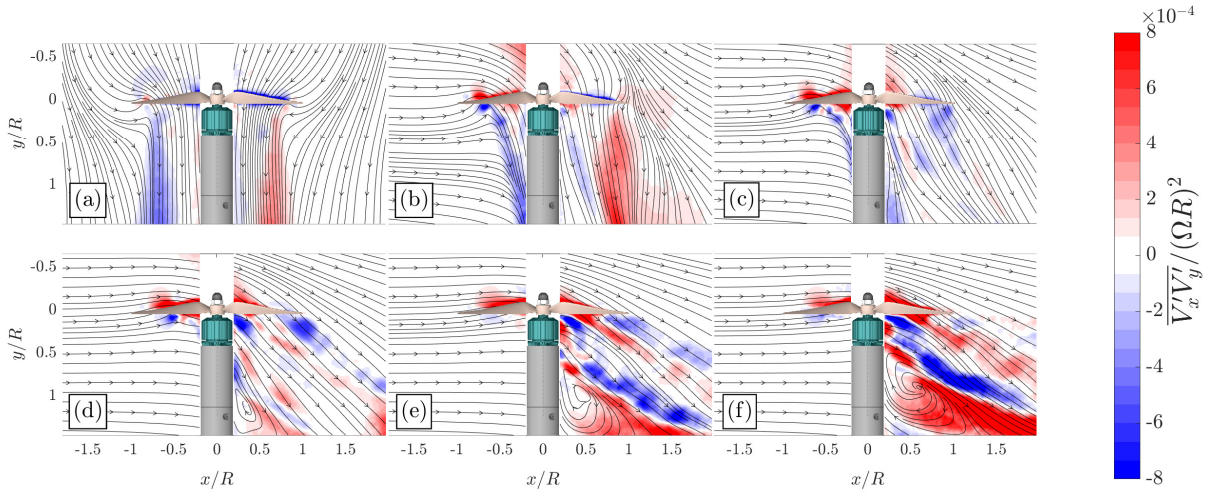

Fig. 3.8 Colourmaps of the normalized time-averaged $\overline{V_x' V_y'}/(\Omega R)^2$ with overlaid streamlines in the x/R-y/R plane. (a) $\mu = 0$, (b) $\mu = 0.04$, (c) $\mu = 0.08$, (d) $\mu = 0.13$, (e) $\mu = 0.17$, (f) $\mu = 0.21$.

3.1.4 Vortical system characterization

The Γ_2-criterion, introduced in section 2.7.1, is hereby used to characterize the evolution of vortices in terms of trajectory and circulation. The criterion used is, however, highly prone to vortex misidentification due to its reliance upon empirical thresholding. As a consequence, the choice of a different threshold value Γ_{2-thr} can severely impact the number of identified structures and should be adapted for the specific purpose. In the present work, Γ_{2-thr} was imposed equal to 0.9 after a dedicated investigation carried out on the hovering case. This case presents, in fact, multiple vortical structures of different dimensions and circulation, which are not advected away from the propeller proximity due to the lack of an external flow. To properly isolate the vortices of interest, shed by the propeller's tips and roots, it is necessary to choose a significantly high Γ_{2-thr}, which allows for isolating the strongest structures. On the other hand, it is likely that excessively increasing the threshold towards the value of 1 may lead to the identification of a small number of vortices, affecting the statistical significance of the results. To this purpose, the vortex identification was carried out for the hovering case with three different Γ_{2-thr} values, and the obtained results are reported in the scatter plots in Figure 3.9. In Figure 3.9(a), the results of the identification carried out with $\Gamma_{2-thr} = 0.85$ are displayed. With such a value, many vortical structures are identified mostly in the wake shear layer, generating a dense region of points where it is not straightforward to isolate the strongest structures. By increasing Γ_{2-thr} to 0.9, as reported in Figure 3.9(b), the strongest structures become more visible as the weakest vortices are neglected. If the threshold value Γ_{2-thr} is further increased to 0.95, the tip vortices are not identified

and consequently not represented in the scatter plot in Figure 3.9(c). As a result of this analysis, the authors opted for $\Gamma_{2-thr} = 0.9$ for the current investigation.

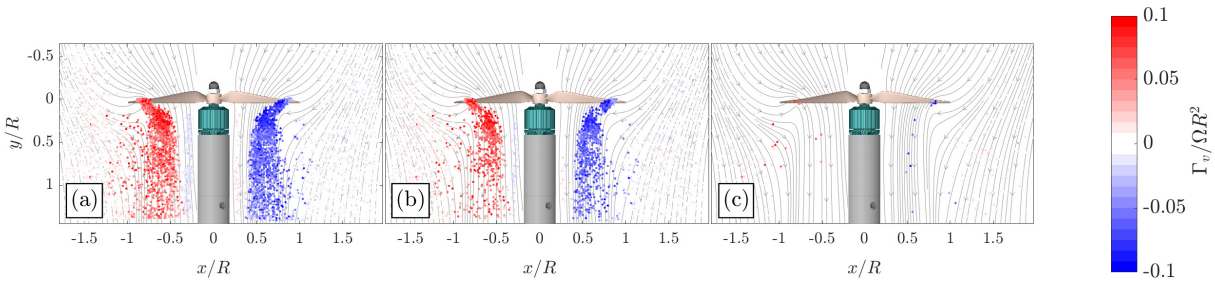

Fig. 3.9 Scatter plots of the identified vortical structures in the hovering condition ($\mu = 0$) at different threshold values Γ_{2-thr}. (a) $\Gamma_{2-thr} = 0.85$, (b) $\Gamma_{2-thr} = 0.9$, (c) $\Gamma_{2-thr} = 0.95$.

The vortical structures identified with the use of the Γ_2 criterion are reported in the scatter plots in Figure 3.10. In particular, the vortices are displayed in correspondence with their identified centres as fixed-size dots, with a colour scale that characterizes their dimensionless circulation. The circulation Γ_v is calculated with the use of the Stokes-Kelvin theorem, as the integral of the vorticity field in the area of a given vortex. As previously mentioned in section 2.7.1, the vortex area corresponds to a singularly connected region whose points present $|\Gamma_2| > 2/\pi$, calculated with the use of Eq. 2.18. For the current analysis, a Γ_{2-thr} value of 0.9 was finally taken into account at each value of μ.

In Figure 3.10(a), two main aggregations of vortical structures are visible in the upwind and downwind ROI, respectively. Such structures are shed from the blades' tip and show a strong circulation of opposite sign in the two regions. Their circulation additionally tends to decrease in absolute value with the distance from the blades. Once they are shed from the blades, the tip vortices tend to move closer to the propeller's hub, as a cumulative effect of the wake shrinking caused by the local acceleration and their own induced velocity. Their mean trajectory is, however, not well defined along a clear path and presents a significant scattering in the direction of the cross-flow. In the absence of an external inflow, the vortices are advected away from the propeller exclusively by the induced velocity generated in the wake. The propeller in hovering hence works in less uniform air conditions, which might result in a drop of the propulsive efficiency [120]. The tip vortices end up scattering outside of the wake and are still visible in the flow field despite their significantly damped circulation. Further weak vortices can be detected close to the propeller's hub. These structures represent the vortices shed from the blades' root, respectively in the upwind and downwind ROI, and their circulation might be enhanced by the interaction with the propeller's support.

As μ is increased, even small cross-flow velocities lead to major changes in the vortices' distribution. In the upwind ROI, the tip vortices present a clearer pattern with respect to the hovering condition. At $\mu = 0.04$ and 0.08 (Figures 3.10(b) and 3.10(c)), the tip vortices appear to be confined to a well-defined trajectory and are shifted towards greater x/R coordinates as μ is increased. As μ is increased above

0.08, the early-age tip vortices undergo a strong deflection along the blade span, eventually interacting with the following passing blades. Such early age vortices are characterized by a small circulation value; thus, if the blades-vortex interaction results, on one hand, more frequently with a stronger cross-flow velocity, the vortices involved in this interaction present a damped circulation, consequently containing the downsides of this phenomenon. The tip vortices are then advected downstream and become visible in the downwind ROI for $\mu > 0.13$. In Figures 3.10(d), 3.10(e) and 3.10(f), the streamlines orientation close to the propeller's support indicates the presence of a major flow recirculation, already discussed in terms of time-averaged flow features when presenting Figure 3.5. In this region, the propeller's wake vortices interact with the propeller support's wake, generating a vortical macro-structure and locally enhancing the tip vortices' circulation. The root vortices are also advected in the downwind ROI and are displayed with a greater circulation as μ is increased.

Regarding the vortices generated in the downwind ROI, it is necessary to make different considerations. The blue-coloured tip vortices are damped in circulation and organized in more defined trajectories as μ is increased. As μ is increased above 0.17, their circulation is reduced to the extent that they are no longer visible in the region of interest. At $\mu = 0.21$ as reported in Figure 3.10(f), only a few vortical structures with a negative value of Γ_v are detected close to the blades' tip, indication that the downstream tip vortices are disrupted by the interaction with the cross-flow and possibly swept away from the blade owing to the cross-stream velocity. In the same region, some weak vortices with a positive circulation become predominant as μ is increased. Such vortices are generated by the blades' root and display an opposite behaviour with respect to the tip vortices. Their circulation is increased as μ is increased, due to the interaction with the support's wake. Furthermore, at $\mu = 0.21$, multiple vortices with positive circulation are detected on the blades. As previously observed in the upwind ROI, the presence of the cross-flow contributes to the enhancement of the blades-vortex interaction, by displacing the early age vortical structures along the blade-span direction and not in the axial direction as an axial inflow would do.

In the downwind ROI for $\mu > 0.13$, it is possible to notice a misalignment between the tip vortices' trajectory and the flow fields' streamlines. This effect might be due to an intrinsic flaw of the chosen methodology for the vortices identification, since it properly works when the vorticity is mostly aligned with the out-of-plane direction. In the hovering case, the vorticity is indeed expected to be mostly directed towards the out-of-plane direction in the wake shear layer, and the remaining vorticity components can be neglected. While this is true in the hovering case, it is not straightforward to predict how the vorticity components evolve with the increase of the cross-flow velocity. For instance, in [130], the formation of a strong counter-rotating vortex pair oriented in the cross-flow direction is observed since small μ values. A considerable increase in the vorticity components along x and y might lead to a misidentification of the tip vortex centres and a miscalculation of their circulation since they might not be mostly aligned with the out-of-plane axis. While this aspect is surely of interest, it is not within the capabilities of the current measurement approach. Indeed, it would be necessary to retrieve all

the vorticity components with the use of different PIV setups, among which the tomographic PIV, or through CFD simulations of the rotating propeller.

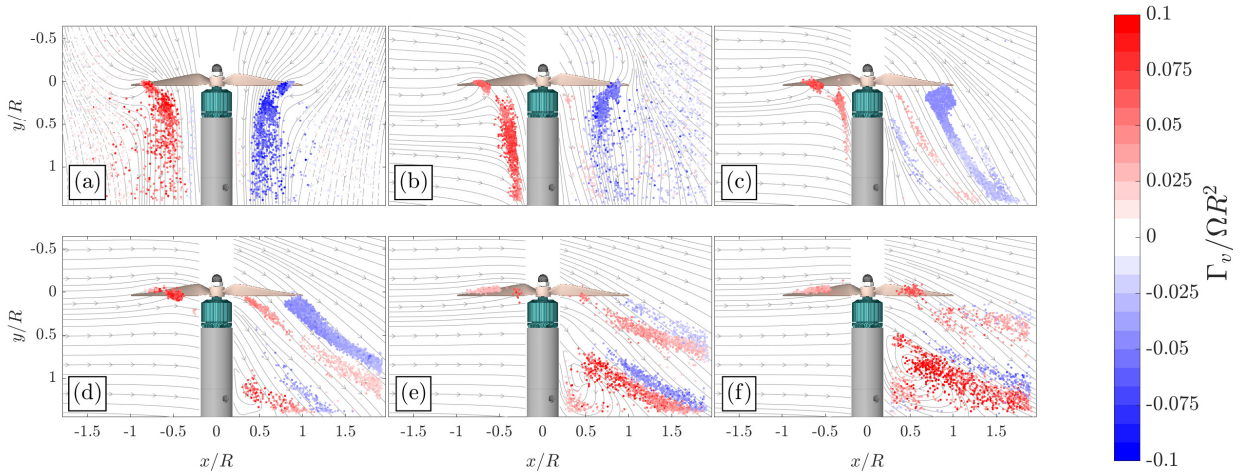

Fig. 3.10 Scatter plots of the identified vortical structures with overlaid streamlines in the x/R-y/R plane. (a) $\mu = 0$, (b) $\mu = 0.04$, (c) $\mu = 0.08$, (d) $\mu = 0.13$, (e) $\mu = 0.17$, (f) $\mu = 0.21$.

3.1.5 Conclusions

The investigated propeller was characterized in terms of thrust and torque at different values of the cross-flow ratio μ. While in axial inflow, both thrust and torque monotonically decrease as the axial velocity increases, in cross-flow conditions the loads exhibit the opposite behaviour. Especially once the cross-flow ratio exceeds approximately $\mu = 0.1$, the thrust and torque increase with μ. This trend is directly linked to the progressive deflection of the streamtube and its wake, which reduces the axial induced velocity across the disk and therefore produces a net increase in effective angle of attack. The experimental data were interpolated with the use of semi-empirical equations derived from the field of helicopter design. The interpolation led to a satisfactory fit, and the computed corrective coefficients resulted in being very close to the ones used in literature. The propeller's mean blade profile drag coefficient was evaluated from its drag coefficient at zero angle of attack with the use of a third corrective coefficient. The value of this coefficient might be generalizable for different geometries and operative conditions, but there would be a need for further experimental campaigns focused on the topic.

Flow field measurements were carried out with the use of the planar PIV. The main findings showed a significant deflection of the velocity vectors in the propeller's inlet and wake regions towards the direction of the cross-flow, even for contained μ values. The flow field's higher-order statistics, such as the turbulent kinetic energy and the cross-component of the Reynolds stress tensor, were inspected. Both quantities showed local increases in the wake shear layer as the μ was increased. The major

effects were, however, due to the interaction with the propeller's support, which led to a significant local enhancement of both quantities.

In conclusion, a thorough analysis of the vortical structures' evolution in the different cases was carried out with the use of the Γ_2-criterion. The strongest vortices were found to be located in the propeller's wake shear layer, after having been shed by the blades' tips. Compared to the hovering case, the vortices were confined in more defined trajectories due to the presence of an external cross-flow. The tip and root vortices generated by the upstream passing blades appear stronger with the increase of the cross-flow velocity. On the other hand, the tip vortices generated downstream appeared to be damped by the cross-flow, while the root vortices still resulted in being enhanced, due also to the interaction with the propeller's support. Further flow and performance features can be inferred with the use of computational tools, if adequately adapted for the low Reynolds number regime. In addition, different propellers' geometries and angles of attack with respect to the inflow need to be investigated to further extend and validate the proposed modifications of the semi-empirical formulas from the literature to small-scale propellers. The open and easily replicable geometry of the present propeller is intended to ensure a continuity of research in this area, to expand the scientific community's knowledge of such complex operative conditions.

3.2 Large Eddy Simulations of the cross-flow influence

The current section aims to expand the experimental results in cross-flow via Large Eddy Simulations. An investigation is conducted on the mechanisms driving the increase in thrust and torque with the cross-flow velocity observed in the experimental campaign. The wake deflection and asymmetric inflow patterns are identified as the primary causes behind this trend. The evolution of the macro-scale vortical structures, such as tip vortices, hub vortex, and the formation of a counter-rotating vortex pair as in jets in cross-flow, is then characterised in detail. The propeller's support, used in the reference experimental campaign, is removed for a thorough assessment of the wake dynamics. Spectral and Proper Orthogonal Decomposition analyses confirm that the support introduces significant perturbations in the near wake, especially in the downwind wake region. Nevertheless, the influence is limited to the induced flow field, while the loads on the propeller are negligibly affected. In the absence of the support interference, the vortices' evolution is tracked using the Γ_2 criterion, allowing for the evaluation of the macro-scale vortices' trajectory. Finally, a simplified model is developed to describe the vortex trajectories as a function of the cross-flow velocity and the thrust distribution on the propeller's disk; thus, the proposed model is not specific to the analysed propeller geometry. The predicted trajectories are then compared to those directly extracted from the flow fields.

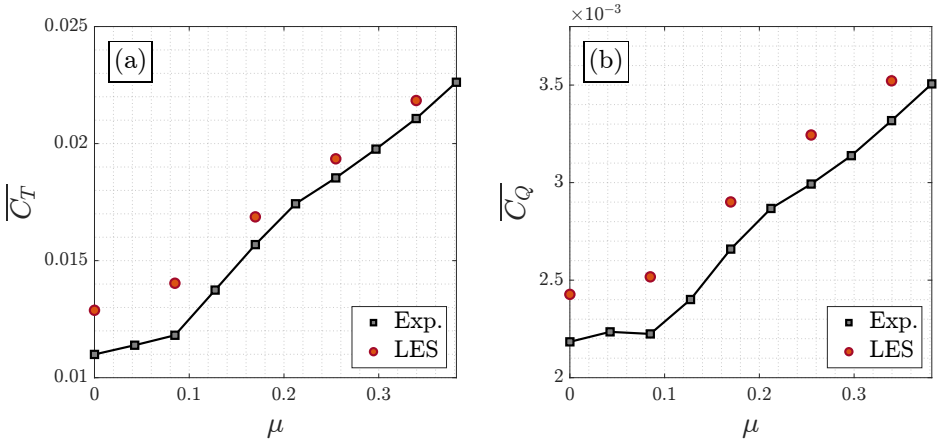

Fig. 3.11 Non-dimensional time-averaged (a) thrust coefficient $\overline{C_T}$, and (b) torque coefficient $\overline{C_Q}$, from LES and experiments.

3.2.1 Tests matrix

The LES simulations were first conducted with the cylindrical support to replicate the experimental setup. An initial validation campaign was carried out at $n = 3000$ rpm and $V_\infty = 0$, 2, 4, 6, and 8 m/s, corresponding to $\mu = 0$, 0.08, 0.17, 0.24, and 0.32, respectively. The effect of the support was then examined in detail by simulating the case at $\mu = 0.24$ without the support. Finally, an additional campaign was performed at $\mu = 0$, 0.04, 0.08, 0.17, 0.24, and 0.32, considering only the isolated propeller. This setup enables the evaluation of the evolution of the macro-scale vortical structures without the influence of the propeller's support. All simulations were run for 21 revolutions, with statistics computed over the last 10.

3.2.2 LES against experimental results

The LES results are compared with the experimental data of section 3.1 to validate the numerical approach. The comparison focuses on time-averaged loads and velocity fields. $\overline{C_T}$ and $\overline{C_Q}$ are shown in Figure 3.11(a) and Figure 3.11(b), respectively, highlighting the agreement in trends between numerical and experimental results. Although some discrepancies are present, the overall trends are well captured. An initial plateau in both thrust and torque coefficients is observed at $\mu = 0$ and $\mu \approx 0.08$, followed by a steep increase for $\mu > 0.08$. The LES tends to overestimate the integral values: thrust is mostly overestimated at low cross-flow ratios, while the torque is systematically overestimated for all values of μ. The largest discrepancies occur in the hovering condition ($\mu = 0$), with relative errors of 16% for $\overline{C_T}$ and 10% for $\overline{C_Q}$ with respect to the experimental values.

A comparison of the LES and PIV time-averaged velocity fields is shown in Figures 3.12 and 3.13, focusing on the components $\overline{V_x}$ and $\overline{V_y}$ in the plane at $z = 0$, which corresponds to the only measurement plane available from the planar PIV data. Three cross-flow ratios are considered: $\mu = 0$, $\mu = 0.08$,

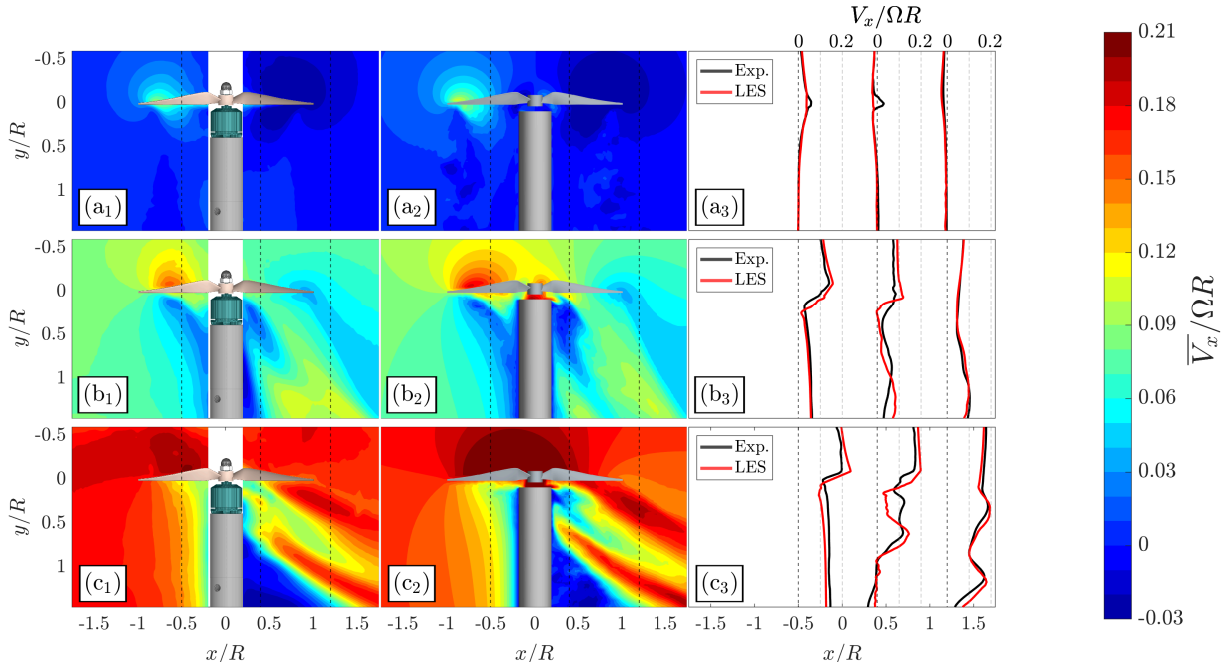

Fig. 3.12 Normalized time-averaged velocity $\overline{V_x}/\Omega R$ (column 1) from PIV experiments, and (column 2) from LES computations: Colourmaps and (column 3) velocity profiles extracted at x/R = -0.5, 0.5, 1.2, (a) at $\mu = 0$, (b) at $\mu = 0.08$, and (c) at $\mu = 0.17$.

and $\mu = 0.17$. For each case, colourmaps of the normalised velocities and velocity profiles at selected coordinates are presented to facilitate quantitative comparison. Overall, the flow fields from LES and PIV are in good agreement across all tested cross-flow ratios, though LES tends to slightly overestimate the wake velocities in both the x and y directions. Considering the x-component of velocity (Figure 3.12), a good agreement is observed upstream of the propeller disk, at $x/R = -0.5$ and downstream at $x/R = 1.2$. Some discrepancies arise at $x/R = 0.6$, particularly for $\mu = 0$, where a local peak appears in the experimental profile near $y/R = 0$. This peak is likely caused by the periodic passage of the blade through the PIV plane, which can introduce measurement errors due to reflections. At $\mu = 0.17$ (Figure 3.12(c_1,c_2,c_3)), a larger discrepancy is observed in the wake of the support structure near the brushless motor, at $x/R \approx 0.25$, $y/R \approx 0.25$. In the LES model, this component is simplified to ease the meshing process, as shown by the different masks superimposed on the velocity fields. As a result, local flow deviations near the support are expected but diminish further downstream, as confirmed by the restored agreement of the velocity profiles at $x/R = 1.2$.

Focusing on the y-component of velocity (Figure 3.13), the agreement between LES and experimental data is still remarkable. The velocity profiles extracted at $y/R = -0.3$ and $y/R = 1.0$ show near-complete overlap between the two approaches. Nonetheless, LES slightly overestimates $\overline{V_y}$ throughout the domain. As with the x-component, the largest discrepancies are localised near the motor support and become more pronounced at high cross-flow ratios. At $\mu = 0.17$, the wake generated by the support is more energetic and spatially extended, increasing the sensitivity of the local flow field to any geometric simplification in the LES setup.

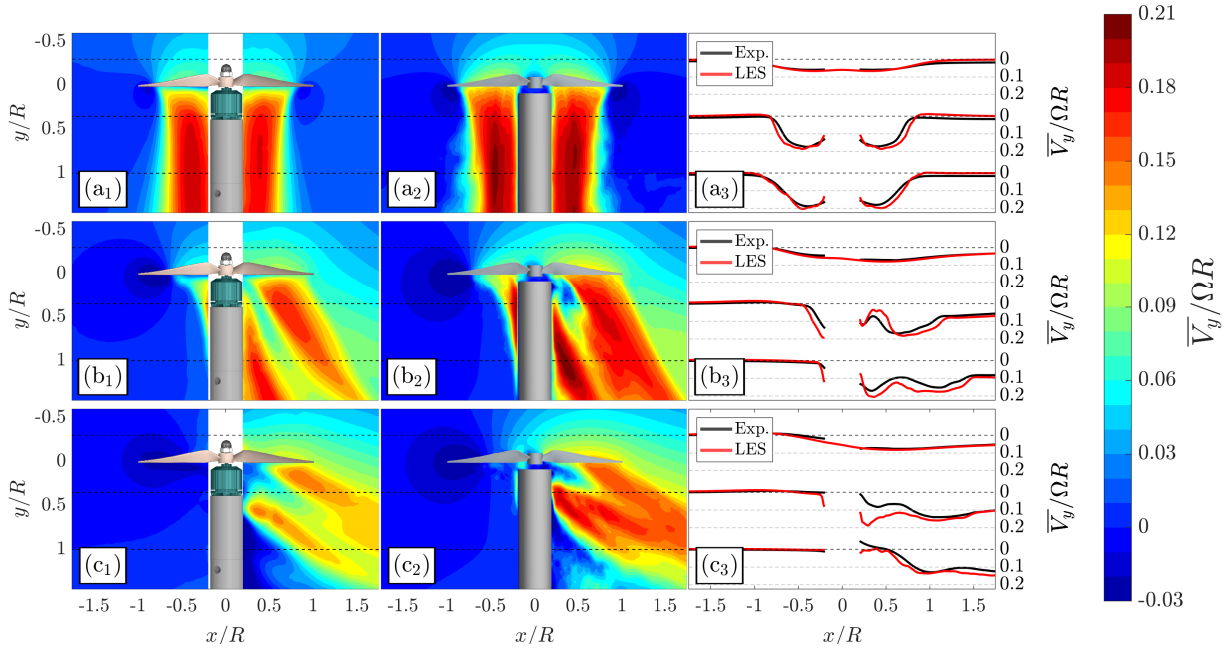

Fig. 3.13 Same caption as Figure 3.12 but for $\overline{V_y}/\Omega R$.

The overall comparison indicates that the LES methodology captures well the trends observed experimentally. However, significant quantitative differences are found, mostly in the integral loads. The velocity fields also show some discrepancies, mainly addressed to simplification in the modelling of the propeller's support. Several factors may further contribute to these discrepancies, among which are geometric differences between the actual 3D-printed propeller and its digital counterpart. These include material-induced deformations and blade flexibility effects, which are not accounted for in the numerical simulations, as well as the blade surface roughness, which might influence the boundary layer transition. Furthermore, the experimental campaign involves measuring low-magnitude forces, particularly at low μ, where thrust and torque fall below the optimal sensitivity range of the sensors employed. For example, in hovering, the measured torque is about 5% of the sensor's rated output (0.07 Nm). Additionally, the inherently unsteady nature of the flow and the mechanical vibrations of the rotating system may introduce further inaccuracies in the experimental evaluation of time-averaged loads.

3.2.3 Aerodynamic loads

This section investigates in detail the influence of the cross-flow on the unsteady aerodynamic blades' loads, with particular emphasis on the thrust. The objective is to assess the physical mechanisms underlying the increase in the time-averaged thrust observed for $\mu > 0.08$. To this end, Figure 3.14 shows the time histories of the thrust coefficient C_T for the individual blades and their combined total, at selected values of μ. The analysis focuses on the final 4 revolutions of each simulation.

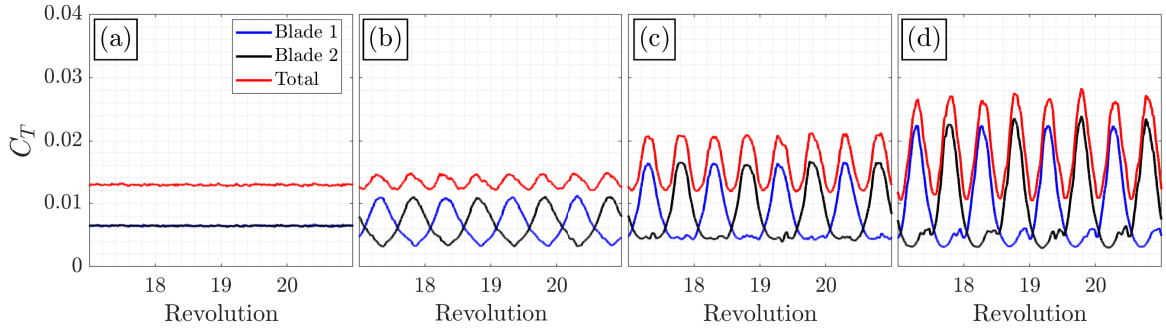

Fig. 3.14 Non-dimensional thrust temporal evolution at (a) $\mu = 0$, (b) $\mu = 0.08$, (c) $\mu = 0.17$, (d) $\mu = 0.24$.

In hovering conditions at $\mu = 0$ (Figure 3.14(a)), the thrust generated by each blade fluctuates around a nearly constant mean value, with high-frequency, low-amplitude oscillations. These almost negligible fluctuations are attributed to the breakdown of the separated shear layer into small-scale vortices. As the cross-flow velocity increases, periodic oscillations emerge with a frequency corresponding to the BPF/2, assuming a double-bladed propeller is considered. These oscillations are driven by the variation in relative velocity experienced by each blade throughout a revolution. In particular, the relative velocity increases in the windward region near $\psi = 270°$, leading to a corresponding increase in the instantaneous thrust. Conversely, in the leeward region around $\psi = 90°$, the blades encounter a reduced relative velocity and therefore generate less thrust compared to the hovering case. At low cross-flow velocities (up to approximately $\mu = 0.08$), these opposing effects are balanced out: the increased thrust in the windward region is balanced by the reduced thrust in the leeward region, resulting in a mean value close to that in hovering. However, at higher μ, the thrust generated in the leeward region is only partly attenuated, while the thrust in the windward region continues to increase. The resulting temporal signal becomes irregular and deviates from the quasi-sinusoidal pattern observed at $\mu = 0.08$. This leads to a net increase in time-averaged thrust, as also evidenced in Figure 3.11.

Interestingly, at low values of μ, the angular position of maximum C_T does not occur at $\psi = 270°$. To highlight this behaviour, the phase-averaged thrust coefficient of a single blade over the final 4 revolutions ($\widehat{C_T}(\psi) = \frac{1}{4}\sum_{Rev=17}^{21} C_T(\psi + Rev \cdot 360°), \psi \in [0, 360°)$) is plotted as a function of azimuthal angle ψ in Figure 3.15. At $\mu = 0.08$, the phase-averaged thrust coefficient $\widehat{C_T}$ attains its maximum at approximately $\psi|_{max(\widehat{C_T})} = 293°$. As the cross-flow ratio increases, $\psi|_{max(\widehat{C_T})}$ shifts progressively toward the windward azimuthal position, approaching $\psi = 270°$ and reaching a value of 271° at $\mu = 0.34$.

The asymmetry arises from the non-uniformity of the induced velocity field, a consequence of the skewed inflow and the wake deflection caused by the cross-flow. The inflow pattern seen by the propeller is no longer axisymmetric, resulting in asymmetric loading, specifically between the upwind and downwind regions. This behaviour is consistent with the inflow patterns shown in Figure 3.13 and

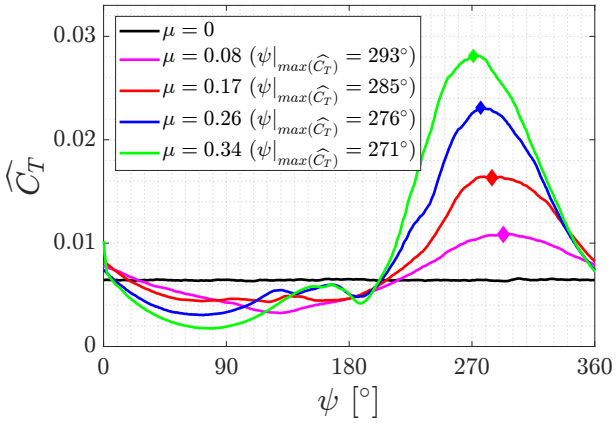

Fig. 3.15 Phase-averaged single blade non-dimensional thrust evolution; maximum values indicated with ♦ markers.

observed in section 3.1, where the axial velocity component above the propeller in the upwind region is significantly reduced compared to the downwind side. The local decrease in axial velocity leads to an increase in the angle of attack, thereby enhancing the local thrust generated by the blade operating in the upwind region. As a result, the distribution of aerodynamic loads becomes skewed towards the upwind region. At greater values of μ, the streamtube is progressively more symmetric between the streamtube in the upwind and downwind regions, being predominantly oriented towards the cross-flow direction. In these conditions, the maximum loading is found around $\psi = 270°$.

The distribution of the non-dimensional thrust per unit length (radial extent) s_{C_T} over the propeller disk, defined in Eq.3.5, is now shown in the two-dimensional contour plots of Figure 3.16.

$$s_{C_T} = \frac{dT_{(r,\psi)}/d(r/R)}{\rho(\Omega R)^2 \pi R^2} \tag{3.5}$$

As expected, the maximum thrust is consistently observed near $r/R = 0.75$ for all azimuthal positions, whereas the inboard portion of the blade, closer to the root, exhibits negligible values of s_{C_T} across the disk. At $\mu = 0.08$, the peak loading occurs at $\psi \approx 300°$, highlighting a clear asymmetry in the thrust distribution between the upwind and downwind regions. This asymmetric pattern induces a pitching moment ($\overline{C_{Mz}}$), which, at low cross-flow ratios, is comparable in magnitude to the roll moment ($\overline{C_{Mx}}$), as shown in Figure 3.17. If at $\mu = 0$ the two moments are null, at $\mu = 0.08$ they are non-negligible and comparable in magnitude. In addition, they are also comparable to the time-averaged torque coefficient at the same cross-flow ratio. As μ increases, the loading distribution becomes more symmetric between the upwind and downwind regions, and $\overline{C_{Mz}}$ starts to drop. On the other hand, the asymmetry between the leeward and windward region becomes more relevant, and the $\overline{C_{Mx}}$ appears to monotonically increase with μ. At $\mu = 0.26$, the two moments significantly differ in magnitude, with $\overline{C_{Mz}}$ being almost negligible compared to $\overline{C_{Mx}}$. As the cross-flow ratio increases, the load distribution becomes more symmetric between the upwind and downwind regions. Already at $\mu = 0.26$, this

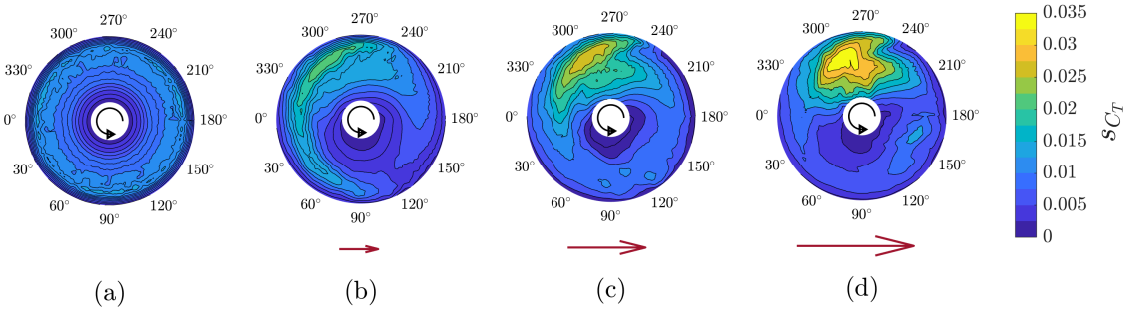

Fig. 3.16 s_{C_T} distribution at (a) $\mu = 0$, (b) $\mu = 0.08$, (c) $\mu = 0.17$, (d) $\mu = 0.24$.

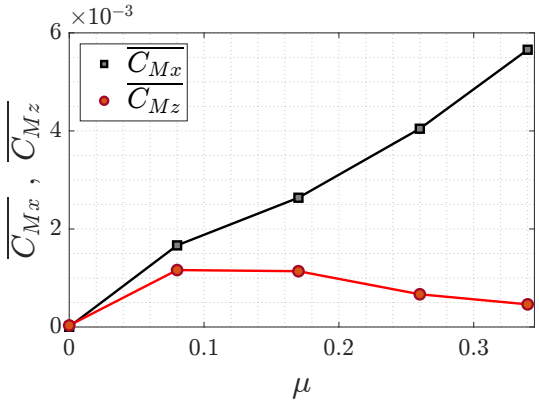

Fig. 3.17 Pitch moment ($\overline{C_{Mz}}$) and roll moment coefficients ($\overline{C_{Mx}}$), at different μ values.

loading asymmetry is significantly reduced, and the roll moment emerges as the dominant aerodynamic moment acting on the system.

The non-dimensional thrust per unit length, s_{C_T}, can be decomposed, as in Eq. 3.6, into two dimensionless parameters to decouple the two main effects of the cross-flow on the blade loading, namely the primary effect of dynamic pressure and the secondary effect of the inflow pattern deflection. In particular, s_{C_T} is decomposed into a normalised dynamic pressure $\widetilde{P}_{dyn}$, and a second term $\widetilde{s_{C_T}}$, i.e., the thrust per unit length normalised with the local kinematic velocity subtracted by the cross-flow contribution. This second term is isolated to highlight the secondary effect of the cross-flow, decoupling s_{C_T} from the dynamic pressure contribution.

$$s_{C_T} = \widetilde{P}_{dyn} \cdot \widetilde{s_{C_T}} = \frac{\frac{1}{2}\rho(\Omega r - sin(\psi)V_\infty)^2}{\frac{1}{2}\rho(\Omega R)^2} \cdot \frac{dT_{(r,\psi)}/d(r/R)}{\rho(\Omega r - sin(\psi)V_\infty)^2 \pi R^2} \tag{3.6}$$

The $\widetilde{P}_{dyn}$ distributions at different μ values are shown in Figure 3.18 with the same arrangement adopted in Figure 3.16. The $\widetilde{P}_{dyn}$ maxima are located at $\psi = 270°$ for all the investigated μ values. In the leeward region, an area with $\widetilde{P}_{dyn} \approx 0$ is observed, where even negative velocity values can be reached due to regions of reverse flow. The distributions of $\widetilde{s_{C_T}}$ on the propeller disk are shown instead in Figure 3.19. At $\mu = 0.08$ and $\mu = 0.17$, greater $\widetilde{s_{C_T}}$ values can be appreciated in the upwind region

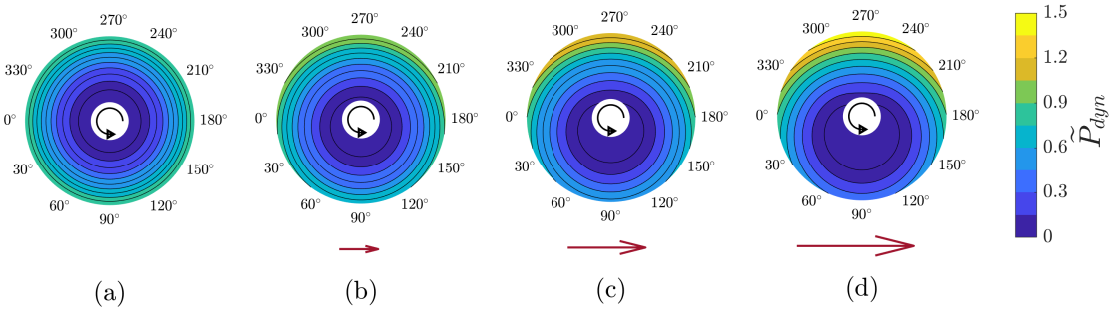

Fig. 3.18 $\widetilde{P}_{dyn}$ distribution (see Equation 3.6) at (a) $\mu = 0$, (b) $\mu = 0.08$, (c) $\mu = 0.17$, (d) $\mu = 0.24$.

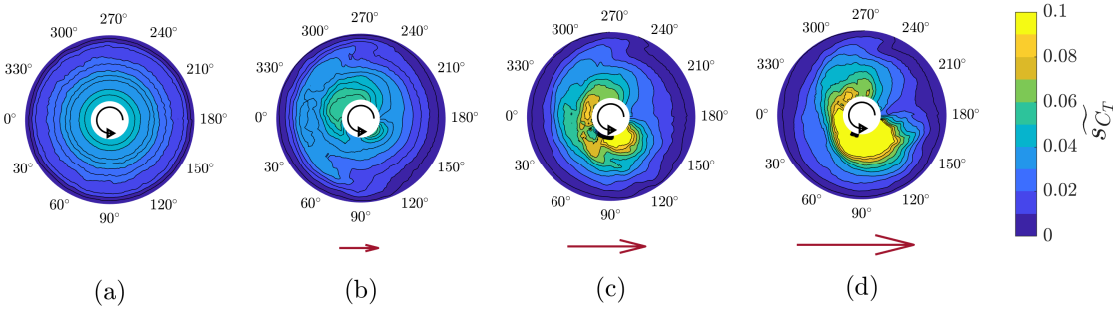

Fig. 3.19 $\widetilde{s_{C_T}}$ distribution (see Equation 3.6) at (a) $\mu = 0$, (b) $\mu = 0.08$, (c) $\mu = 0.17$, (d) $\mu = 0.24$.

compared to the downwind region, reflecting the asymmetry between the two regions also observed in Figure 3.16. This asymmetry is not present in the dynamic pressure plots, which is due to the cross-flow secondary effect of the propeller's wake and inflow pattern deflection. By its definition, $\widetilde{s_{C_T}}$ can be associated with the local lift coefficient and solidity of the blade. When the blades pass through the upwind region, they experience a reduced axial inflow and thus a higher angle of attack that leads to higher blade loading. Unlike s_{C_T}, $\widetilde{s_{C_T}}$ shows high values near the blade root in the leeward region. There, the blade twist is greater, and the relative velocity is lower as the cross-flow velocity is increased, causing the angle of attack to increase significantly. This effect probably compensates for the thrust reduction at greater r/R due to the lower relative velocity, partly explaining why, at high μ, the thrust does not follow a sinusoidal trend as expected, but remains rather constant in the leeward region as μ is increased.

3.2.4 Propeller's support

The influence of the propeller's support is first investigated in terms of thrust and torque coefficients. Subsequently, the influence on the velocity fields is assessed in the plane $z = 0$, previously examined in Section 3.2.2 for the LES validation against PIV measurements. To this end, the LES simulations including the support model (denominated LES_{Sp} in this section) at $\mu = 0.17$ are compared with those

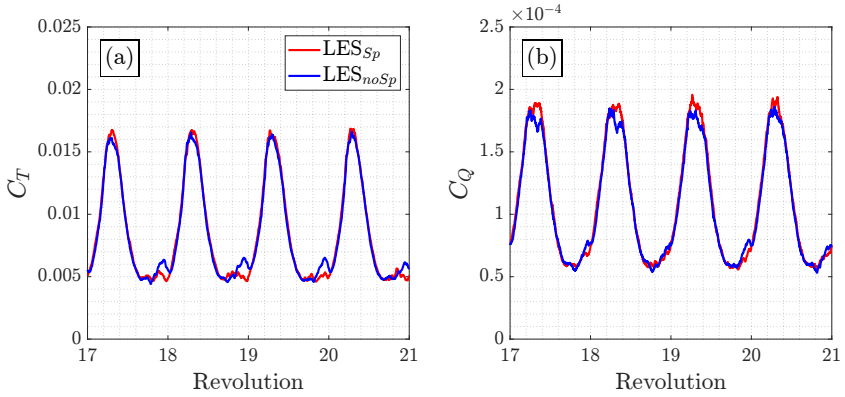

Fig. 3.20 (a) Thrust coefficient C_T and (b) torque coefficient C_Q, for the LES$_{Sp}$ case and for the LES$_{noSp}$ case, at $\mu = 0.17$.

obtained from a simulation of the isolated propeller at the same value of μ (denominated LES$_{noSp}$ in this section).

The C_T and C_Q time histories are displayed over the last 4 propeller revolutions in Figure 3.20. The two compared cases, LES$_{Sp}$ and LES$_{noSp}$, are almost superimposed, indicating a marginal influence of the support on the instantaneous loads. Slight deviations are observed near the local minima in the thrust signal and around the peaks of the torque signal. Consequently, the time-averaged loads are in close agreement, with maximum relative differences around 0.6% for $\overline{C_T}$ and 1.2% for $\overline{C_Q}$. No significant effect of the support is therefore observed on the thrust and torque coefficients.

More pronounced differences emerge instead in the velocity fields. The time-averaged velocity fields $\overline{V_x}$ and $\overline{V_y}$ are shown in Figure 3.21. The $\overline{V_x}$ profiles are taken at $x/R = -0.5$, 0.5, and 1.2 (Figure 3.21(a$_3$)), while $\overline{V_y}$ is evaluated at $y/R = -0.3$, 0.35, and 1.0 (Figure 3.21(b$_3$)), following the same extraction coordinates used in Figures 3.12 and 3.13, respectively. In the upwind region ($x/R < 0$), the flow fields are nearly identical between the LES$_{Sp}$ and LES$_{noSp}$ cases, as expected. This is evidenced by the excellent agreement in both the $\overline{V_x}$ profile at $x/R = -0.5$ and the $\overline{V_y}$ profiles at negative x/R values. However, approaching $x/R = 0$, the support induces a marked decrease in $\overline{V_x}$, visible in Figure 3.21(a$_1$), where the cross-flow is almost zero. A similar, though less pronounced, effect is present in Figure 3.21(a$_2$), where the deceleration is due to the blockage induced by the propeller's wake, even in the LES$_{noSp}$ case. In the downwind region ($x/R > 0$), significant differences arise. The wake of the LES$_{Sp}$ case exhibits both reduced $\overline{V_x}$ and increased $\overline{V_y}$ values, as illustrated in Figures 3.21(a$_3$) and 3.21(b$_3$). This indicates a redistribution of momentum, diverting it from the cross-flow direction towards the propeller's rotational axis. Notably, at $x/R = 0.5$, $\overline{V_x}$ exhibits a strong deficit for $y/R > 0$, and a recirculation region, consistent with the experimental results of section 3.1. Although the discrepancies diminish with downstream distance, differences persist up to $x/R = 1.2$, particularly between $y/R = 0.5$ and $y/R = 1.2$.

The support, therefore, affects the time-averaged velocity field, leading to a significant velocity defect in the downwind region and diverting the wake momentum towards the propeller's rotation axis.

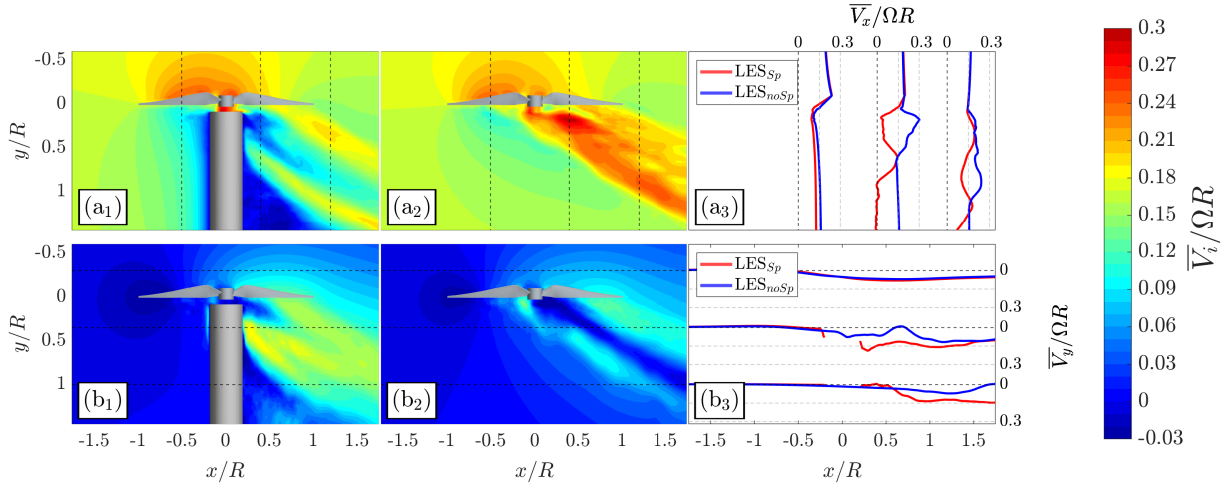

Fig. 3.21 Normalized time-averaged velocity (a) $\overline{V_x}/\Omega R$, and (b) $\overline{V_y}/\Omega R$, (column 1) for the LES$_{Sp}$ case, and (column 2) for the LES$_{noSp}$ case, at μ = 0.17: Colourmaps and profiles of (a$_3$) $\overline{V_x}$ extracted at x/R = -0.5, 0.5, 1.2, and of (b$_3$) $\overline{V_y}$ extracted at y/R = -0.3, 0.35, 1.

Such an effect is due to the coupling between the vortex shedding generated by a finite cylinder and the propeller's induced wake, also featured by a periodic evolution of vortical structures. To gain more insights into the periodic phenomena that occur in the downwind region, spectral and POD analyses are performed on a sequence of 3600 instantaneous velocity fields, extracted with an azimuthal step of 1° over the last 10 propeller revolutions. The frequency content is first analysed via the Welch method ([131]), using Hamming windows with a length equal to one third of the total signal, a 75% overlap between consecutive windows, and a spectral resolution of 7.5 Hz. The spectra are evaluated along a line at x/R = 1.5.

The spectral analysis is carried out on the three velocity components (V_x, V_y, V_z) and the results are respectively shown in Figures 3.22 and 3.23 for the LES$_{noSp}$ and LES$_{Sp}$ cases. Each subplot displays the energy density content of a different velocity component related to the y/R coordinate along the extraction line (x/R = 1.5) and to the corresponding frequency (f), normalised with the BPF. In the LES$_{noSp}$ case (Figure 3.22(a-c)), a dominant tonal spectral peak is observed at $f = 1\,BPF$ for all the velocity components, located around y/R = 1. The LES$_{Sp}$ case spectra (Figure 3.23(a–c)), however, reveal a broadening of the energy density distribution towards lower frequencies. For V_x and V_y, significant spectral content appears between 0.1 and 0.35 BPF. For the V_z component (Figure 3.23(c)), the energy peak shifts to ~0.25 BPF, consistent with the vortex shedding frequency from the cylindrical support, primarily oriented towards the z axis. By evaluating the Reynolds number of the support as $Re_{Sp} = 2R_{Sp}V_\infty/\nu = 7700$, a Strouhal number $St_{Sp} = f_{Sp}2R_{Sp}/V_\infty \approx 0.21$ is obtained ([132]), approximately corresponding to a shedding frequency f_{Sp} of 0.25 BPF, as further proof of the non-negligible contribution to the fluctuations field from the support wake.

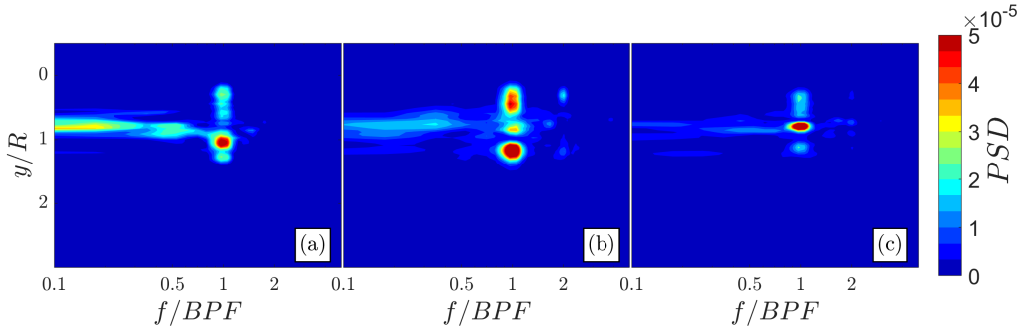

Fig. 3.22 Power spectral density contours of (a) V_x, (b) V_y, and (c) V_z, for the LES$_{noSp}$ case, evaluated along a line at $x/R = 1.5$.

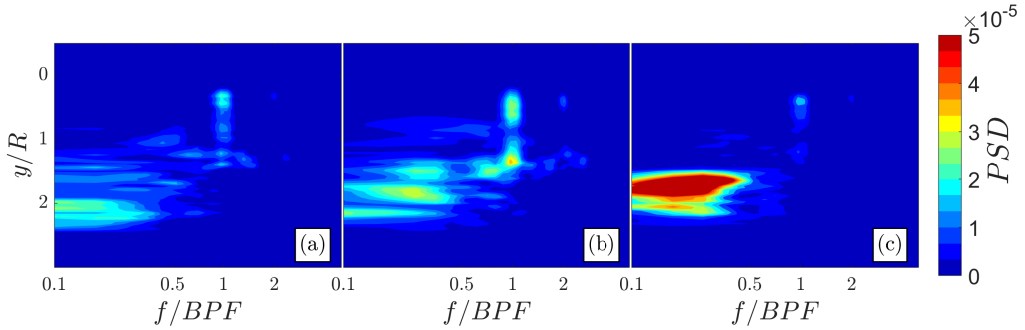

Fig. 3.23 Same caption as Figure 3.22, for the LES$_{Sp}$ case.

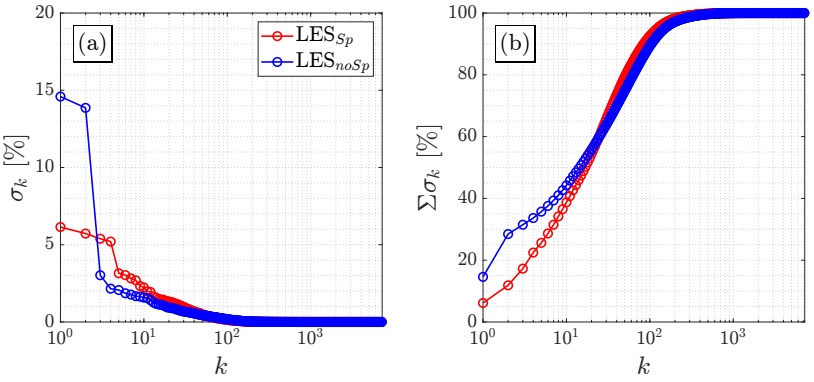

Fig. 3.24 (a) Relative energy content (σ_k) and (b) relative cumulative energy content ($\Sigma\sigma_k$) of the $K = 3600$ POD modes.

A POD analysis is conducted on the velocity fluctuations over the region $0.18 < x/R < 3.5$ and $-0.5 < y/R < 2.5$, specifically tailored to highlight the impact of the support on the wake dynamics in the downwind region. The relative energy content of each mode (σ_k), extracted for both cases LES$_{noSp}$ and LES$_{Sp}$, is displayed in Figure 3.24(a), and the relative cumulative energy content ($\Sigma\sigma_k$) is displayed in Figure 3.24(b). For the LES$_{noSp}$ case, the first two modes each carry about 30% of the total kinetic energy. A sharp decay follows, with mode 3 only accounting for 3% of the total energy. In contrast, the LES$_{Sp}$ case (figure 3.24(b)) exhibits a more uniform energy distribution across the first four modes, each contributing approximately 5-6% of the total energy, followed by a much less significant drop in the modal energy from mode 5 onwards.

The spatial structures of the first four POD modes are visualised in Figures 3.25 and 3.26, respectively showing the contours of the eigenfunctions ϕ_x, ϕ_y, and ϕ_z for the LES$_{noSp}$ and LES$_{Sp}$ cases. For the LES$_{noSp}$ case, the first two modes (Figure 3.25(a_1,b_1,c_1,a_2,b_2,c_2)) exhibit an alternating structure characteristic of the vortex shedding, with strong contributions in ϕ_y, hence aligned with the propeller axis. Mode 3 (Figure 3.25(a_3,b_3,c_3)) instead is dominated by the shear-layer dynamics, with less energetic structures than the first two modes. Mode 4 (Figure 3.25(a_4,b_4,c_4)) finally features alternating structures similar to those observed for the two most energetic modes, but with considerably reduced energy content. For the LES$_{Sp}$ case, the first two spatial modes appear less coherent (Figure 3.26(a_1,b_1,c_1,a_2,b_2,c_2)), being affected by the interaction between the tip vortex and the shedding of the support. The alternate pattern of maximum and minimum energy is still visible across the three spatial components, but the relative energy is lower compared to the LES$_{noSp}$ case. At the same time, modes 3 and 4 (Figure 3.25(a_3,b_3,c_3,a_4,b_4,c_4)) show a significantly increased energy content, mostly for $y/R > 1.2$ for the ϕ_z component (Figure 3.25(c_3,c_4)). The alternate pattern of maximum and minimum ϕ_z regions suggests the presence of vortex shedding with vortices that predominantly induce velocity along the z axis, therefore associated with the shedding from the support. POD manages to separate the contributions of the propeller's wake and the support vortex shedding into different mode pairs. However, by comparing the first two modes between Figure 3.25 and Figure 3.26, it is evident that, in the presence of the support, the first two modes are affected along the three components. As a

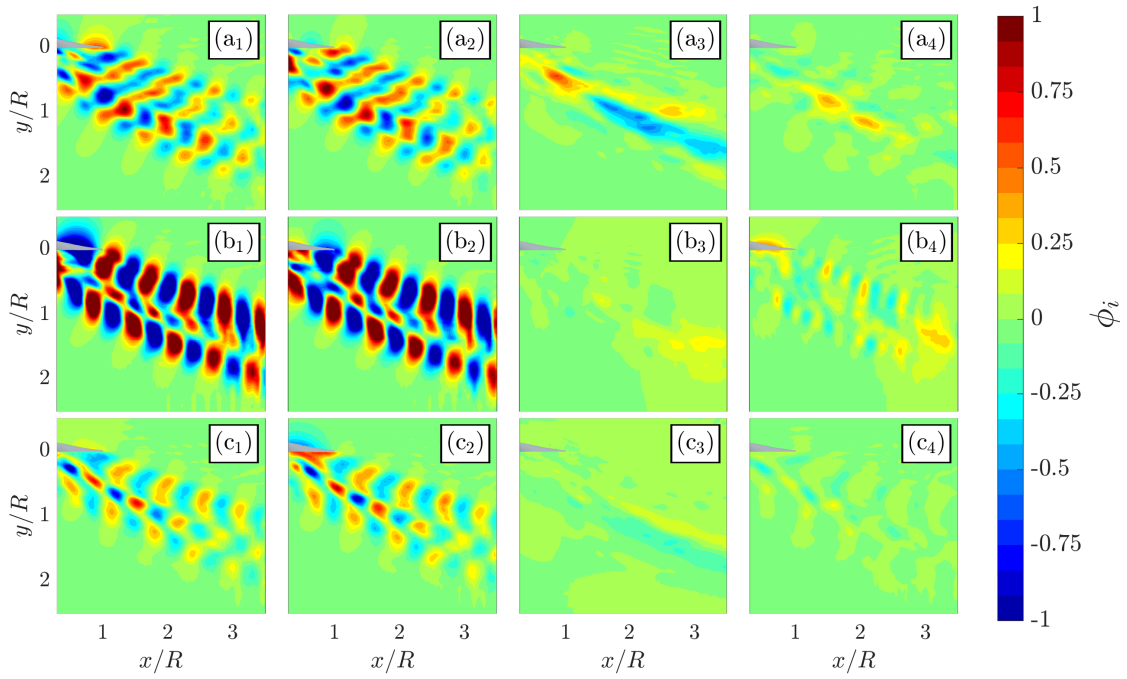

Fig. 3.25 Spatial structures (rows: (a) ϕ_x, (b) ϕ_y, and (c) ϕ_z) of (columns 1-4) the first four POD modes, for the LES$_{noSp}$ case. All modes are normalised by their respective energy contribution.

consequence, it is not straightforward to isolate the effect of the support and depurate the flow field to match the one obtained without the support, at least by implementing a linear approach such as POD.

3.2.5 Wake and vortices dynamics

An additional set of LES simulations was performed for the isolated propeller at $\mu = 0$, 0.04, 0.08, 0.17, 0.24, and 0.32. This allowed for a detailed investigation of the wake dynamics in the absence of the propeller support, whose influence was previously shown to be non-negligible, particularly in the downwind region. The focus of the analysis is placed on the evolution of the macro-scale vortical structures as the cross-flow ratio μ increases. These structures are primarily identified via Q-criterion iso-surfaces, displayed in Figure 3.27. To enhance the visualisation of the large-scale vortices, the Q-criterion fields are phase-averaged with the blades aligned along the cross-flow direction. The phase alignment is also indicated by a propeller mask superimposed on each subfigure for reference.

In hovering conditions ($\mu = 0$; Figure 3.27(a$_1$, a$_2$)), two main structures are observed: the tip vortices (TV) and the hub vortex (HV). TV are shed from the blade tips and evolve into a helical system around the propeller rotation axis. In the absence of the cross-flow, the wake is advected exclusively by the induced velocity field, leading to early interactions between adjacent TV filaments and subsequent breakdown. This is particularly evident from the front view (Figure 3.27(a$_2$)), where helical TV structures dissipate within approximately one radius downstream of the propeller disk. HV forms near

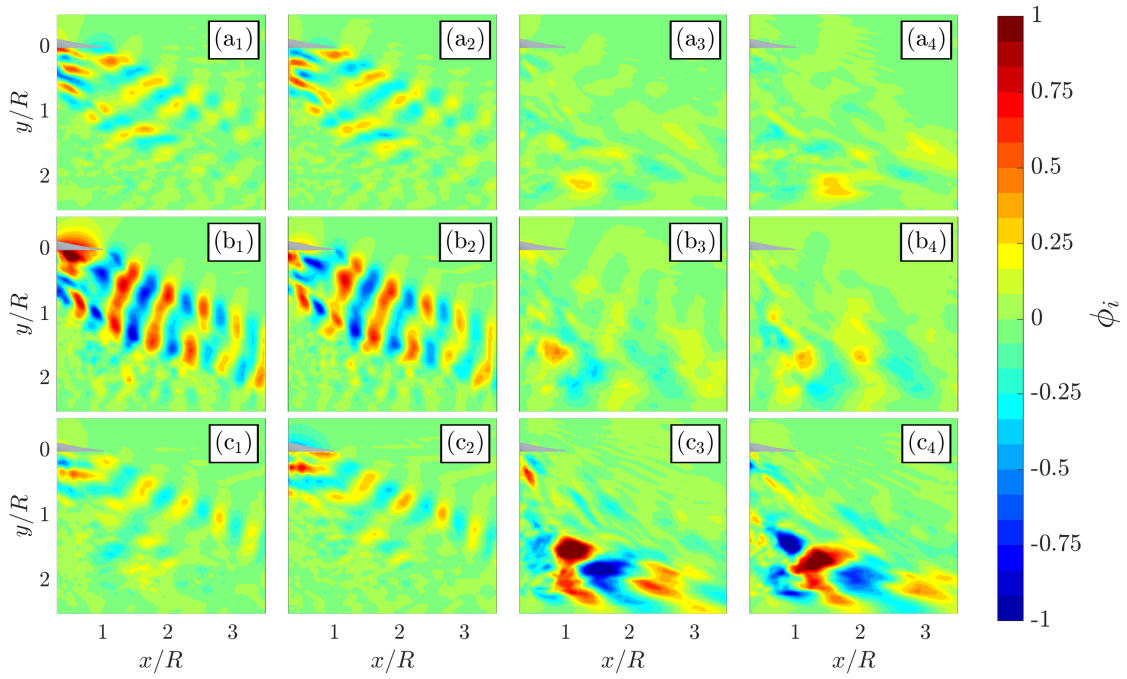

Fig. 3.26 Same caption as Figure 3.25, for the LES_{Sp} case.

the blade roots with a vorticity primarily aligned with the propeller axis. It resides at the centroid of the wake and is associated with the region of minimum axial-induced velocity. Unlike TV, HV is more stable and persists over greater axial distances. Weak root vortices are generated from the blades' roots with the opposite orientation to TV. These weak structures almost immediately collapse on HV and become indistinguishable when looking at the Q-criterion iso-surfaces. At $\mu = 0.04$ (Figure 3.27(b_1, b_2)), the weak cross-flow begins to slightly deflect TV and HV in the x-direction, making the wake lose its axisymmetric property. At $\mu = 0.08$ (Figure 3.27(c_1, c_2)), the wake is further deflected, and two prominent counter-rotating structures appear. These are identified as the windward and leeward branches of CVP and evolve primarily in the x-direction with a vorticity almost aligned with the same axis. As anticipated, the CVP is formed with a mechanism similar to that of jets in cross-flow, as the wake shear layer rolls up due to the pressure differential between the upwind and downwind wake regions ([34]). The first appearance of CVP occurs at a value of μ corresponding to the change in slope observed in the performance coefficients $\overline{C_T}$ and $\overline{C_Q}$ (Figure 3.11). As μ is further increased, the propeller wake is significantly deflected towards the cross-flow direction, featuring a decreased axial induced velocity and an increased effective angle of attack, thereby enhancing the instantaneous and time-averaged thrust and torque values. At $\mu = 0.17$ (Figure 3.27(d_1, d_2)), the wake topology becomes less chaotic. The external flow supports the advection of TV, which now persists as coherent, well-defined structures aligned along the x axis. CVP is more prominent and shows a reduced radial extent due to the wake compression in the z direction. Both TV and HV are still identifiable as distinct structures. At $\mu = 0.24$ (figure 3.27(e_1, e_2)), the increased wake deflection towards the cross-flow

direction leads to a progressive coalescence of TV and HV into an indistinguishable and more chaotic structure (TV+HV). Despite this, CVP remains strong and well-identifiable at both $\mu = 0.17$ and $\mu = 0.24$. The windward portion of CVP (CVP_{ww}), generated by the more heavily loaded blades, appears stronger and more coherent. Conversely, the leeward portion of CVP (CVP_{lw}) is weaker and, at $\mu = 0.17$, is nearly aligned with the x axis, indicating that the local axial induced velocity is insufficient to sustain its advection along the propeller axis.

Tip vortices

The trajectories of the macro-scale vortical structures are now quantitatively examined. To this end, the vorticity field is extracted in different planes to identify vortex cores as they evolve within the induced wake. The evolution of TV is analysed at increasing values of μ by assessing the phase-averaged vorticity component $\widehat{\omega}_z$ in the longitudinal x-y plane located at $z = 0$, as shown in Figure 3.28. This corresponds to the same measurement plane adopted in the validation of LES, as discussed in section 3.2.2. By considering the z component of vorticity ($\widehat{\omega_z}$), the analysis isolates TV, whose vorticity is predominantly oriented along z in the selected plane, while excluding the hub vortex and CVP, whose vorticities are primarily oriented perpendicular to z.

For the hovering case ($\mu = 0$, Figure 3.28(a)), the wake appears almost axisymmetric. High-vorticity structures that can be attributed to TV are visible only near the propeller disk; further downstream, the vorticity rapidly diffuses into a broader radial region of diminished vorticity, particularly at increasing y/R. Additionally, a weaker vorticity region is observed near the hub, corresponding to the root vortices. These originate from the blade roots and rotate in the opposite direction to the corresponding TV shed by the same blade. These vortices are only clearly visible near the propeller and coalesce with HV as they are advected in the y axis direction. At $\mu = 0.04$ (Figure 3.28(b)), the onset of cross-flow induces a slight deviation of the wake in the x axis direction, accompanied by a modest radial contraction. Both root and tip vortices remain distinguishable, with the wake becoming increasingly confined as it evolves downstream. Compared to the hovering condition, the radial spreading of vorticity is notably reduced beyond $y/R > 2$. As μ increases to 0.08 (Figure 3.28(c)), the wake curvature becomes evident, bending toward the x axis. TV shed from the upwind blade (TV_{uw}) are initially advected toward the hub and are identified until approximately half the blade radius downstream of the propeller's disk. Similarly, TV shed from the downwind blades around $x/R = 1$ (TV_{dw}) follow curved trajectories aligned with the cross-flow. At $\mu = 0.17$ (Figure 3.28(d)), the wake is rigidly advected toward the x direction. TV display nearly linear trajectories and appear more coherent, particularly in the case of TV_{uw}, which manifests as distinct, high-vorticity connected regions persisting further downstream than at lower μ. This stabilising effect can be attributed to the cross-flow influence, which enhances vortex coherence through a roll-up mechanism similar to that observed in jets in cross-flow ([e.g. 34]). Although TV_{dw} are likewise strengthened by the cross-flow, they remain less intense and less coherent than their upwind counterparts. At higher cross-flow ratios, namely $\mu = 0.24$ (Figure 3.28(e)) and $\mu = 0.32$

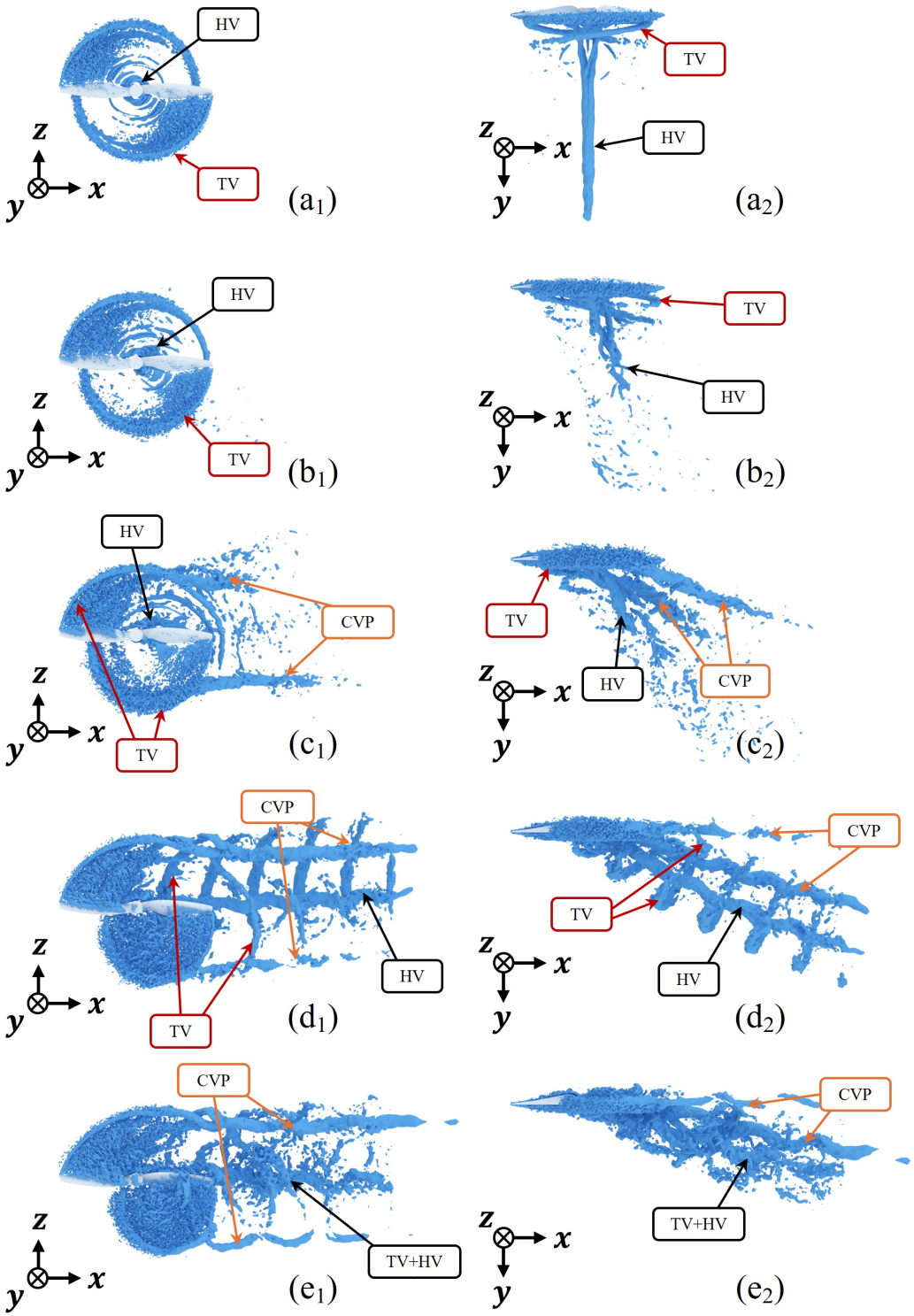

Fig. 3.27 Phase-averaged Q-criterion iso-surfaces (Q = 70000 s^{-2}) of the propeller's wake for (rows a-e) μ = 0, 0.04, 0.08, 0.17, and 0.24; (column 1) top view: x–z plane, and (column 2) front view: x–y plane. Identified HV, TV, and CVP are marked with colour-coded tags.

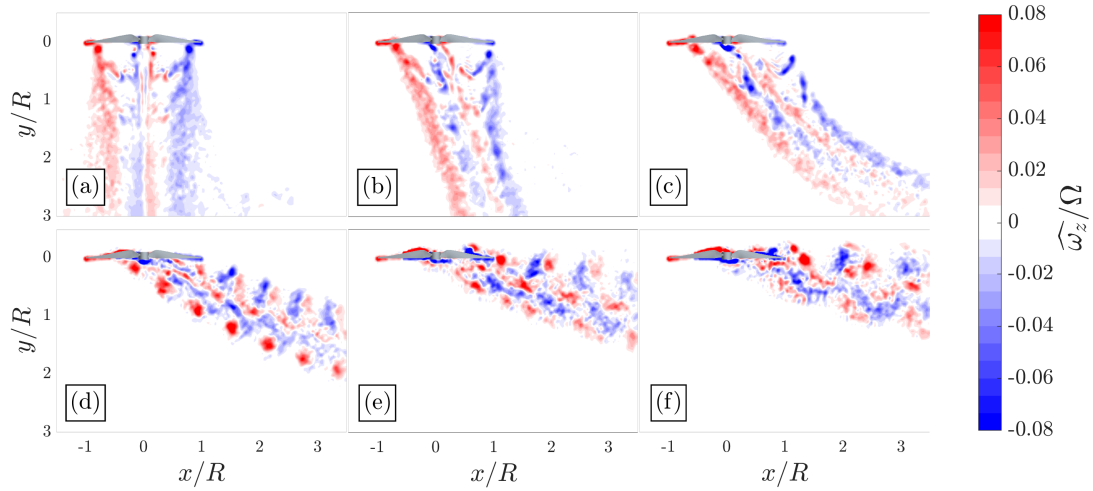

Fig. 3.28 Colourmaps of the normalized phase-averaged $\widehat{\omega_z}/\Omega$ in the x-y plane at $z = 0$ for: (a) $\mu = 0$, (b) $\mu = 0.04$, (c) $\mu = 0.08$, (d) $\mu = 0.17$, (e) $\mu = 0.24$, (f) $\mu = 0.32$.

(Figure 3.28(f)), the wake appears less organized. This is consistent with the chaotic wake topology previously observed in the three-dimensional Q-criterion iso-surfaces at $\mu = 0.24$ (Figures 3.27(e_1, e_2)), where TV and HV were shown to be no longer distinguishable. In the considered longitudinal plane, this interaction manifests as increased complexity and a loss of coherence in the vorticity contours. Individual vortex trajectories become difficult to discern from the vorticity maps alone, though they appear to align predominantly with the x axis, particularly in the downwind region.

The identification of TV is performed using the Γ_2 criterion, as outlined in Section 2.7.1, on the phase-averaged velocity fields extracted in the $z = 0$ plane. A vortex is identified when the local maximum of $|\Gamma_2|$ exceeds the threshold value of $\Gamma_{2-thr} = 0.85$ and the associated non-dimensional circulation satisfies $|\Gamma_v|/\Omega R^2 > 0.3$. These thresholds are intrusively selected to isolate TV from other, weaker substructures such as the root vortices. The calibration of these parameters is carried out in hovering conditions and is extended to the remaining cases. In hovering conditions, the absence of external cross-flow results in the presence of multiple vortical structures of varying size and circulation strength, which remain close to the propeller due to the lack of significant downstream advection. To properly isolate the most coherent and dynamically relevant vortices, it is necessary to employ a relatively high threshold. A value too close to unity, however, may lead to the identification of too few structures, thereby limiting the statistical robustness of the following analyses. To evaluate the effect of the threshold, vortex identification was performed on the hovering case using three different values: $\Gamma_{2-thr} = 0.8$, 0.85, and 0.9. The resulting identified vortex cores are displayed in the scatter plots of Figure 3.29(a–c), colour-coded according to their non-dimensional circulation ($\Gamma_v/\Omega R^2$). The analysed flowfield results from combining all the phase-averaged fields together to highlight the vortices while also showing their evolution in the wake. At $\Gamma_{2-thr} = 0.8$ (Figure 3.29(a)), multiple coherent vortices are identified in the near wake, particularly along the shear layer generated from the blade

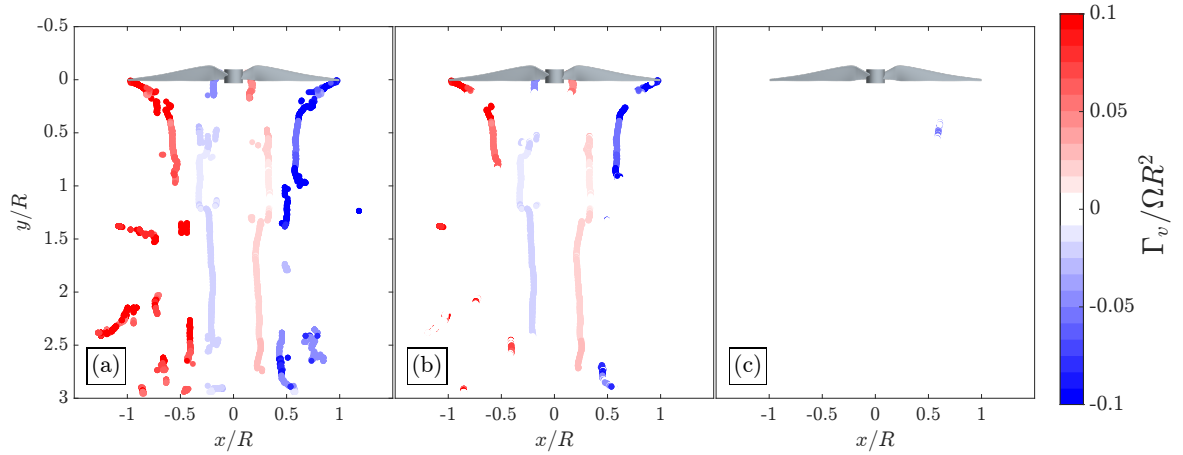

Fig. 3.29 Scatter plots of the identified vortical structures for a flow field combining all the phase-averaged fields, evaluated in hovering conditions ($\mu = 0$) for (a) $\Gamma_{2-thr} = 0.8$, (b) $\Gamma_{2-thr} = 0.85$ and (c) $\Gamma_{2-thr} = 0.9$.

tips. In addition, weaker root vortices are detected near the hub, extending approximately parallel to the propeller's rotation axis. However, several disorganized vortices also appear in the far wake ($y/R > 1$), likely reflecting rotational structures arising from tip vortex breakdown and interaction with the surrounding quiescent fluid. When the threshold is increased to $\Gamma_{2-thr} = 0.85$ (Figure 3.29(b)), only the tip and root vortices are found. To further isolate the tip vortices, a supplementary filter based on circulation magnitude is applied by imposing $|\Gamma_v|/\Omega R^2 > 0.03$. In this fashion, only the tip vortices remain visible in the analysed plane. At the highest tested threshold value, $\Gamma_{2-thr} = 0.9$ (Figure 3.29(c)), very few vortices are identified, indicating that the threshold becomes overly restrictive and excludes even the most energetic structures in the wake.

Based on this parametric assessment, a value of $\Gamma_{2-thr} = 0.85$ was selected for all the analyses presented in the article. This choice balances sensitivity and selectivity, effectively isolating dynamically relevant vortices while suppressing noise and weak flow features. The same threshold is applied to cases with $\mu > 0$, where the presence of cross-flow leads to increased spatial coherence in the vortex field due to the enhanced advection. In all cases, the tip vortices are further discriminated from root vortices using the circulation threshold: $|\Gamma_v|/\Omega R^2 > 0.03$. Nevertheless, care should be used when considering the Γ_2 criterion for vortex identification, given the shown strong dependency of its outcomes on the threshold value. As such, a similar sensitivity analysis is to be encouraged.

The resulting mean trajectories of TV_{uw} and TV_{dw} are shown in Figure 3.30 as solid and dashed lines, respectively. As previously anticipated, at low cross-flow ratios, the tip vortices dissipate rapidly and are no longer identifiable beyond a radial distance of approximately one propeller radius. TV_{uw} trajectories additionally exhibit a marked change in slope near the propeller disk, attributed to the characteristic inboard advection observed under hovering or weak cross-flow conditions. Starting from $\mu = 0.17$, TV_{uw} follow a more linear path, with no significant variation in the trajectory skew angle. In contrast, TV_{dw} originate from the blade tip in the downwind region and exhibit a nearly linear

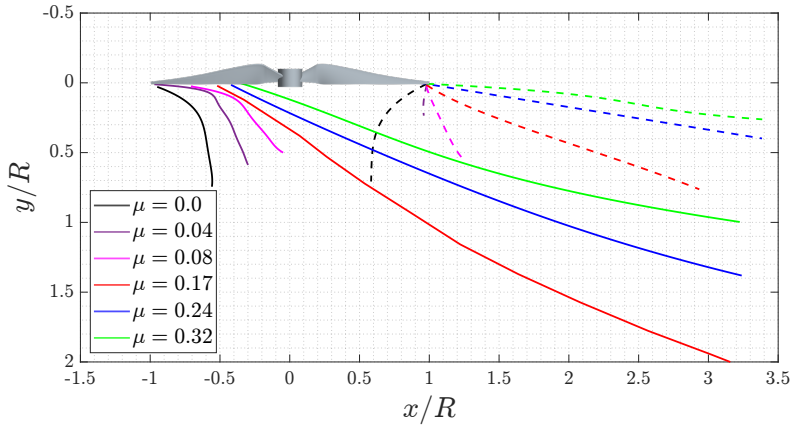

Fig. 3.30 (—) TV_{uw} and (- -) TV_{dw} trajectories in the $[x, y, z = 0]$ plane, at different μ values.

trajectory even at very low μ values. Notably, at $\mu = 0.04$, the vortices are only sporadically detected beyond $y/R > 0.25$, suggesting a rapid loss of coherence or early breakdown.

Hub vortex and counter-rotating vortex pair

The characterisation of HV and CVP is performed by analysing the flow quantities extracted from transversal y–z planes located at $x/R = 0$, 1.2, 1.8, 2.4, and 3. Unlike TV, these structures are characterised by a vorticity that becomes increasingly aligned with the x axis as the cross-flow ratio μ increases. Additionally, in the considered planes, HV and CVP trajectories can be identified with the use of time-averaged fields. In contrast with TV, these vortical structures maintain a fixed position within the propeller's revolution. Therefore, time-averaging provides a wider set of snapshots compared to phase-averaging, and the resultant statistics reveal well-defined structures that are easier to identify. The time-averaged out-of-plane vorticity $\overline{\omega_x}$ fields are hence shown in Figure 3.31. The most prominent structure in these fields is the windward portion of CVP_{ww}, identified as a strong region of positive vorticity aligned with the out-of-plane x axis. It originates near $z/R = +1$ in the $x/R = 0$ plane, coinciding with the tip of the blades passing through the windward region. Its counterpart, CVP_{lw}, is generated near $z/R = -1$ and exhibits opposite vorticity, being aligned with the negative x axis. HV also rotates accordingly to the negative x axis and is generated at $z/R = 0$ near the blade roots. Its rotation sense depends on the direction of propeller rotation, which, being counter-clockwise, leads to a negative axial vorticity. HV, CVP_{ww}, and CVP_{lw} are advected downstream, approximately keeping their position fixed along the z axis while progressively orienting along the x axis as μ is increased. At $\mu = 0.04$ (Figures 3.31(a_1-a_5)), HV is mainly directed along the y axis and is clearly visible only at $x/R = 0$. Weak velocity vectors rotational patterns appear in the $x/R = 1.2$ and $x/R = 1.8$ planes (Figures 3.31(a_2, a_3)) at $z/R \approx \pm 0.9$, marking the onset of CVP formation, although they remain below the Q-criterion threshold used in Figure 3.27(b_1, b_2) and are not yet clearly identified. At $\mu = 0.08$ (Figures 3.31(b_1–b_5)), well-defined HV and CVP structures become visible and persist downstream to at least $x/R = 3$. At this stage, CVP_{lw} exhibits higher absolute vorticity than HV and CVP_{ww}, owing

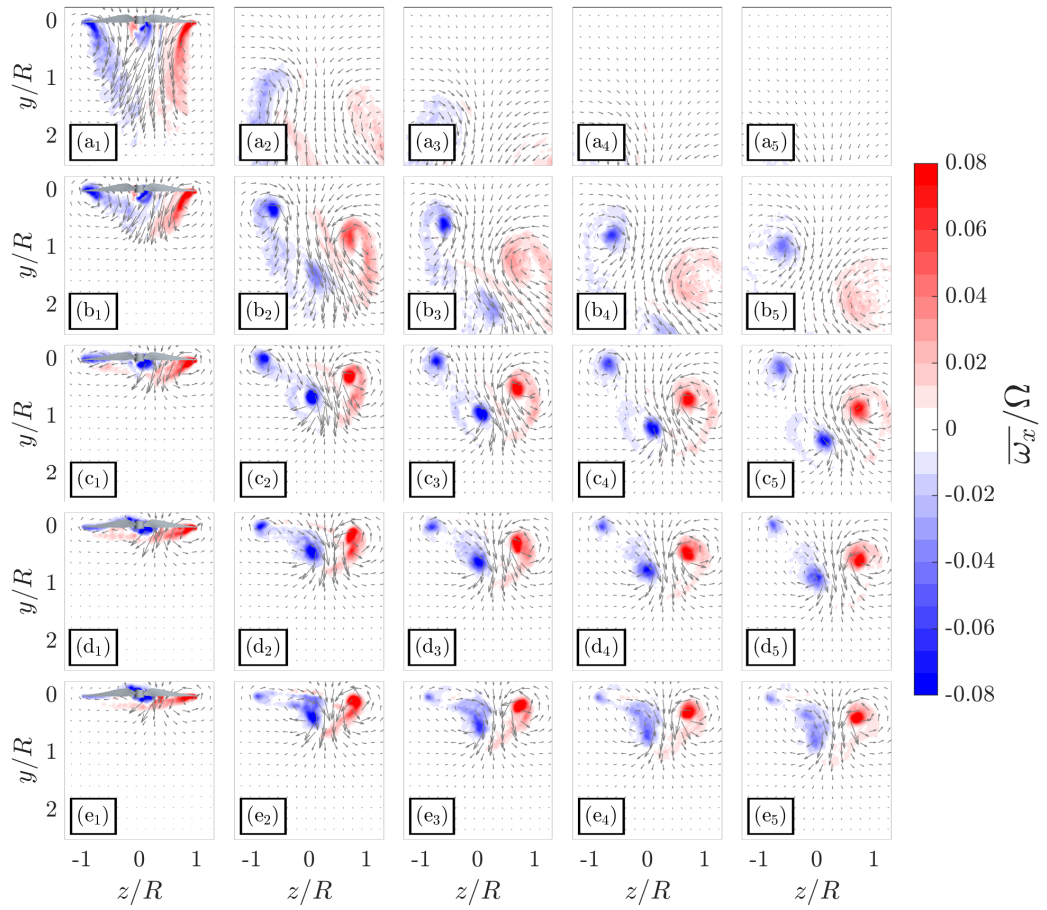

Fig. 3.31 Colourmaps of the normalized time-averaged $\overline{\omega_x}/\Omega$ with overlaid velocity vectors in y-z planes at (rows a-e) μ = 0.04, 0.08, 0.17, 0.24, and 0.32 at (columns 1-5) x/R = 0, 1.2, 1.8, 2.4, and 3.

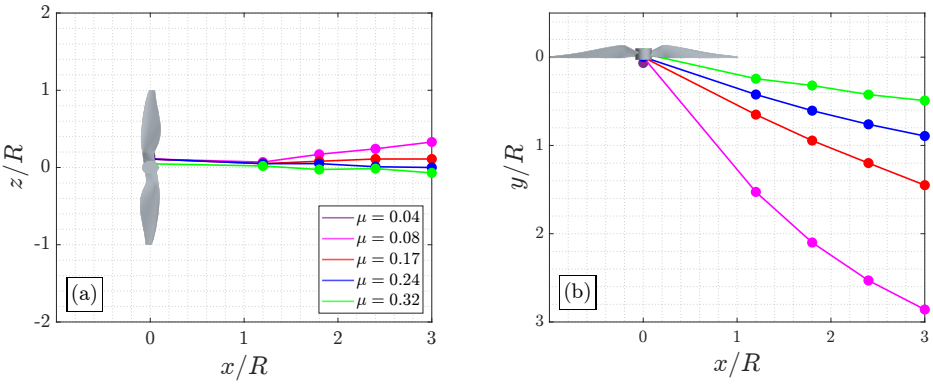

Fig. 3.32 (—•—) HV trajectories at different μ values: (a) Top view: x-z plane, and (b) front view: x-y plane.

to its alignment with the x axis. At the same time, the other structures are still partially misaligned and feature lower $\overline{\omega_x}$ values. For $\mu > 0.08$, both HV and CVP_{ww} progressively align with the x axis and become stronger than CVP_{lw} in terms of core vorticity in all the considered transversal planes. CVP_{lw} increasingly converges toward $y/R \approx 0$ and weakens at increasing μ. This trend is consistent with the reduced thrust produced by the blade sections operating in the leeward region, which limits the intensity of the corresponding CVP_{lw}. The distribution of velocity vectors further highlights the increasing asymmetry of the wake between the windward ($z/R > 0$) and leeward ($z/R < 0$) regions as μ is increased. This asymmetry reflects the differences in the local thrust, which, respectively, lead to greater velocity values along the z axis in the windward region and lower values in the leeward region.

The centres of HV, CVP_{ww}, and CVP_{lw} are identified within the transversal y-z planes extracted at $x/R = 0$, 1.2, 1.8, 2.4, and 3 and displayed in Figure 3.31. In contrast to the analysis of TV, these trajectories are reconstructed from only five discrete spatial locations along the x axis, corresponding to the position of extracted planes. On the other hand, three-dimensional trajectories can be reconstructed by evaluating the centres' positions on the x,y, and z axes. The mean trajectory of HV is shown from a top view in the x-z plane in Figure 3.32(a), and from a front view in the x-y plane in Figure 3.33(b). At $\mu = 0.04$, HV is only detected at the propeller hub, yielding a single vortex centre at $(x/R, y/R, z/R) = (0, 0, 0)$, hence not allowing the reconstruction of the full trajectory as in the other cases. As μ increases, the trajectory of HV progressively aligns with the x axis in the x-z projection (Figure 3.32(a)). Even at $\mu = 0.08$, the maximum lateral deviation does not exceed $z/R = 0.3$ at $x/R = 3$. For $\mu > 0.24$, HV is aligned with the x axis, exhibiting negligible displacements in the z axis direction. From the front view in the x–y plane (Figure 3.33(b)), the trajectory of HV is observed to orient progressively toward the x axis as μ increases. This change in the wake deflection is particularly notable between $\mu = 0.08$ and $\mu = 0.17$, during which the trajectory also becomes increasingly linear. At $\mu = 0.08$, HV exhibits a noticeable curvature toward the x-direction with increasing x/R, while for $\mu > 0.08$, the trajectory stabilises and remains approximately linear over the observed domain.

A similar analysis is conducted for CVP, as shown in Figure 3.33. As observed for HV, at $\mu = 0.04$, CVP is only detected at the blade tips, where they coincide with TV generated in the windward and

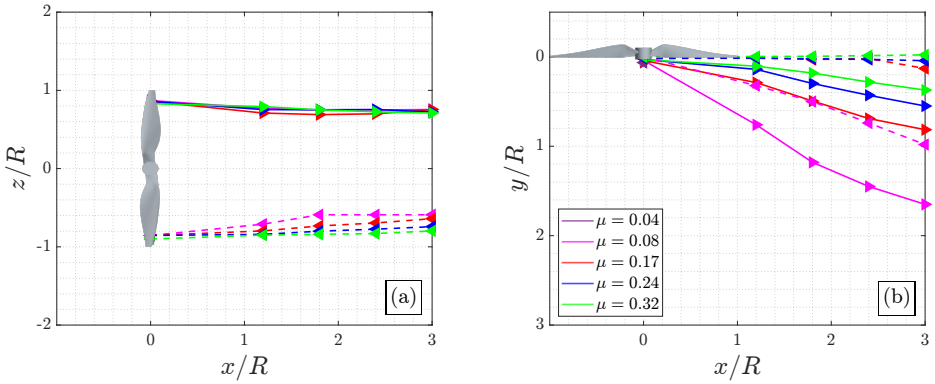

Fig. 3.33 (—►—) CVP_{ww} and (- -◄- -) CVP_{lw} trajectories, at different μ values: (a) Top view: x-z plane, and (b) front view: x-y plane.

leeward regions. For higher cross-flow ratios, CVP cores are identified across the five transversal planes. From the top view (Figure 3.33(a)), the CVP_{ww} trajectory is not affected by the increasing values of μ. Small spanwise displacements in the z direction are exclusively observed between $\mu = 0.04$ and $\mu = 0.08$.

In contrast, CVP_{lw} shows a slight outward shift toward lower z/R values as μ increases, asymptotically stabilising for $\mu > 0.17$. This behaviour suggests that the weaker CVP_{lw} is more strongly influenced by inboard advection at low μ, but converges toward a path symmetric to that of CVP_{ww} at larger values of μ. Both CVP_{ww} and CVP_{lw} exhibit a progressive alignment with the x axis as μ increases, as shown from the front view (Figure 3.33(b)). CVP_{lw} features a quasi-asymptotic trajectory already by $\mu = 0.17$, becoming nearly parallel to the x axis. Conversely, CVP_{ww} continues to shift towards the x axis at higher μ, without having reached a fully asymptotic trajectory within the investigated μ range. Similar to what is observed for HV, the curvature of CVP_{ww} and CVP_{lw} trajectories diminishes with increasing μ, and the paths become progressively more linear as they align with the dominant direction of wake advection.

3.2.6 A simplified model of the wake deflection

The evaluation of the trajectories of the vortices through identification methods, such as the Γ_2 criterion, presents several challenges. Accurate detections require multiple pre-processing iterations to generate an ad-hoc mesh to capture the vortices' evolution. This not only increases the simulations' computational cost, due to the need for finer grids and additional data saving, but also introduces practical issues associated with the storage of large amounts of flow-field data. Furthermore, the post-processing itself is far from straightforward, as it requires a significant amount of input data to achieve high accuracy and may necessitate the calibration of the identification method's parameters, as done in the present analysis. To overcome these limitations, the present study introduces a simplified model based on momentum balance (MB). The proposed model consists of four steps, which are

described in this section, and offers a straightforward way to predict the deflection of the main vortices' trajectories starting from the disk loading distribution. In the next section, the obtained predictions are then compared with those derived from vortex identification methods to assess the proposed MB model.

The trajectories skew angle, estimated from the momentum balance (χ_{MB}), is assumed to be only a function of μ and of the non-dimensional propeller's axial induced velocity $\lambda = v'/\Omega R$ times a correction factor k_χ, as in Eq. 3.7. While μ is known a priori for each test case and is common to the different vortical structures described in Figure 3.27 (TV_{uw}, TV_{dw}, CVP_{ww}, CVP_{lw}, and HV), it is hereby proposed to evaluate a different λ for each vortex type (indicated with the subscript i). Therefore, the first step of the proposed approach is shown with the term at the right side of the arrow in Eq. 3.7.

$$\chi_{MB} = \tan^{-1}\left(\frac{\mu}{k_\chi \cdot \lambda}\right) = f(\mu, \lambda, k_\chi) \xRightarrow[\text{step I}]{\text{model}} f(\mu, \lambda_i, k_\chi) \tag{3.7}$$

Nevertheless, a few operations are needed to implement this new formulation of Eq. 3.7. First, to compute the λ_i, the actuator disk approximation is considered. In cross-flow conditions, this theory provides an analytical expression for λ as a function of the cross-flow ratio μ and $\overline{C_T}$ ([121]), as shown at the left side of the arrow in Eq. 3.8.

The second step of the proposed model involves evaluating λ_i for the different vortices. It consists of substituting $\overline{C_T}$ with a filtered, time-averaged thrust coefficient which is specific to each vortex type ($\overline{C^*_{T,i}}$), as shown on the right side of the arrow in Eq. 3.8.

$$\lambda = \sqrt{-\frac{\mu^2}{2} + \frac{\sqrt{\mu^4 + \overline{C_T}^2}}{2}} \xRightarrow[\text{step II}]{\text{model}} \lambda_i = \sqrt{-\frac{\mu^2}{2} + \frac{\sqrt{\mu^4 + \overline{C^*_{T,i}}^2}}{2}} \tag{3.8}$$

The third step of the proposed model involves the procedure for evaluating $\overline{C^*_{T,i}}$, illustrated in Figure 3.34. First, the s_{C_T} distribution on the propeller disk, for a given μ, is filtered by means of heuristic boolean filters (BF_i). This leads to various $s^*_{C_T,i}$ which are then integrated over the disk to retrieve $\overline{C^*_{T,i}}$ for the different vortex types. These operations are summarized in Eq. 3.9, where the averaging over j will be explained in the next paragraph.

$$\begin{aligned}\overline{C^*_{T,i}} &= \frac{1}{M_i}\sum_{j=1}^{M_i}\int_0^R\int_0^{2\pi} s^*_{C_T,i}(r,\psi,\Delta\psi_j)\,d\psi\,dr \\ &= \frac{1}{M_i}\sum_{j=1}^{M_i}\int_0^R\int_0^{2\pi} s_{C_T}(r,\psi)\cdot \mathrm{BF_i}(\psi,\Delta\psi_j)\,d\psi\,dr\end{aligned} \tag{3.9}$$

The BF_i are specific for each vortex type and are deduced from the flow topology considering the disk region pertaining to each vortex type (see Figure 3.27). They have variable azimuthal width ($\Delta\psi_j$)

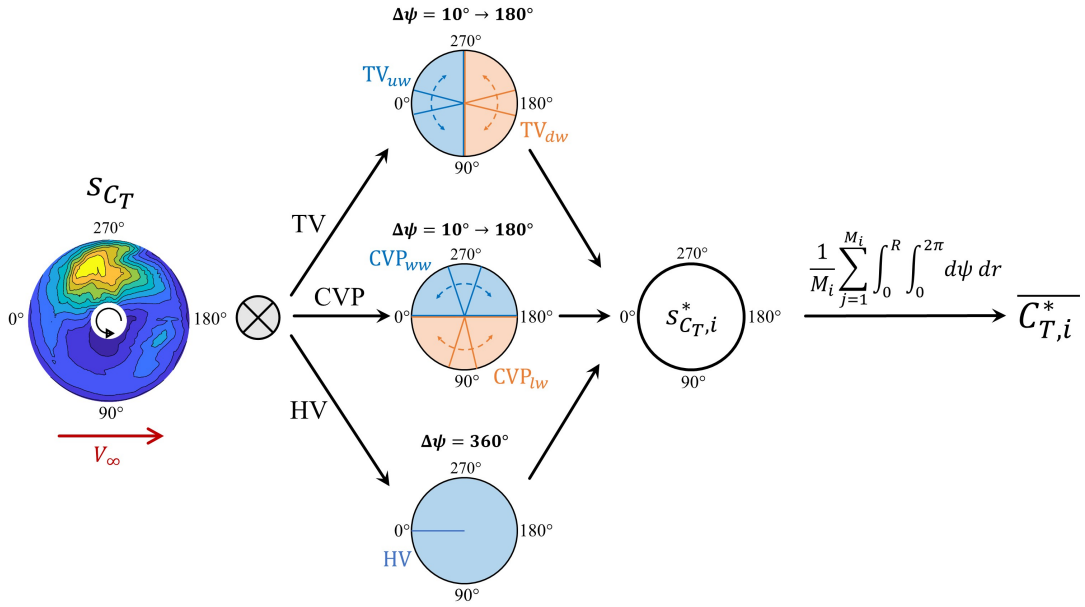

Fig. 3.34 Flowchart of the proposed model step III; from left to right: a s_{C_T} map at a given μ, the boolean filters ($BF_i = 1$ on the disk region coloured as the related vortex tag; the arrow-tipped dashed lines indicate the variable $\Delta\psi_j$), $s^*_{C_T,i}$ and $\overline{C^*_{T,i}}$. The subscript i indicates each vortex type.

and are centred on a different ψ_i value depending on the considered vortical structure. Starting from TV_{uw}, its filter features *true* (1) values in a disk sector centred around the upwind position ($\psi_i = 0°$), and *false* (0) values outside of it. Nonetheless, several disk sectors are considered, progressively extending along the azimuthal direction. The smallest considered sector features $\Delta\psi_j = 10°$, then progressively expanded, with steps of 10°, to $\Delta\psi_j = 180°$, while always keeping the sector centred around $\psi_i = 0°$. The progressive expansion of the *true* disk sector leads to $M_i = 18$ different estimates of $\overline{C^*_{T,i}}$ for TV_{uw}. These are then averaged together to a single value, as shown in Eq. 3.9, to reduce the uncertainty on the relevance of TV_{uw} on the mentioned disk sectors. Clearly, this operation maximises the weight, over the average, of the $\psi_i = 0$ region, which responds to the most expected heuristic allocation of this vortex type. The same operation is then carried out for TV_{dw}, CVP_{ww}, and CVP_{lw}. The respective boolean filters are centred around $\psi_i = 180°, 270°$, and 90°, following the same considerations done for TV_{uw}. Finally, HV being instead related to the whole disk, features a filter spanning the full propeller revolution ($\Delta\psi_j = 360°$ and $M_i = 1$). Therefore, for HV, $\overline{C^*_{T,i}}$ coincides with $\overline{C_T}$. The BF_i are shown in Figure 3.34, where, for each filter, the *true* disk sector is coloured as the related vortex tag, the remaining disk sector features a *false* value, and the arrow-tipped dashed lines qualitatively indicate the variation of $\Delta\psi_j$.

Finally, a correction factor k_χ was introduced in Eq. 3.7 to account for the wake topology modelling. The fourth and final step of the proposed model for the evaluation of χ_{MB} involves the comparison of the three following wake models from the literature with the related k_χ values. The simplest model assumes the hypothesis of rigid wake ([128]). The wake is modelled as a cylindrical structure with a constant induced velocity along the wake's evolution direction, leading to $k_\chi = 1$. A more refined

model adds the downstream wake development under the actuator disk assumption. In this case, the far wake velocity reaches twice the induced velocity at the disk, leading to a correction factor of $k_\chi = 2$ to account for this axial acceleration. A third model, introduced by [26], assumes a highly skewed flat wake topology, such that the wake can be approximated as a planar sheet oriented at χ close to 90°. This model features $k_\chi = 0.5$, and its validity has been empirically demonstrated in the same work for $\mu > 1.15\sqrt{C_T}$. [32] later assessed its applicability to predict the CVP deflection in multi-propeller wakes interactions, such as in multicopters in forward flight. For the χ_{MB} estimates presented in the next section, all these wake models were considered.

The vortex trajectories shown in the x–y planes of Figure 3.30, Figure 3.32(b), and Figure 3.33(b) are now used to compute the mean skew angles $\chi_{V_{ID}}$ of each macro-scale vortical structure with respect to the propeller's axis of rotation. These values serve as the reference values to be compared against the predictions of the simplified model introduced in Section 3.2.6.

The comparison is initially carried out with χ_{MB} evaluated under the assumption of a rigid wake topology ($k_\chi = 1$). The results are shown in Figure 3.35 for $\mu = 0.08$, 0.17, 0.24, and 0.32. A dashed black line representing the identity $\chi_{MB} = \chi_{V_{ID}}$ is also reported in each plot as a reference. Furthermore, each data point includes rectangular error bars: the width represents the standard deviation of $\chi_{V_{ID}}$ associated with trajectory linearity, i.e., how far the fitting is from being linear, while the height accounts for uncertainty in the χ_{MB} calculation due to the azimuthal averaging of the thrust loading, as shown in Eq. 3.9. Notably, the HV data in Figure 3.35(a) feature rectangular error bars collapsed to horizontal bars, since the thrust is integrated across a single azimuthal sector of $\Delta\psi = 360°$, as discussed in Section 3.2.6. However, HV shows relatively large errors in the $\chi_{V_{ID}}$ evaluation, particularly at $\mu = 0.08$, where the standard deviation reaches approximately 10°. As μ increases, the discrepancy between χ_{MB} and $\chi_{V_{ID}}$ decreases, with a prediction error of only 3.4° observed at $\mu = 0.32$. Focusing on TV in Figure 3.35(b), TV_{dw} initially exhibits a large discrepancy of approximately 30° at $\mu = 0.08$, along with a substantial standard deviation due to the significant curvature of the identified trajectory. However, the results show a rapid convergence, with errors reduced to 2–3° already at $\mu = 0.17$. In contrast, TV_{uw} is initially well-aligned with the identity line but diverges from it at higher μ, indicating a systematic overprediction of the simplified model. The CVP angles, shown in Figure 3.35(c), display an overall converging trend. Both CVP_{ww} and CVP_{lw} asymptotically approach the $\chi_{MB} = \chi_{V_{ID}}$ line as μ increases, with both the prediction error and the associated standard deviations decreasing and nearly becoming null at $\mu = 0.32$.

The accuracy of the rigid wake model can be further evaluated by computing the mean absolute error (MAE) between the $\chi_{V_{ID}}$ and χ_{MB} angles. Such errors are displayed in the first row of Table 3.2. For all the considered structures, the MAE remains below 12°, with the largest error observed for TV_{dw}, primarily due to the low prediction accuracy at $\mu = 0.08$. At this low cross-flow ratio, the wake is still transitioning from a hovering-dominated topology to one shaped by cross-flow advection. As a result, vortex trajectories exhibit a marked curvature, which introduces substantial uncertainty in the evaluation of $\chi_{V_{ID}}$ and leads to noticeable outliers in the χ_{MB} predictions relative to higher-μ trends.

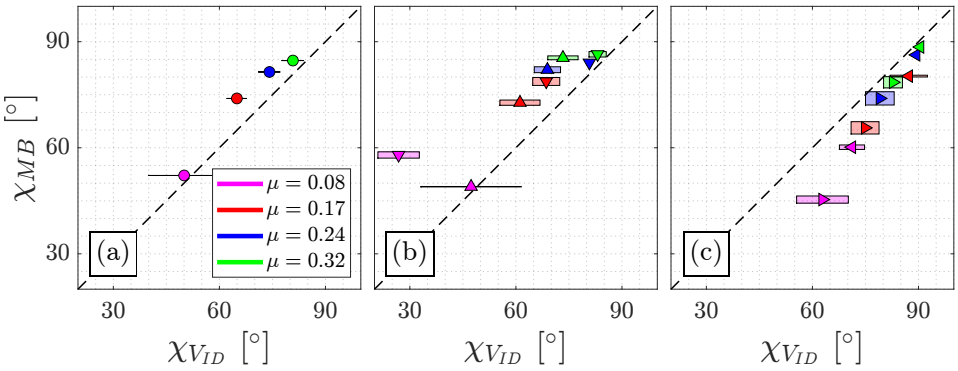

Fig. 3.35 χ_{MB} vs. $\chi_{V_{ID}}$ using the rigid wake model ($k_\chi = 1$) for (a) HV: •, (b) TV_{uw}: ▲, TV_{dw}: ▼, (c) CVP_{ww}: ◄, and CVP_{lw}: ►; $\chi_{MB} = \chi_{V_{ID}}$ identity (- -). The rectangles' width (height) shows the standard deviation of $\chi_{V_{ID}}$ (χ_{MB}) for the related quantity.

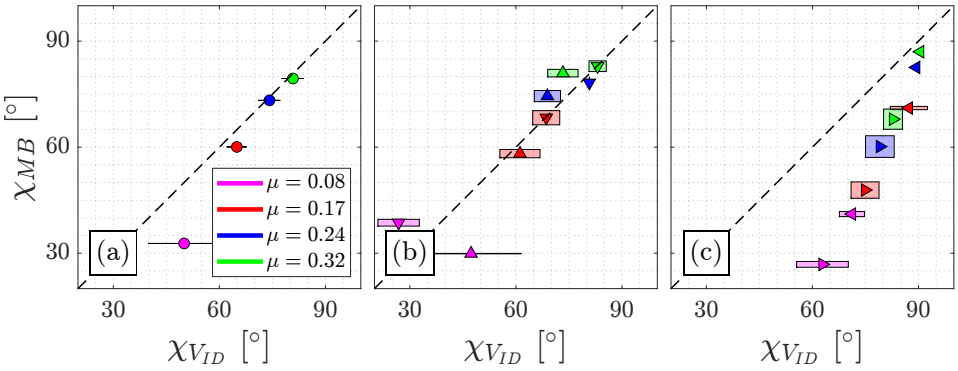

Fig. 3.36 χ_{MB} vs. $\chi_{V_{ID}}$ using the actuator disk wake model ($k_\chi = 2$) for (a) HV: •, (b) TV_{uw}: ▲, TV_{dw}: ▼, (c) CVP_{ww}: ◄, and CVP_{lw}: ►; $\chi_{MB} = \chi_{V_{ID}}$ identity (- -). The rectangles' width (height) shows the standard deviation of $\chi_{V_{ID}}$ (χ_{MB}) for the related quantity.

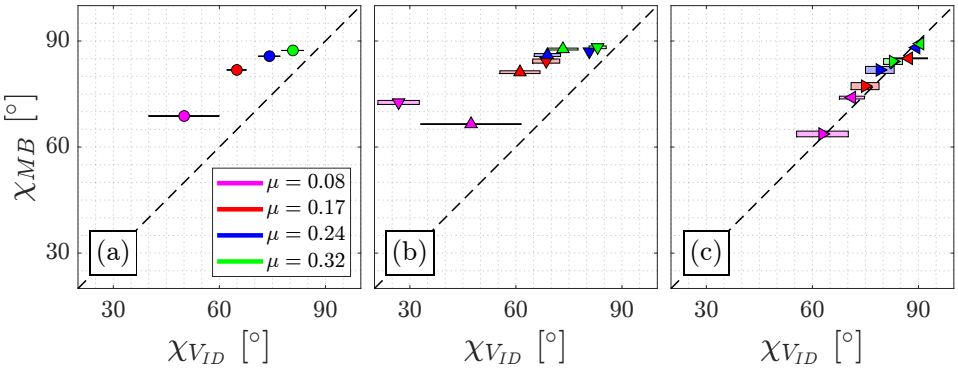

Fig. 3.37 χ_{MB} vs. $\chi_{V_{ID}}$ using the flat wake model ($k_\chi = 0.5$) for (a) HV: •, (b) TV_{uw}: ▲, TV_{dw}: ▼, (c) CVP_{ww}: ◄, and CVP_{lw}: ►; $\chi_{MB} = \chi_{V_{ID}}$ identity (- -). The rectangles' width (height) shows the standard deviation of $\chi_{V_{ID}}$ (χ_{MB}) for the related quantity.

Table 3.2 also includes the MAE values obtained using two alternative low-order models: the actuator disk hypothesis ($k_\chi = 2$) and the flat wake hypothesis ($k_\chi = 0.5$), shown respectively in the second and third rows. The corresponding scatter plots of χ_{MB} as a function of $\chi_{V_{ID}}$ are displayed in Figure 3.36 and Figure 3.37, using the same graphical layout adopted in Figure 3.35.

The actuator disk hypothesis significantly improves the prediction of HV and of both TV_{uw} and TV_{dw}, featuring $k_\chi = 2$. By assuming a progressive flow acceleration downstream of the disk, this model accounts for an increase in induced velocity up to twice that of what is predicted by the rigid wake assumption. This correction yields a reduction in the MAE, with errors falling below 8°, as shown in the second row of Table 3.2. In Figures 3.36(a,b), the HV and TV predictions closely follow the $\chi_{MB} = \chi_{V_{ID}}$ identity line, with deviations below 7° for $\mu > 0.08$. At $\mu = 0.08$, however, a poor agreement is still obtained. The actuator disk model performs worse for the CVP vortices, whose predicted χ_{MB} angles deviate substantially from the $\chi_{MB} = \chi_{V_{ID}}$ line, yielding MAE up to 24°. This discrepancy arises because the actuator disk theory does not account for the formation mechanisms or topology of CVP.

A more suitable prediction for the CVP structures is provided by the flat wake model, which adopts a correction factor of $k_\chi = 0.5$. The corresponding scatter plots are shown in Figure 3.37. In this case, the predicted χ_{MB} angles are nearly superimposed on the $\chi_{MB} = \chi_{V_{ID}}$ identity line, resulting in the lowest MAE among all tested models of approximately 2° for both the CVP_{ww} and CVP_{lw}. The flat wake model, however, is not adequate to accurately capture the skew angle of HV and TV structures. The predictions for these vortices, particularly at low μ, show significant deviations from the identity line, indicating that the model underestimates the axial velocity required to maintain the observed vortex alignment.

Overall, the proposed model, coupled to the best-performing wake model for the specific vortex types, gives good indications of the wake topology. Moreover, the model is not specific to the investigated propeller geometry, as only the thrust distribution and the cross-flow ratio are given as input.

	HV	TV_{uw}	TV_{dw}	CVP_{ww}	CVP_{lw}
$k_\chi = 1$	6°	10°	12°	9°	6°
$k_\chi = 2$	**6°**	**8°**	**4°**	24°	14°
$k_\chi = 0.5$	13°	18°	18°	**2°**	**2°**

Table 3.2 Mean absolute error between $\chi_{V_{ID}}$ and χ_{MB} for the different vortices and wake models; minimum values for each vortex are highlighted in bold.

A simplified momentum-balance model is introduced to estimate the deflection of the main vortical structures in the propeller wake. Traditional identification methods, such as those based on the Γ_2 criterion, require refined meshes, extensive data storage, and non-trivial pre- and post-processing, making them unsuitable for rapid analyses. The proposed model offers a lightweight alternative that directly predicts the main vortical structures' skew angles from the disk loading distribution. The methodology relies on four steps:

1. The momentum-balance approach is applied to the cross-flow case to evaluate the non-dimensional axial induced velocity λ from the thrust distribution on the propeller disk.

2. The approach is specified to the i vortex by averaging the thrust over a certain portion of the disk, based on where the i vortex is initially shed from the blades. A value of λ_i is obtained for each vortex.

3. A correction factor k_χ is introduced to account for the wake topology modelling. The obtained results suggest the use of $k_\chi = 2$ (actuator disk wake model) for the tip vortices and hub vortex, and $k_\chi = 0.5$ (flat wake model) for the counter-rotating vortex pair.

4. The skew angle of the i vortex can be computed as $\chi_{MB\,i} = \tan^{-1}\left(\frac{\mu}{k_\chi \cdot \lambda_i}\right)$, choosing the adequate value of k_χ for each vortex.

Overall, the simplified framework provides satisfactory predictions, with mean absolute errors below 8°, and a clear reduction of the discrepancy as μ increases. The method offers a general and geometry-independent tool for estimating wake deflection using only the thrust distribution, the cross-flow ratio, and a correction factor for the wake modelling, which depends only on the analysed vortex and not on the propeller geometry. The primary benefit of this approach lies in the possibility of reducing the computational cost and data-storage requirements of high-fidelity simulations: when using this model, the mesh in the wake region does not need to be excessively refined to track the vortex trajectories, as an accurate evaluation of the mean skew angle comes from the thrust distribution on the propeller disk and is already ensured by the refinement near the blades. A further advantage concerns the potential reverse use of the model to infer the disk loading from flow-field measurements. By computing the vortex skew angles from PIV data in the wake, the model enables an estimation of the mean thrust in

specific disk sectors and, in addition, an approximate evaluation of the total thrust through the analysis of the hub vortex.

3.2.7 Conclusions

The simulations show satisfactory agreement with experiments in capturing the trends in time-averaged loads and flow features, despite some discrepancies that may be attributed to inherent differences associated with the flexibility of the blade and experimental limitations at low-force regimes. Moreover, the non-trivial Reynolds number regime ought to be accounted for in the simulation of such a flow field, which adds complexity to the investigation.

The analysis of the disk loading highlights how the cross-flow introduces pronounced azimuthal asymmetries in the relative inflow experienced by the blades, resulting in asymmetric thrust distributions and periodic, unsteady loading. At low cross-flow ratios, the flow exhibits asymmetric induction effects on the propeller disk, with increased local angles of attack on the windward side and reduced ones on the leeward side. These effects produce significant pitch and roll moments. The roll moment caused by cross-flow is somewhat expected; however, to the author's knowledge, there is no prior mention in the literature of the generation of a pitching moment. The roll moment is found to overcome the pitch moment as the cross-flow velocity increases, while the pitch moment becomes negligible. The proposed decomposition of the thrust per unit length reveals the presence of a secondary effect linked to the distortion of the local inflow pattern on the propeller's disk, which is the main contribution to the aforementioned pitching moment and adds to a primary kinematics effect linked to the variation in dynamic pressure.

The investigation into the role of the propeller support reveals that the performance coefficients are primarily unaffected by its presence. Conversely, the induced wake is substantially modified near the propeller. Proper Orthogonal Decomposition (POD) and spectral analyses reveal that the support introduces additional periodic disturbances, associated with the vortex shedding from the support, altering the spatial distribution and the coherence of the propeller's wake vortices in the downwind region. The characterisation of the wake and vortex dynamics in the absence of the propeller's support reveals a progressive transformation of the vortical system as the cross-flow velocity increases. The classical hovering vortex system, mainly composed of tip and hub vortices, transitions into an asymmetric configuration marked by the formation of a counter-rotating vortex pair (CVP), initially shed from the leeward and windward regions and predominantly oriented toward the cross-flow direction. This vortex system behaves similarly to that observed for jets in cross-flow, featuring the same pressure differential-driven formation mechanism. However, different from jets, the two branches of the CVP feature different trajectories and intensities, due to the azimuthal dependency of the momentum source, i.e., the blades' thrust. The tracking of the vortex core paths using the Γ_2-criterion displays the appearance of a well-defined CVP where a change in trend is observed in the performance coefficients, as evidenced both experimentally and numerically.

The vortices' trajectories' deflection is additionally evaluated with the use of a simplified approach based on momentum balance. The comparison with the trajectories' deflection evaluated via vortex identification highlights the potential of this simplified approach in capturing essential features of wake deflection in cross-flow conditions. Despite the complex three-dimensional vortex system, the proposed approach provided an accurate prediction of the hub vortex and tip vortices deflection using an actuator disk modelling for the wake topology ($k_\chi = 2$). The flat wake model ($k_\chi = 0.5$), originally derived in the context of helicopter aerodynamics, proved instead particularly effective in predicting the CVP deflection, as the wake becomes quasi-planar especially at high advance ratios. These findings demonstrate that, when carefully parametrised (e.g., via localised thrust estimation), simplified models can offer reliable preliminary predictions of the wake behaviour with minimal computational cost. It is indeed sufficient to dispose of the thrust distribution on the propeller's disk to predict the vortices' mean trajectories in the induced wake.

The present work provides the rotorcraft community with new insight into the fluid-dynamic mechanisms governing the interaction between propellers and cross-flows. Although the quantitative results are specific to the geometry investigated, the physical interpretation of the mechanisms responsible for the increase in thrust and torque with the cross-flow ratio, as well as the detailed description of the induced-flow evolution, can be readily extended to other propeller or rotor configurations. In addition, this study introduces a simplified approach for predicting the wake deflection based solely on the thrust distribution over the propeller disk. Such a method is directly applicable to different propellers and operating conditions. It may prove valuable in several contexts, ranging from propeller-propeller interaction problems to agricultural spraying, where an accurate estimation of wake deflection is essential for design and operational purposes.

Chapter 4

Dynamic operative conditions

4.1 Dynamic rotational speed variation

The scope of the present section is to illustrate, in a more general case, the main effect of dynamic rotational speed variations. The considerations that follow are then supported by the results of section 4.1.2. In particular, the propeller is subject to an axial inflow of velocity V_∞, accelerating from $n = n_A$ to $n = n_B = n_A + dn$, as depicted in Figure 4.1.

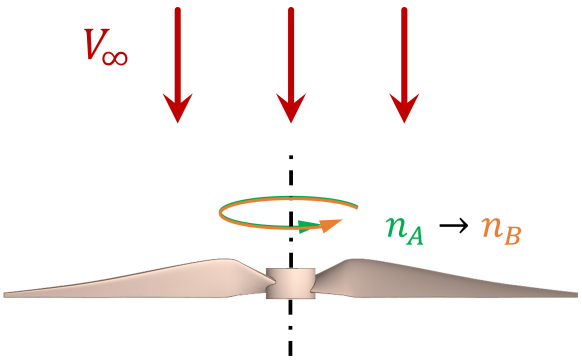

Fig. 4.1 Schematic representation of a propeller in axial inflow subject to a rpm variation.

Under these operative conditions, regardless of the value of V_∞, an acceleration primarily leads to an increase in thrust and torque compared to a steady-state case at the same instantaneous rotational speed. The opposite holds for a deceleration maneuver. From a fluid dynamics perspective, the onset of the effects in the wake associated with the blade motion is characterized by a lag effect. A blade that rotates at $n = n_B$, during the acceleration, interacts with the velocity field induced before by the previously passing blade, when the propeller was rotating at a lower speed. Such lag affects the relative velocity W seen by the blade, since both the tangential induced velocity (u') and the axial induced velocity (v') are different compared to the steady-state values. W is particularly affected in terms of its orientation rather than its magnitude. This change is subsequently reflected in the value of α seen by

the blade and therefore on the loads, such as the propeller's thrust and torque. The magnitude of W is also slightly modified, but this effect is of a lower order compared to that related to the α. If the dynamic rpm variation occurs slowly enough, the lag effects of the induced flow field become almost negligible, and the maneuver can be considered as quasi-steady.

To better illustrate the influence of an acceleration maneuver, it is useful to focus on a single blade element, positioned at a distance r from the propeller hub. The effect of the maneuver is indeed assumed to be primarily related to the plane containing the blade element, which is perpendicular to the radial direction. Two steady-state cases at the same fixed V_∞ value are illustrated for comparison: in the steady-state case A, shown in Figure 4.2(a), the propeller rotates with $n = n_A$. In steady-state condition B, shown in Figure 4.2(b), the propeller rotates at a slightly greater speed $n{=}n_B$, where $n_B = n_A + dn$. Under these conditions, the relative velocity W_B is greater than W_A due to both the increase in the tangential velocity component $(nr\pi/30 - u')$ and to the increase in v'. α remains almost unaffected between the two conditions, while an increase in thrust and torque is observed, hence almost exclusively due to the increase in W.

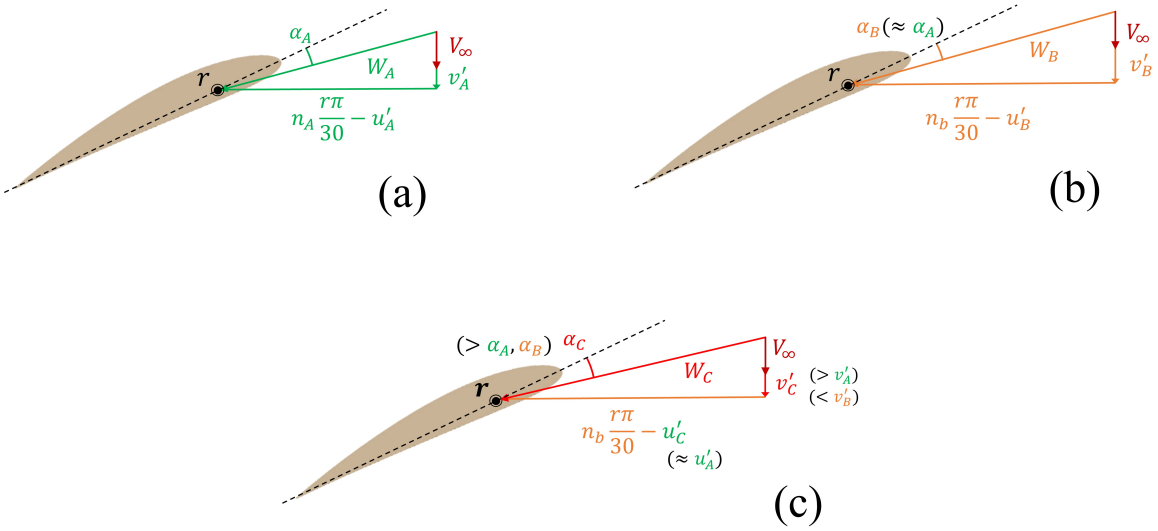

Fig. 4.2 Schematic representation of a blade element under different steady-state and dynamic conditions. (a) Steady-state case with $n = n_A$, (b) steady-state case with $n = n_B = n_A + dn$, (c) dynamic case with $n = n_B$.

Focusing on a third dynamic case C, as shown in Figure 4.2(c), where the propeller is instantaneously rotating at $n = n_B$, accelerating from a previous state where n was equal to n_A. In Figure 4.2(c), it can be first observed that the blade element shows a tangential velocity component which is almost identical to the steady-state case B. This occurs because u' is usually negligible compared to the kinematic contribution $nr\pi/30$. On the contrary, v' is of the same order of magnitude as V_∞ and usually one order of magnitude greater than u'. Its variation consequently has a non-negligible effect on the vector composition of W. The axial induced velocity v'_C will be between v'_A and v'_B, with $v'_A < v'_B$. In particular, v'_C is expected to be closer to v'_A in rapid accelerations, and conversely closer to v'_B in

quasi-steady or slow maneuvers. The vector composition of the axial and tangential velocities, in the dynamic case, leads on one hand to a slight reduction in the relative velocity W_C, but on the other hand to a more relevant increase in α. The increase in α outweighs the decrease in relative velocity, thereby leading to an overall increase in both thrust and torque. Similar considerations can be made for a deceleration maneuver, where the angle of attack decreases compared to the equivalent steady-state case, and consequently, both thrust and torque result in being lower.

The wake topology downstream of the propeller is also modified due to the acceleration maneuver. The flow field tends to adapt to the instantaneous rotational speed of the propeller during the maneuver, and consequently, as the rpm increase, the wake becomes narrower, with the main vortical structures getting closer to the propeller axis. This is due to a dynamic shift from a high efficiency operative condition to a lower efficiency one, as V_∞ is kept fixed. For high rpm variation rates, this topological modification of the wake occurs in a few propeller revolutions, and adjacent vortices can display very different trajectories and strengths. At small inflow velocities, this can anticipate or delay the interaction between vortices and consequently affect the transition to turbulence of the wake. Conversely, at high inflow velocities, the vortices are more widely spaced in the axial direction, and their interaction is rarely observable in the vicinity of the propeller, even at high rpm rates. However, the evolution of the wake still shows a lag, which is particularly evident in the axial velocity component and affects the propeller's performance.

Thrust variation due to the lag effect The relation between the induced velocity lag in dynamic rpm variation maneuvers and the variation of thrust is now explored in detail. As anticipated, the wake lag effect mainly leads to a variation of the angle of attack α and relative velocity W seen by the blades' elements, consequently affecting the propeller's loads. The thrust is shown to be particularly influenced by the variation of the angle of attack, which overcomes the contribution due to the variation of relative velocity, and leads to an increase in thrust in acceleration and a decrease in deceleration.

In particular, let's focus on the isolated blade element illustrated in Figure 4.3, positioned at a distance r from the propeller's hub. The effect of the dynamic maneuver is assumed to be primarily related to the plane containing the blade elements, which is perpendicular to the radial direction. For an isolated blade element, dT is obtained through Eq. 4.1. Since the airfoil is aerodynamically efficient, the drag contribution can be neglected compared to the lift contribution in the first approximation. The elementary thrust can hence be written as in Eq. 4.2.

$$dT = dLcos(\beta - \alpha) - dDsin(\beta - \alpha) \tag{4.1}$$

$$dT \approx dLcos(\beta - \alpha) = \frac{1}{2}\rho c c_L W^2 (\beta - \alpha) \tag{4.2}$$

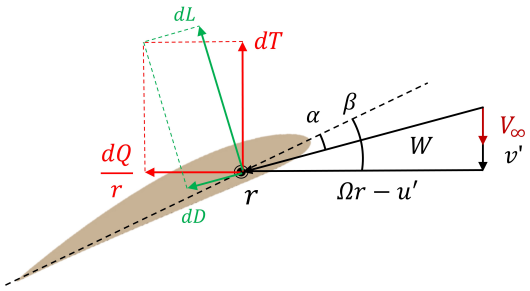

Fig. 4.3 Schematic representation of a blade element at a distance r from the propeller's hub.

c_L can be approximated as a linear function of α for low angles of attack as $c_L \approx c'_L \alpha$, where c'_L is a positive constant parameter. This approximation is mostly suitable for higher Re_c regimes, particularly for larger propellers than the one treated in the present work. However, the purpose is to obtain a general formulation, which establishes a qualitative trend of the thrust as a generic propeller is accelerated or decelerated in axial inflow conditions. As represented in Figure 4.3, α and W^2 can be written as functions of the tangential and axial velocity components as in Eq. 4.3. The ratio between the axial velocity component $(V_\infty + v')$ and the tangential component $(\Omega r - u')$ is denominated λ_v. The elementary thrust can therefore be written in Eq. 4.4. The non-dimensional quantity λ_v includes the two induced velocity components u' and v', which are subject to a lag effect in a dynamic rpm variation maneuver. Nevertheless, u' is usually around one order of magnitude smaller than v' and than Ωr. Therefore, in this context, λ_v is assumed to only vary with v'. The remaining quantities are assumed to be positive and constant and can therefore be gathered in a single quantity $k_{cost} = \frac{1}{2}\rho c c'_L (\Omega r - u')^2$, as written in Eq. 4.5.

$$dT = \frac{1}{2}\rho c c'_L \left(\beta - atan\left(\frac{V_\infty + v'}{\Omega r - u'}\right)\right)\left((V_\infty + v')^2 + (\Omega r - u')^2\right) cos\left(atan\left(\frac{V_\infty + v'}{\Omega r - u'}\right)\right) \tag{4.3}$$

$$dT = \frac{1}{2}\rho c c'_L \left(\beta - atan\left(\lambda_v\right)\right)\left(\lambda_v^2 + 1\right)(\Omega r - u')^2 cos(atan(\lambda_v)) \tag{4.4}$$

$$dT = k_{cost}\left(\beta - atan\left(\lambda_v\right)\right) \cdot \left(\lambda_v^2 + 1\right) \cdot cos(atan(\lambda_v)) \tag{4.5}$$

The non-dimensional elementary thrust $dT_n = dT/k_{cost}$ is displayed as a function of λ_v in Figure 4.4 for different values of β. In particular, this latter parameter is varied between 0° and 60° to account for a wide range of twist angles, considering both low- and high-pitch propellers. λ_v is instead varied from 0 to 1, to cover an extensive range of possible operative conditions.

Regardless of the considered β angle, dT_n results in being a monotonically decreasing function of λ_v, featuring an almost linear trend. As β is increased, the curves are translated towards greater dT_n values, without significant slope variations. Despite the thrust-increasing contribution of the term $\left(\lambda_v^2 + 1\right)$ due to W^2, the two remaining terms related to α dominate in the analysed range, leading to a

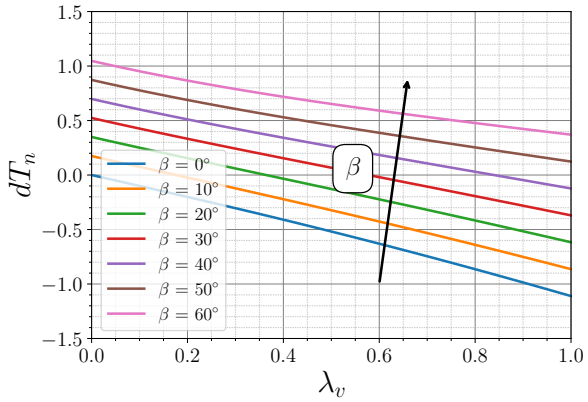

Fig. 4.4 Non-dimensional elementary thrust dT_n as a function of λ_v for different values of β.

monotonically decreasing trend. Small decreases of λ_v are representative of an acceleration maneuver, as v' appears lower than in the steady-state case. Regardless of the blade element considered and of its associated β angle, an increased elementary thrust is observed compared to the steady-state condition, leading to an overall increased integral thrust. The opposite behaviour is observed in deceleration, where λ_v is instead increased, leading to a lower thrust value. A similar handling could be carried out for the elementary torque, but it is avoided for the sake of conciseness. In addition, both elementary drag and lift contributions should be taken into account, leading to the necessity of additional assumptions on the free parameters.

4.1.1 Implementation of the maneuver in VPM and simulations matrix

The dynamic variation of rpm is performed by updating the value of n at each iteration, based on the type and rapidity of the maneuver. In the present work, a simple ramp is considered, corresponding to a linear function of n over time. Different ramps might be more representative of a real rpm variation maneuver, but the scope of the present work is to highlight the differences compared to a steady-state case. The rpm are thus updated at each time t_i to n_i as in Eq. 4.6. The subscript "$Start$" refers to the start of the maneuver, and, for the current simulations matrix, n_{Start} was set to 3,000 rpm for the acceleration and to 7,000 rpm for the deceleration. t_{Start} was chosen to perform around 80 revolutions, reaching a converged steady-state before the start of the maneuver. The value of t_{Start} was consequently chosen around 1.5 s for the acceleration and 1 s for the deceleration maneuvers. The rpm value reached at the end of the maneuvers is indicated with n_{End}, and it was set to 7,000 rpm for the acceleration and to 3,000 rpm for the deceleration. Finally, t_r refers to the time needed to perform the maneuvers. To maintain a constant $\Delta\psi$ equal to 5 degrees throughout the simulations, it is also necessary to update the value of Δt at each iteration. Since it is calculated as $\Delta t = \Delta\psi/(6n)$, it must be updated accordingly with n. In this way, particles are homogeneously shed throughout the propeller's revolution, even if the propeller changes its rotational speed.

$$n_i = n_{Start} + \frac{n_{End} - n_{Start}}{t_r} \cdot (t_i - t_{Start}) \tag{4.6}$$

Multiple simulations were performed with a fixed value of V_∞ = 3 m/s. Three values of t_r are taken into account for the acceleration and deceleration maneuvers, leading to a comparison among three different ramp rates m_r, a quantity that hereby represents the intensity of a linear ramp and is defined as $m_r = \frac{n_{end} - n_{start}}{t_r}$. The ramp rates considered in the present work are: 4,000 rpm/s, 40,000 rpm/s, and 80,000 rpm/s. The results are then compared with steady-state cases, simulated between 3,000 and 7,000 rpm with increments of 500 rpm, in terms of the aerodynamic performance and instantaneous velocity and vorticity fields. The vorticity field is furthermore used in conjunction with the Q-criterion [102] field to investigate the wake topology, particularly characterizing the evolution of the tip vortices.

The acceleration maneuver with m_r = 80,000 rpm/s is furthermore repeated 100 times to obtain the averaged velocity field at mid-maneuver, i.e., at 5,000 rpm. The simulations are carried out considering a random initial azimuthal angle ψ, to avoid phase-locking. The averaged velocity field is then compared with the time-averaged velocity fields evaluated in steady-state conditions at 3,000 and 5,000 rpm. To assess the convergence of the mean flow field in the dynamic case, the relative L^2 norm is evaluated. The norm is calculated every 10 repetitions as in equation 4.7, where $\overline{V}_{z_i}$ is the mean velocity field evaluated after i repetitions and $\overline{V}_{z_{100}}$ is the mean velocity field evaluated after 100 repetitions.

$$L_i^2 = \frac{||\overline{V}_{z_i} - \overline{V}_{z_{100}}||_2}{||\overline{V}_{z_{100}}||_2} \tag{4.7}$$

The effect of the axial inflow on the flow field stemming from the dynamic maneuver is finally investigated, keeping a constant value of m_r = 80,000 rpm/s and varying the inflow velocity to V_∞ = 1.5 m/s and V_∞ = 4.5 m/s.

4.1.2 Results

In this section, the results obtained from the VPM simulations are shown. The primary goal is to analyse the effect of a linear rpm ramp over time at a fixed axial inflow velocity of V_∞ = 3 m/s. To this end, a specific focus is paid to the integral quantities such as the thrust C_T and the torque C_Q coefficients, investigating the causes behind the differences between dynamic and steady-state cases.

Aerodynamic performance

The effect of the dynamic variation of rpm is primarily noticeable on the integral thrust and torque. The non-dimensional coefficients C_T and C_Q are shown as a function of n in Figure 4.5. The acceleration

and deceleration maneuvers are represented with solid and dashed lines, while a different colour is used to highlight each case's ramp rate m_r. The integral values obtained in steady-state conditions are superimposed on the dynamic cases for a quantitative comparison. Both acceleration and deceleration maneuvers are performed by starting from a converged steady-state operative condition; therefore, they show initial thrust and torque values that are equivalent to the values obtained in the static cases. As the ramp rate is increased, C_T and C_Q start to deviate from the steady-state values. In particular, during acceleration, both thrust and torque increase with the ramp rate, while in deceleration, they decrease with the m_r. The maneuver featured by m_r = 4,000 rpm/s is almost superimposed on the steady-state cases, with relative differences of δC_T and δC_Q below 1%. The intermediate ramp with m_r = 40,000 rpm/s already shows marked relative deviations, with a maximum of around 4% deviation at 4,000 rpm in acceleration and 5% at 3,000 rpm in deceleration compared to the steady-state cases. Ultimately, the most intense ramp with m_r = 80,000 rpm/s displays deviations around 10% in both acceleration and deceleration.

The acceleration and deceleration maneuvers are similar in terms of relative deviations compared to the steady-state cases. However, there is a remarkable difference at the end of the maneuver between the two. Since the ramp rate is constant throughout the entire maneuver to ensure a linear variation of rpm over time, the dynamic effect on the propeller's performance will be greater when the ratio between m_r and the instantaneous rpm is also greater. This entails that the effect of both maneuvers will be greater at 3,000 rpm. On one hand, the acceleration maneuvers are constrained to start at 3,000 rpm with C_T and C_Q values which equal the steady-state values, but then suddenly show a significant increase at the start of the maneuver, with maximum differences located around n = 4,000 rpm. Subsequently, towards the end of the maneuver at n_{End} = 7,000 rpm, the differences with the steady-state values decrease, and the dynamic curves appear almost superimposed on the steady-state values. On the contrary, during the deceleration, the differences with the steady-state cases are smaller at the beginning of the maneuver (n_{Start} = 7,000 rpm) and increase as n decreases throughout the maneuver, reaching the greatest relative deviations at the end of the maneuver (n_{End} = 3,000 rpm). This significantly affects the propeller's stability, which undergoes an rpm variation maneuver. Considering a constant ramp rate over time, the acceleration ensures a final condition that is more similar to a steady-state case, while in deceleration, the effect of the maneuver is amplified as the ending rpm decreases, leading to C_T and C_Q values that are far from the steady-state case values. This suggests the inefficiency of a constant m_r ramp, most likely not optimal to perform rpm variation maneuvers.

To investigate in detail the reasons behind the observed trends in the integral quantities, the focus is now shifted to the distribution of thrust per unit length along the blade span. Such quantity is only analysed at mid-maneuver, i.e., at n = 5,000 rpm, for both the acceleration and the deceleration, since qualitatively similar conclusions can be drawn at different n values. In a first instance, the non-dimensional thrust per unit length (s_{C_T}) along the blade span is displayed in Figure 4.6. The s_{C_T} distribution shows the same trend observed for the integral thrust, deviating from the values of the

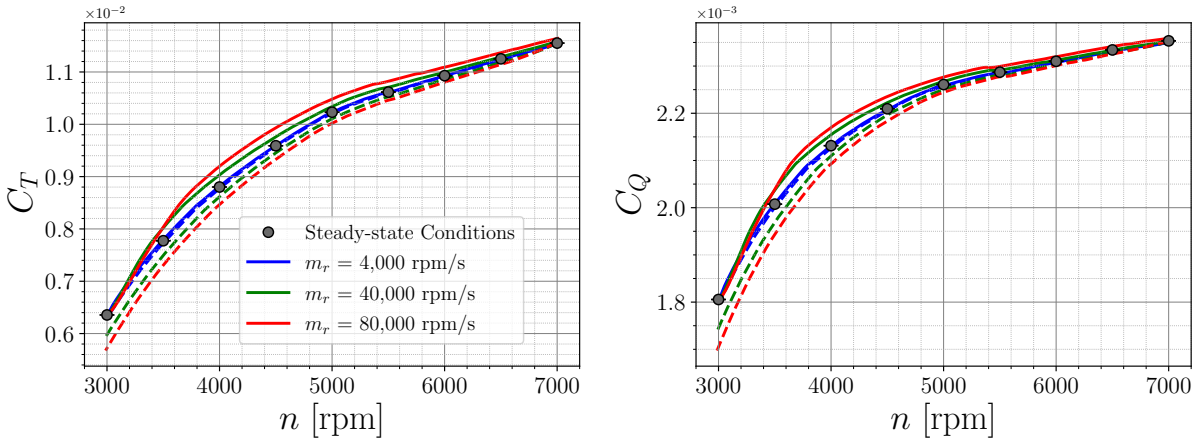

Fig. 4.5 Comparison of C_T and C_Q as a function of n between dynamic maneuvers and steady-state conditions. Solid lines correspond to the acceleration maneuver, while dashed lines indicate the deceleration maneuver.

steady-state case as the ramp rate is increased at almost all radial coordinates. The most significant differences for both acceleration and deceleration are observable between $r/R = 0.5$ and $r/R = 0.9$.

The thrust generated by each element of the lifting line can be approximated as the lift of that element, depending in turn on parameters such as the magnitude of the relative velocity squared W^2 and the angle of attack α. The variation in thrust and torque compared to the steady-state case is hence mostly attributable to the variation of these two quantities. The radial distributions of relative differences of W^2 and α compared to the steady-state case, also extracted at 5,000 rpm, are displayed in Figure 4.6.

The relative differences observed for W^2 result in being small, even considering the fastest maneuver, being below 1% for $r/R > 0.4$, where the blade shows the greatest contribution to the overall thrust. The greatest δW^2 are obtained for $r/R < 0.4$, reaching a maximum of around 2.8% at $r/R = 0.2$. However, in such a region, the blades almost negligibly contribute to the overall thrust. Although the relative velocity decreases in acceleration and increases in deceleration, its deviation from the steady-state case does not represent the main contribution to the variation in the integral thrust and torque values. In particular, the variation of α plays a leading role, showing more significant deviations along the blade span.

Although the highest $\delta\alpha$ values are located close to the hub, significant relative deviations are registered even in the most load-bearing portion of the blade ($r/R > 0.6$). Such quantity furthermore appears to increase as the ramp rate is increased in acceleration and to decrease in deceleration, leading to the variations of integral thrust and torque observed in Figure 4.5. The two quantities, W^2 and α, therefore contribute in opposition to the performance trends, with the variation of the former being negligible or at least overcome by the latter.

It should also be noted that, although the quantities are extracted at the same rpm at mid-maneuver for both acceleration and deceleration, the δ values are not symmetrical for the two maneuvers. In the acceleration, the maximum deviation from the steady-state case has indeed just been reached at lower rpm, around n = 4,000 rpm. For this reason, slightly greater deviations are observed at high r/R in both α and W^2 (although not visible at this scale). On the contrary, in deceleration, the maximum deviation from the steady-state case has yet to occur, and the δ values are smaller. These considerations highlight the presence of a hysteresis effect between acceleration and deceleration maneuvers.

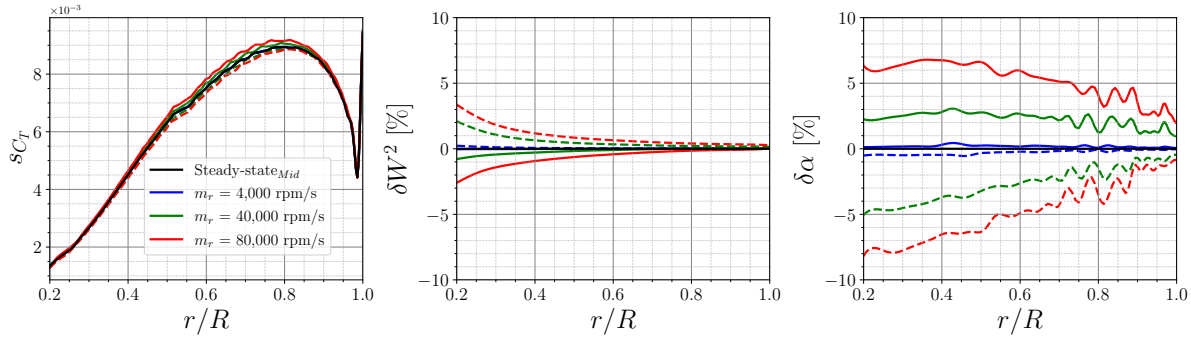

Fig. 4.6 Thrust per unit-length s_{C_T} as a function of r/R at mid-maneuver (n = 5,000 rpm). Solid lines correspond to the acceleration maneuver, while dashed lines indicate the deceleration maneuver.

As anticipated, the differences between steady-state and dynamic cases can be essentially attributed to the lag effect in the induced velocity in the wake. The velocity can be decomposed into a tangential (u') and an axial (v') component. The variation of u' and v' is thus responsible for the variation of α and W^2, consequently affecting the overall performance of the propeller. Again, at mid-maneuver (n = 5,000 rpm), the distributions of $|u'|$ and $|v'|$ along the blade span are extracted and displayed in Figure 4.7, comparing the dynamic cases in acceleration and deceleration with the steady-state case. The two quantities are normalized with respect to ΩR, where Ω is calculated as $\Omega = \frac{n\pi}{30}$, considering n = 5,000 rpm.

The two induced velocities show a significant relative difference compared to their steady-state values. In particular, $|u'|$ increases during acceleration and decreases during deceleration, while $|v'|$ follows the opposite trend. u' is usually slightly underestimated in VPM models that feature a lifting line approach, as the vorticity shed by the boundary layer is not modelled. Since the particles are shed from the blades' trailing edges in the tangential direction, they cannot induce a velocity on the same axis, and, as a consequence, the contribution to the value of u' of the earlier age particles is reduced due to their relative position in the computational domain. Notwithstanding that, u' results in being almost one order of magnitude smaller than $|v'|$ and results in being up to two orders of magnitude smaller than Ωr, which is why it is often neglected in preliminary or approximate calculations [27]. As a consequence, even if the relative variation of the induced velocities is similar, the influence of v' prevails, while the effect of u' can be neglected. The decrease of v' in absolute value during

acceleration and increase during deceleration, respectively, lead to an increase and a decrease in α. On the other hand, W^2 follows the opposite trend, decreasing as v' decreases and increasing as v' increases. In this context, the relative velocity W is composed of a significant, but almost invariant, tangential component ($\Omega r - u'$) and an axial component ($V_\infty + v'$) that, despite being smaller, implies non-negligible variations in dynamic conditions. The effect of the variation of α with v' overcomes the effect of the variation of W^2, leading to increasing loads in the acceleration and decreasing loads in the deceleration.

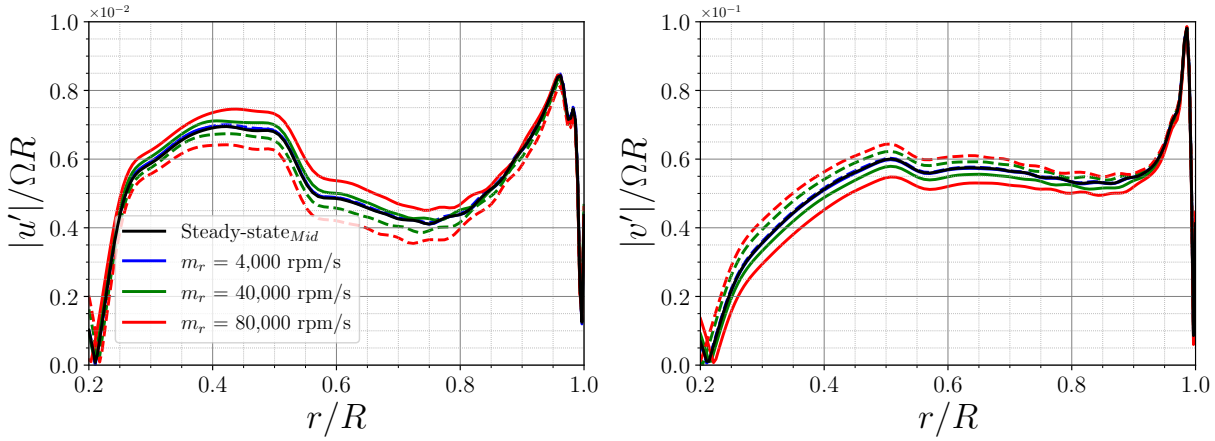

Fig. 4.7 Induced velocities $|u'|$ and $|v'|$ distributions as a function of r/R at mid-maneuver (n = 5,000 rpm). Solid lines correspond to the acceleration maneuver, while dashed lines indicate the deceleration maneuver.

This conclusion can be generalized to other different propellers in axial inflow, even at different rpm, as the tangential velocity component is often much larger than the axial one, especially in the outboard and more load-bearing portion of the blades.

Induced wake instantaneous flow features

In the present section, the main features of the flow field induced in the wake by the different maneuvers are investigated and compared to the steady-state cases. The flow field is extracted on a $x-z$ plane, where, at the shown flow field plane, x corresponds to the axis oriented toward the propeller's radial direction, and z is the axis oriented toward the propeller's rotation axis.

The flow fields are initially displayed in terms of instantaneous axial velocity along the z axis (V_z), again extracting the velocity fields at mid-maneuver with n = 5,000 rpm. The dynamic maneuvers are performed to be phase-locked at n = 5,000 rpm, so the extracted flow fields display the propeller with its blades oriented towards the x axis at the same azimuthal angle ψ. The steady-state flow fields at n = 5,000 rpm are reported for the sake of comparison, namely, steady-state$_{Mid}$ cases. The steady-state flow fields at n = 3,000 rpm in acceleration and n = 7,000 rpm in deceleration are additionally displayed,

namely steady-state$_{Start}$ cases. In this fashion, it is possible to compare the flow features of the dynamic cases with the flow features before the start of the maneuvers. The instantaneous axial velocity fields are displayed in Figure 4.8 in non-dimensional form. For the sake of consistency, the quantity ΩR, used for the normalization, is calculated by taking n = 5,000 rpm even for the steady-state$_{Start}$ cases.

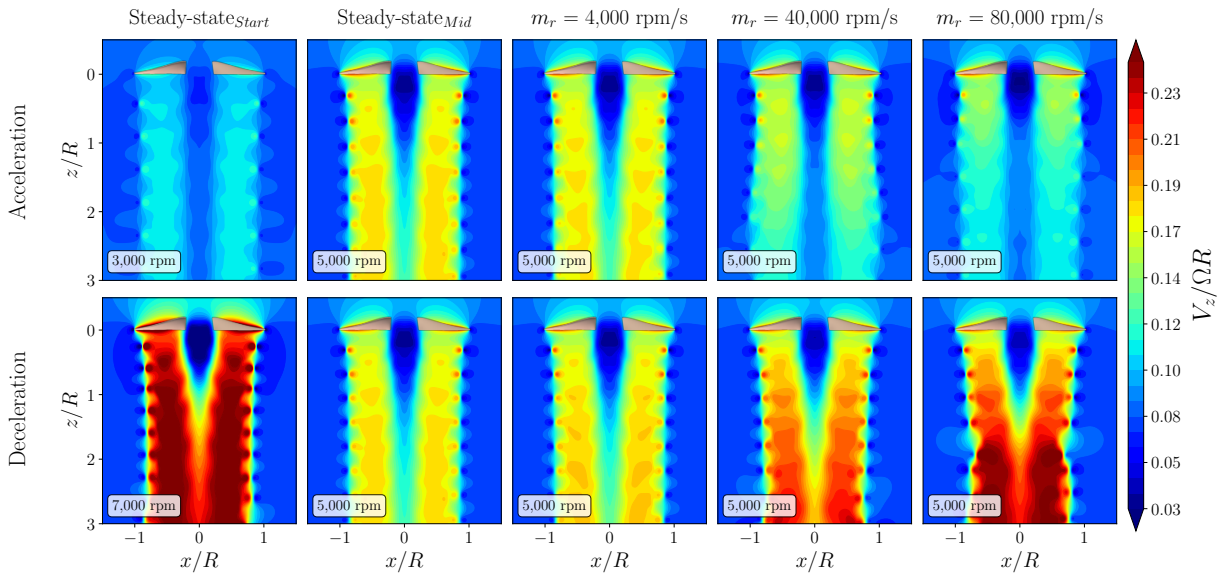

Fig. 4.8 Colourmaps of the normalized instantaneous axial velocity $V_z/\Omega R$ for the dynamic and steady-state cases. The propeller-shaped mask is added to improve the clarity.

The induced flow field resembles the steady-state case carried out at 5,000 rpm in terms of axial velocity values and radial extension of the wake as m_r is lower. The dynamic case featured by m_r = 4,000 rpm/s indeed displays V_z values which are very close to the steady-state$_{Mid}$ case, both in acceleration, where there is a slight underestimation, and in deceleration, where the opposite occurs. At higher ramp rates, a radical change in the wake structure is observed. In particular, a decrease in V_z is noticeable in acceleration while there is an increase in deceleration, approaching the values of the steady-state$_{Start}$ case, especially at high z/R values. Focusing on the acceleration maneuver, the wake widens in the radial direction as m_r is increased. At 3,000 rpm, which represents the starting point for the maneuver, the propeller operates in conditions of high efficiency, displaying a radially wider and therefore more cylindrical-shaped flow tube. Throughout the acceleration, the wake at high z/R shows similar features to those that can be observed also at the beginning of the maneuver at 3,000 rpm, both in terms of V_z values and radial extension. The wake velocity varies significantly in the z direction, leading to a significant axial velocity gradient which also increases as m_r is increased.

Similar considerations can be made for the deceleration maneuver, where the wake corresponding to the steady-state$_{Start}$ case instead displays higher axial velocities and a decreased radial extent. The propeller here operates at lower efficiency, being characterized by n = 7,000 rpm at the same inflow speed. In the deceleration maneuver at m_r = 80,000 rpm/s, the propeller takes about 2.5 revolutions to slow down from n_{Start} = 7,000 rpm to 5,000 rpm. As the propeller is two-bladed, 5 pairs of symmetric

tip vortices are generated in this period in the investigated plane, identifiable by pseudo-circular zones of high axial velocity in the wake adjacent to zones of negative velocity immediately outside the wake. After the fifth pair of tip vortices, located around $z/R = 1.6$, the structure of the flow field is quite similar to that before the start of the maneuver. Despite this portion of the wake being induced under steady-state conditions, it is still affected by the deceleration maneuver, and, locally, the wake velocity is slightly lower at the same z/R compared to the steady-state case.

The different dynamic cases are now compared in terms of the instantaneous vorticity component along the y axis (ω_y). The relative colourmaps are displayed in Figure 4.9 with a similar arrangement to that of Figure 4.8, to compare the dynamic cases with the steady-state cases at the start of the maneuver (steady-state$_{Start}$) and at mid-maneuver (steady-state$_{Mid}$). The vorticity ω_y is normalized with Ω, again evaluated at $n = 5{,}000$ rpm. Figure 4.9 displays the colourmap of the y axis aligned vorticity component, indicating in red (blue) $\omega_y > 0$ ($\omega_y < 0$). A blanking is applied to the colourmap for values of ω_y near zero.

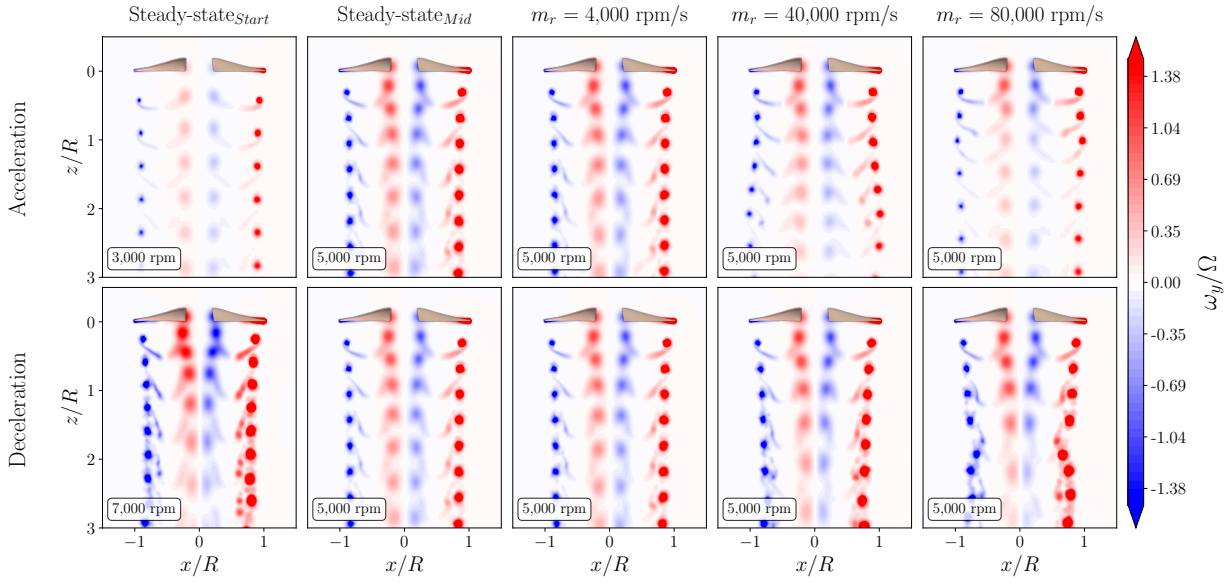

Fig. 4.9 Colourmaps of the normalized out-of-plane vorticity ω_y/Ω for the dynamic and steady-state cases. The propeller-shaped mask is added to improve the clarity.

In each of the displayed cases, two main pairs of vortical structures evolve in the axial direction and are symmetric with respect to the z axis. The first and strongest pair of structures is composed of the tip vortices, with positive vorticity at $x > 0$ and negative at $x < 0$, according to the propeller's rotation direction. The root vortices, on the other hand, are characterized by lower ω_y than the tip vortices shed from the same blades and also an opposite rotation direction. At a ramp rate of $m_r = 4{,}000$ rpm/s, the vortex structures are similar in terms of vorticity values and position to the steady-state$_{Mid}$ cases in both acceleration and deceleration. By increasing the ramp rate, the structures located at high z/R values show a lower ω_y value, and the wake structure instead resembles more the steady-state case at the beginning of the maneuver, corresponding to 3,000 rpm in acceleration and 7,000 rpm in deceleration.

The ω_y fields can be used along with the Q-criterion fields to quantitatively characterize the evolution of the tip vortices. The Q-criterion fields in the plane $x-z$, not shown for the sake of conciseness, indeed allow to identify the regions of the flow field where the rotation prevails over the shear (Q>0) [103].

The trajectory of the tip vortices can be investigated by applying a vortex identification approach, such as the Q-criterion. In this case, a value of Q>0 and equal to 20% of the maximum value recorded in the steady-state case at 5,000 rpm is selected for the identification of the tip vortices. The location of the maximum value of Q is associated with the vortex center. The vorticity ω_y is then integrated over the vortex area according to the Stokes theorem to evaluate its circulation.

The choice of a different threshold to identify the tip vortex is arbitrary and might affect the evaluated vortex circulation. However, in the light of a comparative assessment between the investigated cases, we deem it sufficient to select the same threshold for all cases.

The comparison between the dynamic and steady-state cases in acceleration and deceleration is shown in Figure 4.10 in terms of the vortices' trajectory and circulation Γ_v. The analysis of these structures is also useful to understand how the wake evolves in terms of axial and radial stretching. Due to the symmetry property of the wake, the vortices generated by the blade positioned at $x/R > 0$ are exclusively shown.

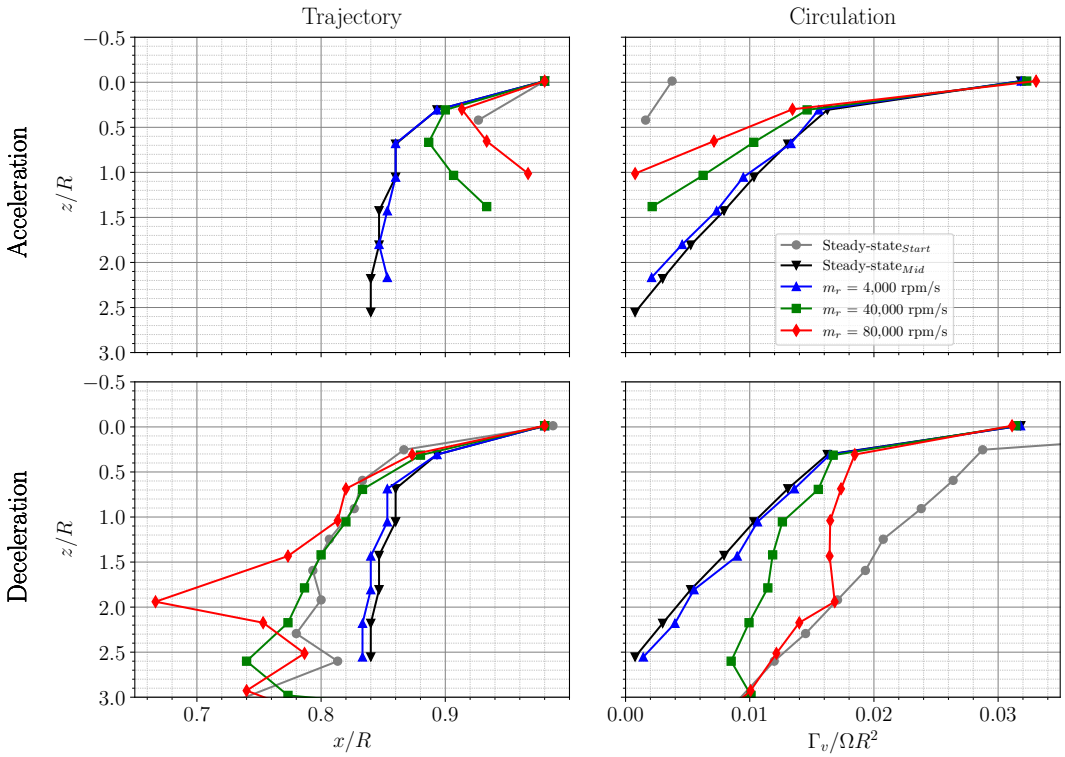

Fig. 4.10 Tip vortex trajectory and circulation for the steady-state and dynamic cases.

Opposite trends can be immediately detected during the acceleration and deceleration maneuvers, both in terms of trajectory and vortex circulation. The tip vortices of the steady-state$_{Mid}$ case are initially identified at $x/R = 0.98$ and then advected inboard, stabilizing around $x/R = 0.85$ for $z/R > 0.7$. In all the analysed cases, the first vortex shows a significantly higher Γ_v value than the vortices at greater axial distances. From the second vortex on, the circulation decreases almost linearly as z/R increases, reaching almost zero for the last identified vortex, located at $z/R = 2.55$. For higher z/R, the Q value is not high enough to overcome the chosen threshold, as the vortices in this region become too weak and eventually break down due to the lower convective velocity of the wake and the shear forces caused by the entrainment of the external flow.

Focusing now on the dynamic acceleration maneuvers, fewer vortices are identified in the wake region than in the steady-state$_{Mid}$ case. Moreover, the vortices are arranged at higher radial coordinates as m_r increases, suggesting that the wake is wider than in the steady-state case. At the same time, the circulation is lower and tends to zero for lower axial coordinates z/R. The inboard shift of the vortices' evolution with increasing values of m_r suggests that the wake is shrunk in the axial direction.

Focusing instead on the deceleration maneuver, an opposite trend is observed. As m_r increases, the tip vortices appear displaced at lower radial coordinates, indicating that the wake is shrunk in the radial direction. At the same time, the circulation increases as the ramp rate increases, and it is particularly interesting to observe that, at m_r = 80,000 rpm/s, the circulation results in being very similar to the steady-state case at the beginning of the maneuver for $z/R > 2$. At such large m_r values, 2.5 revolutions are needed to decelerate from 7,000 rpm to 5,000 rpm; therefore, 5 tip vortices are shed in the analysed plane. The sixth identified vortex located at $z/R = 2$ was shed when the propeller was still rotating at 3,000 rpm before starting the maneuver, showing indeed a circulation which resembles the value obtained for the same vortex in the steady-state$_{Start}$ case.

In conclusion, a further consideration must be added for the highest m_r value in deceleration. An isolated vortex located at $z/R = 1.95$ undergoes a sudden displacement towards lower x/R, deviating from the trajectory followed by the other vortex. This deviation is most likely due to the transition from the steady-state operative condition to the start of the dynamic maneuver. The start of the maneuver generates an instantaneous change in the flow pattern that almost suddenly modifies the radial and axial structure of the wake. Therefore, in the deceleration, the first vortex shed at the beginning of the maneuver is advected more outboard than the one generated before, and their mutual interaction will cause this localized phenomenon. This can favour vortex interactions, leading to the breakdown and an anticipated transition to a wake turbulent state. This phenomenon can be particularly relevant at large rpm values, where the vortex structures are more intense and closer to each other.

Time-Averaged flow topology

In the present section, the main differences in the averaged velocity fields between the steady-state cases and the dynamic acceleration case with m_r = 80,000 rpm/s are explored in detail. To assess the convergence of the averaged dynamic velocity field at mid-maneuver, the relative L^2 norm is calculated according to equation 4.7. Such quantity is displayed as a function of the simulation repetitions used for the averaging of the velocity field in Figure 4.11.

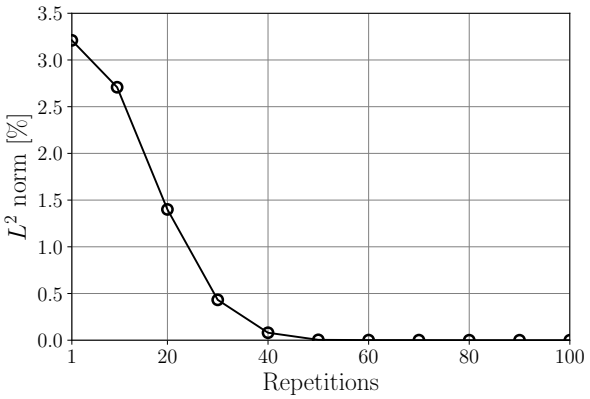

Fig. 4.11 Relative L^2 norm as a function of the repetitions used for the velocity field averaging in dynamic conditions.

The relative L^2 norm trend suggests that the velocity field reaches an almost converged state after having averaged over at least 50 repetitions, where the relative L^2 norm reaches a value of 0.02%. Thus, by increasing the number of repetitions, the averaged flow field does not appear to be significantly affected.

The averaged velocity field obtained after averaging over 100 simulation repetitions is compared with the time-averaged steady-state velocity fields at 3,000 rpm (steady-state$_{Start}$) and at 5,000 rpm (steady-state$_{Mid}$), obtained by averaging over the last 10 revolutions. The colourmaps of the axial velocity fields are displayed in Figure 4.12, along with the axial velocity profiles extracted at z/R = -0.25, 1, and 2. The quantity ΩR, used for the normalization, is calculated again by taking n = 5,000 rpm as a reference for all the flow fields.

The averaged velocity field evaluated in dynamic conditions shows peculiar features already observed in the instantaneous flow features. In particular, a strong velocity gradient is observed in the z direction due to the dynamic evolution of the wake in time. The velocity field close to the propeller appears close to the steady-state$_{Mid}$, as noticeable from the velocity profiles. At z/R = -0.25, the dynamic velocity values approximately overlap with the steady-state$_{Mid}$ case, while the steady-state$_{Start}$ case shows significantly lower axial velocity. Moving towards greater z/R coordinates, the axial velocity in the dynamic case appears smaller than in the steady-state$_{Mid}$ case, approaching the values obtained at the start of the maneuver. Already at z/R = 1, the dynamic case's wake appears wider in

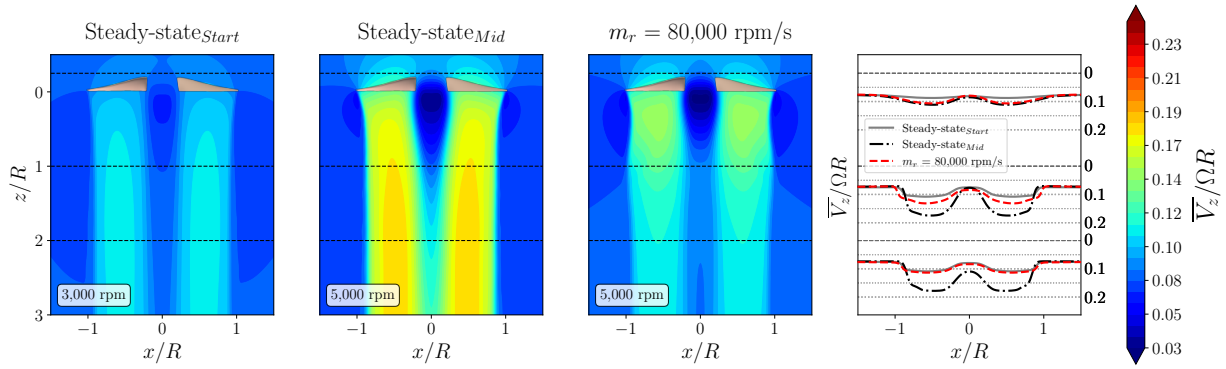

Fig. 4.12 Colourmaps of the normalized averaged axial velocity $\overline{V}_z/\Omega R$ of dynamic and steady-state cases, along with velocity profiles extracted at z/R = -0.25, 1, and 2 (indicated with the black dashed lines in the colourmaps). The propeller-shaped mask is added to improve the clarity.

the radial direction than in the two steady-state cases. At z/R = 2, the axial velocity profiles of the dynamic case and the steady-state$_{Start}$ are instead almost completely superimposed.

Influence of the axial inflow on the propeller performance

In this section, the influence of the axial inflow velocity V_∞ value on the acceleration maneuver is investigated. Specifically, the steady-state cases and the acceleration maneuver with the highest ramp rate (m_r = 80,000 rpm/s) were repeated at two additional values of V_∞ = 1.5 m/s and 4.5 m/s. The observed differences between steady-state and dynamic cases are very similar to those described in previous sections for V_∞ = 3 m/s. In particular, an increase in thrust and torque compared to the steady-state cases is observed, with the difference between the two operating conditions being greater at low rpm.

However, it is interesting to focus on the comparison in terms of absolute differences between the dynamic and steady-state integral loads as V_∞ is varied. The non-dimensional thrust and torque absolute differences between the dynamic and steady-state cases ΔC_T and ΔC_Q are shown in Figure 4.13. These absolute differences are evaluated exclusively at the points where steady-state cases are computed, i.e., between 3,000 and 7,000 rpm with increments of 500 rpm.

Both ΔC_T and ΔC_Q increase at almost every considered n value as V_∞ is augmented. Such a trend is mostly accounted for by the low Re_c range where the propeller is operating in the present work. In particular, $c_L - \alpha$ curves show a nearly-quadratic shape even at low angles of attack, where, for higher Re_c, the two quantities are instead usually linearly related [133]. The increase of V_∞ makes the blades operate at an overall reduced α, where the same difference in angle of attack between steady-state and dynamic conditions $\Delta\alpha$ leads to a greater Δc_L. In Figure 4.14, the distribution of α extracted at mid-maneuver (n = 5,000 rpm) is displayed as a function of r/R for different V_∞ values. Both steady-state and dynamic curves are significantly shifted downwards, as V_∞ is increased.

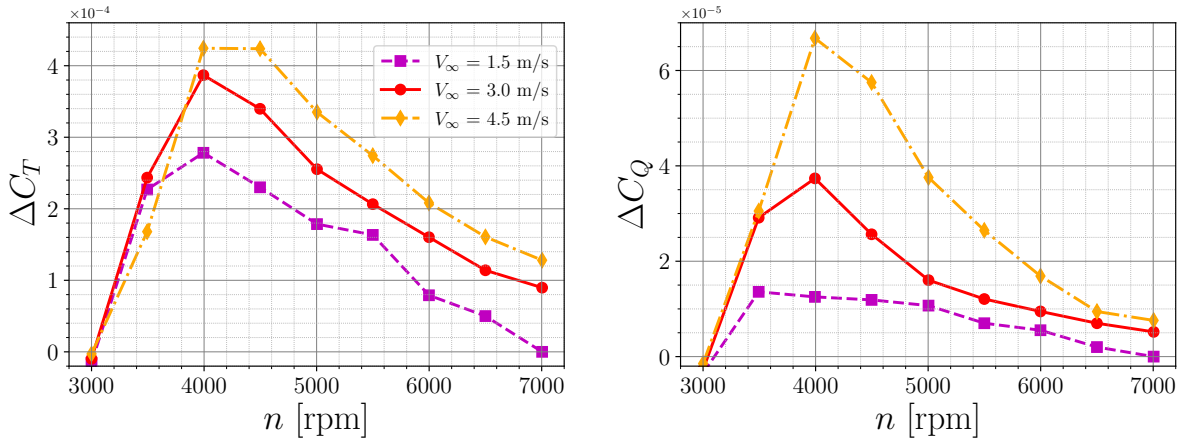

Fig. 4.13 Absolute C_T and C_Q differences between steady-state and dynamic cases with m_r = 80,000 rpm/s for different V_∞ values.

Notwithstanding that, the $\Delta\alpha$ between the steady-state and dynamic cases remains almost unchanged in the most load-bearing portion of the blades for $r/R > 0.6$, as shown in Figure 4.14. Being the $\Delta\alpha$ almost fixed among the different V_∞ values, a greater Δc_L is obtained at increasing V_∞, consequently leading to the increase in ΔC_T and ΔC_Q observed in Figure 4.13.

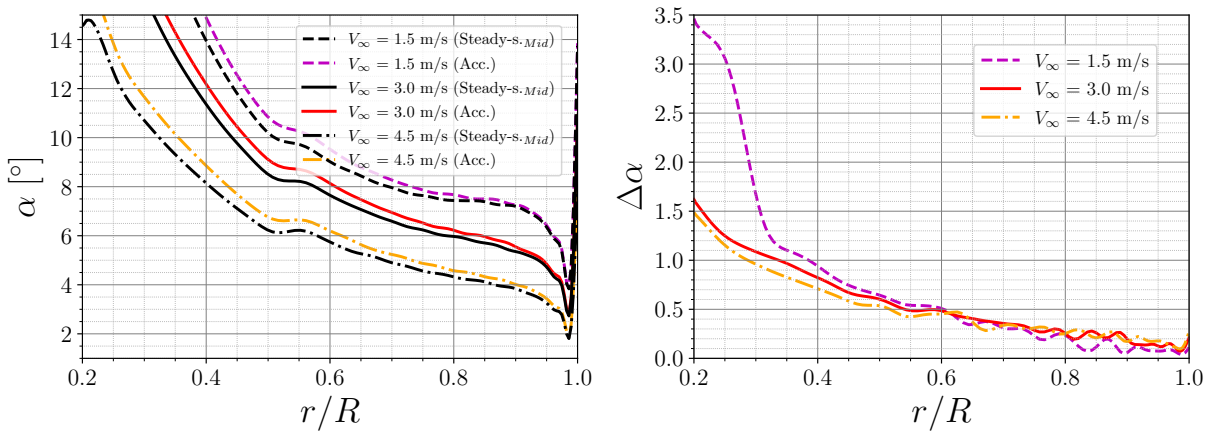

Fig. 4.14 Angle of attack α distribution as a function of r/R in dynamic and steady-state cases at mid-maneuver (n = 5,000 rpm) for different V_∞ values.

As anticipated, the pseudo-quadratic shape of the $c_L - \alpha$ curves is peculiar to most conventional airfoils at low Reynolds numbers [133] and, therefore, the results obtained in the present case are not easily generalizable to larger propellers. Already at Re_c = 50,000, for instance, a more canonical linear $c_L - \alpha$ trend is observed, followed by a bell-shaped behaviour near stall. Under such conditions, the trends observed in this work may no longer be valid.

What instead appears evident and independent of the Reynolds number is the increase in thrust and torque during acceleration and the opposite behaviour during deceleration. This effect appears significant across different values of axial inflow velocity and therefore both near and far from peak efficiency conditions.

4.1.3 Conclusions

The numerical campaign focused on acceleration and deceleration maneuvers performed at different ramp rates, linearly increasing or decreasing the rpm over time.

Key findings revealed that higher ramp rates cause the integral thrust and torque to significantly deviate from the corresponding steady-state values. At a fixed ramp rate, this effect is more significant at lower rpm. The observed increase in thrust and torque during acceleration and decrease during deceleration is mostly attributed to a lag in the induced flow field. The axial induced velocity component is particularly affected in dynamic conditions, affecting the blades' relative velocity mostly in terms of direction, rather than magnitude, and consequently leading to a variation of the aerodynamic loads. This lag effect is visible in both instantaneous and averaged flow fields. The wake adapts its topological structure to the rpm variation, leading to significant axial velocity gradients in the most rapid maneuvers. The far wake retains features that resemble the steady-state case features before the start of the maneuver, as dynamic rpm changes occur over just a few revolutions.

The effect of axial inflow velocity was also investigated. The quickest maneuver in acceleration was repeated for different axial inflow speeds. The results showed that the deviations from steady-state cases increase with the increase in the inflow velocity. This result is supposed to stem from low Reynolds number effects on the aerodynamic polars. At low Reynolds numbers, the $c_L(\alpha)$ curves indeed exhibit a pseudo-quadratic shape, leading to larger slopes at lower α ranges. Greater axial inflow velocities lead to lower blades' angle of attack, enhancing the load differences between steady-state and dynamic cases.

While the simple linear ramp considered in the present investigation might not be optimal in terms of propeller performance, it serves as a representative case for the investigation of rpm variation effects. More realistic maneuvers often follow more exponential-like ramps, featured by sharp initial changes followed by a slower stabilization. The main effects observed in this work, such as the induced velocity lag effect being proportional to the maneuver intensity, are likely extensible to even more complex scenarios and different inflow conditions.

When the propeller operates in axial inflow, it is found that the wake evolves with organized flow structures towards the axial direction, and so the instantaneous flow fields are generally sufficient for a preliminary analysis of the main trends. On the other hand, more complex maneuvers or different inflow conditions may require averaged fields for an accurate phenomenology assessment. However, the averaging operation is computationally expensive, as in maneuvers, unlike steady-state cases, it

is required to perform the full simulation and not just a few revolutions. Mid-fidelity methods, such as vortex particle methods, thus prove to be optimal tools, not requiring excessive computational resources. Moreover, the maneuvers' ease of implementation also enables the simulation of more complex maneuvers beyond simple ramps, enhancing applicability to more realistic scenarios.

4.2 Tilting maneuver

4.2.1 Implementation of the maneuver in VPM and simulations matrix

In the present study, the tilting maneuvers are performed through a rototranslation of the propeller along a circular trajectory with radius $L = 2R$ on the $x-z$ plane, and the centre positioned in the origin of the reference system $(x, y, z) = (0, 0, 0)$, as represented in Figure 4.15. The propeller is tilted between $\theta = 0°$ and $\theta = 30°$, with a tilting angular velocity $\dot{\theta}$. In the adopted reference system, at $\theta = 0°$ the propeller is displaced by a distance L on the x axis, while its rotation axis is aligned with the z axis. All the maneuvers are hence performed around the y axis, with the tilting angular velocity $\dot{\theta}$, therefore aligned with this latter. The maneuvers are performed at a fixed Ω, with $n = 5000$ rpm.

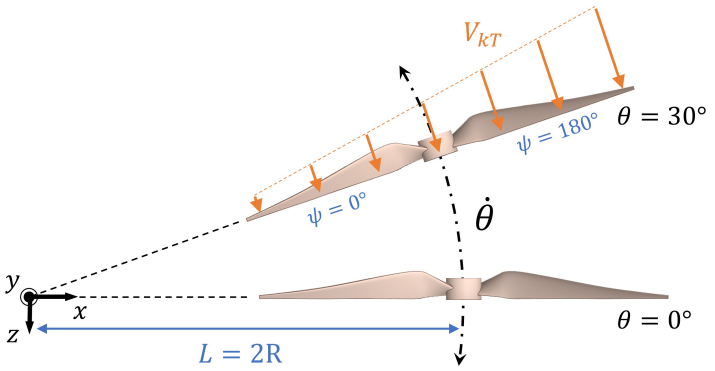

Fig. 4.15 Schematic illustration of the tilting maneuvers with reference system and relevant quantities.

In the VPM code, the tilting maneuvers are performed by updating the position of the propeller's rotation centre and the orientation of its rotation axis at each iteration. To simulate the effect of the propeller's motion along the tilting trajectory, the relative kinematic contribution V_{kT} is added to the lifting lines in the propeller's axial direction. V_{kT} is locally evaluated according to the instantaneous tilting angular velocity $\dot{\theta}$ and to the distance from the tilting centre. For a given $\dot{\theta}$, the dynamic effects are therefore more pronounced as the blades are positioned farther from the tilting centre. In Figure 4.15, the blade positioned at $\psi = 0°$ is therefore less affected by the dynamic tilting effects than the blade positioned at $\psi = 180°$. Throughout their revolution, the blades undergo intermediate conditions between these two extremes, which are hence representative of the least and most affected azimuthal positions.

Three different maneuvers are taken into account. Initially, the transition from hovering to forward flight is simulated, tilting the propeller from $\theta_{Start} = 0°$ to $\theta_{End} = 30°$. The same maneuver is then carried out with the presence of a background flow directed towards the z axis, with a velocity magnitude of $V_\infty = 3$ m/s, to simulate the tilting from a vertical climbing phase to forward flight. In conclusion, the tilting from a forward flight to hovering is finally simulated by tilting the propeller from $\theta_{Start} = 30°$ to $\theta_{End} = 0°$ and adding a transversal cross-flow towards the x axis. This choice is made under the assumption that the tilting maneuver occurs more rapidly than the forward flight deceleration.

For each of the three maneuvers, whose details are summarized in table 4.1, three different ramp rates $m_r = \dot{\theta}L$ values are considered, for a total of nine cases. Since L is kept fixed, m_r depends only on the tilting angular velocity $\dot{\theta}$, which is set to $\dot{\theta} = 30°/s$, $300°/s$ and $600°/s$ to investigate the dynamic effects at different ramp rates. The value of $\dot{\theta}$ is kept fixed throughout the tilting, consequently leading to a linear variation of θ over time. The simulations are initialized as steady-state cases carried out at θ_{Start} for a time of 1 s, approximately performing 83 revolutions to reach a converged state before starting the tilting maneuver.

Table 4.1 Overview of the considered dynamic tilting maneuvers.

Maneuver	$\theta_{\mathbf{Start}}$ [°]	$\theta_{\mathbf{End}}$ [°]	θ [°/s]	**L**	**Background flow** ($V_\infty/\Omega R$)
Hovering to forward flight	0	30	30, 300, 600	$2R$	-
Vertical climb to forward flight	0	30	30, 300, 600	$2R$	0.076 (z axis)
Forward flight to hovering	30	0	30, 300, 600	$2R$	0.076 (x axis)

The maneuver from hovering to forward flight is then analysed considering the case with $\dot{\theta} = 600°/s$ as a reference. The reference dynamic simulation is repeated 100 times to obtain the averaged velocity field at mid-tilting ramp, i.e., at $\theta = \theta_{Mid} = 15°$. The tests are carried out considering a random initial azimuthal angle ψ, to avoid phase-locking. The resulting averaged velocity field is thus compared with the time-averaged velocity fields evaluated in steady-state conditions at the start and mid-tilting ramp in terms of mean flow features, among which are the axial velocity profiles. A further simulation is then carried out by adding the V_{kT} evaluated in the reference dynamic case to a steady-state hovering case. In this fashion, the relevance of the wake dynamics in rapid tilting maneuvers is highlighted, showing the need to perform a complete tilting maneuver to evaluate the loads and the flow field accurately.

4.2.2 Results

This section discusses the integral loads and instantaneous flow fields stemming from the steady-state and dynamic cases. In the first sub-section, the maneuver from hovering to forward flight is considered. In addition, a comparison between steady-state and dynamic cases is carried out. In the second sub-section, the focus is shifted to the transition from vertical climbing to forward flight. Unlike the first analysed maneuver, the propeller is subject to a background flow V_∞ directed along the z axis, to

simulate the vertical climb before the start of the maneuver. In the final sub-section, the tilting from forward flight to hovering is considered. The propeller is tilted from $\theta_{Start} = 30°$ to $\theta_{End} = 0°$ under cross-flow conditions. The background flow is therefore oriented along the x axis.

Tilting from hovering to forward flight

The dynamic effect of the transition from hovering to forward flight is first analysed in terms of the non-dimensional thrust C_T and torque C_Q coefficients, as reported in Figure 4.16. In particular, a comparison between steady-state and dynamic cases is carried out.

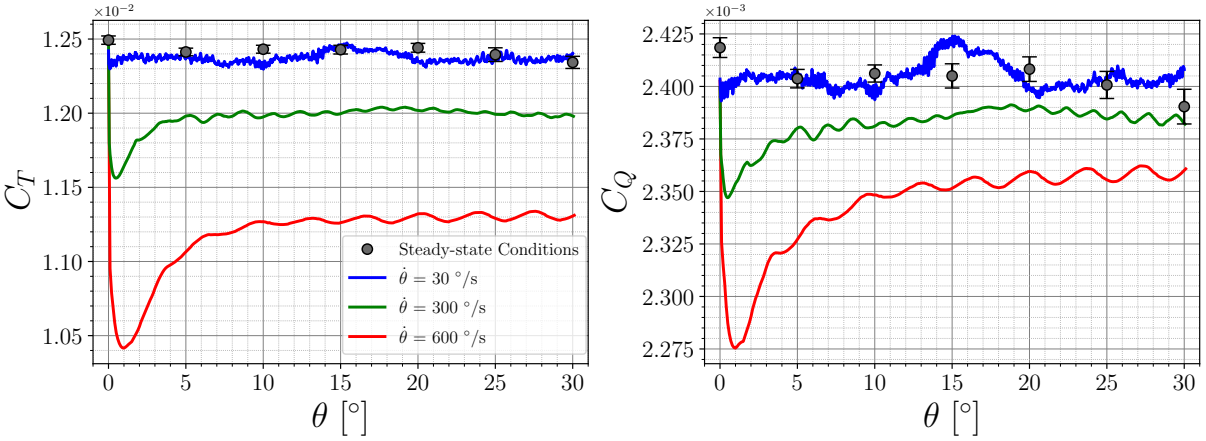

Fig. 4.16 Comparison of C_T and C_Q as a function of θ between dynamic maneuvers and steady-state conditions.

Since the hovering condition is invariant to θ, being in absence of external flow, both the steady-state C_T and C_Q values remain approximately constant between $\theta = 0°$ and $\theta = 30°$. The small observed differences between the averaged steady-state cases at different θ values are mainly due to the nature of the hovering conditions, characterized by loads' oscillations due to the wake unsteadiness, and the complexities in accurately simulating such conditions through numerical simulations. Such oscillations are quantified with the standard deviation of the loads and are represented as error bars superimposed on the mean values of C_T and C_Q in Figure 4.16.

The dynamic simulations start from $\theta_{Start} = 0°$ and end at $\theta_{End} = 30°$. It can be first observed that C_T and C_Q decrease compared to the steady-state values, as $\dot{\theta}$ is increased. At $\dot{\theta} = 30°/s$, both C_T and C_Q show approximately the same values obtained in the steady-state cases throughout the tilting. This suggests that at low values of $\dot{\theta}$, the maneuver can be considered as quasi-steady. As $\dot{\theta}$ increases, C_T and C_Q show a first pronounced reduction at the start of the tilting. Both quantities eventually approach an asymptotic value for $\theta > 10°$, which is still a function of the maneuver's rate. Although the dynamic simulations start from an initial converged hovering condition, the sudden start of the maneuver causes a transitional state with a drop in the values of thrust and torque. This behaviour can likely be restrained

by performing a smoother start, avoiding carrying out a transition with a constant ramp rate throughout the whole maneuver. However, since $\dot{\theta}$ is constant, an asymptotic trend at lower but almost constant C_T and C_Q values is observed. In the fastest tilting at $\dot{\theta}$ = 600°/s, the deviation from the steady-state case is significant, being around -10% for C_T and -3% for C_Q around θ_{Mid} = 15°.

In addition to this, as $\dot{\theta}$ increases, the thrust and torque coefficients exhibit significant oscillations around the asymptotic value. The contributions to C_T by each blade are shown in Figure 4.17. The data are normalized with the averaged C_T value of each case evaluated between θ = 10° and θ = 20° ($\overline{C_{T(\theta_{Mid})}}$), to compare the oscillations' amplitude as a function of $\dot{\theta}$.

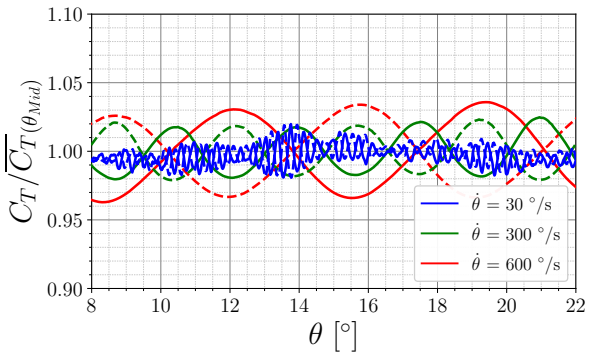

Fig. 4.17 Single blades contributions to C_T for the dynamic cases. Continuous (dashed) lines refer to the blade 1 (blade 2).

The two blades exhibit small and irregular C_T oscillations in the case with $\dot{\theta}$ = 30°/s, mainly due to the chaotic behaviour of the flow in hovering conditions. On the other hand, at greater $\dot{\theta}$ values, the two blades show periodic oscillations with a rather regular phase lag and a frequency equal to the propeller's rotational frequency. Moreover, the amplitude increases with $\dot{\theta}$, even though it is always below 2.5% of $\overline{C_{T(\theta_{Mid})}}$. These oscillations are due to the dynamic tilting effects, which are more pronounced when the blades are farther from the tilting centre. Conversely, when the blades are closer to the tilting centre, the dynamic influence is reduced. In addition, the irregular high-frequency oscillations observed at $\dot{\theta}$ = 30°/s are less visible at higher $\dot{\theta}$ values. Since the propeller is moved away from its wake in this maneuver, this might be related to the increased spacing between the vortical structures in the wake flow for the larger $\dot{\theta}$.

The induced flow field is indeed also significantly affected by the propeller's tilting. To illustrate such an effect, the instantaneous flow field in the steady-state case at θ_{Mid} = 15° is compared with the instantaneous flow fields at the different analysed $\dot{\theta}$ values, also extracted at θ_{Mid} = 15°. The flow fields are represented in the $x-z$ plane in Figure 4.18 in terms of velocity directed along the propeller's rotation axis (V_{Ax}) and vorticity along the y axis (ω_y). In particular, at mid-maneuver, the propeller's rotation axis is oriented at 15° counterclockwise with respect to the z axis. The two quantities are normalized using the propeller radius R and the rotational speed Ω. The simulations are performed to be phase-locked at θ_{Mid}, so the extracted flow fields show the propeller at the same azimuthal angle ψ, as shown in Figure 4.18.

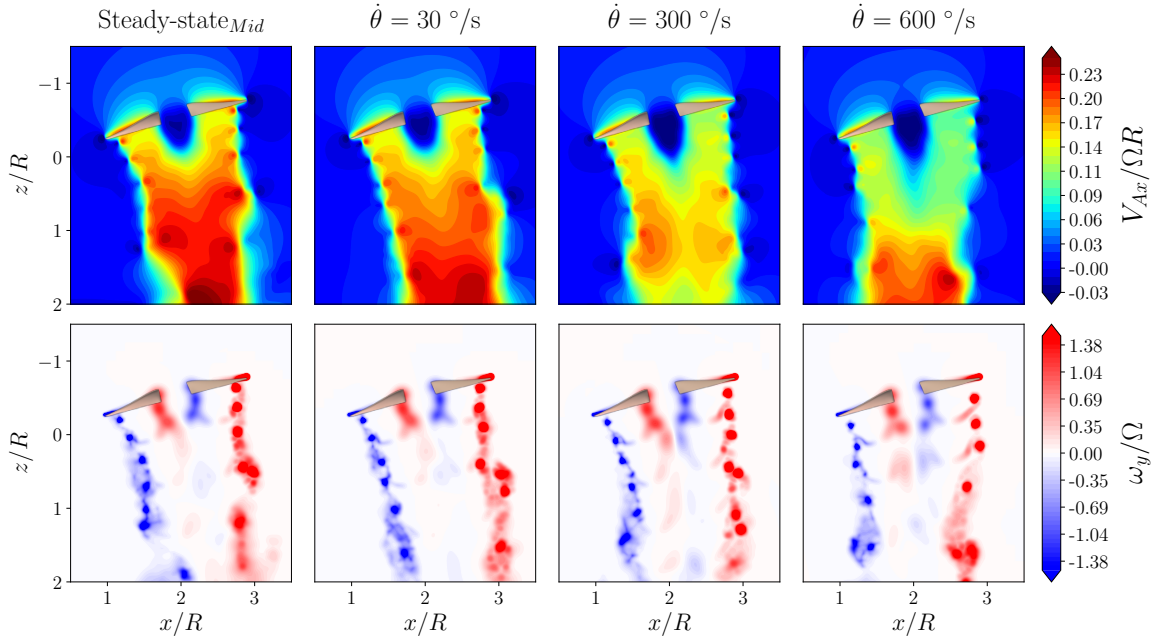

Fig. 4.18 Colourmaps of the normalized instantaneous axial velocity $V_{Ax}/\Omega R$ for the steady-state and dynamic cases. The propeller-shaped mask is added to improve the clarity.

Near the propeller, the axial velocity decreases as $\dot{\theta}$ increases, with the steady-state case showing greater velocity values than the dynamic cases. The dynamic maneuver performed at $\dot{\theta}$ = 30°/s displays flow field features that are rather similar to the steady-state case. The velocity distribution in the wake, however, is not axisymmetric anymore, with lower axial velocity values. At greater $\dot{\theta}$ values, the wake becomes more asymmetric and a significant decrease in the axial velocity can be observed in the wake region. The wake indeed is deflected towards the z axis. This is particularly clear beyond $z/R \approx 1$. This occurs because the wake does not instantly adapt to the propeller rotation axis orientation during the tilting. This effect hence becomes more pronounced during more rapid maneuvers.

The colourmaps of the out-of-plane vorticity reported in Figure 4.18 particularly highlight the evolution of the vortices shed from the blades' tips. It can be seen how, moving away from the propeller, the tip vortices start to mutually interact, eventually merging into more chaotic structures. Determining clear trends of vortex interactions within the wake against $\dot{\theta}$ is challenging. A single test per maneuver is insufficient for accurate statistical evaluation; however, some features can still be observed from the instantaneous flow fields. Specifically, at $\dot{\theta}$ = 600°/s, the tip vortices appear more axially spaced compared to the previous cases. The wake appears more stretched along the propeller's axial direction, increasing the distance between adjacent vortices. The spacing between adjacent vortices is furthermore more pronounced in the outer wake portion for larger x/R coordinates. This might delay the tip vortices' interactions compared with steady-state hovering. As anticipated, this might also explain the more regular oscillations observed in Figure 4.17.

To highlight the importance of the wake dynamics in the tilting maneuvers, an additional steady-state case is simulated. The V_{kT} distribution evaluated in the dynamic case with $\dot{\theta}$ = 600°/s is now added to

a steady-state hovering case, performed at $\theta_{Mid} = 15°$. Such a steady-state approximation, referenced as "steady-state$_{Mid} + V_{kT}$" case, aims to isolate the effects of V_{kT} from the wake dynamics effects due to the propeller's rototranslation motion. The results are first compared in terms of C_T and C_Q with the steady-state$_{Mid}$ case and the dynamic case with $\dot{\theta} = 600°/s$, as reported in Figure 4.19.

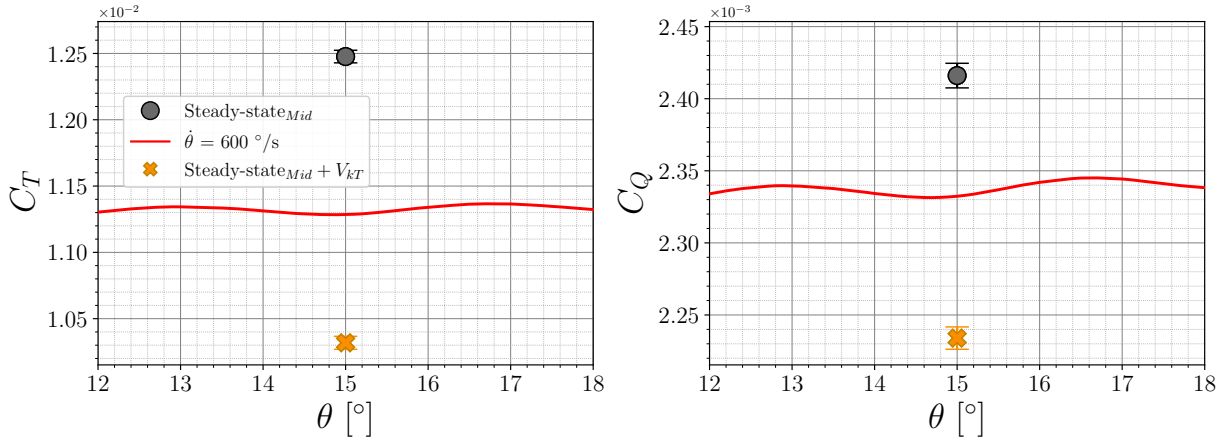

Fig. 4.19 Comparison of C_T and C_Q as a function of θ.

The steady-state$_{Mid} + V_{kT}$ case respectively underestimates C_T and C_Q by 8.5% and 3.8%, respectively, compared to the reference dynamic case. These differences are significant, being almost of the same order as the differences between the steady-state$_{Mid}$ and the reference dynamic case. The addition of V_{kT} therefore leads to a decrease of both thrust and torque, which, however, in the reference dynamic case, is balanced by the maneuver's effects on the wake dynamics due to the rototranslation. As observed in Figure 4.18, the wake is stretched along the propeller's axial direction for the dynamic cases; thus, the distance between the blades and the generated vortical structures increases for faster maneuvers. This mainly leads to a decrease in the axially induced velocity on the blades, increasing the thrust and torque. This topology modification of the wake cannot be retrieved in the steady-state$_{Mid} + V_{kT}$ case, resulting in significant overestimation of the load reduction yielded by the maneuver.

This can be addressed in detail, focusing on the distribution in span of the blade quantities, extracted for the two blades at mid-ramp. The non-dimensional blade span thrust (s_{C_T}), the angle of attack (α), and the non-dimensional axial velocity on the blade elements ($v_{b_{Ax}}/\Omega R = (V_{kT} + v')/\Omega R$) are displayed as a function of r/R for each blade in Figure 4.20. The continuous (dashed) lines indicate the blade 1 (blade 2), positioned at $\psi = 0°$ ($\psi = 180°$), i.e., the closest (farthest) to the centre of rotation at mid-ramp. The steady-state$_{Mid}$ case is the only featuring s_{C_T}, α and $V_{Ax}/\Omega R$ distributions almost overlapping between the two blades. The steady-state$_{Mid} + V_{kT}$ case shows the greatest differences compared to the steady-state$_{Mid}$ case and between the distributions of the two blades. In particular, the blade 2 is subject to greater local V_{kT} values compared to the blade 1, being farther from the tilting centre, consequently leading to greater $v_{b_{Ax}}$ values along the blade span. This results in lower α

and, consequently, in lower s_{C_T}. The dynamic case shows instead intermediate distributions between the steady-state$_{Mid}$ and the steady-state$_{Mid}+V_{kT}$ cases for $r/R < 0.85$. In this blades' portion, $v_{b_{Ax}}$ is significantly lower than in the steady-state$_{Mid}+V_{kT}$ case, leading to angles of attack closer to the steady-state$_{Mid}$ case and consequently to greater thrust values. Since the V_{kT} distribution is the same between the steady-state$_{Mid}+V_{kT}$ and the dynamic case, the differences in $v_{b_{Ax}}$ are associated to the different axial induced velocity v' value, which represents the induced velocity from the shed structures in the wake. In the dynamic cases, due to the wake stretching, the vortices induce a lower axial velocity and consequently lead to a greater thrust. For $r/R > 0.85$, the blade span quantities distributions of the dynamic case appear almost superimposed to the steady-state$_{Mid}+V_{kT}$ results. Near the blades' tips, both for blade 1 and 2, the effect of the V_{kT} appears to prevail over the effects due to the modified wake topology observed in the dynamic case. Nevertheless, this match is relegated to a small blade portion, while for $r/R < 0.85$, the blade span quantities are significantly different, leading to a substantial mismatch in the integral loads.

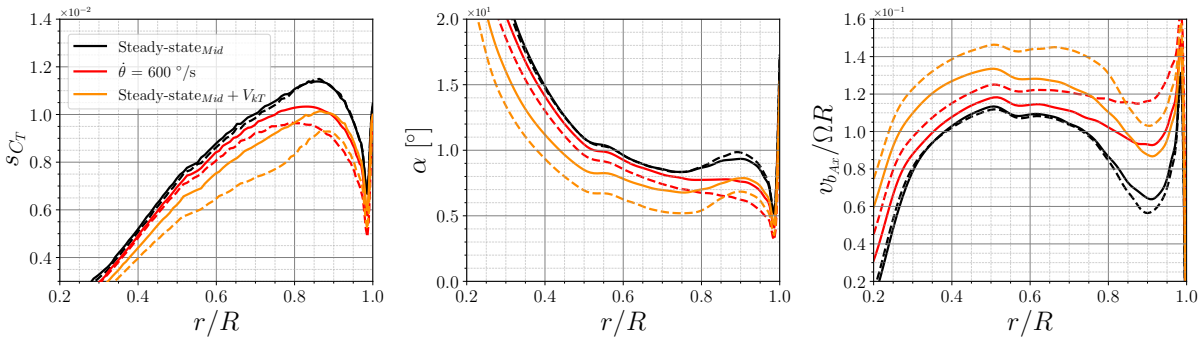

Fig. 4.20 s_{C_T}, α and $V_{Ax}/\Omega R$ extracted at mid-tilting ramp ($\theta_{Mid} = 15°$) as functions of r/R. Continuous (dashed) lines refer to the blade 1 (blade 2) located at the azimuthal position $\psi = 0°$ ($\psi = 180°$).

The main differences in the wake dynamics can be inferred from the instantaneous V_{Ax} fields in the $x-z$ plane at $\theta_{Mid} = 15°$, shown in Figure 4.21. The steady-state$_{Mid}+V_{kT}$ case shows similar features to the steady-state$_{Mid}$ case, rather than to the dynamic case. The addition of V_{kT} leads to a slight asymmetry in the wake region to the propeller's rotation axis, but the V_{Ax} does not significantly decrease as noticeable in the dynamic case. Moreover, the wake does not display a curved trajectory along the z axis as previously observed for the dynamic case. Therefore, the addition of V_{kT} mostly leads to a significant variation in the blades' loads, but slightly influences the wake dynamics.

This steady-state approximation is hence not suitable for the prediction of both the propeller's loads and the flow field, highlighting the importance of carrying out complete tilting maneuvers to account for the dynamic effect in the wake region and consequently obtaining accurate results.

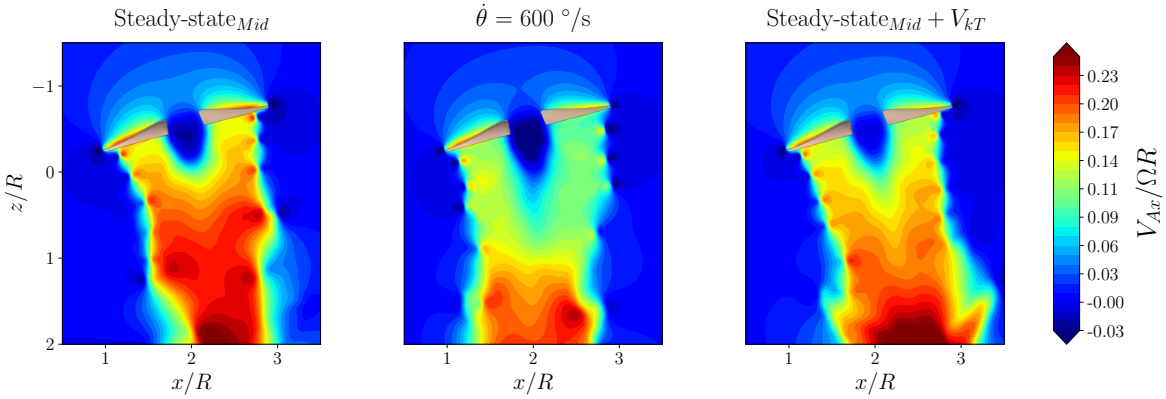

Fig. 4.21 Colourmaps of the normalized instantaneous axial velocity $V_{Ax}/\Omega R$. The propeller-shaped mask is added to improve the clarity.

Time-Averaged flow topology

In this section, the differences in the time-averaged flow fields between dynamic and steady-state cases are explored. To this purpose, the dynamic case with $\dot{\theta} = 600°/s$ in the tilting maneuver from hovering to forward flight is repeated several times, starting with different initial azimuthal angles ψ. An extensive dataset of 2D fields is hence obtained at mid-tilting ramp, featuring a different ψ value for each test to avoid biases from correlated data in the averaging procedure. The convergence of the averaged flow field is ensured by repeating the simulation 100 times, observing that the averaged velocity field changes by less than 2% for sampling ensembles made of at least 80 repetitions.

The averaged velocity field is compared with the time-averaged fields obtained in steady-state conditions at $\theta = 0°$ (steady-state$_{Start}$) and at $\theta = 15°$ (steady-state$_{Mid}$). The comparison is carried out both in terms of the averaged velocity along the z axis ($\overline{V}_z$) in the $x-z$ plane, and with the velocity profiles extracted at two axial locations, namely $z/R = 0.25$ and 1.5, as shown in Figure 4.22.

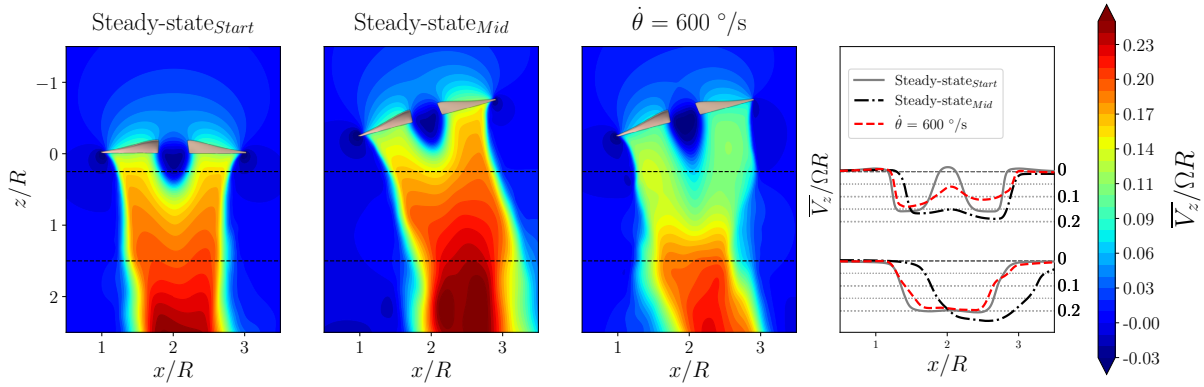

Fig. 4.22 Colourmaps of the normalized averaged velocity along the z axis $\overline{V}_z/\Omega R$ of dynamic and steady-state cases. The colourmaps are reported along with velocity profiles extracted at $z/R = 0.25$ and 1.5 (and shown with the black dashed lines in the colourmaps). The propeller-shaped mask is added to improve the clarity.

The wake region appears axisymmetric for both the steady-state$_{Start}$ and the steady-state$_{Mid}$ cases at small distances from the propeller. Beyond $z/R > 1.5$, a less organized wake is observed, as also previously observed for instantaneous fields in Figure 4.18. In the dynamic case, the wake appears instead deflected towards the z axis direction, and $\overline{V}_z$ additionally results significantly lower than both steady-state cases.

At both $z/R = 0.25$ and 1.5, the velocity profiles in the dynamic case result closer to the steady-state$_{Start}$ case. This is particularly clear at $z/R = 1.5$, where the velocity profiles are almost overlapping, while the steady-state$_{Mid}$ case profile appears significantly different. The wake beyond $z/R > 1.5$ is not yet significantly affected by the dynamic effects of the tilting, and the resulting flow field shows features that are similar to the steady-state$_{Start}$ case. The similarities are primarily identified in the core of the wake, while more significant deviations are instead observable in the outer wake portion. At greater x/R values, the dynamic effects are stronger, and the wake topology is consequently more affected.

Tilting from vertical climbing to forward flight

The tilting from vertical climbing to forward flight differs from the previous maneuver due to the presence of a mean flow directed along the z axis. This background flow serves the purpose of simulating the vertical climbing phase for a propeller undergoing the transition. As a consequence, the steady-state cases are no longer invariant with respect to θ, transitioning from an axial flow condition at $\theta_{Start} = 0°$ to a non-axial flow condition for $\theta > 0°$. More specifically, both C_T and C_Q increase as a function of θ under steady-state conditions, as shown in Figure 4.23. The standard deviation increases along with the mean value, as indicated by the error bars. While at $\theta_{Start} = 0°$ and in axial flow conditions, the loads generated by the blades are independent of the azimuthal angle, the coupling with the non-axial flow generates oscillating loads throughout the propeller's revolution.

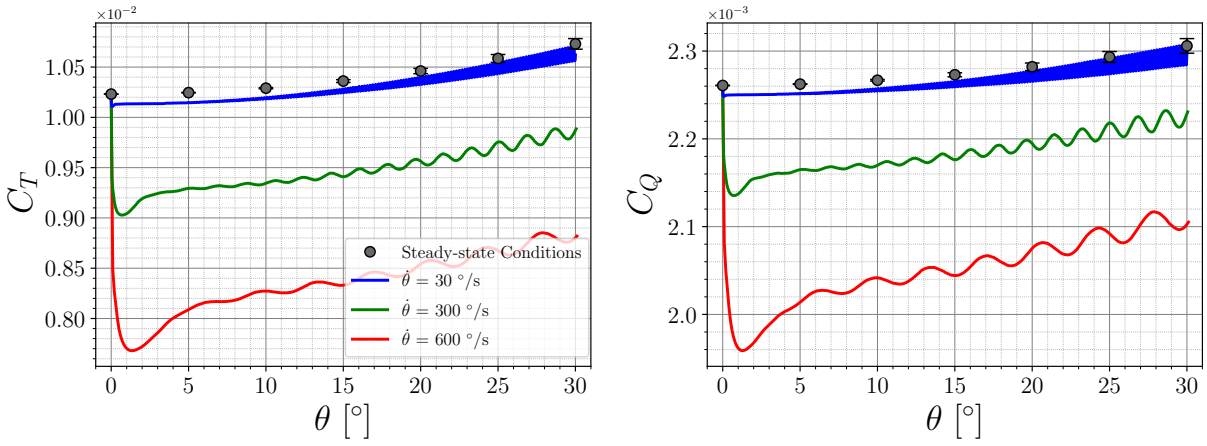

Fig. 4.23 Comparison of C_T and C_Q as a function of θ between dynamic maneuvers and steady-state conditions.

As observed in the previous section, C_T and C_Q for the dynamic cases decrease as $\dot{\theta}$ increases. Even in the slowest case with $\dot{\theta} = 30°/s$, both C_T and C_Q result in being smaller than the mean steady-state values at the same θ. Despite that, the observed differences are rather small (about 0.4%). At $\dot{\theta} = 600°/s$, the greatest differences with the reference steady case can be observed. In particular, at $\theta_{Mid} = 15°$, the dynamic maneuver leads to a value of C_T and C_Q by 17% and 12% respectively smaller than the steady-state case.

The loads' oscillations due to the interaction with a non-axial flow are also observed in the dynamic cases. C_T and C_Q in the dynamic cases exhibit increasing oscillations as θ increases. The flow-induced oscillations add to the tilting-induced oscillations previously observed in the sub-section 4.2.2. The contributions of each blade to C_T are shown in Figure 4.24 for a range of θ between 8° and 22°. The data is normalized with the mean value obtained at $\theta_{Mid} = 15°$. The contributions to C_T by each blade, normalized with $\overline{C_{T(\theta_{Mid})}}$, are shown in Figure 4.24.

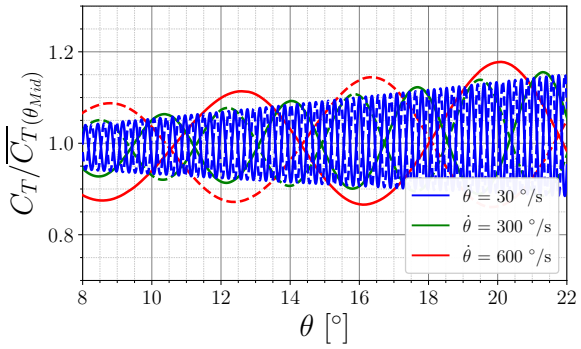

Fig. 4.24 Single blades contributions to C_T for the dynamic cases. Continuous (dashed) lines refer to the blade 1 (blade 2).

In Figure 4.17, the loads' oscillations were almost exclusively due to the dynamic tilting effects, and increasing amplitudes were observed as $\dot{\theta}$ increased. In the present maneuver, the non-axial flow effect dominates in the two slower dynamic cases with $\dot{\theta} = 30°/s$ and $300°/s$, leading to almost equivalent oscillation amplitudes. On the other hand, in the case with $\dot{\theta} = 600°/s$, the effect of the dynamic tilting is still significant, leading to more pronounced C_T oscillations compared to the slower cases. It is also worth mentioning that the amplitude of the oscillations is greater for the considered maneuver than for the hovering to forward flight one.

The V_{Ax} and ω_y fields extracted at mid-maneuver are shown in the colourmaps in Figure 4.25. The vortex structures, initially advected along the propeller's rotation axis direction, interact with the background flow (directed along z). Owing to such interaction, both the axial velocity and, consequently, the out-of-plane vorticity fields appear to be non-axisymmetric. In the dynamic cases, tilting contributes to enhancing the flow field asymmetry, as shown in Figure 4.25. Indeed, the velocity in the wake is, on average, lower as $\dot{\theta}$ increases. In the cases with $\dot{\theta} = 300°/s$ and $\dot{\theta} = 600°/s$, the wake appears significantly deflected towards the z axis. As already discussed in section 4.2.2, the wake has its own non-negligible inertia, and, if the maneuver is sufficiently rapid, the wake does not manage

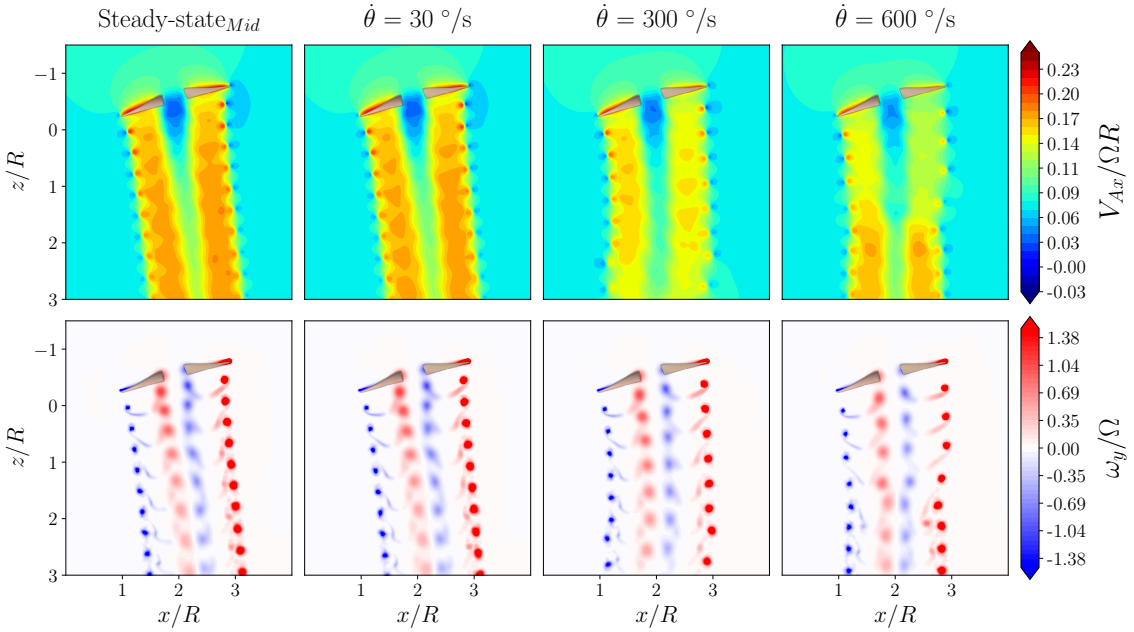

Fig. 4.25 Colourmaps of the normalized instantaneous axial velocity $V_{Ax}/\Omega R$ and out-of-plane vorticity ω_y/Ω of dynamic and steady-state cases. The propeller-shaped mask is added to improve the clarity.

to instantly align with the propeller as it tilts throughout the maneuver. Furthermore, in the present maneuver, the tip vortices appear more spaced in the axial direction, being advected by the background flow along the z axis.

At $\dot{\theta} = 600$°/s, the propeller takes 2 revolutions to tilt from $\theta_{Start} = 0°$ to $\theta_{Mid} = 15°$, shedding 4 pairs of tip vortices in the $x-z$ plane. The fifth pair of vortices is therefore the last generated in steady-state conditions before the start of the maneuver. It is hence possible to retrieve a location along the z axis that approximately separates the wake region shed before and after the start of the tilting. The wake region located at $z/R > 1.2$ was approximately shed before the start of the ramp, showing significantly greater velocity values and a more symmetric vortex pattern with respect to the z axis. Additionally, the tip vortices appear closer to each other in the axial direction, indicating that the wake is more compressed. For $z < 1.2$, the vortical structures instead appear more spaced in the axial direction, and the differences in terms of velocity and vorticity values are more pronounced.

Tilting from forward flight to hovering

The last analysed maneuver aims to simulate the transition from forward flight to hovering. In the initial cruise phase in forward flight, the propeller axis is aligned to $\theta_{Start} = 30°$, while being subject to a background flow oriented towards the x axis. The dynamic transition to the hovering condition is simulated by tilting the propeller to $\theta_{End} = 0°$, while keeping fixed the flow conditions. This choice is made under the assumption that the tilting maneuver occurs more rapidly than the forward flight

deceleration. At θ_{End}, the propeller is hence under cross-flow conditions, with the background flow perpendicular to the propeller's rotation axis.

The non-dimensional thrust and torque coefficients are shown as a function of θ for the steady-state and dynamic cases in Figure 4.26. Focusing on the steady-state mean values, C_T increases monotonically as θ approaches zero, while C_Q remains almost constant. This is due to the reorientation of the propeller's rotation axis with respect to the background flow throughout the maneuver. As θ decreases, the axial component of the background flow ($V_\infty sin(\theta)$) velocity also decreases. As $V_\infty sin(\theta)$ component decreases, the thrust and torque increase. The thrust is more responsive to such a condition, while the torque appears less affected. Such behaviour was already observed in cross-flow in sections 3.1 and 3.2, where C_T showed a steeper increase than C_Q at increasing cross-flow velocities, mostly at low advance ratios. Small cross-flow velocities mainly affect the lift (and consequently the thrust) rather than the drag, due to the steeper slope of the $c_L - \alpha$ curve compared to the $c_D - \alpha$ curve at small angles of attack.

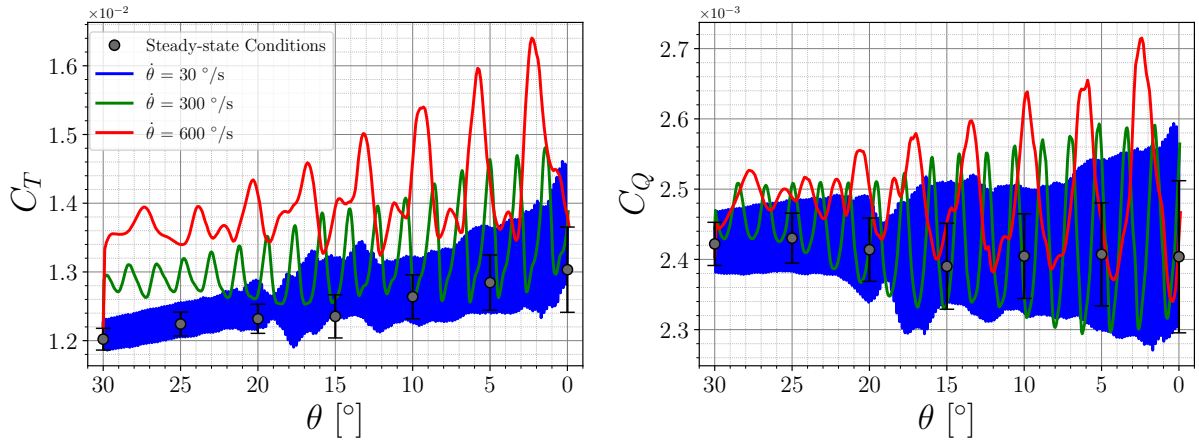

Fig. 4.26 Comparison of C_T and C_Q as a function of θ between dynamic maneuvers and steady-state conditions.

Focusing instead on the dynamic cases, both the thrust and torque coefficients increase as $\dot{\theta}$ increases; however, being characterized by large oscillations, it is not straightforward to establish a clear trend as done in the previous cases. Even in the steady-state results, it is shown that the flow-induced load oscillations play a significant role. Such oscillations increase towards θ_{End} (i.e. when θ approaches 0). The blades indeed undergo highly variable flow conditions throughout a single revolution, with a maximum loading obtained as a blade advances towards the background flow and a minimum loading as it retreats from the background flow. The dynamic cases are also subject to these flow-induced oscillations. The contributions to C_T by each blade, normalized with $\overline{C_{T(\theta_{Mid})}}$, are shown in Figure 4.27.

The C_T oscillations' amplitude appears almost equal among the various dynamic cases, regardless of the ramp rate, indicating that the flow-induced oscillations play a dominant role compared to those

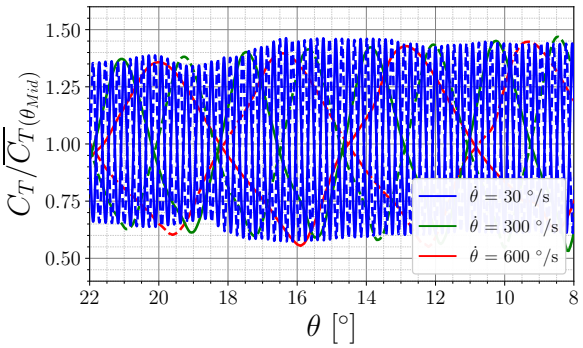

Fig. 4.27 Single blades contributions to C_T for the dynamic cases. Continuous (dashed) lines refer to the blade 1 (blade 2).

induced by the dynamic tilting. Furthermore, at mid-tilting ramp, the C_T oscillations reach values as large as 40% of the local mean value, which is significantly greater than in the previously analysed maneuvers (about 2.5% and 15% for the described maneuvers in section 4.2.2 and 4.2.2, respectively).

Similarly to the previous cases, a comparison of the spatial organization of the axial velocity and of the out-of-plane vorticity is carried out between the dynamic and steady-state cases (see Figure 4.28). Already in the steady-state cases, the wake displays an asymmetric topology with respect to the propeller's rotation axis, both in terms of axial velocity and out-of-plane vorticity. However, the vortical structures are advected downstream according to a more organized pattern compared to the hovering condition due to the presence of the background flow. This primarily leads to a less chaotic far wake. In the vorticity fields, the regions of maximum and minimum vorticity corresponding to the tip vortices appear indeed as distinct and organized structures. Unlike the previously analysed maneuvers, now the propeller is tilted in the opposite direction, towards its shed wake. The wake indeed appears compressed in the axial direction, featuring tip vortices that are mutually closer as $\dot{\theta}$ is increased. Interestingly, increasing $\dot{\theta}$ leads to the coalescence of vortices as shown at $(x,z)/R = (3.8,0)$ for the $\dot{\theta} = 600°/s$ case. This strong vortex induces a high value of axial velocity, effectively reducing the angle of attack and degrading the propeller's performance, following a similar mechanism as the vortex ring state of helicopter rotors during descent [134]. In conclusion, as observed for the previous maneuvers, the wake appears deflected towards the x axis as $\dot{\theta}$ is increased.

4.2.3 Conclusions

This study analysed the influence of different dynamic tilting maneuvers on the aerodynamics of the reference propeller. In particular, three different tilting maneuvers were performed: The first maneuver aimed to replicate the tilting from hovering to forward flight, carried out in the absence of an external flow. The second maneuver was realized to simulate the tilting from vertical climbing to forward flight. The propeller was tilted in the same direction as in the first maneuver, but additionally including a vertical background flow to simulate the initial climbing condition. The last simulated maneuver was

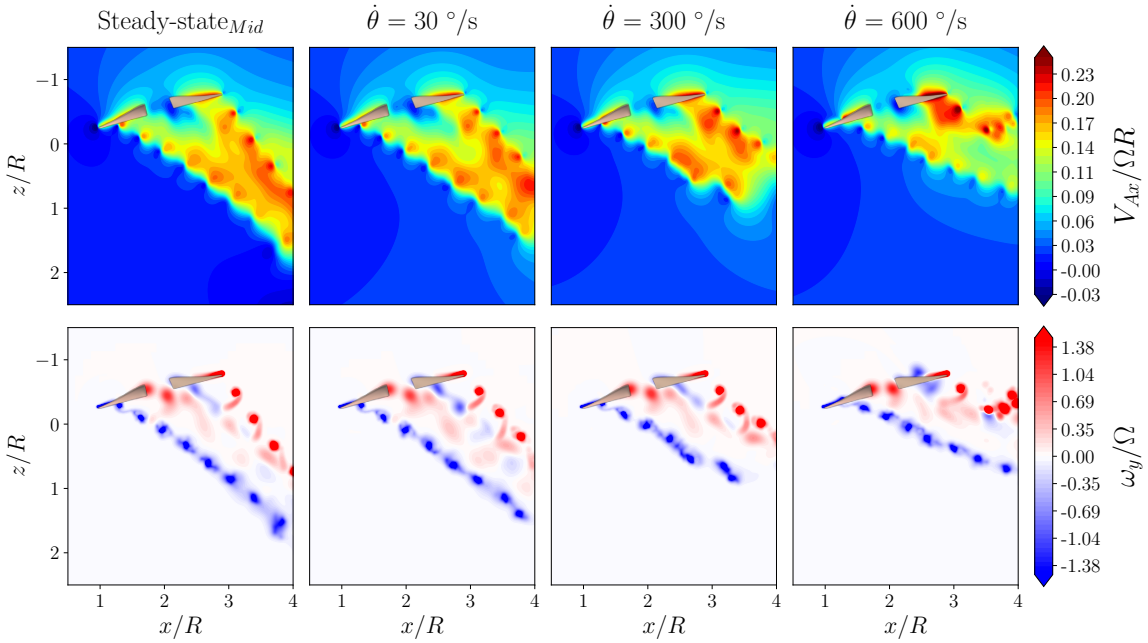

Fig. 4.28 Colourmaps of the normalized instantaneous axial velocity $V_{Ax}/\Omega R$ and out-of-plane vorticity ω_y/Ω of dynamic and steady-state cases. The propeller-shaped mask is added to improve the clarity.

the tilting from forward flight to hovering. The propeller was tilted in the opposite direction compared to the previous cases, with the presence of a background cross-flow to simulate the initial forward flight conditions.

Key findings reveal that higher ramp rates lead to greater deviations from the steady-state cases. In particular, in the first two maneuvers, a significant decrease in thrust and torque is observed. In the last maneuver, a slight increase in both loads is instead observed, due to the opposite tilting direction. The dynamic tilting is additionally found to induce significant loads' oscillations on the propeller's blades. Such oscillations add to the background flow-induced oscillations. Depending on the ramp rate and the orientation and magnitude of the flow, one of the two contributions appears to dominate compared to the other.

The dynamic effects were also evaluated on the instantaneous induced velocity and vorticity fields. Especially in rapid maneuvers, a pronounced asymmetry with respect to the propeller's rotation axis is observed in the wake region. The wake's inertia indeed prevents an instantaneous alignment with the rotation axis, showing a significantly deviated structure compared to the steady-state cases. Furthermore, as the propeller is tilted towards or away from its shed wake, depending on the specific maneuver, the mutual distance between adjacent vortices is also affected. This might lead to more frequent vortex interaction phenomena. Furthermore, local clustering of vortices might contribute to the degradation of the propeller performance, similarly to the vortex ring state mechanism.

The tilting maneuvers considered in this study are computationally expensive to simulate using conventional high-fidelity approaches such as LES or URANS. For instance, simulating the slowest

tilting ramp at 5000 rpm involves approximately 83 propeller revolutions, corresponding to a physical time of 1 second, a scenario that typically entails a significant computational burden for high-fidelity methods. Even in the case of the fastest maneuver, which requires only 4 revolutions, characterizing the averaged flow field features necessitated 100 simulation repetitions, amounting to a total of 400 revolutions for a single case. Furthermore, the study demonstrates that adopting a low-cost, steady-state approximation, which neglects the effects of the rototranslational dynamics, results in substantial inaccuracies in both load predictions and flow field characterization. This highlights the greater suitability of the mid-fidelity VPM approach compared to the higher-fidelity URANS simulations. In conclusion, the maneuvers' ease of implementation in the code also enables the simulation of more complex maneuvers beyond simple ramps, enhancing the applicability of this approach to more realistic scenarios.

Chapter 5

Conclusions

5.1 Summary

This thesis presented a comprehensive investigation into the aerodynamic behaviour of small-scale propellers used in Small Unmanned Aerial Vehicles (SUAVs), addressing the complex flow phenomena that arise in both steady-state and dynamic operative conditions. The research employed a multi-fidelity approach, combining experimental measurements, high-fidelity simulations (Large Eddy Simulations (LES) and Unsteady Reynolds-Averaged Navier-Stokes (URANS)), and mid-fidelity computations (Vortex Particle Method (VPM)) to provide a thorough understanding of the aerodynamic mechanisms governing propeller performance at low Reynolds numbers.

Validation of the VPM code VULCAINS in hovering and axial inflow

The validation of ONERA's VPM code VULCAINS against URANS simulations and experimental measurements established its capability as an efficient tool for preliminary design and analysis of small-scale propellers. The code features a lifting line approach to simulate the lifting surfaces, requiring an aerodynamic polars dataset to compute the blades' loads. The baseline simulation featured XFoil-generated aerodynamic polars with $N_{crit} = 5$ and provided thrust and torque predictions within 5% of experimental values in both hovering and axial inflow conditions. The parametric sensitivity analysis revealed that the number of vorticity sources (N_S) is the most influential parameter, with variations from 20 to 60 particles resulting in thrust changes up to 3.4% and wake axial velocity variations exceeding 20% in hovering conditions. In axial inflow, N_S instead appears to negligibly influence the VPM solution. Other parameters, including the azimuthal discretization ($\Delta\psi$), time integration order, and diffusion scheme, showed minimal impact on integral quantities but significantly affected convergence behaviour and computational efficiency. The investigation of airfoil polar influence demonstrated that XFoil-based polars provided superior agreement with URANS predictions compared

to SSTLM-derived alternatives, successfully capturing the complex flow physics on the blades' suction side peculiar to low Reynolds number flows. Nevertheless, they remain dependent on the chosen N_{crit} value, which significantly affects the aerodynamic coefficient at these low Reynolds numbers and must be calibrated accordingly with the results on the full propeller.

Cross-flow conditions

The experimental investigation conducted in the "Ferrari" wind tunnel at Politecnico di Torino initially provided fundamental insights into the propeller's behaviour in hovering and axial inflow. In the same facility, a detailed focus is made on the cross-flow condition, representative of forward flight, propeller-propeller interactions, and gust encounters. The measurements revealed that both thrust and torque coefficients exhibit a monotonic increase with the cross-flow ratio μ, with an initial plateau observed for $\mu < 0.08$ followed by a steep rise at greater values. The semi-empirical models derived from helicopter theory were successfully adapted to predict the power consumption of small-scale propellers, with fitting coefficients showing close agreement with literature values. The Planar Particle Image Velocimetry (PIV) measurements unveiled the complex wake topology evolution, demonstrating significant deflection of the velocity vectors toward the cross-flow direction and the formation of recirculation regions in the downwind area. The vortical structures analysis using the Γ_2-criterion revealed that the tip vortices generated in the upwind region maintain stronger circulation and more defined trajectories compared to their downwind counterparts, which become increasingly disrupted by the cross-flow interaction. This behaviour was already observed in jets in cross-flow for the vortical structures generated upwind and downwind of the jet nozzle [34].

The LES campaign extended the experimental findings by providing detailed three-dimensional flow field information not accessible through planar PIV measurements. The numerical simulations successfully captured the experimental trends in the thrust and torque evolution, despite slight overestimations attributed to geometric uncertainties and measurement limitations at small loading values. The disk loading analysis revealed pronounced azimuthal asymmetries in thrust distribution. A novel finding was the generation of significant pitching moments at low cross-flow ratios, comparable in magnitude to roll moments, which, to the author's knowledge, had not been previously reported in the literature. The decomposition of thrust per unit length into dynamic pressure and filtered thrust contributions successfully decoupled the primary kinematic effects from secondary inflow pattern distortions, providing new insights into the physical mechanisms driving performance variations. This decomposition highlights the need for a complex three-dimensional modelling to accurately capture the driving aerodynamic mechanisms in cross-flow conditions. Low-order theories, such as Blade Element Theories (BET), indeed adequately capture the primary kinematic effects, but are not able to account for the secondary effects due to the wake deflection and distortion.

The investigation of the experimental support's influence demonstrated that, while integral loads remained largely unaffected (variations below 1.2%), the induced wake underwent substantial

modifications mostly in the downwind region. Spectral analysis revealed the introduction of low-frequency disturbances at approximately 0.25 BPF, corresponding to the vortex shedding from the cylindrical support. The Proper Orthogonal Decomposition (POD) analysis showed that the support redistributes the turbulent kinetic energy across different modes, with the first two modes carrying approximately 30% each in the absence of the support, compared to a more uniform distribution of 5-6% across the first four modes when the support was present.

The characterization of wake dynamics in the absence of support revealed a progressive modification of the vortical system with increasing cross-flow velocity. The classical hovering configuration, dominated by helical tip vortices and a central hub vortex, transitions into an asymmetric structure characterized by the formation of a counter-rotating vortex pair at $\mu \approx 0.08$, similar to that of jets in cross-flow and featuring the same pressure differential-driven formation mechanism. This critical transition coincides with the observed change in slope of the thrust and torque curves, suggesting a fundamental shift in the propeller's aerodynamic behaviour from rotor-like to wing-like configuration. The vortex tracking showed that the vortices' trajectories progressively tend to be linear as the cross-flow ratio is increased. A simplified approach based on the momentum theory for the wake deflection prediction showed remarkable accuracy, with mean absolute errors below 12° for most structures. The actuator disk model ($k_\chi = 2$) provided optimal predictions for hub and tip vortices with errors below 6°, while the flat wake model ($k_\chi = 0.5$) accurately captured counter-rotating vortex pair deflection, achieving mean absolute errors as low as 2°.

Performance in dynamic operative conditions

The analysis of maneuvers such as rpm variations or tilting revealed a significant impact on the propeller's performance at high ramp rates. This investigation suggests the need for accounting for such maneuvers already in the design process, as they might also affect the emitted noise, structural integrity, and efficiency of the SUAV. The analysis of dynamic rotational speed variations revealed fundamental deviations from the steady-state performance in both acceleration and deceleration maneuvers, with thrust and torque differences reaching deviations up to 10% at the highest considered ramp rate.

Focusing on the rpm variation maneuver, the observed performance variations were primarily attributed to lag effects in the induced velocity field, with the axial component playing the dominant role in modifying the blades' angle of attack distributions. Such a lag effect leads to an increase in thrust and torque in acceleration and a decrease in deceleration. At a given fixed ramp rate, the effect is more pronounced as the instantaneous rpm are lower. The instantaneous flow field analysis showed that the wake requires multiple propeller revolutions to adapt to new operative conditions, creating significant axial velocity gradients that persist throughout rapid maneuvers. The influence of axial inflow velocity on dynamic response is finally evaluated, demonstrating that the deviations from steady-state conditions increase with inflow velocity. This is attributed to the pseudo-quadratic shape

of lift coefficient-angle of attack curves at low Reynolds numbers, which amplifies the sensitivity to angle of attack variations in lower angle of attack ranges, corresponding to stronger axial inflows.

The investigation of tilting maneuvers revealed complex interactions between kinematic effects and wake dynamics that cannot be easily captured through steady-state approximations. The transition from hovering to forward flight at the highest tilting rate resulted in significant thrust and smaller torque reductions compared to steady-state values. The analysis demonstrated that the simple addition of kinematic velocity contributions to steady-state simulations significantly underestimates the loads, highlighting the critical importance of accounting for wake stretching and vortex redistribution for the correct simulation of such maneuvers. The transition from vertical climb to forward flight showed even more pronounced effects on the loads, while the reverse maneuver from forward flight to hovering exhibited high load oscillations due to the combined effects of tilting-induced and flow-induced variations. The wake topology during tilting maneuvers exhibited pronounced asymmetries and deflections that persisted well beyond the immediate propeller vicinity. The instantaneous vorticity fields revealed that tip vortices maintain trajectories influenced by their initial conditions for several propeller radii downstream, with the wake showing distinct regions corresponding to pre-maneuver and post-maneuver shedding conditions. The averaged flow field analysis, obtained through ensemble averaging of 100 simulation repetitions, confirmed that wake characteristics at distances beyond 1.5 propeller radii remain closer to initial steady-state conditions than to the instantaneous operating point, demonstrating the significant temporal lag in wake evolution during rapid maneuvers. Although the exact load variations are not easily generalizable to other geometries or operative conditions, the qualitative observations made in the different tilting maneuvers are easily extendable to similar frameworks.

5.2 Research contributions

This thesis has made several significant contributions to the understanding of small-scale propeller aerodynamics, advancing both fundamental knowledge and practical methodologies for SUAV design and analysis.

Experimental and numerical characterization in cross-flow: The comprehensive experimental campaign provided a detailed dataset for small-scale propellers operating in cross-flow conditions, including force measurements and planar PIV fields for a simple open-geometry propeller. The subsequent numerical validation showed the capability of LES to capture complex fluid dynamics phenomena occurring in cross-flow conditions for a low-Reynolds-number propeller. The detailed analysis additionally revealed previously unreported phenomena, particularly the generation of significant pitching moments at low cross-flow ratios. The decomposition methodology developed to separate dynamic pressure effects from inflow pattern distortions provides a new framework for understanding the physical mechanisms driving performance variations in non-axial flow conditions.

The detailed analysis of experimental support influence using spectral and POD techniques demonstrated that while integral loads remain relatively unaffected, local flow structures undergo significant modifications. The identification of support-induced vortex shedding frequencies and their interaction with propeller-generated structures provides important guidelines for experimental setup design and numerical validation strategies.

The systematic characterization of the vortical-structure evolution from hovering to high cross-flow conditions revealed clear relationships between wake-topology transitions and performance variations. At low cross-flow ratios, the periodic effect of the blade-cross-flow interaction dominates the unsteady aerodynamics, yet the time-averaged thrust and torque remain essentially unchanged. As the cross-flow ratio increases, a critical value is reached at $\mu \approx 0.08$, where a strong counter-rotating vortex pair emerges and begins to dominate the induced flow field. This threshold corresponds closely to the classical helicopter-theory criterion $\mu = 1.15\sqrt{\overline{C_T}}$, which separates the low-speed and high-speed forward-flight regimes. Beyond this value, the wake undergoes a marked deflection toward the cross-flow direction, leading to a reduction of the axial induced velocity and a consequent increase in blade angle of attack, thrust, and torque. Consistently, both the $\overline{C_T} - \mu$ and $\overline{C_Q} - \mu$ curves exhibit an initial plateau for $\mu < 0.08$, followed by a monotonic increase once the critical threshold is exceeded. Although the specific load values depend on the geometry investigated, the identification of a critical μ value separating two distinct aerodynamic regimes aligns with findings from the literature and is therefore expected to be generalizable to other configurations, as well as the overall topology of the flow field and the load trends.

Low-order modelling framework: The development and validation of a simplified model for wake deflection prediction demonstrated that simple momentum-based approaches can provide accurate estimates of vortex trajectories when properly parametrized. The identification of optimal correction factors for different vortical structures ($k_\chi = 2$ for hub and tip vortices, $k_\chi = 0.5$ for the counter-rotating vortex pair) enables a rapid assessment of the wake behaviour by only knowing the thrust distribution on the disk at a given cross-flow ratio. The localized thrust estimation methodology for individual vortex structures represents a novel approach to linking disk loading distributions to wake characteristics.

VPM validation and best practices: The comprehensive validation of the VULCAINS VPM code against multiple fidelity levels established clear guidelines for simulation parameters and modelling choices. The identification of $N_S = 50$ particles per timestep as optimal for wake field accuracy, combined with XFoil polars at $N_{crit} = 5$, provides a validated baseline configuration for future studies. The systematic sensitivity analysis quantified the relative importance of various numerical parameters, assessing the robustness of the methodology and enabling users to make informed trade-offs between accuracy and computational cost.

VULCAINS proved to be a promising tool for future SUAV applications due to its extremely low computational cost and ease of use. VULCAINS can be pivotal in preliminary design phases and features a large room for improvement, with the possibility of including higher fidelity solutions close

to the walls with the hybrid method or simulating also non-lifting surfaces. Higher-fidelity simulations and experiments remain the state-of-the-art for detailed aerodynamic characterizations, but can benefit from mid-fidelity tools such as VPM for an optimized setup and initial guesses, saving time and resources.

Dynamic rotational-speed variation characterization: The analysis of dynamic rotational-speed variations demonstrated that the transient response of a small-scale propeller is strongly governed by a lag in the induced axial velocity that can become significant at high ramp rates. Although the exact load variations depend on the geometry and operative conditions, the mechanism driving them is general: as the commanded rotational speed variation becomes more aggressive, the induced field increasingly lags in adapting to the new condition and the blade incidence deviates from its steady-state value, leading to significant variations in thrust and torque. The present work quantifies this effect for the analysed geometry in specific conditions, showing significant effects for realistic maneuvers with the considered setup. This finding, however, provides a practical guideline that can be extended to general SUAV control and modelling: aggressive rpm commands may temporarily overestimate the available thrust, and controllers relying on quasi-steady aerodynamic models should account for this lag. More broadly, the framework developed for linking induced-velocity dynamics to transient load variations offers a basis for future generalization across different propeller geometries, serving as a reference for both experimental validation and numerical modelling.

Tilting dynamics analysis: The study of tilting maneuvers revealed that the wake dynamics plays a role comparable in magnitude to the direct kinematic effects associated with the tilting motion. While the specific thrust and torque variations are geometry- and operative conditions-dependent, the underlying behaviour is general: as the propeller is tilted, the wake lags in instantaneously adapting and produces transient asymmetries in loads and flow field that cannot be reproduced through steady-state superposition techniques. This work provides quantitative evidence of these effects for realistic ramp rates and establishes that neglecting wake dynamics may lead to meaningful under- or over-prediction of loads during attitude transitions. These insights are relevant for SUAV design and control, indicating that structural sizing, fatigue assessment, and maneuver planning should consider not only the instantaneous kinematics but also the wake's finite adaptation time.

5.3 Future outlooks

The present work has demonstrated that even simple transient maneuvers might introduce significant modifications to both the aerodynamic performance and wake development of small-scale propellers. These test cases were deliberately selected to provide fundamental insights into the physical mechanisms that govern the propeller's aerodynamics at low Reynolds numbers. However, the available dataset remains too limited to generalize the observed trends across different propeller geometries and operative conditions. A key challenge that remains open is the identification of suitable non-dimensional

parameters capable of characterizing and scaling maneuver-induced aerodynamic effects, enabling a more general description of propeller response under dynamic operating conditions.

Additionally, the maneuvering conditions investigated here represent only a subset of those encountered in real mission profiles. Small drones routinely perform more complex transitions, including combined rotational and translational motions, aggressive control inputs, and rapid changes in attitude. Larger rotors may additionally exploit collective and cyclic pitch schedules to regulate aerodynamic loading during maneuvering flight. The extension of the present methodology to include these complex scenarios is expected to provide a more comprehensive representation of SUAV operational envelopes. The VPM framework already adopted in this thesis is particularly well-suited for these studies, given its flexibility and computational efficiency.

With respect to the mid-fidelity VPM tool itself, future developments are planned to enhance its predictive capabilities. The coupling of the VPM with aeroelastic and aeroacoustic solvers will enable the assessment of structural deformation effects and noise generation, both of which are crucial for performance and certification in emerging applications such as urban air mobility. The ongoing implementation of a panel method for non-lifting surfaces will further improve the flow modelling accuracy around components such as hubs, fairings, and supports. Moreover, the hybrid Eulerian-Lagrangian approach, already implemented and tested [55], offers a promising pathway toward maintaining high near-wall fidelity while preserving the low computational cost associated with particle-based far field simulation.

Beyond maneuvering flight, the interaction of drones' propellers with atmospheric disturbances remains a critical topic for future investigation. Gust encounters and turbulent inflows strongly affect vehicle controllability and flight safety, particularly in constrained or urban environments. These scenarios can be addressed numerically within the current VPM framework, but also reproduced experimentally, thanks to the WindShaper facility [135] available at Politecnico di Torino.

References

[1] Ki C Kim. Analytical calculations of helicopter torque coefficient (cq) and thrust coefficient (ct) values for the helicopter performance (helpe) model. *US Army Research Laboratory*, 1999.

[2] Wayne Johnson. *Helicopter theory*. Courier Corporation, 2012.

[3] Astute Analytica. Unmanned aerial vehicle (uav) market valuation skyrocketing to reach us$ 119.71 billion by 2032. Technical report, Astute Analytica, 2023.

[4] Michael Gargalakos. The role of unmanned aerial vehicles in military communications: application scenarios, current trends, and beyond. *The Journal of Defense Modeling and Simulation*, 21(3):313–321, 2024.

[5] Nima Moradi, Chun Wang, and Fereshteh Mafakheri. Urban air mobility for last-mile transportation: A review. *Vehicles*, 6(3):1383–1414, 2024.

[6] Laura Aileen Sauls, Jaime Paneque-Gálvez, Mónica Amador-Jiménez, Nicolás Vargas-Ramírez, and Yves Laumonier. Drones, communities and nature: pitfalls and possibilities for conservation and territorial rights. *Global Social Challenges Journal*, 2(1):24–46, 2023.

[7] Taha Benarbia and Kyandoghere Kyamakya. A literature review of drone-based package delivery logistics systems and their implementation feasibility. *Sustainability*, 14(1):360, 2021.

[8] Vikram Puri, Anand Nayyar, and Linesh Raja. Agriculture drones: A modern breakthrough in precision agriculture. *Journal of Statistics and Management Systems*, 20(4):507–518, 2017.

[9] Thomas J Mueller and James D DeLaurier. Aerodynamics of small vehicles. *Annual review of fluid mechanics*, 35(1), 2003.

[10] J. Winslow, H. Otsuka, B. Govindarajan, and Chopra I. Basic understanding of airfoil characteristics at low reynolds numbers (10^{4}˘10^{5}). *Journal of Aircraft*, 55(3):1050–1061, 2018.

[11] M. Cerny and C. Breitsamter. Investigation of small-scale propellers under non-axial inflow conditions. *Aerospace Science and Technology*, 106:106048, 2020.

[12] B. Theys, G. Dimitriadis, T. Andrianne, P. Hendrick, and J. De Schutter. Wind tunnel testing of a vtol mav propeller in tilted operating mode. In *2014 International conference on unmanned aircraft systems (ICUAS)*, pages 1064–1072. IEEE, 2014.

[13] Y. Yang, Y. Liu, Y. Li, E. Arcondoulis, and Y. Wang. Aerodynamic and aeroacoustic performance of an isolated multicopter rotor during forward flight. *AIAA Journal*, 58(3):1171–1181, 2020.

[14] Benjamin R Hein and Inderjit Chopra. Hover performance of a micro air vehicle: rotors at low reynolds number. *Journal of the American Helicopter Society*, 52(3):254–262, 2007.

[15] M. Ramasamy, B. Johnson, and J. Leishman. Understanding the aerodynamic efficiency of a hovering micro-rotor. *Journal of The American Helicopter Society - J AMER HELICOPTER SOC*, 53, 10 2008.

[16] J. Milluzzo and J. G. Leishman. Fluid dynamics of the helicoidal wake sheets trailed from a hovering rotor. *Journal of the American Helicopter Society*, 61(1):1–17, 2016.

[17] M. Carreño Ruiz, M. Scanavino, D. D'Ambrosio, G. Guglieri, and A. Vilardi. Experimental and numerical analysis of hovering multicopter performance in low-reynolds number conditions. *Aerospace Science and Technology*, 128:107777, 2022.

[18] E. Grande, G. Romani, D. Ragni, F. Avallone, and D. Casalino. Aeroacoustic investigation of a propeller operating at low reynolds numbers. *AIAA Journal*, 60(2):860–871, 2022.

[19] E. Grande, D. Ragni, F. Avallone, and D. Casalino. Laminar separation bubble noise on a propeller operating at low reynolds numbers. *AIAA Journal*, 60(9):5324–5335, 2022.

[20] Johan Valentin. *Multi-Fidelity Coupling of Vortex Particles with Lifting Lines and Eulerian Methods for the Simulation of 3D Viscous Aeronautical Flows*. PhD thesis, École Doctorale Physique, Sciences de l'Ingénieur, Matériaux, Énergie, INSA Rouen Normandie, 2024.

[21] Johan Valentin, Luis Bernardos, Elie Rivoalen, and Gregory Pinon. Simulation of lifting bodies with vortex particles through active enstrophy control. *AIAA Journal*, pages 1–15, 2025.

[22] Johan Valentin, Luis Bernardos, Elie Rivoalen, and Gregory Pinon. Vortex particle velocity diffusion method using dynamic turbulence control based on enstrophy. *AIAA Journal*, pages 1–11, 2025.

[23] Dongli Ma, Yanping Zhao, Yuhang Qiao, and Guanxiong Li. Effects of relative thickness on aerodynamic characteristics of airfoil at a low reynolds number. *Chinese Journal of Aeronautics*, 28(4):1003–1015, 2015.

[24] S Wang, Y Zhou, Md Mahbub Alam, and Hongxing Yang. Turbulent intensity and reynolds number effects on an airfoil at low reynolds numbers. *Physics of Fluids*, 26(11), 2014.

[25] Kemal Koca, Mustafa Serdar Genç, Halil Hakan Açıkel, Mücahit Çağdaş, and Tuna Murat Bodur. Identification of flow phenomena over naca 4412 wind turbine airfoil at low reynolds numbers and role of laminar separation bubble on flow evolution. *Energy*, 144:750–764, 2018.

[26] VE Baskin, LS Vildgrube, Ye S Vozhdayev, CI Maykapar, and AK Martynov. Theory of the lifting airscrew. *Transl. into ENGLISH of the book"" Teoriya Nesushchego Vinta" Moscow, Mashinostroyeniye Press, 1973 p 1-364*, 1976.

[27] SJ Newman. Principles of helicopter aerodynamics–second edition jg leishmann cambridge university press, the edinburgh building, shaftesbury road, cambridge, cb2 2ru, uk. 2006. 826pp. illustrated.£ 65. isbn 0-521-85860-7. *The Aeronautical Journal*, 111(1126):825–826, 2007.

[28] P Brotherhood and William Stewart. An experimental investigation of the flow through a helicopter rotor in forward flight. 1949.

[29] IC Cheeseman and WE Bennett. The effect of the ground on a helicopter rotor in forward flight. 1955.

[30] T Berenger, D Favier, C Maresca, and Eric Berton. Experimental and numerical investigation of rotor aerodynamics in forward flight. *Journal of aircraft*, 34(3):394–399, 1997.

[31] Catharina Moreira, Nikolai Herzog, and Christian Breitsamter. Wind tunnel investigation of transient propeller loads for non-axial inflow conditions. *Aerospace*, 11(4):274, 2024.

[32] Jinglin Luo, Longfei Zhu, and Guirong Yan. Novel quadrotor forward-flight model based on wake interference. *AIAA Journal*, 53(12):3522–3533, 2015.

[33] Nur Syafiqah Jamaluddin, Alper Celik, Kabilan Baskaran, Djamel Rezgui, and Mahdi Azarpeyvand. Aerodynamic noise analysis of tilting rotor in edgewise flow conditions. *Journal of Sound and Vibration*, 582:118423, 2024.

[34] Richard Malcolm Kelso, TT Lim, and AE Perry. An experimental study of round jets in cross-flow. *Journal of fluid mechanics*, 306:111–144, 1996.

[35] Sheng Wen, Jie Han, Zhihua Ning, Yubin Lan, Xuanchun Yin, Jiantao Zhang, and Yufeng Ge. Numerical analysis and validation of spray distributions disturbed by quad-rotor drone wake at different flight speeds. *Computers and Electronics in Agriculture*, 166:105036, 2019.

[36] Manuel Carreño Ruiz, Nicoletta Bloise, Giorgio Guglieri, and Domenic. D'Ambrosio. Toward virtual testing of unmanned aerial spraying systems operating in vineyards. *Drones*, 8(3):98, 2024.

[37] Nicoletta Bloise, Manuel Carreño Ruiz, Domenic D'Ambrosio, and Giorgio. Guglieri. Preliminary design of a remotely piloted aircraft system for crop-spraying on vineyards. In *2020 IEEE International Workshop on Metrology for Agriculture and Forestry (MetroAgriFor)*, pages 1–6. IEEE, 2020.

[38] Dariusz Marek, Marcin Paszkuta, Jakub Szyguła, Piotr Biernacki, Adam Domański, Marta Szczygieł, Marcel Król, and Konrad Wojciechowski. Swarm of drones in a simulation environment—efficiency and adaptation. *Applied Sciences*, 14(9):3703, 2024.

[39] SunHoo Park, Sihun Lee, Byeonguk Im, Dongyeol Lee, and SangJoon Shin. Improvement of a multi-rotor uav flight response simulation influenced by gust. *Aerospace Science and Technology*, 134:108156, 2023.

[40] Simon Watkins, Jane Burry, Abdulghani Mohamed, Matthew Marino, Samuel Prudden, Alex Fisher, Nicola Kloet, Timothy Jakobi, and Reece Clothier. Ten questions concerning the use of drones in urban environments. *Building and Environment*, 167:106458, 2020.

[41] Felix Möhren, Ole Bergmann, Carsten Braun, and Frank Janser. Prediction and comparison of dynamic loads of propellers. In *AIAA SciTech 2022 Forum*, page 2267, 2022.

[42] Nickolay Zosimovych. Flight transient estimation of vtol aircraft with propellers. *Advances in Aerospace Science and Technology*, 7(1):85–95, 2022.

[43] Ole Bergmann, Felix Möhren, Carsten Braun, and Frank Janser. Propeller noise prediction for transient evtol missions. In *AIAA SCITECH 2024 Forum*, page 2636, 2024.

[44] Marilena D Pavel. Understanding the control characteristics of electric vertical take-off and landing (evtol) aircraft for urban air mobility. *Aerospace Science and Technology*, 125:107143, 2022.

[45] Ronald J Adrian and Jerry Westerweel. *Particle image velocimetry*. Number 30. Cambridge university press, 2011.

[46] Marcel Lesieur, Olivier Métais, and Pierre Comte. *Large-eddy simulations of turbulence*. Cambridge university press, 2005.

[47] A. M. Pérez Gordillo, J. S. Villegas Santos, O. D. Lopez Mejia, L. J. Suarez Collazos, and J. A Escobar. Numerical and experimental estimation of the efficiency of a quadcopter rotor operating at hover. *Energies*, 12(2):261, 2019.

[48] M. C. Ruiz, M. Scanavino, D. D'Ambrosio, G. Guglieri, and A. Vilardi. Experimental and numerical analysis of hovering multicopter performance in low-reynolds number conditions. *Aerospace Science and Technology*, 128:107777, 2022.

[49] Manuel CARRENO RUIZ et al. *Numerical Simulation and Aerodynamic Design of Small-Scale Rotary-Wing for Unmanned Aerial Systems in Terrestrial and Martian Applications*. PhD thesis, Politecnico di Torino, 2023.

[50] David C Wilcox et al. *Turbulence modeling for CFD*, volume 2. DCW industries La Canada, CA, 1998.

[51] Georges-Henri Cottet. Vortex methods: theory and practice. *Measurement Science and Technology*, 2001.

[52] M Safdari Shadloo, G Oger, and David Le Touzé. Smoothed particle hydrodynamics method for fluid flows, towards industrial applications: Motivations, current state, and challenges. *Computers & Fluids*, 136:11–34, 2016.

[53] Eduardo J Alvarez and Andrew Ning. Reviving the vortex particle method: A stable formulation for meshless large eddy simulation. *arXiv preprint arXiv:2206.03658*, 2022.

[54] Eduardo J Alvarez and Andrew Ning. Modeling multirotor aerodynamic interactions through the vortex particle method. In *AIAA Aviation 2019 Forum*, page 2827, 2019.

[55] Johan Valentin, Luis F Bernardos, Gregory Pinon, and Elie Rivoalen. Hybrid eulerian-lagrangian method for complex 3d viscous flows. In *AIAA AVIATION FORUM AND ASCEND 2024*, page 3865, 2024.

[56] Davide Montagnani, Matteo Tugnoli, Federico Fonte, Alex Zanotti, Monica Syal, Giovanni Droandi, et al. Mid-fidelity analysis of unsteady interactional aerodynamics of complex vtol configurations. In *45th European Rotorcraft Forum (ERF 2019)*, pages 100–110, 2019.

[57] D. Casalino, E. Grande, G. Romani, D. Ragni, and F. Avallone. Definition of a benchmark for low reynolds number propeller aeroacoustics. *Aerospace Science and Technology*, 113:106707, 2021.

[58] Markus Raffel, Christian E Willert, Fulvio Scarano, Christian J Kähler, Steve T Wereley, and Jürgen Kompenhans. *Particle image velocimetry: a practical guide*. springer, 2018.

[59] Ajay K Prasad. Stereoscopic particle image velocimetry. *Experiments in fluids*, 29(2):103–116, 2000.

[60] Gerrit E Elsinga, Fulvio Scarano, Bernhard Wieneke, and Bas W van Oudheusden. Tomographic particle image velocimetry. *Experiments in fluids*, 41(6):933–947, 2006.

[61] T. Jardin, S. Prothin, and C. Magaña. Aerodynamic performance of a hovering microrotor in confined environment. *Journal of the American Helicopter Society*, 62(2):1–7, 2017.

[62] S. Prothin, C. Fernandez Escudero, N. Doué, and T. Jardin. Aerodynamics of mav rotors in ground and corner effect. *International Journal of Micro Air Vehicles*, 11:1756829319861596, 2019.

[63] C. Nardari, D. Casalino, F. Polidoro, V. Coralic, P. Lew, and J. Brodie. Numerical and experimental investigation of flow confinement effects on uav rotor noise. In *25th AIAA/CEAS Aeroacoustics Conference*, page 2497, 2019.

[64] T. Astarita and G. Cardone. Analysis of interpolation schemes for image deformation methods in piv. *Experiments in fluids*, 38:233–243, 2005.

[65] T. Astarita. Analysis of velocity interpolation schemes for image deformation methods in piv. *Experiments in Fluids*, 45:257–266, 2008.

[66] T Astarita. Analysis of weighting windows for image deformation methods in piv. *Experiments in fluids*, 43:859–872, 2007.

[67] Andrea Sciacchitano and Bernhard Wieneke. Piv uncertainty propagation. *Measurement Science and Technology*, 27(8):084006, 2016.

[68] Gerardo Paolillo, Tommaso Astarita, et al. Pairs-unina: A robust and accurate free tool for digital particle image velocimetry and optical camera calibration. In *Proceedings of 21st International Symposium on Applications of Laser and Imaging Techniques to Fluid Mechanics*, 2024.

[69] Massimo Germano, Ugo Piomelli, Parviz Moin, and William H Cabot. A dynamic subgrid-scale eddy viscosity model. *Physics of Fluids A: Fluid Dynamics*, 3(7):1760–1765, 1991.

[70] Douglas K Lilly. A proposed modification of the germano subgrid-scale closure method. *Physics of Fluids A: Fluid Dynamics*, 4(3):633–635, 1992.

[71] Pietro. Catalano and Renato. Tognaccini. Large eddy simulations of the flow around the SD7003 airfoil. In *AIMETA Conference*, pages 1–10, 2011.

[72] Manuel Carreño Ruiz and Domenic. D'Ambrosio. Implicit and explicit large eddy simulations in martian aerodynamics. In *AIAA AVIATION 2025 Forum*, Las Vegas, NV, Jul 2025. AIAA-2025-3585.

[73] Jonathan M Weiss and Wayne A Smith. Preconditioning applied to variable and constant density flows. *AIAA journal*, 33(11):2050–2057, 1995.

[74] Christopher C Nelson, Yushi Yanagita, and Lakshmi N Sankar. Anhedral tip effects on forward flight inflow and airloads. In *AIAA SciTech 2024 Forum*, January January 2024. AIAA 2024-0009.

[75] Florian R Menter. Two-equation eddy-viscosity turbulence models for engineering applications. *AIAA journal*, 32(8):1598–1605, 1994.

[76] Robin B Langtry and Florian R Menter. Correlation-based transition modeling for unstructured parallelized computational fluid dynamics codes. *AIAA journal*, 47(12):2894–2906, 2009.

[77] John Webster, Wayne Neu, and Stefano Brizzolara. Reynolds stress transition modeling for marine propellers at low reynolds number. In *Sixth International Symposium on Marine Propulsors: Smp19*, 2019.

[78] Eric Vargas Loureiro, Nicolas Lima Oliveira, Patricia Habib Hallak, Flávia de Souza Bastos, Lucas Machado Rocha, Rafael Grande Pancini Delmonte, and Afonso Celso de Castro Lemonge. Evaluation of low fidelity and cfd methods for the aerodynamic performance of a small propeller. *Aerospace Science and Technology*, 108:106402, 2021.

[79] Laurent Cambier, Sébastien Heib, and Sylvie Plot. The onera elsa cfd software: input from research and feedback from industry. *Mechanics & Industry*, 14(3):159–174, 2013.

[80] John R Mansfield, Omar M Knio, and Charles Meneveau. Dynamic les of colliding vortex rings using a 3d vortex method. *Journal of Computational Physics*, 152(1):305–345, 1999.

[81] John R Mansfield, Omar M Knio, and Charles Meneveau. A dynamic les scheme for the vorticity transport equation: Formulation anda prioritests. *Journal of Computational Physics*, 145(2):693–730, 1998.

[82] Tingyu Wang, Rio Yokota, and Lorena A Barba. Exafmm: a high-performance fast multipole method library with c++ and python interfaces. *Journal of Open Source Software*, 6(61):3145, 2021.

[83] Paul Mycek, Grégory Pinon, Grégory Germain, and Élie Rivoalen. A self-regularising dvm–pse method for the modelling of diffusion in particle methods. *Comptes Rendus Mécanique*, 341(9-10):709–714, 2013.

[84] Paul Mycek, Grégory Pinon, Grégory Germain, and Elie Rivoalen. Formulation and analysis of a diffusion-velocity particle model for transport-dispersion equations. *Computational and Applied Mathematics*, 35:447–473, 2016.

[85] Sylvie Mas-Gallic. The diffusion velocity method: a deterministic way of moving the nodes for solving diffusion equations. *Transport Theory and Statistical Physics*, 31(4-6):595–605, 2002.

[86] Rio Yokota, Lorena A Barba, Tetsu Narumi, and Kenji Yasuoka. Petascale turbulence simulation using a highly parallel fast multipole method on gpus. *Computer Physics Communications*, 184(3):445–455, 2013.

[87] Walter Tollmien, Hermann Schlichting, Henry Görtler, Walter Tollmien, Hermann Schlichting, Henry Görtler, and FW Riegels. Bericht über untersuchungen zur ausgebildeten turbulenz. *Ludwig Prandtl Gesammelte Abhandlungen: zur angewandten Mechanik, Hydro-und Aerodynamik*, pages 714–718, 1961.

[88] Dochan Kwak, William C Reynolds, and Joel H Ferziger. Three-dimensional time dependent computation of turbulent flow. Technical report, 1975.

[89] AW Vreman. An eddy-viscosity subgrid-scale model for turbulent shear flow: Algebraic theory and applications. *Physics of fluids*, 16(10):3670–3681, 2004.

[90] Gianni Pedrizzetti. Insight into singular vortex flows. *Fluid Dynamics Research*, 10(2):101, 1992.

[91] S. Backaert, P. Chatelain, and G. Winckelmans. Vortex particle-mesh with immersed lifting lines for aerospace and wind engineering. *Procedia IUTAM*, 18:1–7, 2015. IUTAM Symposium on Particle Methods in Fluid Dynamics.

[92] Denis-Gabriel Caprace, Grégoire Winckelmans, and Philippe Chatelain. An immersed lifting and dragging line model for the vortex particle-mesh method. *Theoretical and Computational Fluid Dynamics*, 34(1):21–48, 2020.

[93] Chris C Critzos, Harry H Heyson, and Robert W Boswinkle Jr. Aerodynamic characteristics of naca 0012 airfoil section at angles of attack from 0 deg to 180 deg. *Report No. NASA TN3361*, 1955.

[94] Mark Drela. Xfoil: An analysis and design system for low reynolds number airfoils. In *Low Reynolds Number Aerodynamics: Proceedings of the Conference Notre Dame, Indiana, USA, 5–7 June 1989*, pages 1–12. Springer, 1989.

[95] Leslie M Mack. Transition prediction and linear stability theory. *In AGARD Laminar-Turbulent Transition 22 p (SEE N78-14316 05-34*, 1977.

[96] Alejandra Uranga Uranga Cabrera. *Investigation of transition to turbulence at low Reynolds numbers using Implicit Large Eddy Simulations with a Discontinuous Galerkin method*. PhD thesis, Massachusetts Institute of Technology, 2010.

[97] A Gupta, P Narayana, and G Ramesh. Effect of turbulence intensity on low reynolds number airfoil aerodynamics. *Int. J. Eng. Technol*, 7(4.25), 2018.

[98] Manuel Carreño Ruiz and Domenic D'ambrosio. Validation of the γ-re θ transition model for airfoils operating in the very low reynolds number regime. *Flow, Turbulence and Combustion*, 109(2):279–308, 2022.

[99] Alexandre Joel Chorin. A numerical method for solving incompressible viscous flow problems. *Journal of computational physics*, 135(2):118–125, 1997.

[100] S Venkateswaran and Charles Merkle. Dual time-stepping and preconditioning for unsteady computations. In *33rd Aerospace Sciences Meeting and Exhibit*, page 78, 1995.

[101] Woutijn J Baars, Giulio Dacome, and Myoungkyu Lee. Reynolds-number scaling of wall-pressure–velocity correlations in wall-bounded turbulence. *Journal of Fluid Mechanics*, 981:A15, 2024.

[102] Jinhee Jeong and Fazle Hussain. On the identification of a vortex. *Journal of Fluid Mechanics*, 285:69–94, 1995.

[103] J. Hunt, Alan Wray, and Parviz Moin. Eddies, streams, and convergence zones in turbulent flows. *Studying Turbulence Using Numerical Simulation Databases*, -1:193–208, 11 1988.

[104] L. Graftieaux, M. Michard, and N. Grosjean. Combining piv, pod and vortex identification algorithms for the study of unsteady turbulent swirling flows. *Measurement Science and technology*, 12(9):1422, 2001.

[105] F. De Gregorio and A. Visingardi. Vortex detection criteria assessment for piv data in rotorcraft applications. *Experiments in Fluids*, 61:1–22, 2020.

[106] G. Cafiero, G. Castrillo, C.S. Greco, and T. Astarita. On the effects of square-fractal turbulators on the flow field generated by a synthetic jet actuator. *Experimental Thermal and Fluid Science*, 102:302–315, 2019.

[107] F. De Gregorio, A. Visingardi, and G. Iuso. An experimental-numerical investigation of the wake structure of a hovering rotor by piv combined with a γ_2 vortex detection criterion. *Energies*, 14(9):2613, 2021.

[108] R. Soto-Valle, S. Cioni, S. Bartholomay, M. Manolesos, C.N. Nayeri, A. Bianchini, and C. O. Paschereit. Vortex identification methods applied to wind turbine tip vortices. *Wind Energy Science*, 7(2):585–602, 2022.

[109] John Leask Lumley. The structure of inhomogeneous turbulent flows. *Atmospheric turbulence and radio wave propagation*, pages 166–178, 1967.

[110] Mark N Glauser and William K George. An orthogonal decomposition of the axisymmetric jet mixing layer utilizing cross-wire velocity measurements. In *6th Symposium on Turbulent Shear Flows*, pages 10_1_1–10_1_6, 1987.

[111] Lawrence Sirovich. Turbulence and the dynamics of coherent structures. i. coherent structures. *Quarterly of applied mathematics*, 45(3):561–571, 1987.

[112] Gene H Golub and Charles F Van Loan. *Matrix computations*. JHU press, 2013.

[113] Lloyd N Trefethen and David Bau. *Numerical linear algebra*. SIAM, 2022.

[114] Nadine Aubry, Philip Holmes, John L. Lumley, and Emily Stone. The dynamics of coherent structures in the wall region of a turbulent boundary layer. *Journal of Fluid Mechanics*, 192:115–173, 1988.

[115] Clarence W Rowley. Model reduction for fluids, using balanced proper orthogonal decomposition. *International Journal of Bifurcation and Chaos*, 15(03):997–1013, 2005.

[116] Delphine De Tavernier, Carlos Ferreira, and Anders Goude. Vertical-axis wind turbine aerodynamics. In *Handbook of Wind Energy Aerodynamics*, pages 1–44. Springer, 2022.

[117] Wayne Johnson. *Helicopter Theory*. Princeton University Press, 1980.

[118] Jack L Kerrebrock. *Aircraft engines and gas turbines*. MIT press, 1992.

[119] Nathan S Hariharan, T Alan Egolf, and Lakshmi N Sankar. Simulation of rotor in hover: Current state, challenges and standardized evaluation. In *52nd Aerospace Sciences Meeting*, page 0041, 2014.

[120] FAA. *Helicopter Flying Handbook*. United States Department of Transportation, Federal Aviation Administration, Airman Testing Branch, P.O. Box 25082, Oklahoma City, OK 73125, 2019.

[121] H. Glauert and Great Britain. Air Ministry. *On the horizontal flight of a helicopter*. Reports and Memoranda ; No. 1157. H.M. Stationery Office, 1928.

[122] DR Getsinger, L Gevorkyan, OI Smith, and AR Karagozian. Structural and stability characteristics of jets in crossflow. *Journal of Fluid Mechanics*, 760:342–367, 2014.

[123] Ann R Karagozian. The jet in crossflow. *Physics of Fluids*, 26(10), 2014.

[124] Matthew Misiorowski, Farhan Gandhi, and Assad A Oberai. Computational study on rotor interactional effects for a quadcopter in edgewise flight. *AIAA Journal*, 57(12):5309–5319, 2019.

[125] Patricia Ventura Diaz and Steven Yoon. High-fidelity simulations of a quadrotor vehicle for urban air mobility. In *AIAA SciTech 2022 Forum*, page 0152, 2022.

[126] Albert R George and S-T Chou. A comparative study of tail rotor noise mechanisms. *Journal of the American Helicopter Society*, 31(4):36–42, 1986.

[127] Harry H Heyson and S Katzoff. Induced velocities near a lifting rotor with nonuniform disk loading. Technical report, 1957.

[128] Gordon J Leishman. *Principles of helicopter aerodynamics*. Cambridge university press, 2006.

[129] Bryan K Slinker and Stanton Arnold Glantz. *Primer of applied regression and analysis of variance*. McGraw-Hill, 1990.

[130] Nicoletta Bloise, Manuel Carreño Ruiz, Domenic D'Ambrosio, and Giorgio Guglieri. Preliminary design of a remotely piloted aircraft system for crop-spraying on vineyards. In *2020 IEEE International Workshop on Metrology for Agriculture and Forestry (MetroAgriFor)*, pages 1–6. IEEE, 2020.

[131] P. Welch. The use of fast fourier transform for the estimation of power spectra: a method based on time averaging over short, modified periodograms. *IEEE Transactions on audio and electroacoustics*, 15(2):70–73, 1967.

[132] Anatol Roshko. On the drag and shedding frequency of two-dimensional bluff bodies. Technical report, 1954.

[133] Tianyu Xia, Hao Dong, Liming Yang, Shicheng Liu, and Zhou Jin. Investigation on flow structure and aerodynamic characteristics over an airfoil at low reynolds number—a review. *AIP Advances*, 11(5):050701, 05 2021.

[134] Albert Brand, Mark Dreier, Ron Kisor, and Tom Wood. The nature of vortex ring state. *Journal of the American Helicopter Society*, 56(2):22001–22001, 2011.

[135] Flavio Noca, Thierry Bujard, Geshanth Visvaratnam, Guillaume Catry, and Nicolas Bosson. Flow profiling in a windshaper for testing free-flying drones in adverse winds. In *AIAA Aviation 2021 Forum*, page 2577, 2021.